Novel tissue engineering approaches to enhance natural bone formation

Anthony John Deegan

School of Postgraduate Medicine

Institute for Science and Technology in Medicine

Keele University

Thesis submitted to Keele University for the degree of

Doctor of Philosophy in Biomedical Engineering

July 2016

Abstract

The bone tissue engineering community has been striving to develop novel approaches that mimic natural bone formation. The rapid generation of mineralised bone tissue with a capacity for vascularisation and the selection of highly osteogenic cell sources are still the focus of research today. This study addresses three novel approaches in these key areas.

Mineralisation in bone tissue involves stepwise cell – cell and cell – extracellular matrix (ECM) interactions. Regulation of the osteoblast culture microenvironment can manipulate osteoblast proliferation and mineralisation rates and consequently the quality and/or quantity of the final calcified tissue. Therefore, an *in vitro* model to investigate possible influential factors would be highly sought after. We developed a facile *in vitro* model through the modification of culture surfaces in which an osteoblast cell line and aggregate culture was used to mimic intramembranous ossification. Conventional monolayer culturing was used as a comparative control. The effects of multiple culture parameters, including culture duration and aggregate size, on mineralisation rates and subsequent mineral quantities and distributions have been examined by numerous well established methods alongside certain innovative techniques.

Ultimately, spatial and temporal production of minerals differed depending upon aggregate size with larger aggregates mineralising faster with a distinct gene expression pattern compared to the smaller aggregates. We also demonstrated that mineralisation in the larger aggregates initiated from the periphery, whilst mineralisation in the smaller aggregates initiated from the centre. This implies that aggregate size influences mineral distribution and development over time.

An *in vivo* study using a cell line and primary cell population was conducted to investigate how the observations noted during the short term *in vitro* studies would affect long term *in vivo* aggregate survival and bone formation. Both cell types saw similar results. The large aggregates appeared to disintegrate over the course of the experiment, whilst the small aggregates remained intact and produced an abundant volume of extracellular material. A monolayer cell sample was again used as a comparative control and generated a lower material volume over the same period. The data obtained from this element of the project produced some invaluable insights into how the specific variables of cellular aggregation might affect possible bone formation *in vivo*.

In addition, a novel substrate, substrate X, was used to identify and investigate the possibility of mesenchymal stem cell (MSC) subpopulations within mixed MSC populations and their donor-dependent variations alongside their subsequent influences upon an individual's osteogenic capacity. Substrate X successfully identified what are thought to be three subpopulations within individual MSC populations from multiple donors through distinct cellular attachments. Each of the subpopulations was shown to hold differing osteogenic capacities and their proportions were also shown to be donor-dependent. Subpopulation proportions were shown to correlate with specific cadherin levels and cellular aggregation potential was also shown to be donor-dependent.

Furthermore, the novel aggregation technique developed by this study was pitted against a conventional aggregation technique to assess aggregate vascularisation and mineralisation simultaneously using cellular co-culturing. This study also investigated how mechanical stimulation would affect aggregate vascularisation and mineralisation. The method of aggregation developed earlier in this project was shown to create an inner-aggregate architecture that aided in specific cellular organisation and possible vascularisation more than the conventional aggregation technique. The mechanical stimulation reduced cellular migration from the aggregate body compared to a static culture equivalent but nodule mineralisation within the co-cultured aggregates was inconclusive due to the short culture period.

To conclude, simple yet effective substrate chemistry modifications enabled us to evaluate a variety of parameters for refined bone tissue engineering. These included the development of an aggregate model for the study of developing mineralisation, possible MSC subpopulation identification, measurement and assessment and the evaluation of aggregate vascularisation.

Contents

List of Figures

List of Tables

Acknowledgements

I would firstly like to acknowledge and thank my supervisor Prof. Ying Yang for her guidance, support and patience throughout this project. Without Ying's drive and unrivalled enthusiasm for research this thesis would not have come to fruition. I'd also like to thank my co-supervisor Sandeep Konduru for his expertise and continued input.

I'd like to thank Dr Gianfelice Cinque, Dr Katia Wehbe, Dr Jacob Filik and Dr Paul Donaldson of Beamline B22, Diamond Light Source, for introducing me to and guiding me through the intricacies of microspectroscopy. The team at Diamond were so knowledgeable and helpful they made the long working hours at the synchrotron both profitable and enjoyable.

I'd also like to acknowledge and thank Dr Jeroen Rouwkema and Dr Wim Hendrikson for the opportunity to collaborate with them on the vascularisation study. This element of the project I found hugely interesting and I am immensely grateful for the opportunity to visit and work at the University of Twente, Netherlands. Jeroen and Wim were an absolute pleasure to work with and I'd consider myself very lucky if I were given the opportunity to work with them again.

I would also like to acknowledge and thank Leeds University Animal House for making my *in vivo* work possible. I couldn't have asked for a more accommodating and professional team to work with.

I'd like to thank Dr Hu Bin for her help with the PCR work and David Emley for his contribution to my SEM-EDX work. I'd like to acknowledge Dr Jan Herman Kuiper for his invaluable contributions to many aspects of this project. And to my fellow PhDs and postdocs at Guy Hilton, a genuine and heartfelt thank you for all your help with literally every aspect of my research and for making my Guy Hilton experience a truly enjoyable and unforgettable one; particularly, Tina for all of her help with just about everything, Abbie for her help with my FTIR work, Lanxin, Ipek and Sue for their contributions to my subpopulation work, Faiza, Hati, Yanny and Sandhya for all of their varied and many contributions to my work and procrastination, and James for all the laughs, desktop backgrounds and portraits left on my desk.

I'd also like to express my gratitude to my parents, Mary and Billy, and my twin, Ann-marie, who supported me wholeheartedly in too many ways to mention throughout my entire education.

Associated Publications

Deegan AJ, Aydin HM, Hu B, Konduru S, Kuiper JH, Yang Y. A facile *in vitro* model to study rapid mineralisation in bone tissues. *Biomed Eng Online*, **2014** Sept;13:136

Deegan AJ, Cinque G, Wehbe K, Konduru S, Yang Y. Tracking calcification in tissue-engineered bone using synchrotron micro-FTIR and SEM. *Anal Bioanal Chem*, **2015** Feb;407(4):1097

Abbreviations

Table 1: A complete list of abbreviations and their meanings used throughout the thesis.

Abbreviation	Full Terminology
2D	Two-dimensional
3D	Three-dimensional
α-MEM	Minimum essential medium eagle alpha
A	
A + A	Antibiotic-antimycotic solution
AFM	Atomic force microscopy
ALP	Alkaline phosphatase
ANOVA	Analysis of variance
AU	Arbitrary unit
B	
BCS	Bovine calf serum
BMP	Bone morphogenetic protein
BMP-2	Bone morphogenetic protein 2
BMSC	Bone marrow stromal cell
BSA	Bovine serum albumin
C	
Ca:P	Calcium-to-phosphorus ratio
CaO	Calcium oxide
CapG	Macrophage-capping protein
CCE	Counterflow centrifugal elutriation
cDNA	Complimentary deoxyribonucleic acid
CI	Confidence interval
CK2	Casein kinase II
COL 1	Collagen type I
D	
DAH	Differential adhesion hypothesis
Dlx5	Distal-less homeobox 5

DMEM	Dulbecco's modified eagle medium
DSLR	Digital single-lens reflex
E	
EC	Endothelial cell
ECM	Extracellular matrix
EDX	Energy-dispersive X-ray
EGF	Epidermal growth factor
ESC	Embryonic stem cell
F	
FACIT	Fibril associated collagens with interrupted triple helices
FACS	Fluorescence-activated cell sorting
FBS	Fetal bovine serum
FGF-2	Basic fibroblast growth factor
FOV	Field of view
FTIR	Fourier transform infrared spectroscopy
G	
GAG	Glycosaminoglycan
gDNA	Genomic deoxyribonucleic acid
GVHD	Graft versus host disease
H	
H & E	Haematoxylin and eosin
HA	Hydroxyapatite
HGF	Hepatocyte growth factor
HIF-1	Hypoxia-inducible factor 1
hMSC	Human mesenchymal stem cell
HSC	Haematopoietic stem cell
HUVEC	Human umbilical vein endothelial cell
I	
IBMX	3-isobutyl-1-methylxanthine
IGF	Insulin growth factor
IGF-1	Insulin growth factor 1
IGF-2	Insulin growth factor 2
IL-10	Interleukin 10
IL-1β	Interleukin 1β
IL-6	Interleukin 6
IR	Infrared
ISCT	International Society of Cellular Therapy
ITS	Insulin-transferrin-selenium
L	
LSGS	Low serum growth supplement
M	
MAP	Multipotent adult progenitor cell
M-CSF	Macrophage colony-stimulating factor

MEST	Mesoderm specific transcript isoform b
MicroCT/µCT	Microcomputerised tomography
MicroFTIR	Fourier transform infrared microspectroscopy
MMP-13	Matrix metallopeptidase 13
MMP-9	Matrix metallopeptidase 9
MNC	Mononuclear cell
MSC	Mesenchymal stem cell
Msx2	Msh homeobox 2
MUSE	Multilineage-differentiating stress-enduring cell
N	
Na_2CO_3	Sodium carbonate
NaCl	Sodium chloride
$NaHCO_3$	Sodium bicarbonate
NaOH	Sodium hydroxide
NEAA	Non-essential amino acids
O	
OCN	Osteocalcin
OCT	Optimal cutting temperature compound
OI	Osteogenesis imperfecta
OPN	Osteopontin
Osx	Osteoblast-specific transcription factor osterix
P	
PBS	Phosphate buffered saline
PBS-Tx	Triton X-100 in PBS
PCR	Polymerase chain reaction
PDGF	Platelet-derived growth factor
PEM	Polyelectrolyte multilayer
PEMF	Pulsed electromagnetic field
PEO	Polyethylene oxide
PFA	Paraformaldehyde
PO_4	Phosphate
POSS-PCU	Polyhedral oligomeric silsesquioxane poly(carbonate-urea) urethane
PPO	Polypropylene oxide
Q	
qPCR	Quantitative polymerase chain reaction
R	
RANKL	Receptor activator of nuclear factor-kappaB ligand
RNA	Ribonucleic acid
RT	Reverse transcription
Runx2	Runt-related transcription factor 2
S	
S:N	Signal-to-noise ratio
SEM	Scanning electron microscopy

sFBS	Standard foetal bovine serum
SOBL	Haversian system osteoblasts
T	
TBST	Tris-buffered saline and Tween 20
TCP	Tissue culture polystyrene
TGF-β	Transforming growth factor-β
TGF-β1	Transforming growth factor-β1
TGF-β3	Transforming growth factor-β3
THY1	Thy 1 membrane glycoprotein precursor
TNF-α	Tumour necrosis factor-α
U	
UNG	Uracil N-glycosylase
UV	Ultraviolet
V	
VEGF	Vascular endothelial growth factor
VSEL	Very small embryonic-like stem cell

Chapter One

Literature Review

Overview

Knowledge of current research trends and accomplishments is essential before any additional research can be conducted efficiently and/or successfully. A researcher needs to understand and learn from the advantages and disadvantages of previously conducted studies if any level of success is to be achieved and novelty maintained.

The following literature review describes natural bone formation pathways during growth and also regeneration following injury or defect. Current research trends designed to replace and/or replicate such processes are also discussed with the intention of providing a basic understanding as to why this research project was undertaken.

1. Introduction

The term 'regenerative medicine' was first coined back in 1992 by Leland Kaiser who forecasted that "a new branch of medicine will develop that attempts to change the course of chronic diseases and in many instances will regenerate tired and failing organ systems"[1]. Since then research has been carried out to find and develop new cell-based techniques and technologies that can aid in the regeneration of damaged tissues[2].

Regenerative medicine can be divided into two primary strategies for cell-based therapy. The first of which, known as 'cell therapy', simply involves the injection of cells into the circulation of damaged tissue. These cells are intended to replace those damaged cells within a tissue that impair its integrity or function. The second of which, is called 'tissue engineering'. Tissue engineering has been described as a more complex approach that involves the addition of cells to a three-dimensional (3D) matrix. This cell/matrix construct is designed to replicate *in vivo* tissue which can be used to replace large portions of damaged or lost tissue or even whole organs[2]. This, however, is not exclusively the case as many studies have researched tissue engineering strategies that forego the need for additional 3D biomaterial matrices, such as pellet culture models[3,4].The transplantation of organs and tissues for the treatment of organ and tissue loss and/or failure has a number of drawbacks, most notably limited donor supply and often severe immune complications. Regenerative medicine strategies, however, may hold the potential to bypass such obstacles[5]. This is especially true for bone tissue with engineered bone tissue being deemed a conceivable alternative to more conventional bone grafts[6].

1.1 The anatomy and physiology of bone

Bone can essentially be thought of in two different ways: as a tissue, bone simply includes the bone cells and mineralised matrix, but as an organ, bone includes numerous tissues, such as bone, cartilage, blood vessels, fibrous tissue and bone marrow[3] (fig. 1.1). Bone tissue is comprised of three primary components: the first of which is the inorganic phase, consisting largely of hydroxyapatite (HA), the second being the organic phase which is made up of collagen, non-collagenous proteins and lipids, and the third component being water. Various factors influence the ratios of these constituents, such as bone type, age, nutrition and health[7]. Typically though, bone consists of approximately 65% minerals, the majority of which are in the form of HA, and 35% organic matrix[8]. Collagen type I (COL 1), being the most abundant protein in the extracellular matrix (ECM) of bone, accounts for nearly 90% of the matrix (organic matrix)[9]. The remaining 10% of the matrix is composed of smaller molecular-sized proteoglycans and non-collagenous proteins, such as osteocalcin (OCN) (Gla protein), which is of particular interest here because it is specific to bone tissue. Another important component in bone is the sialoprotein, osteopontin (OPN)[8].

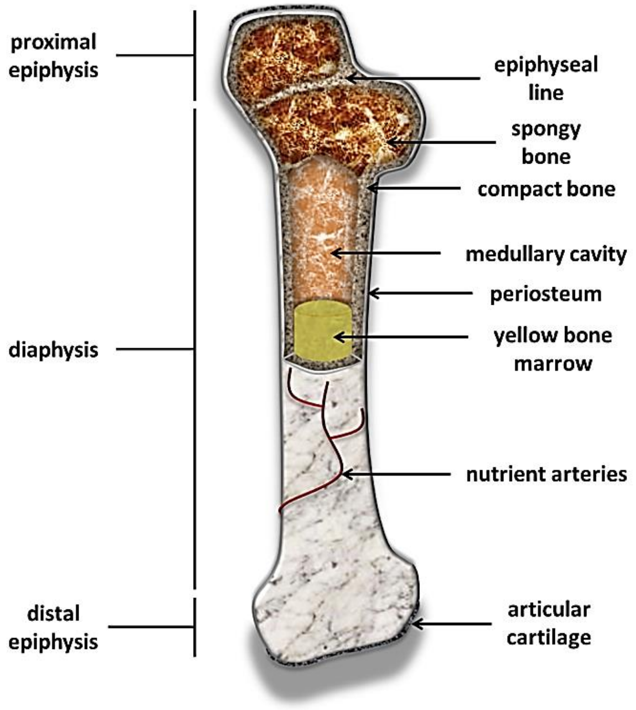

Figure 1.1: A dissected bone. Shown is the fundamental structure and primary components of bone (adapted from www.classes.midlandstech.edu, copyright © 2006 Pearson Education, Inc.)

Whilst the human skeleton is on average composed of 80% cortical bone and 20% trabecular bone[10], different bones and regions within such bones may have different ratios. The vertebra for example, comprise 25% cortical bone and 75% trabecular bone, the femoral head is 50% cortical bone and 50% trabecular bone, and the radial diaphysis is 95% cortical bone and 5% trabecular bone[11]. Cortical bone is a dense, solid tissue that surrounds the marrow space, whereas trabecular bone comprises a honeycomb-like network of trabecular plates and rods dispersed throughout the marrow space. Both cortical and trabecular bone are made up of osteons which in cortical bone are called Haversian systems and in trabecular bone are called packets[10]. Haversian systems are required to add to the permeability of the dense cortical bone through concentric layers of lamellae surrounding the Haversian canals. These canals carry the blood and nerve supply through the bone[10]. Surrounding the outer cortical surface of bone, except at joints where bone is lined by articular cartilage, is a fibrous connective tissue sheath called the periosteum. This sheath contains blood vessels and nerve fibres along with bone cells, osteoblasts and osteoclasts. The periosteum is closely affixed to the outer cortical surface of bone by thick collagenous fibres, called Sharpey's fibres, which reach into the underlying bone tissue. Counter to the periosteum is the endosteum. This is a membranous structure covering the inner surface of cortical bone, trabecular bone, and the blood vessel canals (Volkman's canals). The endosteum is in contact with the bone marrow space, trabecular bone, and blood vessel canals and like the periosteum, contains blood vessels, osteoblasts, and osteoclasts[11].

1.1.1 Important extracellular matrix proteins

The ECM of bone is composed of 85 – 90% collagenous proteins, predominantly COL 1[12]. Trace amounts of types III, V and fibril-associated collagens with interrupted triple helices (FACIT collagens) are also present at certain stages of bone formation. FACIT collagens serve as molecular bridges that are important for the organisation and stability of the ECM and may help in determining collagen fibril diamter[11]. Conversely, non-collagenous proteins constitute 10 – 15% of total bone protein. Approximately 25% of such non-collagenous protein is exogenously derived, such as serum albumin and α2-HS-glycoprotein, which are thought to bind to HA because of their acidic properties. Serum-derived non-collagenous proteins may help in controlling matrix mineralisation, whilst α2-HS-glycoprotein could regulate bone cell proliferation. The remaining exogenously-derived non-collagenous proteins are composed of growth factors and numerous trace molecules that are thought to affect bone cell activity[11]. Non-collagenous proteins can be subdivided into several categories: proteoglycans, glycosylated proteins, glycosylated proteins with potential cell attachment activities and ϒ-carboxylated (Gla) proteins. Many of these proteins seem to play multiple roles, including the regulation of bone mineralisation and turnover and the regulation of bone cell activity[11]. Proteoglycans for example, are thought to obstruct mineralisation by cloaking collagen fibrils or occupying critical spaces within the fibrils diminishing the diffusion of calcium ions or calcium phosphate complexes[13].Glycosylated proteins play a variety of roles. The main glycosylated protein present in bone is alkaline phosphatase (ALP). ALP in bone is bound to osteoblast cell surfaces via an inositol phosphate linkage but it is also found free within mineralised matrix[14]. The ALP enzyme is thought to play a crucial role in bone mineralisation but exactly how is as of yet unidentified. It is thought, however, to regulate the transport of phosphate[9]. Another common glycosylated protein found in bone is osteonectin. Osteonectin is thought to affect osteoblast growth and/or proliferation and matrix mineralisation[11]. It is a bone cell marker produced by mature osteoblasts during mineralisation[15] and the presence of such is thought to initiate bone turnover as it is found in the more mature, mineralised matrix[16,17]. Fibronectin is an abundant glycosylated protein known to be present in the early stages of bone formation[18] and in the bones of adult rats[19]. Its role in early bone formation is not yet fully understood but it is known to be involved in a number of other biological processes such as wound healing, haematopoiesis and development. Some studies have suggested that fibronectin may be necessary for the migration, adhesion, differentiation and proliferation of the mesoderm[20]. OPN is another multifunctional glycosylated protein found in numerous tissue types, but at higher levels in bone[21]. It has been shown to be an important protein for cell – matrix and cell – cell interactions, facilitating the attachment of osteoclasts to bone matrix via an interaction with cell surface αvβ3 integrin and CD44[22].

1.2 Natural bone formation and remodelling

Bones continually undergo process of longitudinal and radial growth, modelling and remodelling[11]. Osteogenesis or ossification is the process of new bone formation[23].

1.2.1 Bone formation

There are two distinct processes known to form bone tissue depending upon which or what type of bone is being developed: endochondral and intramembranous ossification. Endochondral ossification, which occurs in the long bones of the body, involves the development of a cartilage model prior to bone formation, whereas intramembranous ossification, which occurs in the flat bones of the skull, involves the direct differentiation of mesenchymal stem cells (MSCs) into bone cells or osteoblasts[24,25]. The terminologies endochondral and intramembranous, when used in relation to bone formation, refer to tissue being replaced as opposed to the eventual synthesising of bone, which is actually the same process in both pathways. It should also be noted that there are occasions when endochondral and intramembranous ossification pathways are seen to work in unison. During the formation of the pelvis, vertebrae, scapula, clavicle, sternum and ribs for example, both sequences can be identified[26].

1.2.1.1 Endochondral ossification

As mentioned, endochondral ossification requires the formation of a cartilage model prior to bone formation. This cartilage model is formed through the condensation and differentiation of MSCs into chondrocytes. These chondrocytes subsequently secrete the necessary components of a specific cartilage ECM which include COL 1 and the proteoglycan, aggrecan. Proliferation of the chondrocytes causes the model to expand. Hypertrophy of the chondrocytes within the mid-shaft of the bone and their further differentiation into osteoblasts surrounding this mid-shaft precedes the model’s ossification.

The newly differentiated osteoblasts surrounding the mid-shaft are responsible for the deposition of a periosteal bone collar. To form the primary centre of ossification from this bone collar, blood vessels, osteoclasts, bone marrow and osteoblast precursor cells colonise the model. The osteoclasts then remove the cartilage ECM while the osteoblasts deposit bone on the remnants of cartilage to expand the primary ossification centre towards the ends of the model. For the formation of long bones, secondary ossification centres are then seen to form at each end of the cartilage model. At this point, a cartilaginous growth plate is present between the primary and secondary ossification centres with the future permanent articular cartilages at each end of the bone. This growth plate is responsible for the longitudinal growth of long bones. As the expanding primary ossification centre continues to grow, it meets and combines with the secondary ossification centres, thus, eradicating the growth plate[24] (fig. 1.2).

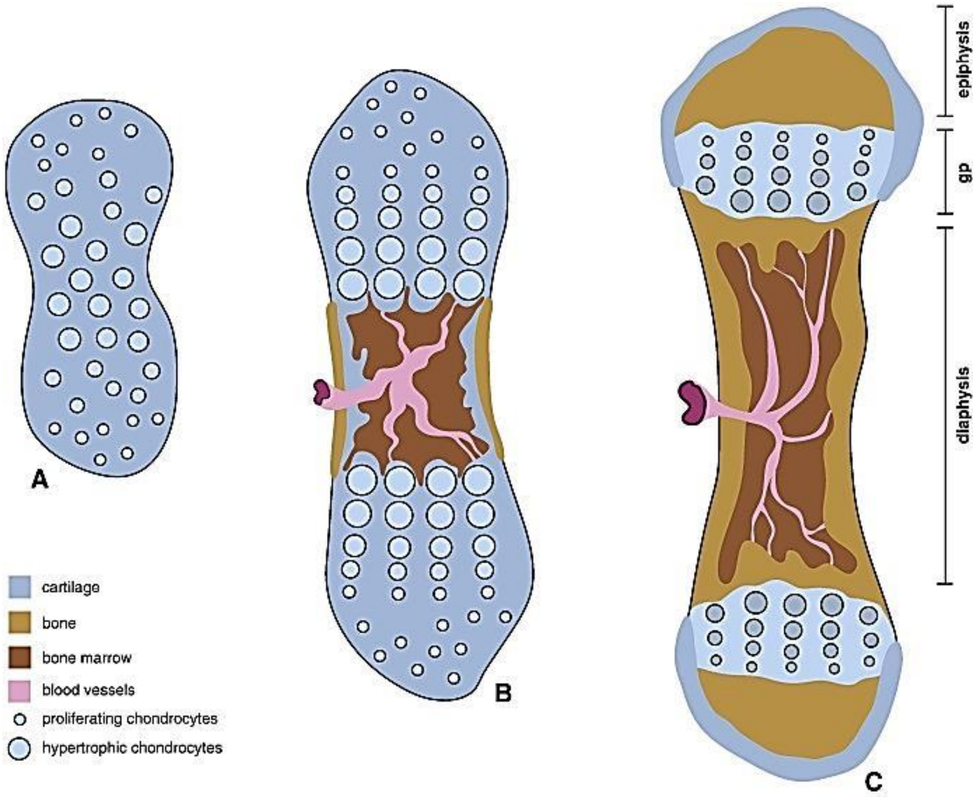

Figure 1.2: Endochondral ossification. A simplified depiction of the primary process involved[27]. Permission for reuse granted, license number 3704811231973.

1.2.1.2 Intramembranous ossification

A specific sequence of events is required for intramembranous bone formation to occur. In the case of embryonic intramembranous ossification, connective tissue acts as a seed around which bone is deposited. During such a developmental period, intramembranous ossification plays a lesser role in bone formation and is restricted to the construction of the vault of the skull, the mandible, the maxilla and numerous other facial bones, along with certain parts of the clavicle. During adulthood, however, the intramembranous ossification pathway plays a more significant role and is often reactivated for fracture repair and the regeneration of certain bone tissue defects. In the case of fracture healing, the granulation tissue, that until that time synthesised the blood clot, now functions as a matrix for bone ingrowth[28]. Intramembranous ossification involves the condensation of the mesenchyme which, with the formation of osteoblasts, then becomes vascularised. A number of specific ECM proteins are known to be secreted by differentiating osteoblasts, such as COL 1, OPN and OCN, fibronectin and bone sialoprotein. It is these proteins that form the osteoid seam which eventually mineralises to form bone[9] (fig. 1.3).

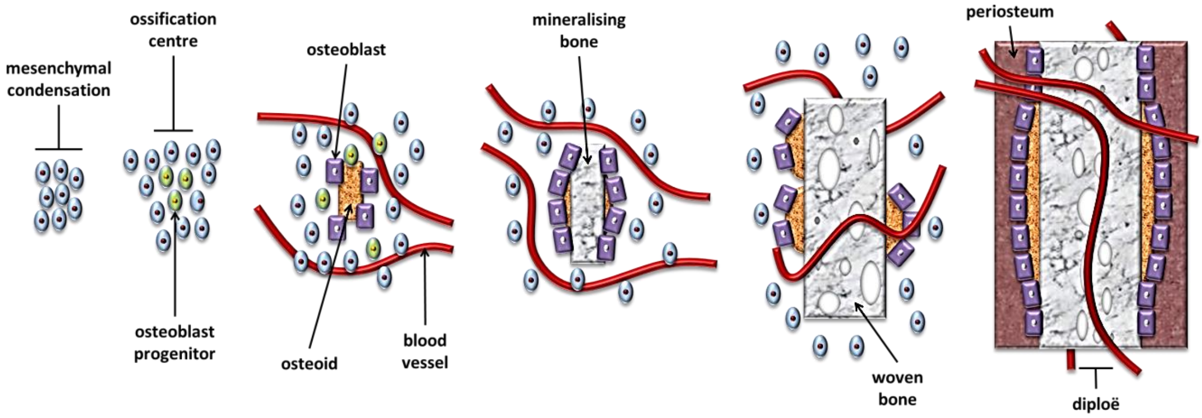

Figure 1.3: Intramembranous ossification. A simplified overview of the primary processes involved (adapted from Bradley *et al.*[29])

1.2.1.3 Bone vascularisation

Vascularisation is an essential process during bone development that is known to precede mineralisation[30]. During endochondral bone formation, the ossification process begins with the vascular invasion of the calcified cartilage. The differentiation and proliferation of osteoblast precursors is subsequently confined to the proximate locality of the invading vessel sprout[31]. The osteoid-producing osteoblasts then arrange themselves as a monolayer of secretory cells with their bases positioned along the invading vessel endothelium and their secretory faces positioned towards the osteoid front, where a bone strut forms[32]. During intramembranous bone formation, the process begins with avascular mesenchymal condensation. The subsequent differentiation of central cells into pre-osteoblasts prior to their further differentiation into secretory osteoblasts coincides with the vascular invasion of the bone nodule. This indicates a close relationship between the differentiation of osteoblasts and the processes of angiogenesis[33].

1.2.1.4 Mineralisation

During the process of mineralisation, osteoblasts secrete osteoid which is the organic component of bone matrix comprised of collagen and non-collagenous proteins, such as glycoproteins and proteoglycans[34]. This organic bone matrix is subsequently mineralised by the deposition of calcium phosphate crystals and HA which gives the bone its hardness and strength[35]. Such minerals are initially deposited in the "hole" regions of collagen fibrils[36], a process enabled by matrix extracellular vesicles. Such vesicles are produced by chondrocytes and osteoblasts and act as sheltered microenvironments where concentrations of calcium and phosphate can increase to the point of precipitating crystal formation[37].

1.2.2 Bone remodelling

Bone is a dynamic tissue that is continuously being formed, resorbed and reformed by its own cells[38] in response to stimuli, such as hormones, mechanical loading and/or growth factors[35]. The balance between two opposing actions, resorption and formation, ensures the microstructural nature and function of bone (fig. 1.4). Osteoclasts produce acids and enzymes that work on dissolving mineralised bone matrix. Osteoblasts, in contrast, secrete bone ECM which then subsequently mineralises[39]. Although acting in opposing directions, both cell types cooperate to synchronise and regulate bone remodelling. Osteoblasts express a number of factors that regulate the differentiation and activity of osteoclasts[40], whilst osteoclasts, in turn, employ modulatory signals to influence osteoblastogenesis[41]. In addition, the functions of both cell types are controlled by a third, osteocytes, whose roles include the maintenance of mineral equilibrium and the target of distant organs such as the kidneys for the adjustment of mineral excretion[42] (fig. 1.4).

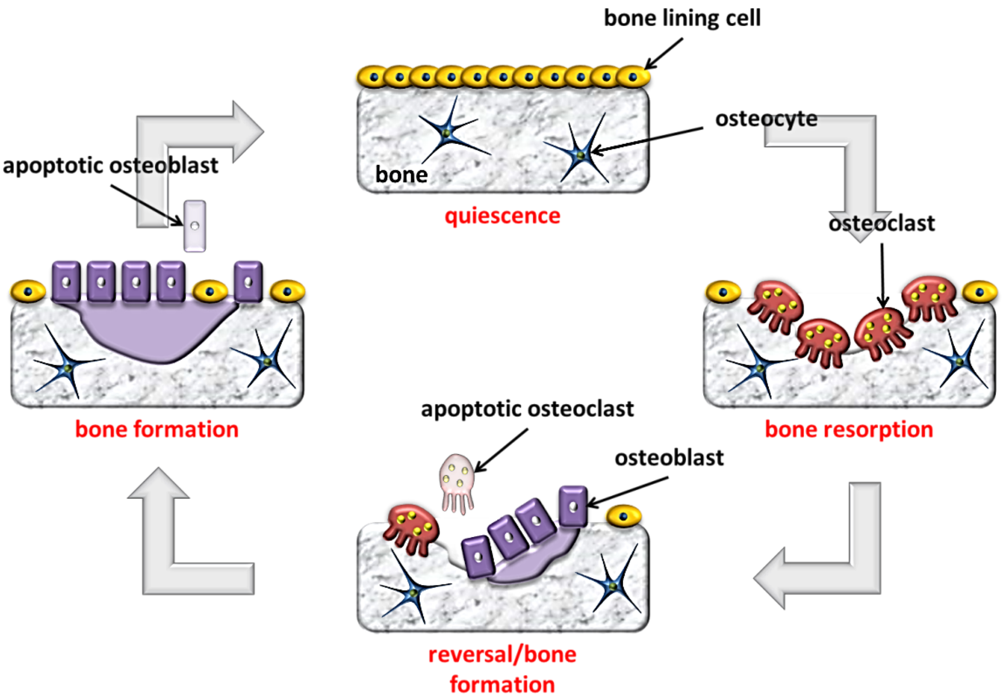

Figure 1.4: Bone remodelling. A simplified overview of the primary processes involved (adapted from Idris[43])

1.2.2.1 Osteoblasts

Osteoblasts originate from multi-potential mesenchymal progenitors[34] and are specialised stromal cells exclusively responsible for the formation, deposition and mineralisation of bone tissue[40]. Osteoblasts synthesise new collagenous matrix and regulate the mineralisation of such matrix by releasing small, membrane-bound matrix vesicles that subsequently concentrate calcium and phosphate and enzymatically-abolish mineralisation inhibitors, such as pyrophosphate or proteoglycans[37].

Alongside the secretion of osteoid, osteoblasts also produce a number of bone morphogenetic proteins (BMP) and growth factors such as insulin-like growth factor (IGF), transforming growth factor-β (TGF-β) which are then stored within the mineralised bone matrix[39]. Interestingly, under the regulation of the parathyroid hormone, osteoblasts have also been shown to secrete matrix metalloprotease-13 (MMP-13) which suggests that these cells may also contribute to the degradation of collagen during bone resorption[39,44]. Osteoblasts have also been shown to enhance osteoclastogenesis through the release of macrophage-colony stimulating factor (M-CSF) which is known to be important for the proliferation of osteoclast progenitors and their differentiation into mature osteoclasts[35]. The fibroblast-like morphology of osteoblasts seen when cultured *in vitro* in a low density monolayer is indicative of those found *in vivo* in a resting or non-active state. Once activated *in vivo*, the cells' morphology becomes 'cuboidal' which indicates their ability to now influence the bone surfaces around them and to lay down osteoid in which they will become entrapped transforming them into osteocytes[45].

Osteoblasts are known to possess a number of distinguishing properties, such as the ability to synthesis COL 1, osteonectin, OPN, OCN and ALP, as well as the ability to respond to certain hormones such as parathyroid hormone and growth factors such as epidermal growth factor (EGF). The changes in the levels of protein expression and cellular responsiveness seen within osteoblastic populations may be indicative of different stages in the cells' maturity[46]. For example, *in vitro* models of osteoblast differentiation have shown increases and subsequent decreases in the levels of COL 1 and ALP. OPN expression becomes apparent before both bone sialoprotein and OCN. Bone sialoprotein is detected in differentiated osteoblasts and OCN is detected with mineralisation[47–49]. However, it is noted that one could argue that these changes in protein expression could be the work of already mature cells and so more work is needed to identify the earlier stages in cellular differentiation[46]. This work is currently ongoing and explained in more detail later in the review.

1.2.2.2 Osteoclasts

Osteoclasts are extremely large cells comprised of acidophilic cytoplasm and anywhere from 2 – 100 nuclei derived from myeloid progenitors of the monocyte-macrophage lineage[50]. The multistep differentiation process is thought to be primarily mediated by two cytokines, the M-CSF and the receptor activator of nuclear factor-kappaB ligand (RANKL)[51]. Mature osteoclasts possess the unique ability to degrade bone for the processes of bone remodelling, bone morphogenesis, the repair of microdamage and the adaptation to mechanical loading. On the bone surface, osteoclasts interchange between migratory phases and static resorption phases. Osteoclast resorption begins with the development of a sealing zone which subsequently leads to apicobasal polarisation and the formation of a ruffled border. Below this ruffled border, a resorption pit is formed. The degradation products derived from this pit are removed by a process called endocytosis and trafficked through the cell by a process called transcytosis before being released into the extracellular medium[52]. The sealing zone then disassembles via the action of a thyroid hormone, calcitonin[39]. The cell then moves away and forms a new adhesion structure next to the former resorption pit before the process starts again. The alternation between both phases can result in the formation of resorption pit trails on the bone surface[52].

1.2.2.3 Osteocytes

Osteocytes are terminally differentiated osteoblasts that function with syncytial networks to support bone structure and facilitate metabolism. They lie within mineralised bone with extensive filipodial processes that stretch out within the canaliculi of mineralised bone[53]. Until recently it was theorised that an osteoid-producing osteoblast becomes entrapped within the mineralised matrix as neighbouring osteoblasts lay down osteoid over the embedding cell[45]. However, a number of arguments have developed disputing osteocytogenesis as being such a passive process.

One of the first changes to occur within embedding cells is the formation of dendritic processes. Morphologically, the cell transforms from a polygonal shape to a cell with dendritic extensions outspreading from the mineralising front to either the vascular space or bone surface. Once embedded the cell has a polarity. The osteocyte now has two major functions, to regulate mineralisation and form connective dendrites. In addition to the osteocyte being able to control and regulate mineralisation[54], osteocytogenesis has also been shown to be an actively invasive process with the cleavage of collagen and potentially other matrix proteins[42]. As an osteoblast transforms into an osteocyte, several molecules and proteins are known to fluctuate. Changes in the distribution of actin-binding proteins, such as spectrin, filamin, villin and fimbrin, have been shown to correlate with osteocyte differentiation[55] along with molecules required for cytoskeletal rearrangement such as macrophage-capping protein (CapG) and destrin[56]. Additionally, during this transition ALP is reduced, and casein kinase II (CK2) and OCN are raised[57].

Whilst osteocytes constitute 95% of the bone cells in the adult skeleton, with this amount increasing with age and bone size, they are not thought to play a major role in embryonic bone development and are suspected of playing only a secondary role in postnatal growth and development. They do, however, appear to play a crucial role in maintaining bone homeostasis within the adult skeleton. The osteocyte is thought to orchestrate bone remodelling by regulating both osteoblast and osteoclast activity. They also act as mechanosensors for the control of responses to mechanical loading placed on the skeleton and may be a target cell for the actions of the parathyroid hormone. Thus, the osteocyte appears to incorporate mechanical and hormonal signalling into the management of bone mass[58].

1.3 The processes of fracture repair

The processes of fracture repair are postnatal but echo many of the processes that take place during embryonic skeletal development. The occurrence of such processes is thought to make fracture healing one of the few postnatal practices that is truly regenerative by restoring pre-injury cellular composition, structure and biomechanical function (reviewed in[59,60]). All of the pathways utilised during embryonic skeletal development are expressed in fracture calluses[61].

1.3.1 Local inflammation

During the initial inflammatory phase post-injury, specific cell-mediated immune functions remove necrotic tissues, promote angiogenesis and initiate bone repair[62–64]. The first step in fracture healing is the formation of a haematoma around the site of damage, without which healing would be delayed[65]. The haematoma not only contains the fracture debris but also instigates a cascade of pro-inflammatory events by recruiting immune cells from the surrounding soft tissues. A low pH environment is formed within the haematoma within which the inflammatory cells secrete pro-inflammatory cytokines (tumour necrosis factor-α (TNF-α), interleukin-1β (IL-1β), and interleukin-6 (IL-6)) in order to activate the polymorphonuclear neutrophils and pro-inflammatory or M1 macrophages[66]. The haematoma produces a fibrin network which acts as a temporary scaffold for the leukocytes. This pro-inflammatory phase has been shown to have a positive effect on fracture healing[67] through the promotion of cell proliferation via IL-1β[68] and basic fibroblast growth factor (FGF-2)[69], and cell differentiation via matrix metalloproteinase-9 (MMP-9)[70] and BMP[71]. During this pro-inflammatory phase lactate levels are also raised[72–76] which results in an upregulation of angiogenic factors such as angiopoetin-1, platelet-derived growth factor (PDGF) and vascular endothelial growth factor (VEGF)[77,78]. Whilst the initiation of fracture healing is dependent upon the pro-inflammatory response, continued healing is dependent upon the cessation of the pro-inflammatory response. The anti-inflammatory phase is resultant of the phenotypic alteration of the macrophages to anti-inflammatory or M2 macrophages. The now anti-inflammatory macrophages secrete a number of cytokines and growth factors to promote tissue repair and angiogenesis, such as interleukin-10 (IL-10), PDGF, VEGF, TGF-β, EGF and arginase[79]. In addition, numerous studies have linked MSCs with the maintenance of a hypoimmunogenic state[80] through the release of immunosuppressive paracrine factors[81–83] or through their direct interactions with immune cell populations, such as T cells[84,85]. Such actions are thought to protect the developing tissues by stifling proliferation of T cells during stem cell recruitment and endochondral bone formation[86].

1.3.2 Angiogenesis

Compromised angiogenesis during the onset of fracture healing has a significant negative effect on the progression of repair. Ischemia at the site of injury dramatically reduces the rate of fracture repair and can potentially lead to non-healing fractures, clinically termed "nonunion”[87,88]. For this reason, the ischemic microenvironment created following injury activates a series of biological events leading to the regeneration or repair of bone. Such an environment firstly requires an oxygen and nutrient supply and so stimulates the hypoxia-inducible factor 1 (HIF-1) pathway which results in the upregulation of angiogenic factors such as VEGF[89]. The expression of such growth factors triggers the migration of endothelial cells (EC) into the hypoxic zone arranged with oxygen sensing cells at the forefront followed by proliferating stalk cells at the rear, thus, forming a vascular network[89,90]. Fibronectin is a major element of the ECM and is known to encourage cell migration, adhesion and spreading, and cytoskeletal organisation[91]. Given that its synthesis is upregulated during wound healing[91–93], it is believed to play a vital role in MSC migration to the site of injury.

Reiterating the need for adequate angiogenesis following injury are the studies showing hypoxia resulting in the decreased adipogenic and osteogenic differentiation capacity of MSCs[94], whilst increasing the release of angiogenic factors that promote vascularisation[95,96]. Fundamentally, MSCs retain their stemness and remain undifferentiated until the hypoxic environment has been normalised via the infiltration of EC and the repair or construction of a viable vascular network. Once normoxic conditions have been restored, endochondral or intramembranous ossification is free to regenerate bone.

1.3.3 Bone regeneration

Histological studies have shown that the growth of regenerating bone is very similar to that of numerous stages of bone and cartilage growth explained above (fig. 1.5). Therefore, it is thought that the molecular sequences are at the very least similar[97,98]. These similarities have been outlined in several studies[59,60,99]. Depending upon the biophysical environment, bone regeneration can occur via different patterns, i.e. endochondral, primary, direct and distraction osteogenesis[26].

Endochondral regeneration refers to bone growth by callus formation. This form of regeneration is mediated by the inner periosteal layer and marrow tissues which synthesise cartilage followed by woven and lamellar bone. Primary regeneration refers to direct contact repair which is mediated solely by intraosseous Haversian system osteoblasts (SOBL) and osteoclasts. This form of bone regeneration does not include a cartilage phase but instead involves the resorption of necrotic bone on either side of the fracture by osteoclasts, followed by the synthesis of lamellar bone by osteoblasts. Direct regeneration refers to gap repair or direct transformational repair. This process is again accomplished without the need for cartilage tissue formation and is mediated by marrow-derived vessels and mesenchymal cells. Distraction osteogenesis refers to a process called callotasis which again, is mediated by the inner periosteal layer and marrow tissue. Woven and then lamellar bone is synthesised within the gradually broadening gap[26].

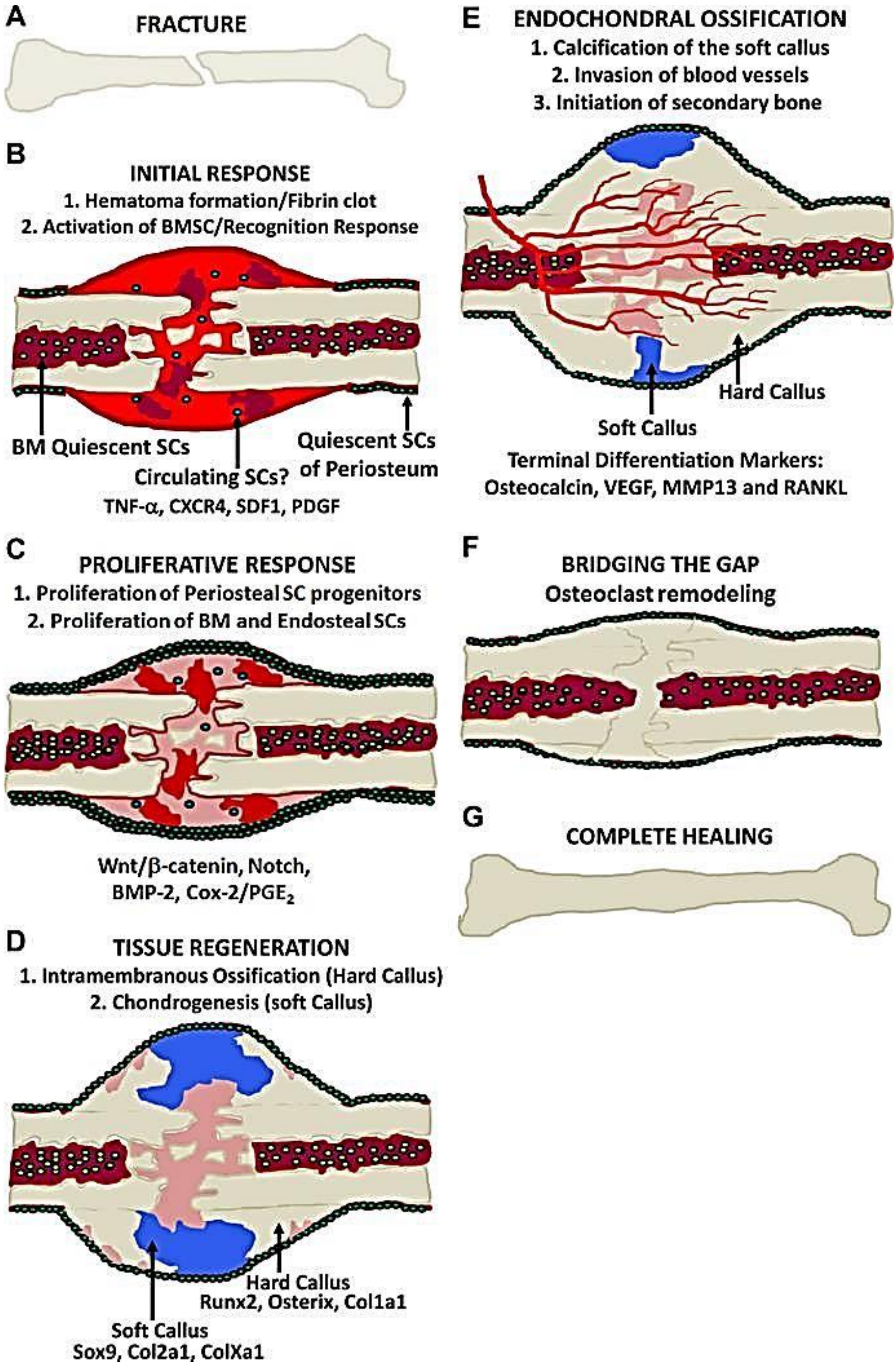

Figure 1.5: The processes of fracture repair[100]. Permission for reuse granted, license number 3705490402145.

1.4 Treatment strategies for damaged bone

Large defects found within the bone are generally caused by trauma, infection or tumours and are worsened by atrophic non-union which is the result of an inadequate blood supply, the presence of soft tissue, or the aftermath of an infection[101]. There are numerous treatments available for the repair of bone defects and/or loss.

1.4.1 Conventional treatment approaches

One such treatment is with the use of cement[102,103]. Cement is versatile and readily conformable to fit the size and shape of the bone defect but over time it has been proven to be the least stable of several similar alternatives[102]. Cement is not a biological scaffold and may cause thermal necrosis of the surrounding bone and blood supply[104,105]. For this reason, it is mainly recommended for repairing small contained defects[106]. Another alternative is to simply secure the same cement with screws. This has been shown to result in a 30% decrease in displacement[102,107] with no signs of failure after 15 years[102]. Like cement alone, it is reliable, reproducible, easily preformed and inexpensive[108]. However, also like cement it carries the risk of thermal necrosis[106] and it is only recommended for small uncontained bone defects[109].

The use of metal augments is another treatment available for both femoral and tibial defects[110]. Their versatility and availability in various shapes and sizes makes them suitable to replace bone defects of various severities[106]. They do, however, run the risk of fretting and corrosion[111–113] and in the long run the differences in elasticity between bone and metal may cause stress shielding and increase potential bone loss[114]. For these reasons this technique is mainly used in elderly, low-demand patients[115]. The gold standard for current treatments, however, is bone grafting with a novel treatment strategy being regenerative medicine[101].

1.4.2 Bone grafting

When treating bone disease, specifically large bone defects, autologous bone grafts are widely used and generally produce good clinical outcomes. The most common form of autograft is fragmented cancellous bone from the iliac crest which includes angiogenic factors from the bone marrow in order to promote the regeneration of vascularised bone. A similar treatment is an autologous fibula graft transfer or the transplant of an allogeneic bone graft. Alternatively, structural vascular autografts can be utilised for repair. However, each of these procedures has drawbacks. Given that autologous bone is a limited resource, such a graft is often accompanied by high rates of morbidity and allogeneic grafts are always shadowed by the possibility of an infection or the graft's rejection[116–118].

1.4.3 Regenerative medicine

Current graft treatments offered for orthopaedic defects are often associated with limitations or drawbacks[116–118] and can result in decreased musculoskeletal function or even loss of the patient's mobility. The worst case scenario for such diseases results in the patient's loss of autonomy[101]. For this reason, recent years have seen many studies being conducted under the guise of regenerative medicine in the hope of enhancing natural bone healing and regeneration and to even generate functional bone tissue intended to replace lost bone. Various stem cells have been studied *in vitro* such as embryonic stem cells (ESC) and numerous adult MSCs with promising results being demonstrated with osteogenic differentiation, enhanced bone healing and vascularisation. However, the use of ESCs *in vivo* is currently forbidden making MSCs the only stem cell currently under consideration for therapeutic treatments[119]. MSCs have shown remarkable capacity for osteogenic differentiation making them an ideal candidate for bone tissue engineering and regenerative medicine[120]. It is hoped that orthopaedic defects, such as cartilage damage, arthritis, large bone defects or atrophic tendon ruptures, will benefit greatly from the field of regenerative medicine. Because current surgical treatments are insufficient, however[121–128], novel techniques need exploring.

2. Bone tissue engineering

As previously mentioned, tissue engineering, typically but not exclusively, involves the combination of specific cells with 3D matrices and particular molecular signals intended to replicate tissue-specific cells and ECM[101]. Engineered bone tissue is considered a plausible substitute for the use of standard bone grafts[6]. Bone tissue has a remarkable capacity for regeneration that involves a series of biological events, e.g. cell adhesion, migration, proliferation and differentiation, regulated by growth factors secreted by both resident bone cells and reactive cells responding at the site of damage[129,130]. In saying that, however, large bone defects, regardless of their origin, congenital disease, trauma etc., might not possess the capacity to regenerate or heal instinctively and so may require clinical intervention. Such situations would profit from therapeutic strategies that stimulate tissue regeneration or replace lost or damaged bone tissue[131]. This is where bone tissue engineering becomes attractive. Bone tissue engineering is simply a division of tissue engineering specifically dedicated to bone. The demand for engineered bone tissue within clinical situations is globally widespread and growing. In the United States alone, more than 500,000 patients are treated annually for bone defects costing more than $2.5 billion. These figures are expected to double by 2020[6].

Naturally, the most effective bone regeneration would replicate the *in vivo* processes known to develop bone; therefore, numerous cell types, biomaterials, culture conditions and combinations of such, have been rigorously investigated and documented. A critical challenge for *in vitro* bone formation, through a tissue engineering approach for example, is to create a cellular/matrix niche for bone cells or stem cells to follow *in vivo* pathways[132]. The ultimate goal for bone tissue engineering is to generate a construct that closely mimics the physical and biological characteristics of natural bone tissue[133].

2.1 Current bone tissue engineering strategies

There are several principle components to be considered when discussing tissue engineering. These include biomaterials or scaffolds, cell sources, mechanical/chemical stimulation and various combinations of such.

2.1.1 The use of biomaterials/scaffolds

Scaffolds for bone tissue engineering are typically made from porous degradable biomaterials that provide the mechanical support during the repair and regeneration of damaged or diseased bone[134]. *In vitro* research revolving around bone tissue engineering, in contrast to the majority of other tissues, has been mainly focussed on the development of scaffolds that enhance bone tissue regeneration through the infiltration of host cells once implanted *in vivo*, as opposed to the *in vitro* development of actual bone tissue. However, recent years have seen an increase in the number of studies being conducted to develop replacement bone tissue *in vitro* with the aid of appropriate cell lines, biomaterial scaffolds, bioactive agents and bioreactors[135].

Biomaterial scaffolds must fulfil a number of prerequisites prior to being used for bone tissue engineering. These include biocompatibility, osteoinductive or osteoconductive properties, controllable degradation, high levels of porosity enabling mass transport, permeation of cells and interstitial fluid flow[135]. Numerous biomaterials have been developed for use as scaffold matrices in tissue engineering and specifically bone tissue engineering. Despite this research and development, however, mainly organic biomaterials are employed in scaffold formation. These materials can be derived from natural sources, such as collagen, gelatin, agarose, fibrin, alginate, silk or hyaluronic acid[101]. Given its prevalence in native bone tissue, HA is another biomaterial that has been investigated thoroughly as a potential candidate for orthopaedic implants[136–138]. Synthetic sources have also been explored with such materials consisting mainly of polyhydroxyacids, such as polylactides and polyglycolides[101]. Despite the advances made in biomaterial research, bone growth is often limited due to the biomaterial's lack of osteoinductive or osteoconductive properties[139]. There is currently no scaffold material that fulfils all the required necessities[131]; however, there are options available to enhance the effectiveness of these biomaterials. In an attempt to control the rate of biomaterial degradation and matching it to that of tissue regeneration for example, recent studies were carried out using hydroxyl acid copolymers[101]. Given that the majority of synthetic polymers are lacking in bioactivity, recent studies have also examined various surface modifications in an attempt to influence cell adhesion, migration, proliferation and differentiation. This was accomplished by adhering bioactive materials or functional groups to the polymer chain prior to scaffold manufacturing[140–142]. Other methods involve the direct adherence of cytokines to the scaffold, such as bone morphogenetic protein 2 (BMP-2) bound to keratin sponge[143], or coatings of genetic vectors to transfect the seeded cells with various growth factors[144].

2.1.2 Cell sources for engineering bone tissue

Various cell types have been used for tissue engineering bone grafts, such as bone marrow aspirates, lineage-specific osteoblasts and differentiated stem cells[145,146].

2.1.2.1 Primary- and cell line-derived bone cells

The cells used for bone tissue engineering include bone cells derived from a cell line or primary culture. It has been noted that the cell types and the characteristics of the substrates used to culture them can and do influence the osteoblasts' ability to maintain their phenotype and level of activity which can vary dramatically[147]. Immortalised cell lines, such as MG-63[148], UMR106 and Saos-2[149], are a popular choice for the study of osteoblast models because of their specific characteristics and known differentiation state. The MG-63 cell line for example, which represents an immature osteoblast phenotype, was first derived from the left femur of a 14 year male diagnosed with juxtacortical osteosarcoma[150]. The similarities between this osteosarcoma cell line and normal osteoblasts has made them an attractive model for hormonal regulation; however, their inconsistent matrix protein expression due to clonal heterogeneity limits their use in osteoblast phenotype and mineralisation studies[151]. MLO-A5, a murine cell line, is another popular cell line for investigating potential mechanisms of bone mineralisation. This cell line comprises post-osteoblast/pre-osteocyte-like cells derived from 14 day old transgenic mice. The cells have very similar Fourier transform infrared (FTIR) spectra to that of normal bone and are known to express high levels of ALP, OCN, OPN, periostin, bone sialoprotein, and parathyroid hormone receptor in comparison to primary osteoblasts or other osteoblast cell lines. Also, with the addition of osteogenic supplements, β-glycerophosphate and ascorbic acid, this cell line was seen to spontaneously mineralise after just 3 days making them an ideal candidate for mineralisation and mechanical strain studies[152]. It has been said, however, that no immortalised cell line can truly replicate the phenotype of a primary osteoblast making a primary cell culture model, although inherently more difficult to accurately replicate, a more truthful model[153].

2.1.2.2 Stem cells

Stem cells can be defined as pluripotent or multipotent cells displaying two distinctive characteristics: self-renewal and the ability to differentiate into any one of several cell lineages. Depending upon their source of origin, stem cells can be categorised as ESCs or adult stem cells. These adult stem cells can be further subdivided into two primary categories: haematopoietic stem cells (HSC) and MSCs[154–156].

2.1.2.3 Mesenchymal stem cells

MSCs are stem cells that have been isolated from numerous tissues, including bone marrow, adipose tissue, the synovial membrane and the periosteum, amongst others[157]. Given the numerous sources and techniques from which MSCs have been isolated, in 2006 the International Society of Cellular Therapy (ISCT) suggested minimum criteria for the cells’ characterisation. MSCs should adhere to tissue culture polystyrene (TCP) under standard culture conditions, whilst positively expressing CD73, CD90 and CD105, and negatively expressing CD11b, CD14, CD19, CD34, CD45, CD79α and HLA-DR. Histological staining should also demonstrate the cells' ability to differentiate into adipocytes, chondrocytes and osteoblasts[158].

The differentiation capacity of MSCs has been studied extensively *in vitro* demonstrating an ability to differentiate into mesenchymal cells, such as bone, tendon, cartilage, fat and fibroblasts[128]. However, as research continues it would appear that MSC differentiation may not be restricted to cells of the mesenchymal lineage. Cells of other germinal layers may also be within their reach, such as neurons, glia cells, ECs, cardiomyocytes and hepatocytes[159–162]. Interestingly, MSCs have shown differing differentiation potentials dependent upon their tissues of origin[163]. Although similar in many ways, a number of studies have reported differences between MSCs isolated from different sources. These differences include proliferation rates, surface markers, multipotency and several other markers. This may be an opportunity for regenerative medicine to identify the best source of MSCs for specific therapies[164,165]. When comparing neonatal sourced MSCs to adult derived MSCs, MSCs taken from neonatal sources possess an initial advantage over those isolated from adult tissues in the respect that their isolation avoids the intrusive procedure which can often be associated with infection[166] and donor site morbidity[167]. Those neonatal-sourced MSCs have also been reported to possess a higher capacity for expansion and engraftment when compared to those isolated from bone marrow[168,169]. In addition, contact inhibition was observed with bone marrow-derived MSCs but not with umbilical cord blood-derived MSCs[170,171]. Interestingly, not only were differences in population doubling times noted between MSC populations derived from different tissues, but also between MSC populations derived from different regions of the same tissue[172–174]. Numerous other differences such as morphology, surface markers, cell population and life span, are described in great detail by Zhang and colleagues[146].

MSCs may have characteristics and properties that we do not yet fully understand. Many of the studies conducted using MSCs reported the beneficial effects of their presence without any detectable engraftment to the damaged tissues. MSCs are also known to encouragingly influence cohabiting cells derived from other tissues, such as skin, muscle, endothelial and renal epithelial layers[175]. Tumour growth for example, has been seen to be enhanced by MSCs through an increase in the secretion of proangiogenic factors and enhanced blood vessel formation[176]. In addition, protein extracts and conditioned media obtained from MSC cultures resulted in organ function improvements for liver disorders and heart ischemia[177,178]. When investigated further, MSCs were seen to release paracrine factors, such as insulin-like growth factor 1 (IGF-1), insulin-like growth factor 2 (IGF-2), hepatocyte growth factor (HGF), VEGF, basic fibroblast growth factor (bFGF) and pre-microRNAs, which are thought to protect the host cells, encourage cell proliferation and augment angiogenesis[179,180]. MSCs have also been shown to secret paracrine factors thought to enhance lung function via the regulation of endothelial and epithelial permeability, lowering inflammation and enhancing tissue repair, whilst also preventing the growth of bacteria in acute lung injury and acute respiratory syndrome[181].

In addition to MSCs remarkable differentiation and cytokine secretion capacity, there is growing evidence to suggest that these cells possess a non-immunogenic characteristic that may render them transferable from one patient to another without any immune response[182]. These cells have been shown, both *in vitro* and *in vivo*, to be capable of curbing an immune response by preventing immune cells, such as helper T, cytotoxic T, dendritic, and B cells, from maturing. Cytokines, such as transforming growth factor-β1 (TGF-β1), prostaglandin-E2, and IL-10, which are known to be responsible for repressing inflammation, have also been shown to be secreted by MSCs[163].

2.1.2.3.1 Mesenchymal stem cells and osteogenic differentiation

The potential for MSCs to enhance bone fracture healing has been demonstrated in numerous preclinical animal models [183–186] and clinical trials[146] meaning the osteogenic differentiation pathway of MSCs is well-defined[187]. A small group of factors are thought to regulate the commitment and differentiation of MSCs towards an osteogenic lineage[188]. The most prevalent of these markers appears to be runt-related transcription factor 2 (Runx2). Runx2 is known to initiate and regulate osteogenic differentiation via two distinct signalling pathways through TGF-β1 and BMP-2[189,190]. Alongside Runx2, BMP-2 and distal-less homeobox 5 (Dlx5) are thought to encourage MSCs to commit towards an osteogenic lineage[191,192]. In addition to this, Runx2 prevents MSCs from differentiating towards an adipogenic lineage[193] (fig. 1.6).

Once committed, MSCs differentiate to form pre-osteoblasts which are elliptical in shape with an elongated nucleus. These cells are capable of proliferation and are known to express Runx2, Dlx5, msh homeobox homologue 2 (Msx2), P2Y4 and P2Y14[165,194]. They are also known to express numerous osteoblast markers, such as ALP, COL 1, and OPN, although at weaker levels than immature osteoblasts. The differentiation of pre-osteoblasts into immature osteoblasts involves β-catenin, Runx2 and osteoblast-specific transcription factor osterix (Osx). These immature osteoblasts are spindle-shaped and express BMP, bone sialoprotein and OPN[146]. Also, the expression of Osx is induced by BMP-2 independently from Runx2[195]. Further down this line, Runx2 is thought to obstruct the development of osteoblasts[196]. Osx induces the terminal maturation of osteoblasts and opens the door for OCN expression[197] (fig. 1.6).

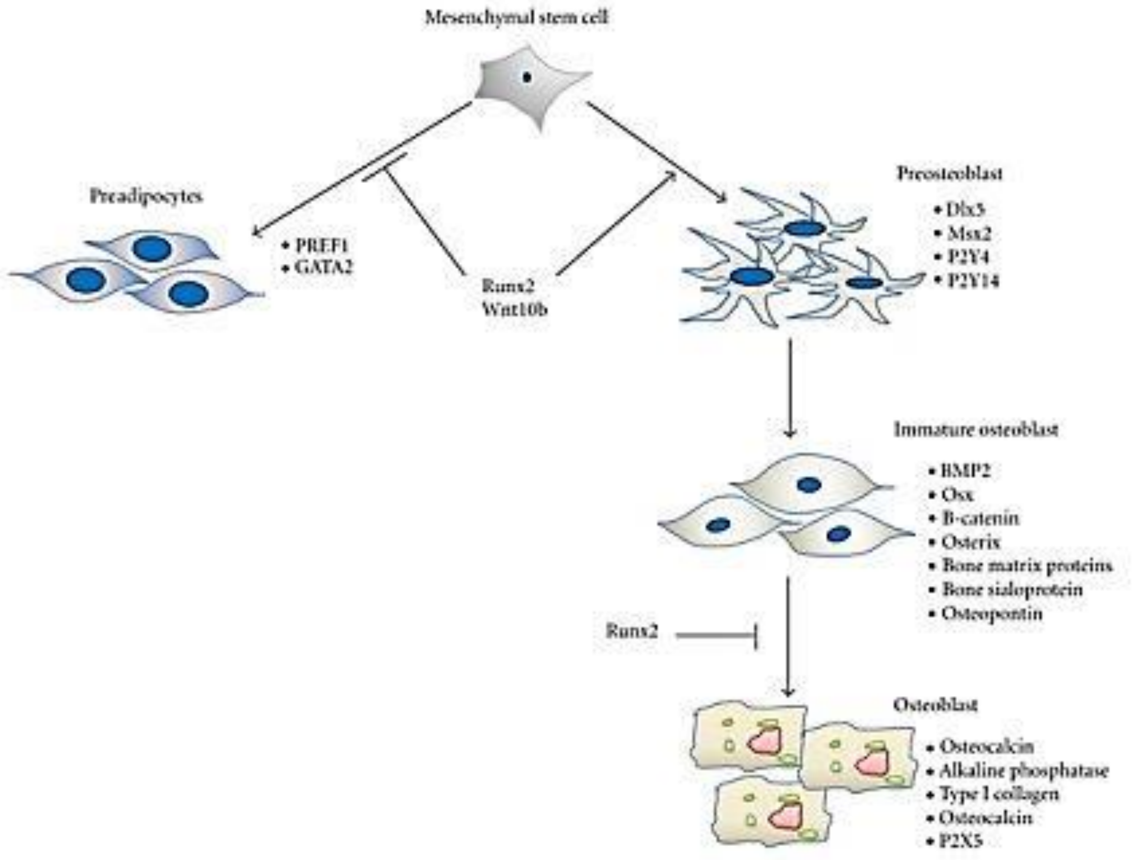

Figure 1.6: MSC differentiation down the osteogenic lineage[146].

For some time now, the processes of *in vitro* osteoblast differentiation have been known and well documented. Three distinct phases are known to occur, proliferation, matrix maturation and matrix mineralisation. The first, proliferation, occurs at the onset of *in vitro* differentiation and involves the growth of osteoblast numbers forming a dense multi-layered culture. It is at this point that the cells undergo morphological changes expressing high levels of COL 1. During the onset of the second phase, matrix maturation, a significant increase in ALP activity is noted[47]. As differentiation continues, a balance between cell death and proliferation is reached. It is at this point that the cells begin to express non-collagenous ECM proteins, such as OPN[198] and OCN[199]. The incorporation of HA crystals within the newly synthesised matrix symbolises the final stages of ECM maturation. Mineralised nodules now become apparent *in vitro*. Osteoblasts have the potential to mature further by becoming embedded within the matrix and differentiating into osteocytes[153]. Fully differentiated osteoblasts are cuboidal in shape and produce a self-mineralised organic matrix[146]. Mature osteoblasts have well developed Golgi bodies and rough endoplasmic reticula to correspond with an increased demand for protein production. Mature osteoblasts also see a reduced OPN expression, whilst experiencing an increase in P2X5[165], ALP[200], COL 1[200,201], and OCN[201] expression.

2.1.2.3.2 The use of mesenchymal stem cells in therapy

Cell therapy, as described earlier, involves the injection of specific cells into the circulation or at the site of tissue damage. MSCs are currently one of the most successful examples of such therapies in use today.

For example, when a patient requires a bone marrow transplant, haematopoietic stem cells (HSC) are injected into their circulating blood which remarkably then, with the aid of chemokines and through a process known as 'homing', find their way to the bone marrow[202–204]. A large number of animal models have been used to demonstrate the ability of a number of stem cell types to home to the sites of injured or damaged tissues[205–207] and in humans, systemically injected MSCs were shown to benefit graft-versus-host disease (GVHD) and osteogenesis imperfecta (OI)[208,209]. MSCs' ability to home has also been demonstrated for fracture healing in a mouse model. In this case, the cells migrated to the fracture site after systemic application where they were seen to enrich the area and aid regeneration through the paracrine induction of tissue healing, lowering of inflammation (both systemic and local) and their differentiation into bone cells[210]. It was noted, however, that the majority of MSCs systemically applied to the mice became trapped in the lungs. Therefore, it would appear more logical to practice local application for bone regeneration[211].

These seemingly remarkable traits of MSCs have rendered them a promising candidate for clinical trials. Although a number of trials have already been conducted using MSCs with positive results and no serious side-effects being reported[212], randomised trials are required to confirm these results[101]. Currently, MSCs are undergoing clinical trials at various stages to investigate their potential use as therapies for diseases such as OI, GVHD, and chronic and acute myocardial infarction[208,213,214]. Year 2010 alone saw 123 studies investigating MSCs for a wide range of therapeutic applications[215].

2.1.2.4 Mesenchymal stem cell sources

As mentioned, MSCs have been attained from numerous tissues and below are two such sources.

2.1.2.4.1 Periosteum

The periosteum has been seen to play a crucial role during fracture healing[216] with the outer cambium layer being responsible for initiating angiogenesis and osteogenesis and differentiating stem cells down the bone lineage[217]. The periosteum is a thin but extensively vascularised tissue membrane that is attached to the surfaces of bone through a network of collagenous fibre bundles known as Sharpey's fibres. This membrane comprises two layers, the outer of which is dense and consists of fibroblasts, the inner of which is the cambium layer comprising of MSCs capable of differentiation into bone and cartilage for the regeneration of bone[218,219]. The inner cambium layer is, therefore, believed to play an important role in bone remodelling[217,220]. The osteogenic and angiogenic potential of the periosteum has been investigated in numerous *in vitro* and *in vivo* studies which have shown a revitalisation of allografts and enhancement of bone regeneration[217,220–223].

2.1.2.4.2 Bone marrow aspirate

Whilst MSCs have been isolated from numerous tissues[157], those obtained from bone marrow are of particular interest to this study. Studies have shown that bone marrow is a multifarious tissue composed of haematopoietic cells, their differentiated offspring and a connective matrix call a stroma[224,225]. This connective tissue or stroma is an assortment of various cell types, such as ECs, adipocytes, reticulocytes and fibroblastic cells, which are all in direct contact with the haematopoietic constituents of the marrow. Primary bone marrow cultures have been shown to produce an adherent cell layer comprised of at least three distinct cell populations[226,227].

When using bone marrow aspirates, bone regeneration studies have experimented with directly implanted aspirate as well as isolated culture-expanded MSCs[228]. Cultured bone marrow-derived MSCs are of interest to regenerative medicine because of their readiness to proliferate and produce differentiated progeny but also because they are relatively simple to isolate from bone marrow aspirate samples and willingly form single cell-derived colonies[227]. Their characterisation, however, is not so straightforward. Although a number of studies have used stem cell surface markers to isolate and characterise human mesenchymal stem cells (hMSC)[229], their expression of mesenchymal, endothelial, epithelial and muscle surface markers[230] and no specific stem cell or mesenchymal progenitor antibody profile has impeded their purification through these methods alone[227].

Typically, MSCs are isolated from bone marrow aspirate through their selective adherence to plastic surfaces. MSCs present in bone marrow will adhere to TCP allowing for their isolation[231,232]. One aspect associated with this method of purification is the haematopoietic cell contamination and the cellular heterogeneity of cultures[233]. Although typical human bone marrow aspirate contains a surprisingly low concentration of MSCs, approximately 10 – 100 MSCs/1 x 10^6 bone marrow stromal cells (BMSC)[234–236], bone marrow-derived MSC colonies have been shown to be capable of approximately 50 population doublings (PD) within 10 weeks of culturing[237]. Although the cells' differentiation potential may diminish prior to reaching 50 PDs, research has shown that when cultured with FGF-2, telomere size is increased, thus maintaining an osteogenic differentiation potential over a longer culture period. The cells were seen to reach more than 70 PDs and maintain an osteogenic differentiation potential up to 50 PDs[238].

The advantages of using bone marrow aspirate as a cell source are numerous. Whilst various studies have been carried out using MSCs derived from a host of different tissues, bone marrow-derived MSCs in particular, have shown an immense potential in numerous small and large animal studies and in a wide range of medical applications concerning fracture repair and bone regeneration (see review Asatrian *et al.*[239]). Because of their bone formation capabilities, bone marrow-derived MSCs are currently thought of as being one of the most important cell sources for bone regeneration[240]. Bone marrow aspirates are so highly used that investigations have been carried out to assess the potential of various different donor sites. Traditionally, the iliac crest has been the most common source of bone marrow-derived MSCs but several reports have shown that these cells are also available within the marrow of the vertebral body, humeral head and sternum[241–244]. An interesting study carried out by Narbona-Carceles and colleagues compared bone marrow aspirates from three different sites, i.e. the distal femur, proximal tibia and iliac crest[245]. Whilst MSCs were obtained from all sites tested, higher cell numbers combined with a higher success rate in establishing cell cultures from the iliac crest were reported. No differences, however, in cell viability, immunophenotype or differentiation potential were observed.

When compared to cell populations derived from adipose tissue, only 21% of the MSC clones obtained from such tissue were tripotent compared with 50% of the clones derived from bone marrow-derived MSCs[246]. Tripotent cells were shown to be highly proliferative, possessed large colony-forming efficiencies and accumulated a more highly mineralised ECM than cells from unipotent osteogenic clones[247].

Bone marrow-derived MSCs have also been shown to continue expressing Runx2 regardless of differentiation suggesting an ability to shift phenotype and redifferentiate into osteoblasts[248,249] making them particularly appealing to the field of bone tissue engineering. Variations between samples have been noted, however. There have been a multitude of studies conducted that suggest donor-dependent variations of numerous levels exist within MSC populations. Siegel *et al*. for example, noted that phenotype, donor age and gender can all affect the function of bone marrow-derived MSCs[250]. In addition, variations in growth kinetics and gene expression[251], variable clonal properties[252] and surface markers identifying possible subpopulations[253–255] have also been identified alongside large donor variations in the concentration of nucleated cells and the multi-lineage differentiation potential of bone marrow-derived MSCs[251,256].

2.1.3 Dynamic culturing through mechanical stimulation

Under physiological conditions, loading placed on the bone through compression and/or tension via movement drives interstitial fluid flow through the lacunae of the bone resulting in the application of fluid sheer stresses[257]. This creates hydrostatic and dynamic shear forces detectable by the cells[258–261]. Such mechanical stimuli are known to influence embryonic bone formation[262–264] as well as post-embryonic bone repair[265]. Therefore, replicating such physiological conditions should enhance or encourage bone tissue growth or regeneration.

Given that dynamic culturing has been demonstrated to improved cell survival and mineralisation in both *in vitro* and *in vivo* studies[266,267], numerous different types of bioreactors have been developed for tissue engineering with MSCs, including shear stress bioreactors[268], pulsed electromagnetic field (PEMF) bioreactors[269], hydrostatic pressure bioreactors[270], perfusion bioreactors[271–273], magnetic bioreactors[274] and spinner flasks[275], all with positive results. Cyclically-placed hydrostatic pressure in particular, was shown to have a synergistic effect for the osteogenic induction of MSCs when combined with biochemical cues[270,276]. Vascularisation as well as bone formation is well documented under such dynamic conditions[277–283].

The use of a hydrostatic bioreactor is particularly appealing because previous studies have shown that not only is such a loading mechanism important for influencing the direction of cell fate in various tissues, such as the intervertebral disc, vascular system, articular cartilage and bone[276,284,285], but that it is also thought to enhance the transfer of small molecules, such as O_2 and CO_2, into the tissue matrix[286]. When using hydrostatic loading to pressurise a closed chamber containing a gas-liquid interface, the solubility of O_2 and CO_2 is increased resulting in higher concentrations of dissolved gases in the medium[284,287]. pH levels and dissolved O_2 concentrations have been shown to influence cellular mechanisms, such as inter-cellular signalling, cell proliferation and differentiation[288,289], as well as the cell cycle, apoptosis and protein synthesis[290–295]. Culturing osteoblasts *in vitro* under hyperbaric oxygen conditions has been shown to not only boost cell proliferation and differentiation but to also improve ALP activity and COL 1 production leading to enhanced osteogenesis[296].

2.1.4 Chemical stimulation via osteoinductive and osteoconductive agents

Three supplement agents frequently used to influence MSCs down an osteogenic lineage are ascorbic acid, a source of phosphate (commonly β-glycerophosphate) and dexamethasone[297]. Ascorbic acid acts as a cofactor for enzymes that hydroxylate proline and lysine in pro-collagen[298]. Its role in osteogenic differentiation is, therefore, mainly attributed to the secretion of COL 1 into the ECM[297]. β-glycerophosphate provides a source of phosphate that is not only needed to produce the HA mineral but also operates as an intracellular signalling molecule that regulates the expression of numerous osteogenic genes, such as OPN[299,300] and BMP-2[300]. Whilst the precise concentration of dexamethasone to be used for optimal differentiation has been a source of debate[301], its importance is nevertheless undisputed. Dexamethasone is known to induce the expression of Runx2, Osx and bone matrix proteins[302–304] and when combined with ascorbic acid and a source of phosphate, it promotes the osteoblastic differentiation of hMSCs, stimulates the expression of ALP, COL 1 and OCN and promotes mineralisation[305–309], whilst also inhibiting cell proliferation[305,307,310].

There are a number of other drivers being explored for use in bone tissue engineering strategies. BMPs for example, are specific bone growth factors known to be heavily involved in *in vivo* bone formation[311–314]. They are known to be secreted during bone resorption and are actively involved in the differentiation of MSCs into osteoblasts, thus stimulating osteogenesis[40]. Currently, 20 structurally related BMPs have been identified with two of them, BMP-2 and -7, being highlighted for use in research concerned with the healing of bone defects[315,316]. There are, however, difficulties associated with the clinical use of BMPs. Given the proteins' high rate of diffusion and to avoid excessively high initial doses, a carrier system may be required to allow for their prolonged and steady release at a rate that is comparable to that of natural tissue[315]. Currently, those carriers that have been examined still require high initial doses of BMPs and so questions have been raised surrounding the safety and costs of such a system[131]. Other growth factors that have been examined for their possible therapeutic uses in bone regeneration include PDGF[317], VEGF[318,319], IGF[180], FGF[320] and TGF-β[321]. It is hoped that these factors will aid in the migration, differentiation and proliferation of osteoprogenitor cells, as well as vascular ingrowth to the site of regeneration[130].

2.2 Limitations to current engineering protocols

Although small bone-like constructs have been developed using various combinations of MSCs and different matrices, several of which have been proven successful by surviving *in vivo* in animal models[322], no laboratory has successfully developed these bone constructs in large volumes or as whole bones. This may be due to the size of the diffusion tract where 200 μm is thought to be the crucial threshold. That is to say, if the bone constructs or nodules have a radius exceeding 200 μm, the oxygen and nutrients crucial for maintaining cell viability cannot diffuse to the centre of the tissue. Thus, functional vascularisation becomes an ever increasing prerequisite for larger solid tissue samples. This issue has yet to be resolved and may be the most critical issue inhibiting the translation of bone tissue engineering in to the clinic[323].

3. Novel approaches to bone tissue engineering

Given the aforementioned limitations affiliated with current bone tissue engineering protocols, the field of regenerative medicine has been working tirelessly over recent years to both refine current techniques and research/explore novel approaches to local and systemic bone tissue regeneration through cell therapies[208]. Such novel regenerative therapies were so far found to improve fracture/osteotomy treatment, remedy pseudoarthrosis, plug bone defects and cysts, resolve osteonecrosis and augment spinal fusion[101]. Further studies are required, however, before any significant advances can be made and regenerative medicine becomes a commonly used therapeutic solution.

3.1 Biomaterial surface modification

Scaffolds are usually required to fulfil at least one of several roles, including delivering cells and/or biochemical cues, influencing cell attachment and/or migration, enabling diffusion of nutrients and expulsion of waste, and exerting mechanical and/or biological effects[324]. Whilst numerous factors are responsible for determining how cells respond to a scaffold, surface characteristics are one criteria being explored as a key component. Surface properties, such as wettability, chemistry and topography, hold significant influence over protein interactions which subsequently sway cell response[325]. For the development of scaffolds, a biomaterial should not only be biocompatible, but should also actively encourage specific cell responses[326].

There is a multitude of different surface modification techniques, each combining various elements for specific reactions. For example, the topography of polyimide was altered using reactive ion etching and multibeam laser interference to enhance the osteogenic and adipogenic differentiation of MSCs[327], the surface chemistry and wettability of polyhedral oligomeric silsesquioxane poly(carbonate-urea) urethane (POSS-PCU) was altered using plasma surface polymerisation to enhance tissue integration and angiogenesis[328] and a reduction in the inflammatory response of biomaterials was investigated through the coating of glass with polyelectrolyte multilayers (PEM) composed of glycosaminoglycans (GAG) and chitosan[329].

3.1.1 Enhanced functionality with extracellular matrix proteins

Cellular adhesion is typically triggered by the adsorption of proteins which influence subsequent cellular responses[324]. Salasznyk and colleagues set out to investigate if and how ECM proteins might influence MSC differentiation[330]. To do this, tissue culture plates were coated with ECM proteins found in bone marrow, such as collagen types I and IV, laminin-1 and vitronectin. The investigation showed that culturing hMSCs on purified vitronectin and COL 1 coated TCP and without the presence of osteogenic-supplemented medium was adequate to induce osteogenic differentiation. COL 1 has been proposed to bring about the calcification of the stromal cell matrix[331], and both COL 1 and vitronectin have been reported as being responsible for the differentiation of MSCs down the osteogenic lineage[332].

Matrigel has also been used to coat the substrate surfaces of TCP[146]. Matrigel is known to be comprised of numerous proteins, such as collagen type IV, laminin, heparin sulphate, proteoglycan, nidogen and entactin, and growth factors, such as TGF-β, bFGF, EGF, IGF-1 and PDGF[333]. The study conducted by Eslaminejad and associates cultured hMSCs on both matrigel coated and non-coated TCP substrates and demonstrated that those cultured on the coated substrates experienced significantly enhanced osteogenic differentiation compared to those cultured on the non-coated TCP[146].

3.1.2 Impact of surface modifications on suspension/pellet culture models

Biomaterial surface modifications are not solely used for enhancing cell adhesion, but can also be used to prevent adhesion; thus, instigating different cellular responses. To thoroughly appreciate and exploit the full potential of MSCs as a source for cell-based therapeutics, it is important to understand the factors involved in deciding cell fate so we may control the direction of cell differentiation. However, well established conventional monolayer culturing techniques do not replicate the formation of complex *in vivo* tissues. Numerous studies have recently demonstrated that by adopting a micromass or cellular aggregation approach for tissue engineering instead of using conventional monolayer cultures, we may be able to utilise a more productive solution for bone tissue engineering[297,334]. The use of micromass culturing or cellular aggregation relies on the hypothesis that cellular condensation and aggregate formation can greatly enhance bone tissue development by mimicking the intramembranous ossification pathway. Whilst there are two principle pathways for bone formation, endochondral ossification and intramembranous ossification, the latter bypasses the development of a cartilaginous phase through the development of an ossification centre for more rapid bone regeneration[24]. It is well established that cell – cell contact and condensation in the presence of the correct protein-rich ECM are essential niches for bone formation[335,336] and so the development of cellular aggregate models is intended to replicate such *in vivo* processes for the reduction of mineralisation times. It is thought that 3D aggregate cultures better represent the intricacies of tissues with the replication of essential bone development processes, such as proliferation arrest, terminal differentiation and the formation of osteoid for the deposition of minerals[46,337,338]. In addition, they may also offer an insight into the regulatory signalling cascades induced by particular bioactive elements and factors[339].

Wang and co-workers developed a 3D spheroid culture system to investigate and refine the differentiation efficiency of MSCs[3]. The particular culture method utilised throughout that study used photolithography and micropatterning techniques to produce uniform MSC spheroids of precise dimensions prior to their induction into adipocytes and osteoblasts. The study demonstrated that such a culture method could be used to significantly increase the differentiation efficiency of MSCs. Those spheroids cultured within that study were shown to not only enhance adipogenic and osteogenic specific gene expression levels, but to also down-regulate the genes specifically associated with sustaining MSCs self-renewal phenotypes, mesoderm specific transcript isoform b (MEST) and Thy 1 membrane glycoprotein precursor (THY1).

Another recent study conducted by Hildebrandt and colleagues aimed to develop a scaffold-free 3D *in vitro* model for hMSC osteogenic differentiation[4]. The study used a number of spheroid forming techniques in combination with culture medium supplemented with agents known to induce osteogenesis, i.e. ascorbic acid, dexamethasone and β-glycerophosphate. It was only after the aggregates were formed that the osteogenic-supplemented medium was added for further culturing. Prior to this, basic culture medium was used. The study concluded that the 3D culture techniques provided the cells with an environment corresponding to that of *in vivo* biological conditions within which the cells are surrounded by other cells and fibrous layers[339]. It has been reported that engaging the integrins in such a way can and does influence MSC adhesion, differentiation and proliferation[340,341], and such cultivation practices result in improved intercellular and ECM interactions without any influences from a scaffold matrix[3]. Thus, this method of culturing can be said to provide a link between the conventional methods of monolayer culturing and whole organs[338].

However, all of the techniques tested were reported to have significant drawbacks. The most convenient, effective and efficient method was said to be the suspension cultures within the 96-well non-adhesive culture plates[4]. In saying that, the culture period was still quite extensive with the first signs of osteogenic differentiation, ALP expression, not being detected until day 18 of culturing in osteogenic-supplemented medium. The expression of COL 1 and the deposition of mineralised ECM were detected at day 21 and after 25 days of cultivation, an increase in the gene expression of collagen types I and III, BMP-2, and OPN were noted[4].

Of course, once osteogenic aggregates or bone nodules have been formed and characterised, an injectable carrier system is required for delivery to the patient. This necessity has been tackled by Ma and colleagues[342] in a study conducted using MSCs cultured under monolayer conditions. Previously conducted studies have shown that it is relatively simple and safe to inject autologous bone marrow for the treatment of non-unions[236]. However, given the small percentage of MSCs present in bone marrow, the efficiency of such treatment strategies could be compromised[236]; therefore, it should be assessed for possible refinement. This is where Ma and colleagues[342] have taken the next step in developing an injectable suspension of *in vitro*-cultured multicellular aggregates. Previously developed carriers have included the use of collagen, fibrin, agarose, alginate, hyaluronate, and pluronic[343–345], however, each of these products were associated with numerous disadvantages, such as heightened inflammatory response, the potential for immunogenicity, possible toxicity from degradation products, inconsistent degradation rates, unpredictable gelation kinetics and unmanageable cell-biomaterial interactions[343,344,346].

The MSC aggregates for this study were cultured using rabbit BMSCs under monolayer conditions. A dense cell sheet was grown on TCP and allowed to culture for 2 weeks without passage. An osteogenic-supplemented medium was used from the initial seeding consisting of ascorbic acid, β-glycerophosphate and dexamethasone. Once ready, the cell sheet was removed in tact using a cell scraper instead of enzymatic reactions and cut into sections approximately 1 mm in diameter with a scalpel. These aggregates were then resuspended in serum-free DMEM and injected into nude mouse models to assess osteogenic potential.

That study demonstrated that BMSCs can be cultured *in vitro* and injected *in vivo*, whilst still maintaining their endogenous ECM and cell – cell connections without the need for exogenous scaffolding; thus, biocompatibility is maintained because the suspension is entirely derived from autologous cells. Higher levels of ALP, OCN, COL 1 and OPN were also noted with such culturing techniques when compared to disassociated cells under similar conditions. Six weeks post-treatment saw a significant improvement in bone healing when compared to the control. Although both the aggregated cells and disassociated cells enhanced bone healing, respectively, the former was far more impressive. These results would indicate that aggregated cells are more efficient in eliciting bone regeneration when compared to their disassociated counterparts.

Although promising, these results have their own accompanying limitations. The multicellular aggregates obtained from this study were heterogeneous in size and shape and since reproducible results are dependent upon uniformity, this is an issue that needs addressing and further optimisation. Additionally, size is increasingly important when considering the injectability of the aggregates. The aggregates must not only be small enough to fit through a needle and be capable of receiving sufficient nutrient supply *in vivo*, but also big enough so as to be entrapped in the tissue interstices, thus, preventing the loss of cells[342].

3.2 Cellular co-culturing

Large tissue-engineered bone grafts often suffer from poor core cell viability which subsequently leads to compromised graft integration and possible graft failure[25]. Uneven cell integration, cellular necrosis and eventual graft failure are often the results of an inadequate supply of oxygen and nutrients[323,347,348]. Such an inhibition to the viability of implants poses a major obstacle to the progression and translation of tissue engineering[349]. In response to this, research is currently ongoing to both refine bone tissue engineering techniques and to vascularise the resulting tissue-engineered constructs[323,350].

The co-culturing of cells is one method being explored for the vascularisation of tissue-engineered constructs. ECs for example, are being co-cultured with various other cell types in an attempt to achieve *in vitro* pre-vascularisation within scaffold constructs[25,351–354]. MSCs and ECs would appear to be a sensible combination for co-cultured constructs with the interactions between both cell types being a highly regulated process. Paying close attention to and mimicking the *in vivo* bone vascularisation processes where possible is as important as ever when co-culturing. It is thought that the most successful microvasculature formation to date was achieved with the delayed addition of MSCs to ECs encapsulated in collagen[355]. Such an experimental procedure was carried out because this arrangement was thought to better mimic the natural *in vivo* environment where MSCs are only recruited to the site of vascularisation after ECs have begun vascular construction[355]. A benefit to *in vitro* pre-vascularisation is the shortened time required for effective vascularisation within tissue-engineered grafts because the host vessels need only grow to the outer regions of the construct where they can then anastomose to the existing vessels within the construct[25].

3.3 Stem cell subpopulations

Since their initial isolation from guinea pig bone marrow by Friedenstein *et al.*[356], MSCs have been used extensively in research for a number of reasons but what is of particular interest to this study is their extraordinary differentiation capacity giving rise to the belief that an MSC population may contain numerous subpopulations. Tissue-derived adult stem cells are thought to usually only generate cells that are inherent of the tissues within which they reside, as is the case for haematopoietic and neural stem cells[357,358]. MSCs, however, have been shown to possess the ability to differentiate into cells of all three germ layers. Whilst belonging to the mesodermal lineage, they have been shown to cross from mesodermal to ectodermal and endodermal lineages[359–361]. The precise mechanisms behind this extraordinary triploblastic differentiation potential are continuing to elude researchers[362].

One theory for this exceptional differentiation capacity suggests that MSCs may contain a mixture of phenotypically, biochemically and functionally different cells comprising subpopulations[211,363,364]. From a population of bone marrow mononuclear cells (MNC) for example, a variety of adherent cell types have been shown to exist within an MSC culture. These include embryonic-like stem cells, lineage-committed progenitor cells and mature cells, such as osteoblasts and fibroblasts[365–368]. With this in mind, it has been said that bone marrow-derived MSC cultures may provide numerous stem cell types with varying differentiation potentials[369]. Interestingly, two theories exist on this subject. In brief, one hypothesis states that MSCs comprise a multitude of different stem cells adding up to a ‘pluripotent-like’ cell culture, and the second states that amongst this multitude of different stem cells is a small proportion of true pluripotent stem cells. Both of these theories rely on subpopulations. If they do exist, the amount of primitive stem cells within such cultures is thought to be rare and varies depending upon donor and cell isolation and cultivation methods[370,371].

Numerous attempts have been made to isolate single bone marrow stem cell subpopulations using a variety of techniques, such as size sieving[372,373], long term culturing under specific conditions[367,374,375], fluorescence-activated cell sorting (FACS)[368,376,377] and counterflow centrifugal elutriation (CCE)[369], but few have claimed to have actually discovered pluripotent stem cells within bone marrow-derived MSCs. Two studies that have claimed to have isolated cells with true pluripotent stem cell characteristics, however, are Jiang *et al*. (multipotent adult progenitor (MAP) cells)[365] and Kucia *et al*. (very small embryonic-like (VSEL) stem cells)[378,379]. Both have since been called into question. Kuroda *et al*. is another who carried out a study to demonstrate that bone marrow-derived MSCs and dermal fibroblasts contain pluripotent stem cells capable of self-renewal and individual differentiation into cells of all three germ layers[380]. They named these cells multilineage-differentiating stress-enduring (MUSE) cells. What is interesting about that particular study is that it was carried out using clones of single cells to show that MUSE cells are both pluripotent and mesenchymal cell-like.

With the possibility existing that an MSC population comprises numerous unipotent/bipotent stem cells responsible for ectodermal, endodermal and mesodermal lineage differentiation[362], how such a population is utilised becomes increasingly important. Knowledge of the inner workings of such a population would not only offer the prospect for the accurate evaluation of an individual’s regenerative capacities prior to treatment but also holds the potential for refined donor-specific treatments.

4. Aims and objectives of the current research project

The aims and objectives of this research project were numerous but essentially relied on substrate modifications. The initial investigations were focused on the development of a novel substrate modification technique to create an MLO-A5 aggregate model for the examination of influential parameters in developing mineralisation over time. To do this, two separate culture environments were used to form different-sized MLO-A5 aggregates that acted as ossification centres replicating natural intramembranous bone formation. The differing-sized aggregates were monitored and assessed using several modes of analyses to evaluate and compare the potential for bone development. In addition, an 8-week *in vivo* investigation was carried out with the hope of shedding light on the potential for long term bone nodule survival using this model. This project also attempted to identify donor-dependent subpopulations within MSCs isolated from human bone marrow MNCs that may play a role in determining an individual's osteogenic capacity. Again, using a novel substrate modification technique, denoted as substrate X, cells were encouraged to self-sort into identifiable cellular arrangements indicating the presence of subpopulations. Quantification of such arrangements found within multiple donor cell populations was attempted and their osteogenic potential evaluated alongside the aggregation of cells into bone nodules. An *in vivo* investigation using MSCs was also carried out to confirm the data obtained from the MLO-A5 study. The intention was to verify the MLO-A5 aggregate study using different-sized aggregates comprised of primary cells. Once again, using a substrate modification technique, the simultaneous vascularisation and mineralisation of cellular aggregates under mechanical loading was also investigated. The influences imparted by mechanical loading on cellular arrangement and mineralisation levels within MSC and human umbilical vein endothelial cell (HUVEC) aggregate co-cultures was assessed. Cellular arrangements were assessed via monitoring of the inner-aggregate HUVEC arrangements and aggregate mineralisation was assessed using microCT.

Chapter Two

Materials and Methods

Overview

This chapter outlines the general materials and methods used in this thesis. The individual experimental chapters will specify parameters and modified procedures for some of the methods depicted in this chapter.

Materials and instruments

Details of the agents, compounds, cells and materials including the instruments and software used in this thesis have been listed in table 2.1. Unless specifically stated, all agents and chemicals were used without further purification.

Table 2.1: Materials list. A complete list of materials and equipment used throughout this research project, their supply companies and where possible, their product codes.

Product	Supplier
0.22 µm filter	Sarstedt, UK, 83.1826.001
24-well cell adhesive plate	Greiner, UK, 662160
24-well cell suspension plate	Sarstedt, UK, 83.1836.500
α-MEM	Invitrogen, UK, 11900-016
β-glycerophosphate	Sigma-Aldrich, UK
A	
Acetic acid	Sigma-Aldrich, UK, 320099-500
Alcian blue	Sigma-Aldrich, UK, A5268-10G
Alexa-fluor 594-conjugated goat anti-mouse IgG1	Life Technologies Ltd., UK, A-11032
Alizarin red	Sigma-Aldrich, UK, A5533
Alkaline phosphatase (ALP) detection kit	Millipore, UK, SCR004
Antibiotic-antimycotic solution (A + A)	Sigma-Aldrich, UK, LZ17-745e
Ascorbic acid	Sigma-Aldrich, UK
B	
Biopsy punches (ø 8 mm)	Williams Medical Supplies, UK, D7480
Bovine calf serum (BCS)	Fisher, UK
Bovine serum albumin (BSA)	Sigma-Aldrich, UK, A7030-50G
C	
CaF_2 coated windows (ø 13 x 0.5 mm)	Crystran, UK, CAFP13-0.5
Carbon tape	Agar Scientific, UK, AGG3939
CD31 primary antibody, monoclonal mouse anti-human	Dako UK Ltd., UK, M0823

CD31 secondary antibody, goat anti-mouse	Life Technologies Ltd., UK, A11032
Cell tracker (cell linker kit) (HUVECs)	Sigma-Aldrich, UK, PKH67GL-1KT (FITC)
Cell tracker (cell linker kit) (MSCs)	Sigma-Aldrich, UK, PKH26GL-1KT (TRITC)
Collagen hydrogel, rat tail type I	BD Biosciences, UK, 354236
Confocal microscope	Olympus IX83, Olympus Corp., Japan
Cryostat-microtome	Thermo Shandon, UK
CXP software	Beckman Coulter Inc., USA
D	
Dako target retrieval solution	Dako UK Ltd., UK, S170084
Dexamethasone	Sigma-Aldrich, UK
Diffusion chamber membrane filters	Millipore, UK, HAWP01300
Diffusion chamber plexiglass ring	Millipore, UK, PR0001401
DMEM w low glucose and w/o l-glutamine	Lonza, Belgium, LZBE12-707F
DSLR camera	Nikon D5000, Nikon Corp., Japan
Durapore membrane filters	Millipore, UK, HVLP01300
E	
E-cadherin primary antibody, goat polyclonal	Santa Cruz Biotechnology, Inc., USA, SC31020
E-cadherin secondary antibody, donkey anti-goat	Santa Cruz Biotechnology, Inc., USA, SC-2094
Epifluorescent microscope	Nikon Eclipse Ti, Nikon Corp., Japan
Ethanol	Sigma-Aldrich, UK, E7023-500ML
F	
Fibronectin	Sigma-Aldrich, UK, F1141-1MG
Flow cytometer	Cytomics FC 500, Beckman Coulter Inc., USA
Flow cytometry antibodies	Miltenyi Biotec Ltd., UK
Flowing Software 2 software	Perttu Terho, Finland
Foetal bovine serum (FBS), ISB020	Lonza, Belgium, DE14-801
Formalin	Sigma-Aldrich, UK, HT501320-9.5L
G	
Glass slides	Menzel-Glaser, Germany, 100857
H	
Haematoxylin and eosin (H & E) stain	Sigma-Aldrich, UK, GHS316/HT110116-500ml
Hand held digital camera	Samsung S3 GT-I8190, Samsung, South Korea
Histoclear	National Diagnostics, UK, HS-200
Human umbilical vein endothelial cells (HUVEC)	Life Technologies Ltd., UK, C-015-10C
Hydrostatic chamber	Tissue Growth Technologies (TGT), UK
I	
IBMX bioultra	Sigma-Aldrich, UK, I7018
Image J software	Java, USA
Image-Pro Insight software	MediaCybernetics, USA
Immunocompromised nude mice (MF1-Nu/Nu)	Harlan UK Ltd., UK
Indomethacin	Sigma-Aldrich, UK, I7378

Insulin	Sigma-Aldrich, UK, I9278-5ML
Inverted optical light microscopy	Olympus CKX41, Olympus Corp., Japan
Isopropanol	Sigma-Aldrich, UK, 34965-2.5L
ITS liquid media supplement	Sigma-Aldrich, UK, I3146
L	
L-glutamine 200 mM	Lonza, Belgium, BE17-605E
Low serum growth supplement (LSGS)	Life Technologies Ltd., UK, S-003-10
L-proline	Sigma-Aldrich, UK, P0380
M	
Medium 200	Life Technologies Ltd., UK, M-200-500
Mesenchymal stem cells (MSC)	Bone marrow MNC, Lonza, Belgium, 2M-125B
Micro-centrifuge tubes	Alpha Laboratories, UK, LW2375
MicroCT	Scanco µCT 40, Scanco Medical AG, Switzerland
Microtome	Shandon AS325, Thermo Shandon, UK
MIRIAM beamline B22	Diamond Light Source, Oxfordshire, UK
MirrIR slides	Kevley Technologies, UK, CFR
MLO-A5 murine cell line	Prof. Lynda F Bonewald, University of Texas, USA
MxPro software	Agilent Technologies, UK
N	
Neoveil mesh sheet	CalMedical Ltd., UK, NV-L-015G
Non-essential amino acids (NEAA)	Sigma-Aldrich, UK, M7145
O	
OCT compound	Tissue-Tek, Sakura Finetek, UK
Oil red O	Sigma-Aldrich, UK, O-0625
OPUS software	Opus Software Solutions, USA
OriginPro 8 software	Originlab, USA
P	
Phosphate buffered saline solution (PBS)	Fisher, UK, BR0014G
Pluronic F127 solution	BASF, USA
Q	
qPCR genes; 18S, COL 1, ALP, OPN, and OCN	TaqMan, Applied Biosystems, UK
qPCR machine	Mx3000P, Agilent Technologies, UK
Quantax 70 software	Bruker, USA
R	
Reflective microscope	Leica S6D, Leica Microsystems, Germany
Reverse transcription kit	Quantitect RT, Qiagen, Netherlands
RNA Spectrophotometer	Nanodrop 2000, Thermoscientific, USA
S	
SEM-EDX microscope	TM-3000, Hitachi, Japan
Silver nitrate	Sigma-Aldrich, UK, 209139
Sodium bicarbonate ($NaHCO_3$)	Sigma-Aldrich, UK, S5761-500G

Sodium carbonate (Na_2CO_3)	Sigma-Aldrich, UK, S-6139
Sodium chloride (NaCl)	Sigma-Aldrich, UK, S-7653
Sodium hydroxide (NaOH)	Timstar Lab Supplies, UK, SO5658
Sodium pyruvate	Sigma-Aldrich, UK, S8636
Standard foetal bovine serum (sFBS)	Fisher, UK
T	
TGF-β3	PeproTech EC Ltd., UK, 100-36E
Tissue culture polystyrene (TCP) flasks	Greiner, UK, 658175
Tri reagent lysis buffer	Sigma-Aldrich, UK, T-9424
Tris-HCL	Sigma-Aldrich, UK, T-5941
Triton X-100	Sigma-Aldrich, UK, T8787-250ML
Trypsin	Lonza, Belgium, LZBE02-007E
Tween-20	BDH Laboratory Supplies, UK, 66368
V	
vWF, monoclonal mouse anti-human	Dako UK Ltd., UK, M0616
W	
Wax embedder	Shandon Histocentre 2, Thermo Shandon, UK
Wax embedding cassettes	Simport, Canada, M491-6
Whatman paper	Sigma-Aldrich, UK, 1001 240

Methods

1. Cell culturing

All proliferative culturing was carried out using standard tissue culture polystyrene (TCP) T25 or T75 flasks. All of the cells were enzymatically-cleaved with trypsin and passaged once they reached 80% confluency. A passage refers to every time a population of cells is enzymatically-cleaved and transferred to a fresh culture substrate for further culturing or experimentation.

1.1 MLO-A5 cells

The late osteoblast/early osteocyte murine cell line, MLO-A5,[7] (kindly donated by Professor Lynda F Bonewald, University of Texas, USA) was cultured in Modified Essential Medium Eagle Alpha (α-MEM) supplemented with 5% standard foetal bovine serum (sFBS), 5% bovine calf serum (BCS) and 1% antibiotic-antimycotic solution (A + A) (Penicillin-Streptomycin – stock concentration 10 x

10^3 U Penicillin/ml, 10 x 10^3 ug Streptomycin/ml, 25 ug Amphotericin B/ml) at 37 °C and 5% CO_2 (adapted from Kato *et al.*[152]). The cells were used between passages 24 and 28.

1.2 Mesenchymal stem cells

Human mesenchymal stem cells (MSC) were isolated from donor samples of bone marrow mononuclear cells (MNC) purchased from Lonza, Belgium. The cryopreserved bone marrow MNCs were isolated by Lonza from whole bone marrow via density gradient separation. The MSCs were then further isolated from the MNCs in our laboratory using a conventional attachment isolation protocol (adapted from D'Ippolito *et al.*[381]). Four x T75 flasks, combined surface area of 300 cm^2, were coated with fibronectin (10 ng/ml phosphate buffered saline (PBS)) for at least one hour prior to cell seeding. The fibronectin was then removed from the flasks. One vial of MNCs was then thawed and pipetted into a universal tube containing 3 ml proliferative medium. The cells were now suspended in 4 ml medium. The 4 ml medium was then separated in to the four x flasks at 5 – 6 x 10^3 cells/cm^2. Each of the flasks was then topped up with 12 ml proliferative medium bringing the total medium volume in each flask to 13 ml. The cells then received a half medium change after 7 days and a full medium change after 14 days. They were optically imaged at both time points (section 8.1.1).

The MSCs were cultured using proliferative/basal medium consisting of low glucose (1 g/l) Dulbecco's Modified Eagle Medium (DMEM), 10% foetal bovine serum (FBS), 1% A + A, 1% non-essential amino acids (NEAA) and 2 mM l-glutamine. The cells were maintained at 37 °C and 5% CO_2.

1.3 Human umbilical vein endothelial cells

Human umbilical vein endothelial cells (HUVEC) were purchased from Life Technologies, UK and each population was pooled from multiple donors. The HUVECs were cultured using Medium 200 combined with 2% low serum growth supplement (LSGS) at 37 °C and 5% CO_2[382]. The cells were used for experiments at passage 4.

1.4 Differentiation media

To supplement the proliferative medium further producing a lineage-specific differentiation medium, the following supplements were added to the cells' proliferative medium at specific concentrations.

1.4.1 Adipogenic supplementation

Dexamethasone (0.5 µM), 3-isobutyl-1-methylxanthine (IBMX) (0.5 mM), insulin (10 µg/ml) and indomethacin (100 µM) (adapted from Neuhuber *et al.*[383]).

1.4.2 Chondrogenic supplementation

1% FBS, insulin-transferrin-selenium (ITS) (1% v/v), dexamethasone (0.1 µM), ascorbic acid (50 µM), l-proline (40 µg/ml), sodium pyruvate (1% v/v) and TGF-β3 (10 ng/ml) (adapted from D'Ippolito *et al.*[381]).

1.4.3 Osteogenic supplementation

Dexamethasone (10 nM), ascorbic acid (50 µg/ml) and β-glycerophosphate (10 mM) (adapted from D'Ippolito *et al.*[381]).

2. Tri-lineage differentiation

2.1 Differentiation culturing

Cells from multiple donors were seeded at a density of 2.5×10^3 cells/cm^2 in standard TCP 24-well plates. The different differentiation media was added immediately upon seeding and the cell populations were cultured for 30 days before termination. Six samples were cultured from each donor per lineage, adipogenic, chondrogenic and osteogenic. The specific constituents of the media can be found in section 1.4.

2.2 Differentiation confirmation

Confirmation of successful differentiation was carried out by optical imaging (section 9.1) and histochemical staining (section 12). Adipogenesis was confirmed with Oil red O staining, chondrogenesis was confirmed with Alcian blue staining and osteogenesis was confirmed with Alizarin red staining. A number of samples were optically imaged prior to staining to monitor cell morphologies and all of the samples were imaged post-staining.

3. Cell tracking

For general cell membrane labelling, the procedure outlined below followed the manufacturer's protocol supplied with the PKH fluorescent cell linker kit. A cell population of up to 2 x 10^7 cells was washed once in serum-free medium and then centrifuged for 10 minutes at 400 x g to form a cell pellet. The majority of the supernatant was removed from the pellet leaving only 25 µl approximately. Then, 1 ml of Dilute C was added to the pellet before the cell/Dilute C solution was thoroughly mixed. One ml of 4 x 10^{-6} M working dye solution (4 µl stock dye in 1 ml Dilute C) was then added to the cell solution. The cell/dye solution was then incubated at room temperature for 10 minutes. Two ml of 1% bovine serum albumin (BSA) was added and the solution was again incubated for 1 minute at room temperature. The solution was then centrifuged for 10 minutes at 400 x g. The resulting cell pellet was resuspended and washed 3 times with fully supplemented medium, centrifuging and resuspending after each wash. The cells were then ready for use. The specific volumes used were adjusted depending on the cell number being labelled, i.e. the working dye solution volume would have been halved if working with 1 x 10^7 cells.

4. Modification of cell culture substrates, aggregation and subpopulation identification

A number of substrates were used/modified throughout this project to achieve particular cellular reactions. The first modification was made in order to create a suspension culture for aggregate formation (described in section 4.1.1). The second modification was used to induce particular cellular attachment arrangements; thus, identifying and separating MSC subpopulations (described in section 4.2).

All monolayer controls were cultured on standard TCP well plates.

4.1 Substrate modification and aggregate formation

Aggregates of differing sizes and densities were formed primarily from three different culture methods. Two methods used suspension cultures of different wettability properties and the third used a pellet culture technique.

4.1.1 Suspension culture aggregation

Two different suspension cultures were used throughout this research project. The first was a standard commercially available hydrophobic suspension culture plate (denoted as non-coated), the second was the same hydrophobic suspension culture plate coated with a Pluronic F127 solution (denoted as coated). To create the coated suspension culture plate, 500 µl of a sterile 2% Pluronic F127 solution (in dH_2O) was added to each of the wells of a 24-well suspension culture plate and allowed to incubate at room temperature for 24 hours. After such time, the remaining solution was removed and the plate was allowed to dry for a short time (1 – 2 hours) before being seeded with cells[7]. Both suspension culture substrates, modified and unmodified, produced aggregates of different sizes. Aggregate size and number was dictated by which suspension culture was used. MLO-A5, MSC and MSC/HUVEC aggregates were formed using this method. Specific seeding protocols are described in the methods sections of the experimental chapters.

4.1.2 Pellet culture aggregation

Up to 1 x 10^5 cells were added in 1 ml basal medium (those MLO-A5 cells that were aggregated using this method were done so in MLO-A5 basal medium (chapter 2, section 1.1), those MSCs that were aggregated using this method were done so in MSC basal medium (chapter 2, section 1.2) and those MSC/HUVEC co-cultures that were aggregated using this method were done so in a 1:1 ratio of MSC:HUVEC basal medium (chapter 2, sections 1.2 and 1.3, respectively)) to a 1.5 ml micro-centrifuge tube. The micro-centrifuge tube was then centrifuged for 4 minutes at 1000 rpm before being placed in an incubator at 37 °C and 5% CO_2. The cell pellets were allowed to develop into aggregates within the micro-centrifuge tubes for 24 – 48 hours before being used elsewhere. Only one aggregate per tube was formed using this method. Aggregate size was dictated by cell number. MLO-A5, MSC and MSC/HUVEC aggregates were formed using this method. Specific seeding protocols are described in their respective experimental chapters.

4.2 Substrate modification and subpopulation identification

MSC subpopulations were identified through particular cellular arrangements using a substrate with particular characteristics that cannot be divulged at this time due to pending intellectual properties (denoted as substrate X). MSCs were seeded through pipetting onto substrate X at a density of 5 x 10^4 cells/cm^2 in 1 ml osteogenic-supplemented medium. The medium was not changed over the following 7 days. Once seeded, the cells would self-organise and attach to substrate X in distinct arrangements, a monolayer arrangement, a ‘sunflower-like’ arrangement and an aggregate arrangement (fig. 2.1). Each arrangement is thought to represent a subpopulation of cells. The cellular arrangements were then monitored optically for up to 7 days. Multiple images were taken at regular time points for subsequent subpopulation quantification and donor comparisons.

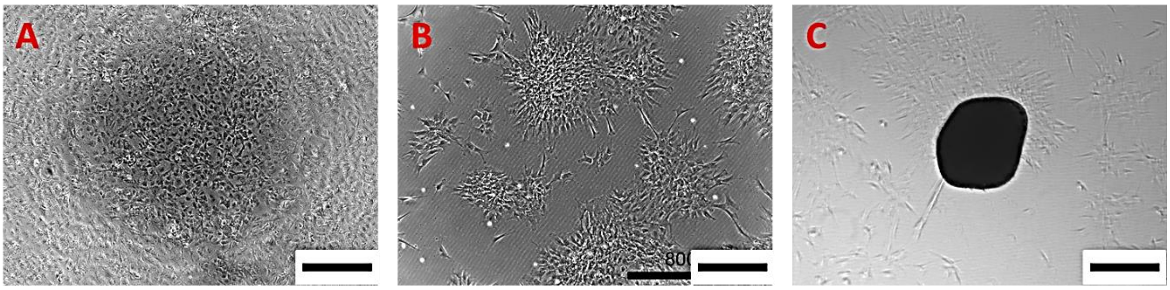

Figure 2.1: Examples of three different cellular arrangements obtained from MSCs cultured on substrate X. A monolayer arrangement (**A**), a sunflower-like arrangement (**B**) and an aggregate arrangement (**C**). Scale bar represents 400 µm.

5. *In vivo* diffusion chamber construction, seeding, implantation and termination

5.1 Construction of the diffusion chamber

The individual components of the diffusion chambers were constructed and sterilised prior to use (fig. 2.2). The pre-drilled injection hole of each chamber ring was sealed with the provided nylon thread and glue. One Durapore membrane was then used to seal each of the chamber rings on one side. A single but constant bead of glue (10 µl) was added to one side of the chamber ring before the membrane was dipped in sterile dH_2O to swell them slightly. The excess dH_2O was then removed by blotting and the membrane was immediately placed over the glued ring. Forceps were then used to gently apply pressure between the membrane and the ring to facilitate a water-tight seal. The semi-assembled chambers were allowed to dry completely before being sterilised alongside extra Durapore membranes via ultraviolet (UV) light for 15 minutes on both sides. Two hundred µl PBS was added to each chamber for 90 minutes to assess water-tightness.

Two blank chambers were also constructed to act as control blanks during analysis. One chamber remained completely empty (a control for the aggregate samples) and the second chamber contained a section of Neoveil mesh that was the same size (ø 8 mm) as those used to seed the monolayer controls (a control for the monolayer samples). Neoveil mesh is an absorbable reinforcement polyglycolic acid (PGA) felt typically used for strengthening tissue defects or, when combined with fibrin glue, suturing soft tissues[384]. In this case, however, it was used as a carrier to house the monolayer controls (adapted from Komura *et al.*[385]).

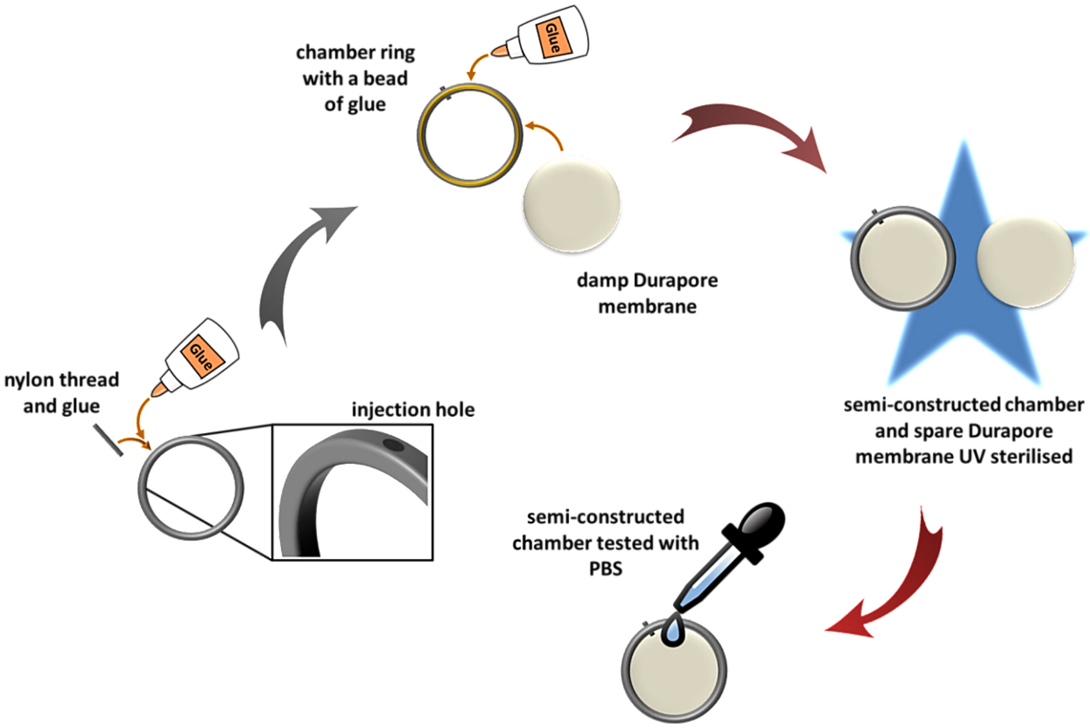

Figure 2.2: A basic overview of how the diffusion chambers were constructed.

5.2 Aggregate formation and diffusion chamber seeding

Both MLO-A5 cells and MSCs (donor D3591A) were used for the *in vivo* study. The aggregates were formed using the pellet culture method described in section 3.1.2. Each of the small aggregates was formed using 1 x 10^5 cells and each of the large aggregates was formed using 3 x 10^5 cells. Both MLO-A5 and MSC cellular aggregates were produced in the same way.

The required number of aggregates, 9 x small or 3 x large per chamber, was added to each semi-assembled chamber (96 hours prior to implantation for MSCs and 72 hours for MLO-A5 cells) in 200 µl basal medium (the constituents of the medium depended upon which cells were being placed into each chamber). Neoveil mesh was cut in to sheets (ø 8 mm) using a biopsy punch and sterilised via UV light for 15 minutes before being seeded directly within the chambers 48 hours prior to implantation. Each mesh sheet received 2 x 10^3 cells in 50 µl osteogenic medium. The cells were allowed to attach to the mesh for 2 hours before an additional 150 µl osteogenic medium was added bringing the total medium volume in the chamber to 200 µl, equal to the aggregate samples. Monolayer controls were prepared using both MLO-A5 cells and MSCs. Extra Neoveil mesh sheets were seeded with MLO-A5 cells and MSCs to confirm cell attachment. After 24 hours, the extra mesh sheets were fixed with formalin (a 40% aqueous solution of formaldehyde) for 20 minutes. Post-fixing, the mesh sheets were quartered with a fresh scalpel and stained with haematoxylin and eosin (H & E) as described in section 12.1. Forty-eight hours pre-implantation, osteogenic media was added to each of the aggregate-seeded chambers. Twenty-four hours pre-implantation, each of the chambers was placed on a clean/dry surface (a sterile square petri dish) and sealed with a second UV-sterilised Durapore membrane. Seventy µl supplemented medium was removed from each chamber before being sealed bringing the total volume within each chamber to 130 µl. The membranes were glued in place in the same way as the initial membranes only using PBS instead of dH_2O to swell the membranes and ensure a water-tight seal.

5.3 Diffusion chamber implantation

Whilst all of the preparation work for the *in vivo* experiment was carried out by the author, the surgical procedures required for this study were carried out by the University of Leeds Animal House. In total, 20 male immunocompromised nude mice (MF1-Nu/Nu, 4 – 5 weeks old, 20 – 24 g) and 30 chambers were used throughout this study. Three sample variables, i.e. large aggregates, small aggregates and monolayer controls, were assessed using 2 cell types, i.e. MLO-A5 cells and MSCs, giving 6 sample variables in total and 5 samples per variable. Ten of the animals were implanted with 2 chambers and 10 were implanted with just 1 chamber. The chambers were implanted in the intra-peritoneal cavity of each animal with great care being taken not to implant a single animal with two of the same experimental variable. This can be seen below in table 2.2.

As the chambers were being implanted, each one was thoroughly checked by the surgeon to ensure they were all securely sealed.

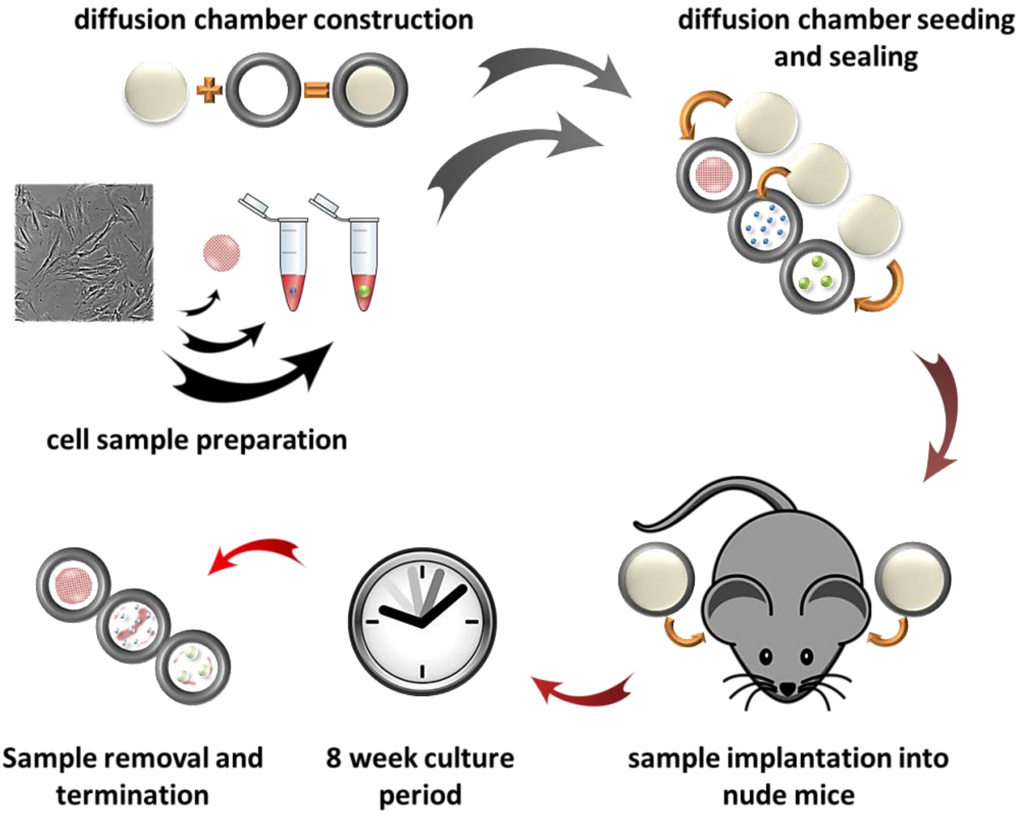

Figure 2.3: A basic overview of the *in vivo* experimental plan.

5.4 Diffusion chamber termination

After 8 weeks, the animals were culled and chambers removed. As the chambers were being removed, they were each checked thoroughly for integrity. Each chamber was logged and imaged repeatedly before being opened. The membrane was removed from one side of the chamber and the contents were immediately imaged again. The chambers were then fixed in either 100% ethanol, formalin or 4% PFA. An equal number of chambers were fixed with each fixative. Each chamber was placed into an individual container to avoid any cross-contamination.

Table 2.2: *In vivo* experimental plan. A complete list the animals used, the number of chambers implanted into each animal, the cell type used within each animal and the sample type used within each chamber.

Animal	Chambers	Cell Type	Sample Type
1	2	MSC	Large aggregates and monolayer
2	1	MSC	Small aggregates
3	1	MSC	Large aggregates
4	1	MSC	Large aggregates
5	2	MLO-A5	Small aggregates and monolayer
6	2	MLO-A5	Large aggregates and monolayer
7	1	MLO-A5	Small aggregates
8	1	MLO-A5	Large aggregates
9	1	MSC	Large aggregates
10	2	MSC	Small aggregates and monolayer
11	2	MSC	Large aggregates and monolayer
12	2	MSC	Small aggregates and monolayer
13	2	MSC	Small aggregates and monolayer
14	1	MSC	Small aggregates
15	1	MLO-A5	Large aggregates
16	2	MLO-A5	Small aggregates and monolayer
17	1	MLO-A5	Large aggregates
18	2	MLO-A5	Small aggregates and monolayer
19	2	MLO-A5	Large aggregates and monolayer
20	1	MLO-A5	Small aggregates

6. Collagen encapsulation

Collagen gel was prepared using commercially acquired rat tail type I collagen with either 10 x α-MEM or 10 x PBS depending upon the gels intended use. The procedure outlined below closely followed the manufacturer’s protocols. The main applications for the collagen gel were in two experiments; the co-culture of MSCs and HUVECs, for which 10 x α-MEM was used, and the encapsulation of cellular aggregates for further sample characterisation, for which 10 x PBS was used.

6.1 Ten x α-MEM preparation

A full bottle of α-MEM powder (10 g) was added to 50 ml dH_2O. The solution was placed onto a magnetic stirrer for several hours for the powder to completely dissolve before 3.7 g sodium bicarbonate ($NaHCO_3$) was added to adjust the pH. Another 50 ml dH_2O was added before the solution was again placed back onto the magnetic stirrer. The pH was checked and adjusted if necessary to 7.0. The solution was then filtered through a 0.22 µm filter to ensure sterility.

6.2 Ten x phosphate buffered saline preparation

One x PBS tablet was added to 20 ml dH_2O. This took up to an hour to dissolve fully. Once fully dissolved the pH was checked and adjusted (the pH should ideally be neutral). The solution was then filtered with a 0.22 µm filter to ensure sterility.

6.3 Gelation

The four constituents of the collagen gel were 10 x α-MEM (or 10 x PBS), 1 N sodium hydroxide (NaOH), dH_2O and collagen. For a particular final collagen solution conc. (i.e. 3.5 mg/ml) and volume (i.e. 500 µl), the following calculations were carried out:

1. final solution volume / 10 = volume of 10 x α-MEM (or 10 x PBS), **2**. (final solution volume x final desired concentration of collagen) / original concentration of collagen used = final volume of collagen to be used, **3**. volume of collagen x 0.023 = volume of 1 N NaOH, **4**. final solution volume – (volume of 10 x α-MEM + volume of collagen + volume of 1 N NaOH) = volume of dH_2O

The individual constituents were added to a universal vial in the order of 10 x α-MEM (or 10 x PBS), 1 N NaOH, dH_2O and collagen. It was essential to ensure the solution was thoroughly mixed but in saying that, care was also taken to slowly pipette the collagen as its increased viscosity could have led to inaccurate amounts being pipetted. Creating bubbles in the gel solution was also avoided. The individual ingredients and the universal vial containing the final collagen solution were constantly kept on ice throughout this procedure to prevent their temperature rising which could have led to premature gelation. After thorough mixing, the final collagen solution was transferred to where it was needed. The collagen solution was then placed into an incubator (37 °C) for a minimum of 20 minutes to allow the collagen to set into a gel. Once the gel had set properly, it was topped up with an appropriate volume of medium or PBS until it was completely covered. If the gel was intended to house living cells, it was covered with a specifically supplemented medium to supply the required nutrients to the cells; however, if the gel was intended to house fixed aggregates for further analyses, it was covered with PBS to prevent the samples from drying out.

7. Hydrostatic loading

The hydrostatic chamber was sterilised before use via autoclaving. The well plate was placed inside the chamber with the plate lid removed (fig. 2.4). The lid of the chamber was then bolted in place before the chamber was connected to the pressure generator. The whole chamber was then placed inside an incubator set to 37 °C and 5% CO_2 (fig. 2.4). Loading was then carried out for 1 hour every 24 hours for 7 – 10 days at a pressure of 280 kPa and a frequency of 1 Hz (adapted from Henstock *et al*.[386]).

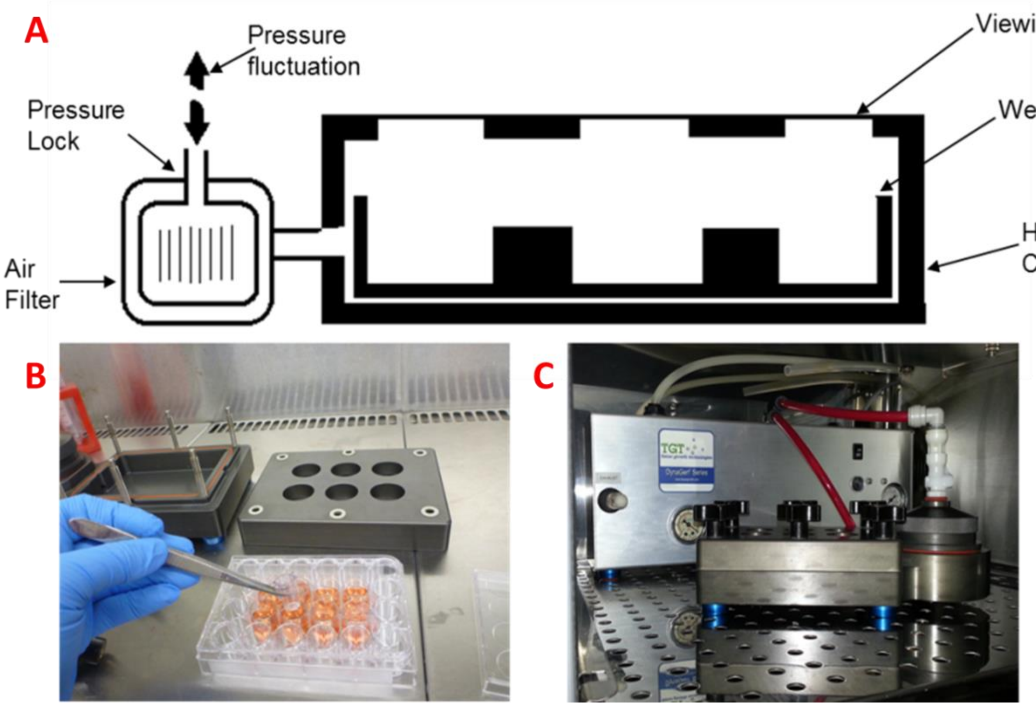

Figure 2.4: The hydrostatic bioreactor. A diagram outlining the basic structure of the hydrostatic bioreactor (**A**), a common well-plate being prepared for insertion into the bioreactor (**B**) and the bioreactor connected to the air inlet valve and pressure regulator which are maintained at 37 °C and 5% CO_2 in an incubator (**C**). Images were kindly provided by Dr Katie Bardsley, Keele University, UK.

8. Aggregate sectioning

To facilitate the characterisation and monitoring of the spatial and temporal distribution of minerals within the aggregates, they were sectioned into thin slices 3 – 8 µm thick. This was done using a microtome on wax-embedded samples or within a cryostat at -25 °C facilitating frozen sample sectioning (cryosectioning). Typically, those samples intended for histochemical staining, FTIR or SEM were sectioned using a microtome; those intended for immunohistochemical staining were sectioned using a cryostat.

8.1 Paraffin wax embedding

To section the samples using a benchtop microtome, they were first embedded in wax. To facilitate wax embedding, the aggregates were transferred to glass vials and dehydrated in varying ethanol concentrations, i.e. 50%, 70% and 90% ethanol for 45 minutes each, two cycles of 100% ethanol for 45 minutes each and two cycles of Histoclear for 45 minutes each. The samples were then transferred to plastic wax embedding cassettes where they were dipped in 56 – 58 °C wax for 2 hours in a wax embedder. The wax embedding cassettes were then inverted with the samples still inside and placed into metal chambers. The metal chambers containing both the embedding cassettes and samples were then filled with molten wax and left to cool and harden. The metal chambers were removed leaving behind the embedding cassettes which each still retained a wax block containing the sample inside. The sample was then ready for sectioning with a microtome. For improved sectioning, the wax blocks containing the samples were stored in a 4 °C refrigerator and were only removed immediately prior to sectioning.

8.2 Microtome sectioning and rehydrating

The wax embedding cassette with the wax block attached was placed into the microtome. The wax block was then sectioned to 3 or 5 µm thick slices. The slices containing sample sections were placed into a water bath set to 50 °C to flatten and smoothen out the slices, after which they were collected on conventional glass slides. The glass slides were then placed into a 60 °C oven for 40 minutes. The glass slides were rehydrated to remove all of the remaining wax as follows: Histoclear for 2 minutes, twice, 100% ethanol for 2 minutes, twice, 90% ethanol for 2 minutes, 70% ethanol for 2 minutes, 50% ethanol for 2 minutes and finally, dH_2O. The samples sections were then ready for staining and imaging.

8.3 Cryosectioning

To accommodate the cryosectioning of samples at -25 °C, they were first prepared and frozen. If the samples were not fixed prior to cryosectioning, they were snap-frozen in liquid nitrogen to prevent the formation of crystals and damaging of the samples. If the samples were pre-fixed, however, they were sectioned without snap-freezing, a process referred to as slow-freezing. Slow-freezing simply involved placing the sample into the cryostat for several minutes until it was frozen solid. The individual samples, snap- and slow-frozen, were placed on a glass slide and covered in an optimal cutting temperature (OCT) compound. The slide/sample/compound set-up was then placed inside a cryostat until the OCT had turned completely white, indicating that it was suitably frozen solid. The OCT compound, which then contained the sample, was transferred to a sample holder. The sample holder was placed back into the cryostat for several minutes to ensure the sample was thoroughly frozen solid. The sample was then sectioned to 8 µm thick slices. The slices were placed onto glass slides which were then left at room temperature for the OCT to melt and ensure the samples were sufficiently adhered to the glass slide. The remaining OCT was gently washed off with dH_2O. If the samples were not pre-fixed prior to cryosectioning, as was the case for those sections intended for CD31 staining (chapter 5), the glass slides containing the sample sections were placed into a cylinder of cold acetone to fix the samples and remove the OCT compound.

9. Imaging

9.1 Visible light microscopic imaging

The vast majority of *in vitro* samples were monitored with an inverted optical microscope (Olympus, Japan). Image-Pro Insight software was used to acquire the images. A graticule was used to manually calibrate the scale on the microscope and sample images were taken at regular intervals to ensure the image scale bars remained accurate.

The animals and chambers used for the *in vivo* investigation were optically imaged using a number of cameras. The animals and surgical procedures were imaged using a hand held digital camera (Samsung, South Korea). Post-termination, the chambers and their contents, including Neoveil mesh sheets, were imaged using a reflective dissection microscope (Leica, Germany) with an attached digital single-lens reflex (DSLR) (Nikon, Japan) camera.

9.2 Epifluorescent microscopic imaging

All epifluorescent imaging was carried out using a Nikon Eclipse Ti microscope. NIS-Elements Br 3.2 software was used to adjust the acquisition settings and capture the images.

Fluorescence intensity was measured using Image J software. Care was taken to ensure all of the epifluorescent images from each data set were taken using identical parameters. The images were converted to 8 bit in Image J and measured using the developer's guidelines.

9.3 Confocal laser scanning microscopy

All confocal imaging was carried out using an Olympus IX83 microscope. FluoView FV1000 software was used to adjust the acquisition settings and capture the images. Single images and z-stacks were acquired using the software developer's guidelines. Z-stack analysis was carried out using Image J software.

10. Aggregate measurements

10.1 Aggregate size

Aggregate size was measured using optical images taken with at least three replicates per variable. The length and breadth of the aggregates were measured and an average (mean ± standard error of the mean) was taken from both to get the approximate aggregate size. Aggregate length was accepted as the longest measurement taken from the aggregate centre, whilst breath was taken to be the distance measured perpendicularly to the length from the aggregate centre. Image J software was used to obtain each measurement and was calibrated separately for each image using the scale bars acquired from the Image-Pro Insight software.

10.2 Aggregate aspect ratio

The aspect ratio of each aggregate was acquired from measuring the aggregate length and breadth and dividing one onto the other to acquire a ratio. A value of 1 represents a perfect circle.

A higher aspect ratio indicates a more elongated or irregularly-shaped aggregate. Image J software was calibrated according to the images' scale bars separately for each image.

11. Mesenchymal stem cell subpopulation quantification

Using 85 optical images in total (85 was the total number of available images), the MSC populations from multiple donors seeded on substrate X were assessed over two time points: 96 and 168 hours (table 2.3). The proportions of the cellular arrangements were visually quantified using percentages, i.e. 50% monolayer arrangement, 50% sunflower-like arrangement and 0% aggregate arrangement. The images were blindly evaluated by three individuals unrelated to the study but familiar with the subpopulation arrangements and without influence from the investigator. The three individuals assessed each of the 85 images twice to account for any possible discrepancies. No discrepancies were noted.

Table 2.3: MNC donors and the images used for subpopulation quantification. All eight donors who had their MSC subpopulations measured using the method outlined above are shown along with the number of images per donor per time point that were used for the quantification.

Donor	D3737A	D3120B	D1908B	D3736A	D3741A	D3433B	D3549B	D2884D
96 hours	7	3	10	6	6	3	6	7
168 hours	10	4	6	3	3	3	4	4

12. Histochemical staining

Histological analysis involves the fixing, dehydration and embedding, slicing, rehydration and histochemical staining of samples for further qualitative analysis[387]. For the analysis of 3D aggregates, the samples can be prepared using histological techniques and histochemically-stained to show the structural and biochemical make-up of the aggregate centres. Histochemical staining can be used as a qualitative analytical tool to observe tissue structure[342] and to determine the presence of ALP activity[388,389] and minerals associated with bone formation (e.g. Alizarin red stain for calcium ions)[390].

12.1 Haematoxylin and eosin staining

Samples intended for H & E staining were first fixed with formalin for 20 minutes approximately. Once the fixative was removed and the samples were washed with PBS, they were covered with haematoxylin for approximately 2 minutes (3 minutes maximum) and washed with tap water for approximately 5 minutes. They were then covered with eosin for approximately 7 minutes before being washed again with tap water for approximately 2 minutes (adapted from the manufacturer's protocols). The samples were then ready for imaging.

12.2 Alkaline phosphatase staining

Alkaline phosphatase (ALP) staining was carried using an ALP detection kit. The samples were fixed using 4% paraformaldehyde (PFA) for no more than 2 minutes. The PFA was removed and the samples were rinsed twice with a tris-buffered saline and Tween 20 (TBST) solution. Fast Red Violet solution:Naphthol AS-BI phosphate solution:ddH_2O was mixed in a ratio of 2:1:1 (working solution). The samples were covered in working solution and incubated in the dark for 15 minutes at room temperature. The remaining working solution was removed and the samples were washed 2 – 3 times with dH_2O before imaging (adapted from the manufacturer's user guide).

TBST: 20 mM Tris-HCL, pH 7.4, 0.15 M sodium chloride (NaCl), 0.05% Tween-20

12.3 Alizarin red staining

Samples intended for Alizarin red staining were first fixed with formalin. Alizarin red staining solution was made up to a concentration of 40 mM with dH_2O. The pH was then adjusted to 4.1 by adding 1 M NaOH dropwise. This pH adjustment created extensive precipitation so filtering with Whatmann paper or a 0.22 µm filter was required before use.

After removing the fixation solution, the sample was washed twice with dH_2O. Enough Alizarin red staining solution was added to completely cover the sample which was then left at room temperature and under gentle agitation for 30 minutes. The sample was washed 3 – 5 times with dH_2O to remove any unbound stain precipitates before imaging (adapted from Gregory *et al.*[391]).

12.4 von Kossa staining

Samples intended for von Kossa staining were fixed with formalin. For von Kossa staining, solutions were made up fresh every time. The samples were covered with 5% silver nitrate solution (in dH_2O) and incubated for 30 minutes at 37 °C without an additional light source. Then the samples were thoroughly rinsed with dH_2O and incubated with 5% sodium carbonate (in 25% formaldehyde) for 5 minutes at room temperature. The samples were then thoroughly rinsed with dH_2O and imaged (adapted from Karp *et al.*[392]).

12.5 Oil red O staining

Firstly, Oil red O stock solution was made up by adding 0.5 g Oil red O to 100 ml isopropanol. Secondly, Oil red O working solution required 30 ml of the stock solution to be added to 20 ml dH_2O. This was then left to stand for 10 minutes before filtering with Whatmann paper. The stock solution could be stored but the working solution had to be made up fresh for each staining session.

The samples were fixed in formalin to avoid stripping the globules. Once fixed, the formalin was removed and the samples were rinsed with tap water for 1 – 10 minutes. The samples were then rinsed with 60% isopropanol and enough Oil red O working solution was added to cover the samples. The samples were then left to stand for 15 minutes before the remaining working solution was removed and the samples were rinsed again with 60% isopropanol (adapted from Kinkel *et al.*[393]). The samples were then ready for imaging.

12.6 Alcian blue staining

1% Alcian blue stain solution was prepared by adding 1 g Alcian blue to 3 ml acetic acid and 97 ml dH_2O. The pH of the solution was then checked and adjusted to 2.5. Samples intended for Alcian blue staining were fixed with 100% ethanol or formalin. After the fixation solution was removed, the samples were washed several times with dH_2O. Enough Alcian blue solution to completely cover the samples was added and they were then left at room temperature for 40 minutes. The remaining stain solution was removed and the samples were washed several times with dH_2O (adapted from Mowry[394]). The samples were then ready for imaging.

13. Immunohistochemical staining

Immunohistochemistry fundamentally identifies the presence of antigens or proteins in tissue sections by means of specific antibodies. Antigen – antibody interactions are seen via a coloured histochemical reaction that is visible by light or fluorescent microscopy[395]. Immunohistochemical staining has been used in numerous studies for the identification of osteogenic markers, such as bone-specific ALP, COL 1 and OCN[396], for EC surface markers (i.e. CD31)[397,398] and for E-cadherin expression[399,400].

13.1 CD31 staining

The PFA- (whole aggregates) or acetone- (aggregate sections) fixed samples were incubated for 30 minutes in 10% FBS (diluted in PBS) to prevent non-specific background staining (blocking). As much of the FBS as possible was removed without letting the samples dry. The samples were then incubated for 1 hour in the primary antibody, mouse anti-human CD31 (clone: JC70A, isotype: IgG1), at a dilution of 1:20 in PBS. The remaining antibody solution was removed and the samples were washed 3 times in PBS. The samples were then incubated for 1 hour in the secondary antibody, alexa-fluor 594-conjugated goat anti-mouse IgG1, diluted 1:200 in PBS. Again, the remaining antibody solution was removed and the samples were washed 3 times with PBS (adapted from Rouwkema *et al.*[401]). The samples were then ready to be imaged.

13.2 E-cadherin staining

Staining for E-cadherin followed the protocols supplied by Santa Cruz. E-cadherin staining was carried out on 96 and 168 hour samples fixed by PFA in situ on substrate X. Samples were washed with PBS to remove any remaining fixation solution. They were then permeabilised using 0.3% Triton X-100 in PBS (PBS-Tx) for 5 minutes. The samples were then covered in 3% BSA in PBS for 1 hour to block any non-specific binding sites. The BSA was then removed. The samples were covered with the primary antibody E-cadherin (clone: S-17, isotype: IgG-R) (1:100 in PBS-Tx) and incubated for 3 hours at room temperature. The samples were washed by PBS-Tx 3 times. The secondary antibody (donkey anti-goat) was added (1:100 in PBS-Tx) and incubated for 2 hours at room temperature. The samples were then washed 3 times before being imaged.

14. Real-time polymerase chain reaction

Measuring specific gene expression levels has been a critical aspect in determining osteogenic differentiation in previously conducted studies[3,4,342]. Real-time quantitative polymerase chain reaction (PCR) allows for the quantification of particular nucleic acids[402] and can be used to measure specific genes associated with osteogenesis, i.e. ALP, osteopontin (OPN), osteocalcin (OCN) or collagen type I (COL 1)[25,396,403,404].

The PCR assay and data analysis was carried out by Dr Hu Bin (Keele University, UK). For the monolayer samples, Tri Reagent lysis buffer was added to each well and pipetted. The lysed solutions were collected and stored at -80 °C until ribonucleic acid (RNA) extraction was to be carried out. The aggregate samples were transferred from their wells to micro-centrifuge tubes prior to lysing. The supernatant was removed from the aggregates and Tri Reagent lysis buffer was then added to each of the micro-centrifuge tubes. The aggregate pellets were thoroughly pipetted and mixed to obtain a complete lysis before being stored in a -80 °C freezer for later RNA extraction.

RNA extraction was carried out using the Tri Reagent protocol and was quantified using spectrophotometry, the results of which were then used to establish the required amounts of RNA for the next stage of the analysis. Once the quantities of RNA had been calculated, reverse transcription (RT) was carried out using an RT kit and complimentary deoxyribonucleic acid (cDNA) synthesis followed manufacturer’s protocols. The RT process required several reactions, 2 minutes at 42 °C followed by ice (genomic deoxyribonucleic acid (gDNA) elimination reaction), 15 minutes at 42 °C (reverse transcription of template RNA to cDNA) and 3 minutes at 95 °C (reverse transcriptase inactivation).

PCR analysis was carried out using quantitative PCR (qPCR) with MxPro software. Four genes were analysed: COL 1, ALP, OPN and OCN. The PCR primers were used following the TaqMan Gene Expression Assays protocol. Thermal cycling followed a predetermined regime: 2 minutes at 50 °C (AmpErase uracil N-glycosylase (UNG) activation step), 10 minutes at 95 °C (initial denaturing or melting step), followed by 40 cycles of 15 seconds at 95 °C (denaturing step) and 1 minute at 60 °C (annealing and extending step). The final extending step required 10 minutes at 72 °C. Gene 18S was used as the endogenous control for normalisation of expression levels for the genes of interest using the delta delta CT (ΔΔ CT) method. Each ΔΔ CT value was used in the formula $2^{-\Delta\Delta CT}$ to give a comparative fold change of gene expression levels relative to that same gene in the monolayer sample at 24 hour culture. Each culture condition had a minimum of three samples.

15. Microcomputerised tomography

Microcomputerised tomography (microCT/µCT) has quickly become the gold standard for the assessment of bone morphology and microarchitecture in mice and other small animal models. This technique uses X-ray attenuation data collected from multiple viewing angles to reconstruct a 3D image that highlights the spatial distribution of material density[405]. Such an analytical tool is invaluable to the field of regenerative medicine as it provides an opportunity to examine the skeletal system both *in vivo* and *ex vivo*[406]. MicroCT has been used in previous studies for the visualisation of bone development and distribution[135,407,408] and recent advances in technology means microCT is also becoming a frequently used tool for *in vivo* studies allowing for time-lapse microCT analysis of bone formation to be acquired[409–411].

All of the microCT scanning in this study was carried out using a specific protocol comprised of predetermined parameters, scanning increments – 157 µm, E (kVp) – 45, I (µm) – 177, resolution was set to high, field of view (FOV) diameter – 12.3 mm and 30.1 mm (12.3 mm for the *in vitro* aggregate samples and 30.1 mm for the *in vivo* chambers), voxel size – 6 µm and 15 µm (again, dependent upon which samples were being scanned), integration time – 200 ms. The resultant scans were then evaluated using a pre-installed mode of analysis ‘BV/Density only Bone Eval.’.

15.1 Microcomputerised tomography scanning of *in vitro* aggregates

15.1.1 Samples encapsulated in collagen

Initially, the aggregate samples were encapsulated in 200 µl of 3 mg/ml collagen hydrogel (as described in section 5) before conducting microCT to facilitate handling of the small-sized specimens. An identical blank hydrogel was used as a control to define the minimum density threshold required for analysis. The microCT scanning was carried out at a resolution of 8 µm using the provided software and protocols from the manufacturer. A density threshold of 110 was set as the minimum threshold for determining the formation of dense collagenous material within the aggregates given that the blank collagen gel no longer appeared above a density threshold of 100. This method did not allow us to analyse any material below a threshold of 110 and simply allowed us to visually confirm the presence of dense material at or above a threshold of 110. This method was, therefore, considered to need refinement.

15.1.2 Samples scanned without collagen encapsulation

This more refined process did not use a collagen hydrogel to house the samples. All aggregates were scanned at a resolution of 8 µm using the Scanco µCT 40 and accompanying software in a polystyrene holder designed specifically for this purpose. Given that the smaller MLO-A5 aggregates of the non-coated suspension culture were so small and numerous, they were combined and scanned as a single sample per time point. The larger aggregates, from both MLO-A5 cells and MSCs, from the coated suspension culture were large enough to be scanned as single aggregates. This resulted in vastly different material volumes and so when comparing the levels of densification or mineralisation between culture methods over time, the volume of dense material was normalised to the total material volume of each sample. Using this method, a density threshold of 60 was set as the minimum threshold required to determine the whole sample volume because this was the lowest threshold where background noise was eliminated. A threshold of 110 was again set as the minimum threshold required to determine dense collagenous material volume because this was the lowest threshold where the blank collagen gel control was no longer detected.

15.2 Microcomputerised tomography scanning of the *in vivo* chambers

The diffusion chambers from the *in vivo* experiment were scanned whole at a resolution of 15 µm using the Scanco µCT 40 and accompanying software. A density threshold of 110 was set as the minimum threshold for determining the formation of dense collagenous material beyond which all background material would be removed from the analysis. A threshold of 170 was used to quantify the volume of very dense material within the chambers because this was the highest threshold where all samples scanned still had a detectable volume.

Two blank control chambers constructed in the same way as those used *in vivo* (described in section 4.1) were also scanned and used as blank controls. The chambers were then analysed whole for volume and density measurements with the blank chambers subtracted to solely assess the chamber contents. The empty control chambers were subtracted from the aggregate sample chambers and the Neoveil mesh control chambers were subtracted from the monolayer sample chambers. The volume of very dense material was then normalised to the collagenous material volume of each sample.

16. Fourier transform infrared microspectroscopy

Fourier transform infrared spectroscopy (FTIR) is another common method used to determine the molecular structure and chemical composition of given samples[7]. The entire make-up of a sample can be assessed or one could concentrate on a particular area of interest, i.e. inorganic mineral composition[7]. Using a synchrotron source, more powerful Fourier transform infrared microspectroscopy (microFTIR) is possible. When combining chemical analysis specificity with microbeam accuracy[412] in an advanced synchrotron facility for microFTIR, mapping of spatial distribution and chemical composition at the micron scale is enabled. This magnifies the microstructural details of a biomedical specimen, delivering high quality infrared (IR) spectroscopic data on the biochemical fingerprint of the sample. Briefly, this is achieved because of the one – one correspondence between chemical bonds and molecular vibration excitation induced within the molecular framework by the IR light illumination. In the presence of an electrical dipole moment change, the molecule will absorb a specific IR frequency. Such absorptions will give a spectrum which will allow for information to be acquired concerning the subtle interactions between the surrounding groups of a molecule[413]. Thus, the presence of proteins, lipids, cell nuclei and minerals within a sample will have separate absorption peaks, the so-called IR fingerprint, in a single FTIR spectrum. In the past, a number of studies have used microFTIR to track mineralisation during animal bone development[414].

16.1 Sample preparation

After fixing with 100% ethanol, the aggregate specimens were encapsulated in 200 µl of 3 mg/ml collagen hydrogel (section 5) and wax embedded prior to sectioning (section 7.1). The wax-embedded samples were sectioned into 3 and/or 5 µm thick slices (section 7.2) and placed on MirrIR slides and/or CaF_2-coated windows. The MirrIR slides received both 3 and 5 µm thick sections, whilst the CaF_2-coated windows received only 3 µm thick sections (for comparative purposes only). The sections were then rehydrated using multiple alcohol dilutions (section 7.2) to remove any remaining wax[415].

16.2 Microspectroscopy analysis

MicroFTIR spectral acquisition and analysis were carried out using the MIRIAM beamline B22 at Diamond. Spectra were collected using an aperture size of 10 x 10 μm^2. To compare culture duration and aggregate size effects, 3 µm thick sections of small and large aggregates cultured for 24 and 72 hours were scanned (128 scans per point with a resolution of 8 cm^{-1}) on MirrIR slides using a grid mapping sequence in reflection mode. Thirty points were chosen at random for spectral comparison and 15 points were chosen at random for quantitative analysis. The grid mapping sequence allowed for whole aggregate mapping and spatial distribution of calcification to be visually compared. At least two aggregates per experimental group (aggregate size and culture duration) have been mapped.

From the spectra, protein (amide I region, 1625 – 1694 cm^{-1}) and phosphate (PO_4 region, 960 – 1143 cm^{-1}) ratios[416,417] from 15 spectra were used to quantify and differentiate the levels of mineralisation between culture duration and aggregate size since the relative intensity of the mineral and protein bands have been accepted as accurate measures of the mineral-to-protein ratio of the samples[416,417].

To compare sample thickness effects, 3 and 5 µm thick sections of aggregates cultured for 24 and 72 hours on coated and non-coated suspension culture substrates were scanned (128 scans per point on 3 µm sections, 256 scans per point on 5 µm thick sections, both at a resolution of 8 cm^{-1}) on MirrIR slides in reflection mode. Ten points were chosen at random for spectral comparison and quantitative analysis. Amide I and PO_4 ratios were again acquired.

All spectra were baseline corrected through OPUS software using the concave rubber band correction with 10 iterations and 64 baseline points excluding the CO_2 region.

17. Scanning electron microscopy – energy-dispersive X-ray

Scanning electron microscopy (SEM) uses a fine probe of electrons focused on a specimen and scanned in parallel lines. Numerous signals are generated as a result of the impact of the electrons which are then collected to form a sample surface image or analysis. These collected electrons are primarily secondary electrons, high-energy electrons back-scattered from the primary beam and characteristic X-rays[418]. SEM allows for detailed images to be taken of materials and structures at magnifications that would be difficult to obtain under normal optical microscopic conditions.

Energy-dispersive X-ray (EDX) is used primarily to identify or measure inorganic elements, i.e. the detection of inorganic graphene[419], the monitoring of sulphur speciation in Li-S batteries[420] and the observation of the crystallisation of the porous zirconium terephthalate UiO-66[421], but it can also be used to detect heavier inorganic elements in biological samples, such as those minerals associated with bone formation, calcium and phosphorus. When combined with SEM, SEM-EDX offers enhanced imaging capabilities combined with an insight into the elemental makeup of materials and structures.

17.1 Sample preparation

Aggregate samples intended for SEM imaging and EDX analysis were prepared in the same way as those used for microFTIR analysis. The aggregates were dehydrated and wax-embedded (section 7.1), sectioned into 5 µm thick sections and placed onto MirrIR slides before being rehydrated (section 7.3). Prior to SEM imaging, a ring of carbon tape was placed around the sample that was also in contact with the metal stand onto which the sample slide was placed to dissipate the build-up of static charge during imaging and analysis.

17.2 Scanning electron microscopy – energy-dispersive X-ray analysis

SEM images and EDX mineral analyses of the aggregates were taken and evaluated (15 kV for 5 minutes per sample) using an SEM microscope. The elemental distribution of calcium and phosphorus within the aggregates was mapped and analysed. Three replicates have been taken for all of the analysis representing the average (mean) value and standard error of the mean. Analysis was carried out using Quantax 70 software.

18. Flow cytometry

Flow cytometry provides a method to rapidly and accurately measure the physical and chemical attributes of individual cells[422]. It has become a commonly used analytical technique for various applications, such as a screening method for urinary tract infections[423], murine HSC analysis[424] and cell cycle analysis[422]. Given that the presence, or lack thereof, of certain cell surface markers has been outlined as one of the minimum criteria for MSC verification[158], it is central to almost all MSC-based research.

18.1 Antibody staining

Twelve cell samples were prepared from each donor for flow cytometry analysis, one blank, three positive (CD73, CD90, and CD105), five negative (CD14, CD19, CD34, CD45, and HLA), one additional antibody (CD324) for donor comparisons and two isotype controls (IgG1 and IgG2). The eleven samples that required antibody tagging followed the same Miltenyi Biotec protocols as supplied by the company. Given the small number of cells being analysed, 1 – 3 x 10^4 approximately, the manufacturer's recommended antibody volumes were reduced by a factor of 10. The volumes used in the manufacturer's protocols were designed for cell counts of 1 x 10^7.

18.2 Flow cytometry protocol

Flow cytometry was carried out using the Beckman Coulter Cytomics FC 500 and CXP software. Before any analyses were carried out, a series of checks were performed to ensure the equipment was working correctly. Once satisfied, the antibody-stained cell samples were prepared. Each of the cell samples were filtered immediately prior to use in the flow cytometer to ensure that no cell aggregates or debris greater than 40 µm would block the fluidics. These preparation steps made approximately 1 – 3 x 10^4 events available for assessment. To ensure consistency between individual donor data sets, the first cell population to be assessed was used to establish a protocol on the software specific to this study. The antibodies used to stain the cells were conjugated to a PE dye, so FS linear, SS linear and FL2 log were selected as the protocol parameters. The acquisition limits were set to 40,000 events or 300 seconds. Colour Dot Plots, Density Plots and Histogram Plots were selected for the protocol using the parameters mentioned above. For each donor assessed, the blank cell sample was run through the flow cytometer first with the Quick Set option selected to fine tune the slider bars and calibrate the specific population location on the Histogram Plot. The stained cell samples then followed one at a time.

18.3 Data analysis

Flow cytometry data analysis was carried out using Flowing Software 2. The isotype controls, IgG1 and IgG2, were used to establish positive and negative events for each of the nine antibodies measured. A Density Plot, two Histogram plots (one for the isotype control and one for the specific antibody being measured) and an Overlay Histogram Plot were used to acquire the quantitative data from each antibody for each donor. A marker was used on the negative control Histogram Plot to include 95% of the cells and to record any stain greater than this as being positive.

19. Statistical analysis

A minimum of three specimens per variable were tested. Recorded data was initially sorted using Microsoft Office Excel software before being transferred to GraphPad Prism for statistical analysis and graphing. Data was averaged and represented as a mean value ± standard error of the mean. Groups were compared using independent t-tests, f-tests and one-way or two-way analysis of variance (ANOVA). A p-value below $p = 0.05$ was denoted to indicate statistical significance. In graphs, statistical significance is indicated at four levels: $*p \leq 0.05$, $**p \leq 0.01$, $***p \leq 0.001$ and $****p \leq 0.0001$.

Chapter Three

Aggregate Size Effect on Mineralisation Rates

Overview

This study used a novel substrate modification technique to create an MLO-A5 aggregate model for the examination of developing mineralisation over time. The model comprised a commercially available hydrophobic substrate and a Pluronic coating to create two culture environments, one hydrophobic and one extremely hydrophilic, to form differing-sized MLO-A5 aggregates that acted as ossification centres replicating natural intramembranous bone formation. The differing-sized aggregates were monitored and assessed over 72 hours, whilst being compared with a conventional monolayer control.

Several modes of analyses were used to evaluate and compare the potential for bone development, such as histochemical staining, real-time polymerase chain reaction (PCR), microcomputerised tomography (microCT/µCT), synchrotron-sourced Fourier transform infrared microspectroscopy (microFTIR) and scanning electron microscopy (SEM) combined with energy-dispersive X-ray (EDX). The data obtained from each mode of analysis is discussed with the aim of understanding the underlying mechanisms of aggregate mineralisation. In addition, an 8-week *in vivo* investigation was carried out with the hope of shedding light on the potential for long term aggregate survival and potential bone formation using this model.

1. Introduction

Numerous studies have recently demonstrated that by adopting a micromass or cellular aggregation approach for tissue engineering instead of using conventional monolayer cultures, we may be able to utilise a more productive solution for bone tissue engineering[297,334]. The use of micromass culturing or cellular aggregation relies on the hypothesis that cellular condensation and aggregate formation can greatly enhance bone tissue development by mimicking the intramembranous ossification pathway. Whilst there are two principle pathways for bone formation, endochondral ossification and intramembranous ossification, the latter bypasses the development of a cartilaginous phase through the development of an ossification centre for more rapid bone regeneration[24]. It is well established that cell – cell contact and condensation in the presence of the correct protein-rich extracellular matrix (ECM) are essential niches for bone formation[335,336] and so the development of a cellular aggregate model is intended to replicate such *in vivo* processes so that we can greatly reduce the time required for mineralisation. It is thought that three-dimensional (3D) aggregate cultures better represent the intricacy of tissues with the replication of essential bone development processes, such as proliferation arrest, terminal differentiation and the formation of osteoid for the deposition of minerals[46,337,338]. In addition, they may also offer an insight into the regulatory signalling cascades induced by particular bioactive elements and factors[339].

Each of the studies centred around cellular aggregation have developed or refined a number of aggregation techniques, such as shaker flasks, hanging drop cultures, 3D rotary wall vessels and agarose coated multiple well plates[4,425–427]. Whilst effective in establishing reliable cellular aggregate models, these studies have used techniques that retain numerous disadvantages that have restricted their ability to answer some key questions regarding bone formation and how we might best mimic *in vivo* processes *in vitro*. For this reason, our study has developed a novel yet simple aggregation technique that will allow for the rapid and replicable development of aggregates of varying sizes. This model is intended to not only confirm the bone formation accelerating effects of aggregation but to also investigate how aggregate size might influence the rate and quality of mineralisation.

To do this, we have developed a simple yet effective substrate modification technique to alter surface chemistry and create aggregates of varying sizes. Such a technique takes a previously established hydrophobic substrate (denoted as non-coated) used for culturing cells in suspension and coating it with a Pluronic solution (F127) (denoted as coated) to create an extremely hydrophilic substrate. Each substrate, coated and non-coated, discourages cell attachment and so maintains a cell population in suspension. In doing so, the cells will attach to one another, rather than the substrate, creating cellular aggregates. How the coated and non-coated substrates differ from one another is in the magnitude by which they deter cell attachment. The coated substrate, being extremely hydrophilic, has a higher repulsive force compared to the non-coated substrate, being hydrophobic, deterring cell attachment to a higher degree. This results in the formation of small aggregates on the non-coated substrate and large aggregates on the coated substrate.

With the model developed, the next step was deciding how best to analyse the aggregates to extrapolate as much information as possible. One of the most interesting challenges associated with aggregate culturing is uncovering how the close cell – cell/cell – matrix interactions lead to mature bone tissue through bone nodule progenies. Various qualitative and quantitative techniques have been used by previous cellular aggregate studies, such as histochemical staining for the presence of mineralised matrix, e.g. Alizarin red and von Kossa staining[387], computerised tomography for the visualisation of bone formation in a mouse model[387], the use of various protein assay kits (ELISA) and quantitative PCR (qPCR) for the measurement of specific genes[342]. However, it is difficult to accurately measure the concentration of matrix and mineral phases simultaneously with spatial and temporal distribution using a single aforementioned technique. Therefore, a combination of analytical techniques may be required. With that in mind, numerous qualitative and quantitative techniques have been adopted in this study, such as optical imaging, histochemical staining, real-time PCR and microCT. In addition, a number of off-site facilities have been utilised, such as synchrotron-sourced microFTIR for molecular fingerprinting and spatial mapping and SEM-EDX analysis for high resolution imaging combined with elemental analysis and quantification. Despite the use of numerous modes of investigation, however, a key question remained. How does aggregate size affect actual bone formation *in vivo*? Therefore, in conjunction with various *in vitro* assessments, an *in vivo* experiment was also carried out.

In this study we aimed to further the aggregate culture principle by using substrate chemistry modifications to induce bone aggregate formation in large quantities and with variable sizes. We intended to develop a facile model enabling us to identify the variables that control the mineralisation process and the quality and distribution of minerals formed in *in vitro* 3D aggregates. This was done by examining gene expression profiles and mineral production rates, whilst also evaluating mineral properties and spatial distributions over time. We postulated that the outcome of the quantitative examination comparing culture environments over time may help to establish distinct models which are in different formation stages. Such models will allow for the investigation of parameters that dictate the quality and quantity of mineralisation, important for generating implantable bone for clinical applications.

2. Materials and Methods

The MLO-A5 *in vitro* aggregation study was carried out on three separate occasions with a minimum of three samples per variable. The MLO-A5 *in vivo* aggregation study was carried out on one occasion with five samples per variable. MLO-A5 cells were the only cell type used throughout this chapter.

2.1 Cell culture

A late osteoblast murine cell line, MLO-A5 (kindly donated by Professor Lynda F Bonewald[152]) was used for the development of this model. A comprehensive cell culture protocol can be found in chapter 2, section 1. The supplemented medium used prior to aggregation (basal media) is described in chapter 2, section 1.1.

2.2 Modification of cell culture substrates and aggregate formation

A full description of the substrates used and a detailed explanation of how they were modified to form aggregates of different sizes is available in chapter 2, section 4. Suspension aggregation is described in chapter 2, section 4.1.1. Both suspension culture aggregation techniques described in chapter 2, section 4.1.1 were used in this study. The process of aggregation used an osteogenic-supplemented medium as described in chapter 2, section 1.4. The aggregate samples and monolayer controls were cultured for up to 72 hours in osteogenic medium with samples being collected after 24 hours, 48 hours, and 72 hours. Given the high proliferation rate of the cells, the monolayer controls were seeded with different initial densities depending upon when they were intended for termination to avoid them becoming over confluent. The controls were seeded with 1.2 x 10^5 cells for samples intended for collection after 24 hours, 1 x 10^5 cells for samples intended for collection after 48 hours and 0.8 x 10^5 cells for samples intended for collection after 72 hours. Both suspension cultures were seeded with 3 x 10^5 cells regardless of time point collection.

2.3 *In vivo* diffusion chamber construction and seeding

Diffusion chambers were used to house the aggregated cell samples and monolayer controls during the *in vivo* experiment. Details of how the diffusion chambers were constructed, seeded, implanted and terminated can be found in chapter 2, section 5.

2.4 Optical microscopic imaging

Optical imaging was carried out on all variables within three separate MLO-A5 *in vitro* aggregation studies and one MLO-A5 *in vivo* aggregation study.

2.4.1 In vitro samples

Optical microscopy was used to monitor cellular morphology and aggregation. Images were taken using the equipment and software outlined in chapter 2, section 9.1. All samples were imaged using at least three replicates per variable.

2.4.2 In vivo chambers

Optical imaging was used to monitor surgical procedures, chamber integrity post-implantation, possible engraftment and contents immediately following the *in vivo* experiment termination and sample fixation. Equipment and software used are outlined in chapter 2, section 9.1.

2.5 Aggregate size measurement

Aggregate size was measured using a minimum of three images per variable from separate samples collected over three separate MLO-A5 *in vitro* aggregation studies and one *in vivo* aggregation study. Aggregate size was determined using the software described in chapter 2, section 10.1. All measurements were made using a minimum of three images per variable.

2.6 Histology

Histochemical staining was carried out on a minimum of three samples per variable collected from two separate MLO-A5 *in vitro* aggregation studies. Staining was conducted using an ALP detection kit, Alizarin red stain and von Kossa on all aggregate and monolayer control samples cultured for 24, 48 and 72 hours. The monolayer control samples were stained in situ for each stain mentioned. The aggregate samples, however, required additional preparation. Those aggregates stained with the ALP detection kit were stained whole and immediately post-fixation due to the rapid decline in ALP activity post-fixation using the protocol described in chapter 2, section 12.2. The aggregates intended for Alizarin red and von Kossa staining were fixed in formalin for 20 minutes, collagen encapsulated, wax embedded and sectioned prior to staining. The small size of the aggregates required them to be encapsulated in collagen prior to any further analyses to facilitate their handling. The collagen encapsulation process is described in chapter 2, section 6. The wax embedding and sectioning protocols can be found in chapter 2, sections 8.1 and 8.2, respectively. Detailed protocols for ALP, Alizarin red and von Kossa staining can be found in chapter 2, sections 12.2 – 12.4, respectively.

2.7 Real-time polymerase chain reaction

PCR was conducted on one MLO-A5 *in vitro* aggregation study with a minimum of three samples per variable. A detailed protocol outlining how PCR was conducted can be found in chapter 2, section 14. Details of data analysis are also described.

2.8 Microcomputerised tomography

MicroCT scanning was conducted on a minimum of three samples from each variable over two separate MLO-A5 *in vitro* aggregation studies. Scanning of collagen-encapsulated MLO-A5 aggregates was conducted on samples acquired from the first of two *in vitro* aggregation studies, whilst scanning of non-encapsulated aggregates was carried out using samples acquired from the second of two *in vitro* aggregation studies. Scanning was also carried out on five samples for each variable within one MLO-A5 *in vivo* aggregation study.

2.8.1 Aggregate size effect

To measure aggregate density and mineralisation over time, microCT scanning was carried out. Given the small size and integrity of the aggregate samples to be scanned, two methods of sample preparation were tried and tested. The first was with collagen gel encapsulation (as described in chapter 2, section 15.1.1) and the second was with aggregate samples alone (as described in chapter 2, section 15.1.2). Although the collagen gel encapsulation made handling of the samples easier, it lessened the level of detail that could be acquired from the microCT, especially from the samples with lower densities. The second method made handling of the samples more difficult but ultimately more successful given that more accurate results could be obtained from all samples regardless of density. The monolayer controls could not be analysed via microCT. The microCT data described in the results section of this chapter is taken from scans carried out using the second method of preparation described above, aggregate samples without collagen gel encapsulation. Thresholds of 60 and 120 were used to quantify the total aggregate volumes and dense material volumes, respectively. A normalised value was then acquired using both volume measurements giving a dense material volume normalised to total material volume.

The total aggregate volume represents all of the material that was present at a threshold of 60. The threshold of 60 was chosen because at this threshold the microCT imaging did not show any background interference yet the whole aggregates were visible suggesting that any material that remained at this threshold was solely aggregate. The dense material volume represents all of the material remaining at a threshold of 120. The threshold of 120 was chosen because previously conducted microCT scans of collagen hydrogel of a known concentration suggested that only dense extracellular material remained at a threshold of 110 or above.

2.8.2 In vivo chambers

MicroCT was the primary mode of analysis for evaluating levels of mineralisation within the *in vivo* samples. To avoid any sample contamination or loss of material during scanning, each diffusion chamber was microCT scanned and analysed in its entirety, as described in chapter 2, section 15.2. Because of the lengthy duration of the *in vivo* experiment and the subsequent increase in material density compared to the *in vitro* samples, the density thresholds had to be increased for the quantitative analysis. Therefore, a threshold of 110 was used to show the total volume of material within each of the chambers and a threshold of 170 was used to show the volume of dense material within each of the chambers.

2.9 Fourier transform infrared microspectroscopy

MicroFTIR spectra acquisition was carried out at MIRIAM beamline B22, Diamond Light Source, on two separate occasions using a minimum of three samples per variable from two separateMLO-A5 *in vitro* aggregation studies. Mapping images were taken of two samples per variable acquired from one MLO-A5 *in vitro* aggregation study. Aggregate samples were sectioned and prepared for microFTIR scanning following the protocols outlined in chapter 2, section 16.1.

Analysis protocols are described in full in chapter 2, section 16.2. Initially, analysis was carried out solely on 5 µm thick sections that were placed on MirrIR slides and scanned in reflection mode. Typical sample sections scanned in this way were reported to be 5 – 30 µm thick with the majority of polymers, non-mineralised biological tissues and organic materials being 10 – 15 µm thick. Fully mineralised bone is typically tested using 3 – 5 µm sections[412]. The intention was simply to assess and compare aggregate size and culture duration. However, due to higher-than-expected variances in sample thickness between proteinaceous regions and regions of mineralisation (later confirmed by atomic force microscopy (AFM) analysis, data not included) and the resulting decreased signal-to-noise ratio (S:N), fresh 3 µm thick sections were prepared and placed on MirrIR slides. A comparison could now be made between sample thicknesses for the purposes of preparation refinement. During this preparation phase, the decision was made to also use CaF_2 slides. This was due to literature suggesting the use of such slides for measuring biological tissues in transmission mode[412]. Three µm thick sections of large aggregates from both 24 and 72 hour culture durations were then placed on CaF_2 slides so that we could confirm the observations noted from MirrIR slides in reflection mode with CaF_2 slides in transmission mode.

The use of paraffin wax as an embedding tool and the possible effect it might have on infrared (IR) spectra was also considered and believed to be irrelevant. Before any analyses were carried out, each specimen was dewaxed, rehydrated and cleaned to ensure there was no wax present. However, should any residues have remained they would not have had any effect on our areas of interest within the spectra. The most intense absorbance features of paraffin wax are limited to 2800 – 3000 cm^{-1}, the C – H stretch region, with weaker features occurring around 1465 cm^{-1}, the C – C stretch region[412]. These qualities could not affect our data.

MicroFTIR analysis was carried out using the specifics discussed in chapter 2, section 16.2. The decision to use peak ratios as opposed to absolute values for specific peak quantification was taken with the intention of negating any possible data discrepancies caused as a result of peak oscillations from variations in sample thickness[413]. In the case of mineralised tissue, the ratio of the phosphate (PO_4) band to any of the amide bands is considered an accurate representation of the amount of mineral present normalised to the amount of collagen present[428].

2.10 Scanning electron microscopy – energy-dispersive X-ray

SEM-EDX imagining and analysis was carried out a minimum of three samples per variable acquired from two separate MLO-A5 *in vitro* aggregation studies. SEM-EDX analysis was used to confirm elemental observations and quantities. How the samples were prepared for SEM-EDX analysis is explained in full in chapter 2, section 17.1. SEM-EDX scanning and analysis is described in chapter 2, section 17.2.

2.11 Statistical analysis

Sample groups were compared using independent t-tests or one-way analysis of variance (ANOVA). A p-value below 0.05 was taken to indicate statistical significance. Graphically, statistical significance is indicated at four levels: * $p \leq 0.05$, ** $p \leq 0.01$, *** $p \leq 0.001$ and **** $p \leq 0.0001$.

3. Results

3.1 Aggregate morphology and size

MLO-A5 cellular aggregation on both coated and non-coated culture substrates was observed to occur within just 8 hours of seeding. The size and shape of the aggregates formed showed a large variation between both suspension cultures, coated and non-coated, with considerable differences in aggregate size already evident after just 24 hours of culturing (t-test, $p = 0.0255$). The aggregates formed after 24 hours on the coated substrates appeared to clump together over the following 24 hours creating larger irregular-shaped aggregates. In contrast, the smaller aggregates formed on the non-coated substrates did not clump together and remained separate and more uniformly spherical in shape (fig. 3.1).

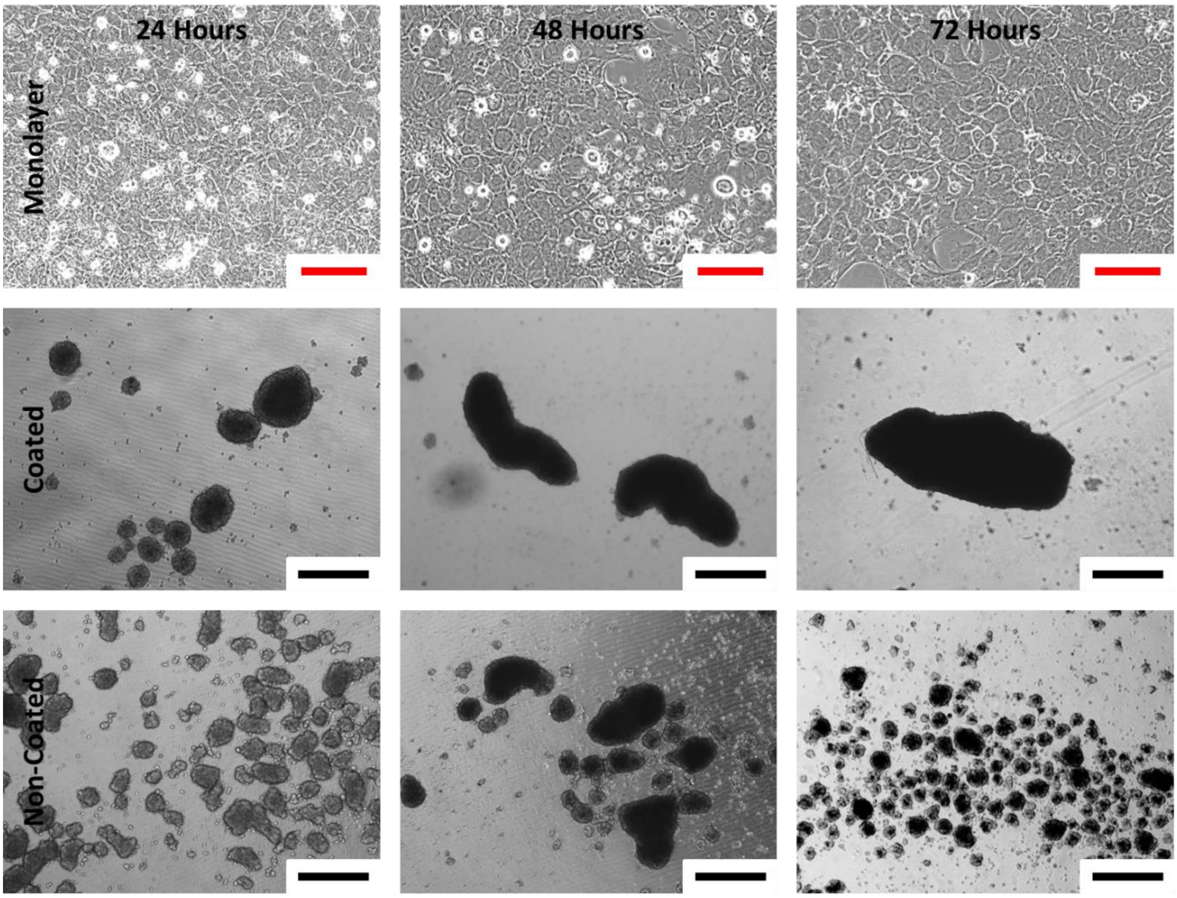

Figure 3.1: MLO-A5 cell aggregates and the monolayer control. Optical images of MLO-A5 cell aggregates formed on both coated and non-coated suspension culture substrates over three time points: 24 hours, 48 hours and 72 hours. Also shown are the monolayer controls over the same three time points. Red scale bar represents 150 µm and black scale bar represents 400 µm.

After 48 hours in culture, the average (mean ± standard error of the mean) size of the non-coated suspension aggregates had ceased to increase and by 72 hours had started to condense and shrink in size (fig. 3.1 and 3.2). Contrastingly, continuous growth was noted for the aggregates cultured on the coated substrates up to the 72 hour time point. This increase in aggregate size is thought to be caused by smaller, earlier-formed aggregates joining together and forming large, ellipse-shaped aggregates (fig. 3.1). After 72 hours in culture, the average (mean ± standard error of the mean) size of the aggregates was 79 µm for those formed on non-coated substrates and

607 µm for those formed on coated substrates (fig. 3.2). After 72 hours, the number of aggregates obtained also varied between suspension cultures with approximately 20 – 30 per well for the non-coated substrates and between 2 and 3 per well for the coated substrates. The monolayer control cells attached within 2 hours of seeding and their morphology remained unchanged throughout the 72 hour culture period.

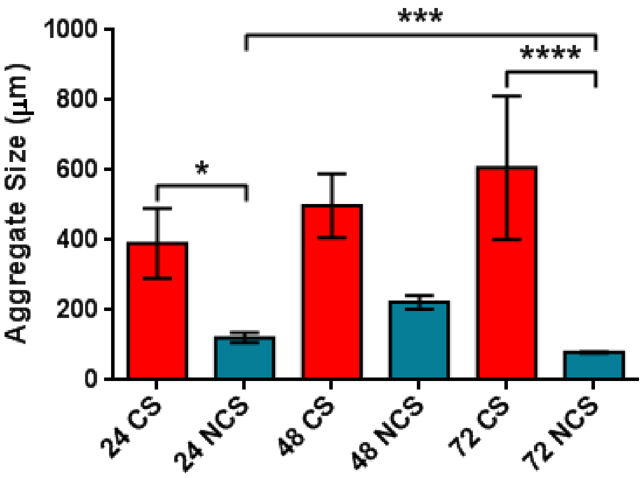

Figure 3.2: The average size of the MLO-A5 aggregates. Quantitative measurements showing the average (mean) size of the MLO-A5 cell aggregates from both suspension cultures over three time points. 24 denotes 24 hours, 48 denotes 48 hours and 72 denotes 72 hours. CS denotes coated suspension culture and NCS denotes non-coated suspension culture. Error bar represents standard error of the mean. * signifies $p < 0.05$, *** signifies $p < 0.001$ and **** signifies $p < 0.0001$.

3.2 Histochemical staining

At all three time points, the monolayer culture specimens showed only marginal ALP staining. At 24 hours, the aggregates from both suspension cultures, coated and non-coated, showed very faint staining. At 48 hours, both the large and small aggregates showed improved staining but this failed to be captured on the images of the large aggregates. At 72 hours, both large and small aggregates were positively stained for the presence of ALP but again, this was difficult to see in the images of the large aggregates (fig. 3.3). The increased size and density of the large aggregates is responsible for the poor image quality.

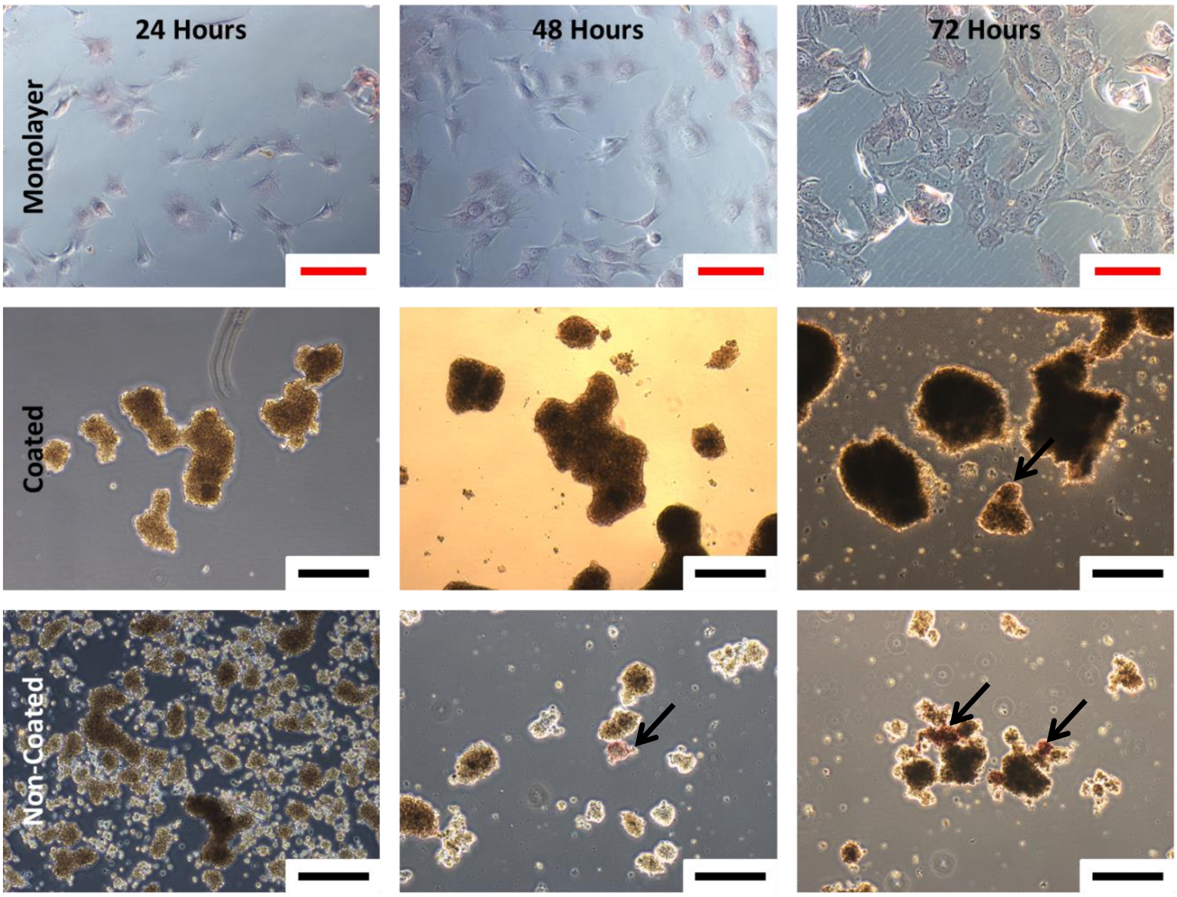

Figure 3.3: ALP staining carried out on MLO-A5 cell aggregates. The aggregates were formed using both suspension cultures over three time points: 24 hours, 48 hours and 72 hours. Also shown are the monolayer controls over the same three time points. Cell aggregate staining was carried out on whole aggregate samples. Red colouration indicates positive staining. Black arrows highlight the areas where positive staining can be seen. Red scale bar represents 150 µm and black scale bar represents 400 µm.

Similar staining results were noted with Alizarin red staining which identified the presence of calcium deposits (fig. 3.4). Calcium deposits were identified within both aggregates, small and large, after just 24 hours in culture. Calcium was not detected in the monolayer controls after 72 hours in culture. The encapsulating collagen surrounding the aggregate sections was not stained by Alizarin red indicating that physical entrapment of the reagents was not an issue and so did not result in any false positive staining.

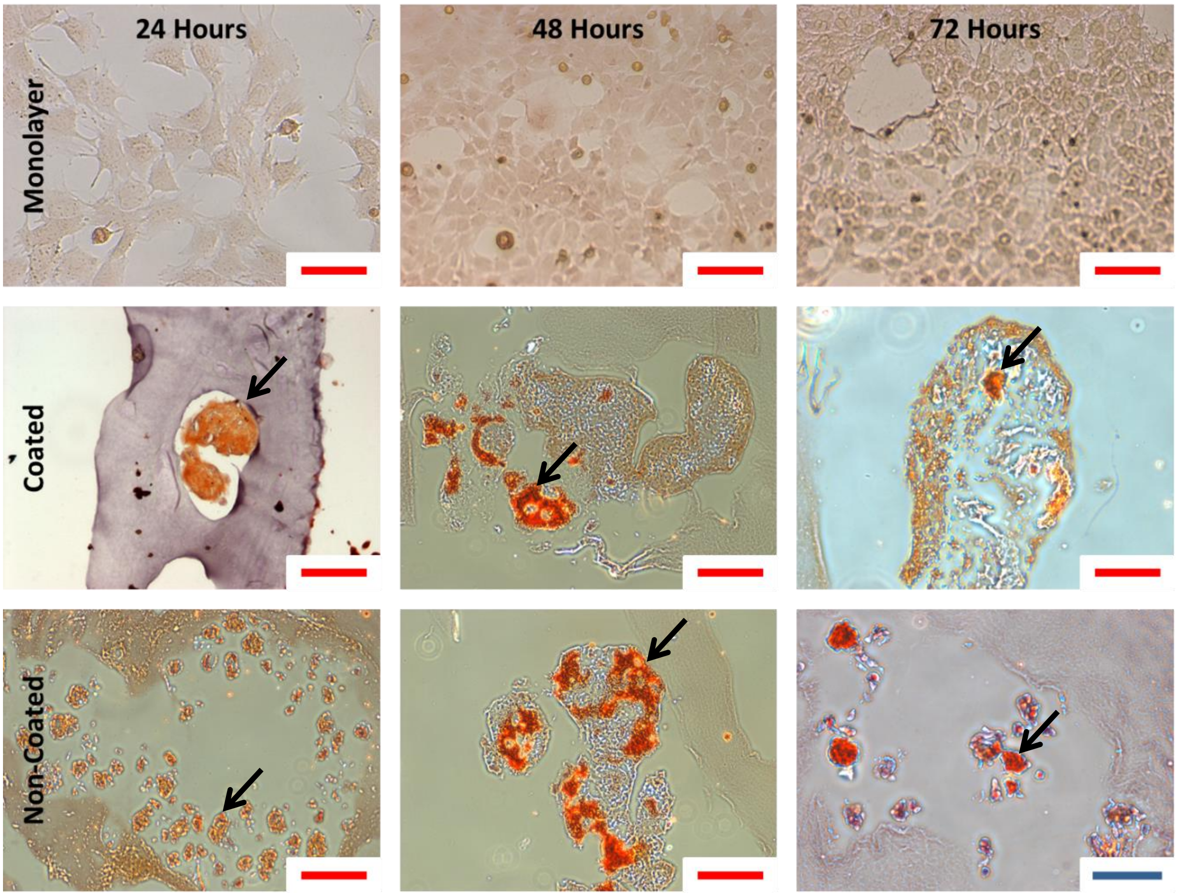

Figure 3.4: Alizarin red staining carried out on MLO-A5 cell aggregates. The aggregates were formed using both suspension cultures over three time points: 24 hours, 48 hours and 72 hours. Also shown are the monolayer controls over the same three time points. Aggregate staining was carried out on 5 µm thick sections. Red colouration indicates positive staining. Black arrows highlight the areas where positive staining can be seen. Blue scale bar represents 80 µm and red scale bar represents 150 µm.

Similar staining results were again noted with von Kossa staining which highlighted the presence of phosphate deposits (fig. 3.5). Phosphate was detected in both small and large aggregate samples after 24 hours in culture; whereas, monolayer controls did not stain positively for phosphate after 72 hours in culture.

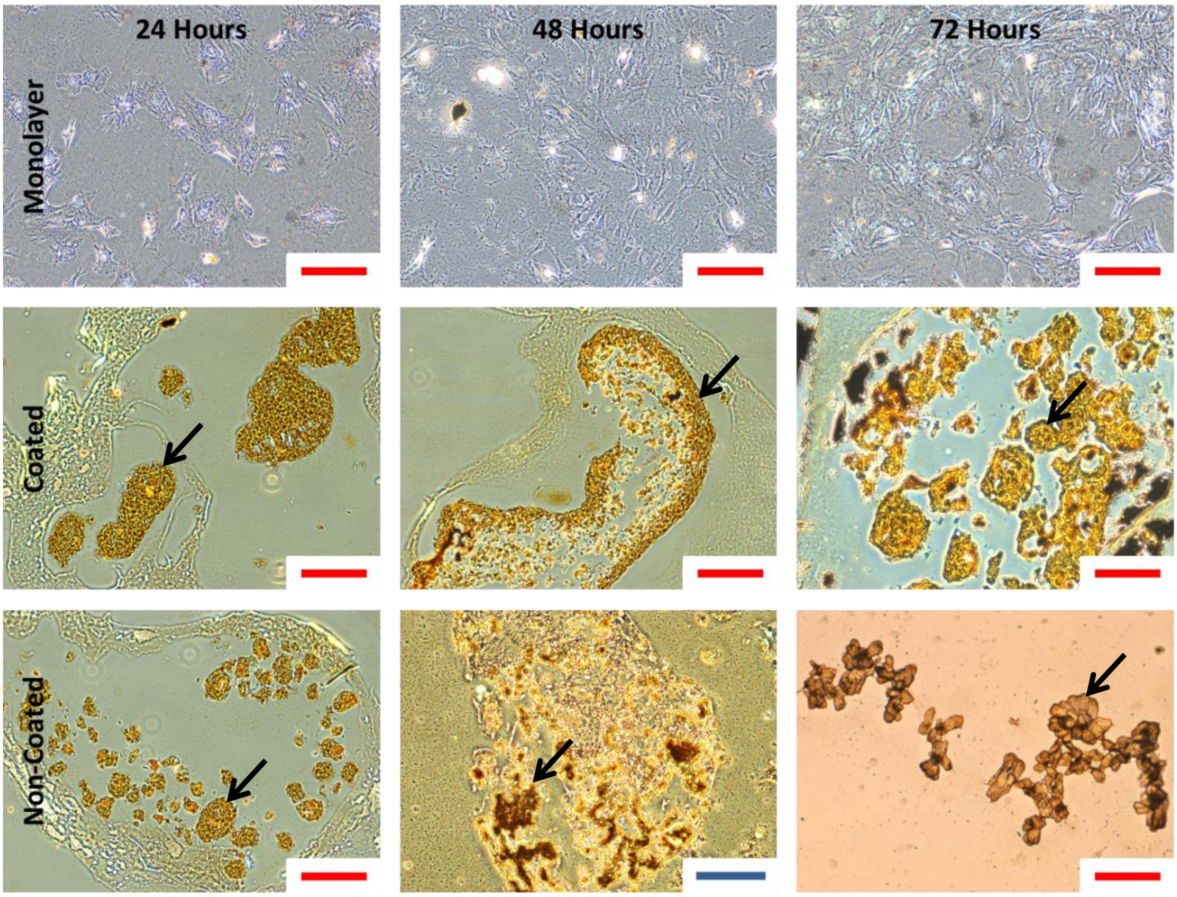

Figure 3.5: von Kossa staining carried out on MLO-A5 cell aggregates. The aggregates were formed using both suspension cultures over three time points: 24 hours, 48 hours and 72 hours. Also shown are the monolayer controls over the same three time points. Aggregate staining was carried out on 5 µm thick sections. Brown to black colouration indicates positive staining. Black arrows highlight the areas where positive staining can be seen. Blue scale bar represents 80 µm and red scale bar represents 150 µm.

3.3 Osteogenic gene expression

The four genes, i.e. collagen type I (COL 1), ALP, OPN and osteocalcin (OCN), were expressed under all three culture conditions but the expression patterns varied depending upon culture substrate and culture duration. Except for COL 1, the smaller aggregates from the non-coated substrates had higher gene expression levels when compared to the other two groups, monolayer and coated substrate cultures (fig. 3.6).

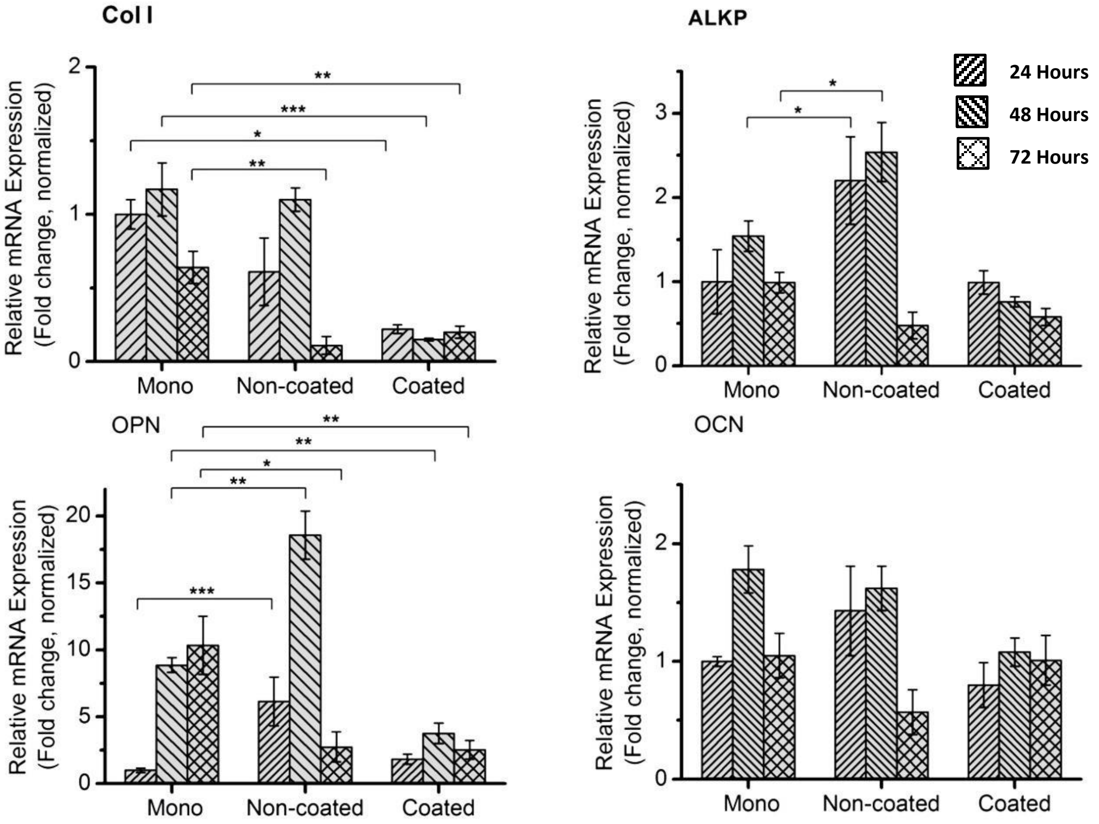

Figure 3.6: Gene analysis comparing MLO-A5 cell aggregates to a monolayer control. Real time-PCR analysis comparing the fold increase of specific genes associated with bone development across three sample variables, i.e. two MLO-A5 aggregate cultures and one ML0-A5 monolayer control, over three time points: 24 hours, 48 hours and 72 hours. Error bar represents standard error of the mean. * signifies p < 0.05, ** signifies p < 0.01, *** signifies p < 0.001 and **** signifies p < 0.0001.

3.3.1 Collagen type I

At 24 and 48 hours, mean collagen expression levels in the monolayer and non-coated substrate specimens were higher than in the coated substrate specimens. At 24 hours, the monolayer culture had a 4.5 fold increase (95% confidence interval (CI) 3.04 – 7.19) over the coated substrate specimens, whilst the non-coated substrate specimens had a 2.7 fold increase (95% CI 0.21 – 6.02) over the coated substrate specimens. At 48 hours, the monolayer culture had a 7.8 fold increase (95% CI 4.76 – 11.26) in COL 1 expression over the coated substrate specimens, whilst the non-coated substrate specimens had a 7.3 fold increase (95% CI 5.72 – 9.33) over their coated substrate counterparts. At 72 hours, the mean expression level in the non-coated substrate specimens had dropped to that of the coated substrate specimens, whereas mean expression levels remained relatively high in the monolayer culture specimens with a 5.8 fold increase (95% CI N/A) over the non-coated substrate specimens and 3.2 fold increase (95% CI 1.63 – 6.78) over the coated substrate specimens (fig. 3.6).

3.3.2 Alkaline phosphatase

At 24 and 48 hours, aggregates formed on the non-coated substrate expressed the highest levels of ALP compared to the other two culture groups with a 2.2 fold increase (95% CI 0.75 – 3.1.74) at 24 hours and a 1.6 fold increase (95% CI 1.02 – 2.57) at 48 hours. Whilst the monolayer and non-coated substrate specimens had their peak ALP expressions at 48 hours, the coated substrate specimens had their ALP peak expression at 24 hours which continually decreased thereafter (fig. 3.6).

3.3.3 Osteopontin

The three culture conditions exhibited dramatically different OPN expression patterns. The large aggregates of the coated substrate maintained a relatively constant expression for all three time points, whilst the monolayer culture specimens and the non-coated substrate aggregates experienced changes in expression throughout the culture period. At 24 and 48 hours, the non-coated substrate specimens expressed a 6 fold increase (95% CI 1.63 – 13.21) and a 2 fold increase (95% CI 1.54 – 2.73), respectively, over the monolayer specimens, which in turn expressed a 2.35 fold increase (95% CI 1.52 – 4.71) and a 4 fold increase (95% CI 2.68 – 6.5) over the coated substrate specimens at 48 and 72 hours, respectively. The peak expression along the culture time points was different for all three culture type specimens. The peak expression in both aggregate culture specimens was at 48 hours, whereas that in the monolayer culture specimen was at 72 hours (fig. 3.6).

3.3.4 Osteocalcin

The mean expression levels of OCN were similar in the three culture groups, with the highest mean expression seen at 48 hours. At 72 hours the non-coated substrate specimens exhibited the lowest mean expression levels amongst the three culture groups with a 0.5 fold increase (95% CI 0.09 – 1.25) when compared to both the monolayer and the coated substrate specimens. The coated substrate specimens showed quite similar levels throughout the three culture time points (fig. 3.6).

3.4 Observations noted during *in vivo* sample termination

All of the diffusion chambers used to house the aggregate and monolayer samples were checked and confirmed to have remained sealed throughout the 8-week culture duration. Increased vascularisation was noted covering some of the chambers but no correlation could be made between a particular sample type, i.e. aggregates of a particular size or the monolayer samples, and the varied vascularisation (fig. 3.7). The monolayer samples had in several cases developed extracellular material within the sealed chambers confirming the presence of cellular activity (fig. 3.7). With regards to the aggregates, the small aggregates (those produced on the non-coated suspension substrate) appeared to better maintain their structure over the course of the experiment when compared to the large aggregates. A large number of small aggregates were found in each of their chambers, whilst many of the large aggregates (those produced on the coated suspension substrate) appeared to have disintegrated *in vivo* (fig. 3.7). The surgeon also noted at the time of termination that the small aggregates felt more solid when being examined. The small aggregates too appeared to have created more extracellular material over the course of the experiment that often had stronger colouration when compared to the large aggregates (fig. 3.7).

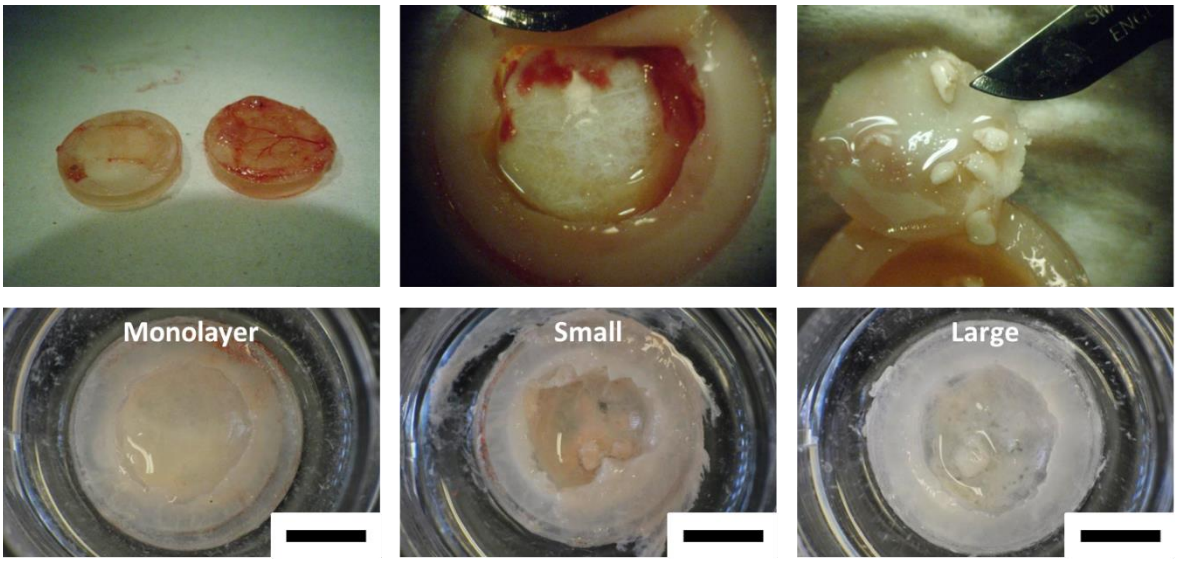

Figure 3.7: *In vivo* chambers post-termination. Optical images showing the initial *in vivo* chamber terminations and the varied chamber vasculature followed by the condition of the chamber contents. Scale bar represents 500 µm.

3.5 Microcomputerised tomography

3.5.1 MLO-A5 in vitro aggregates

fig. 3.8 shows the coated and non-coated suspension aggregates over the three culture time points, 24 hours, 48 hours and 72 hours, and fig. 3.9 shows the quantitative measurements acquired from such scans. The total volume of material within each of the samples at a density threshold of 60 (provided by the software mode of analysis 'BV/Density only Bone Eval.') after 24 hours were 0.219 and 2.189 mm³ for the coated and non-coated culture specimens, respectively. After 48 hours, the volumes were 0.458 and 2.288 mm³ for the coated and non-coated culture specimens, respectively. After 72 hours, the volumes were 0.379 and 0.414 mm³ for the coated and non-coated culture specimens, respectively. The volumes of dense material within these samples at a density threshold of 120 after 24 hours were 0.002 mm³ and 0.035 mm³ for the coated and non-coated culture specimens, respectively. After 48 hours, the volumes of dense material were 0.020 mm³ and 0.139 mm³ for the coated and non-coated samples, respectively. After 72 hours, the volumes were 0.078 mm³ and 0.078 mm³ for the coated and non-coated culture specimens, respectively. Given the way in which the aggregate samples were scanned, the volume of dense material within the aggregates at a density threshold of 120 was normalised to the total volume of the aggregate samples at a density threshold of 60. This gave normalised figures of 0.01 mm³ and 0.016 mm³ for the coated and non-coated culture specimens, respectively, after 24 hours. After 48 hours, the normalised figures were 0.042 mm³ and 0.060 mm³ for the coated and non-coated culture specimens, respectively. After 72 hours, the normalised figures were 0.218 mm³ and 0.190 mm³ for the coated and non-coated culture specimens, respectively (fig. 3.9).

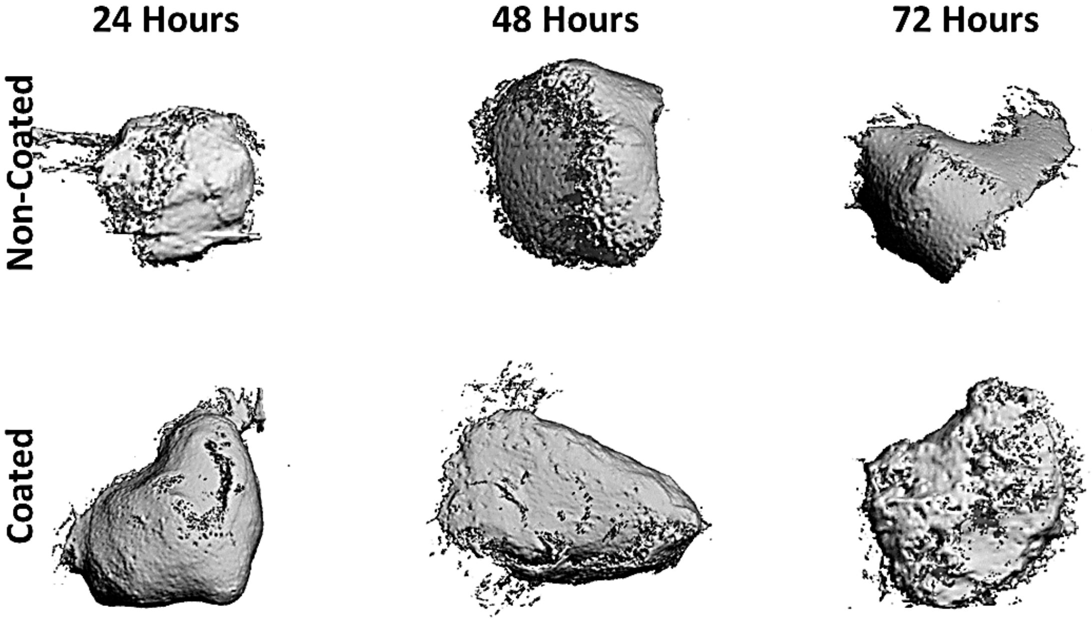

Figure 3.8: MicroCT scan images of both MLO-A5 cell aggregate cultures. Shown are the coated and non-coated culture aggregates over three time points, 24 hours, 48 hours and 72 hours, at a density threshold of 60. The three scan images representing the non-coated suspension culture specimens comprise multiple small aggregates combined into one; whereas, the three scan images representing the coated suspension culture specimens are of single aggregates.

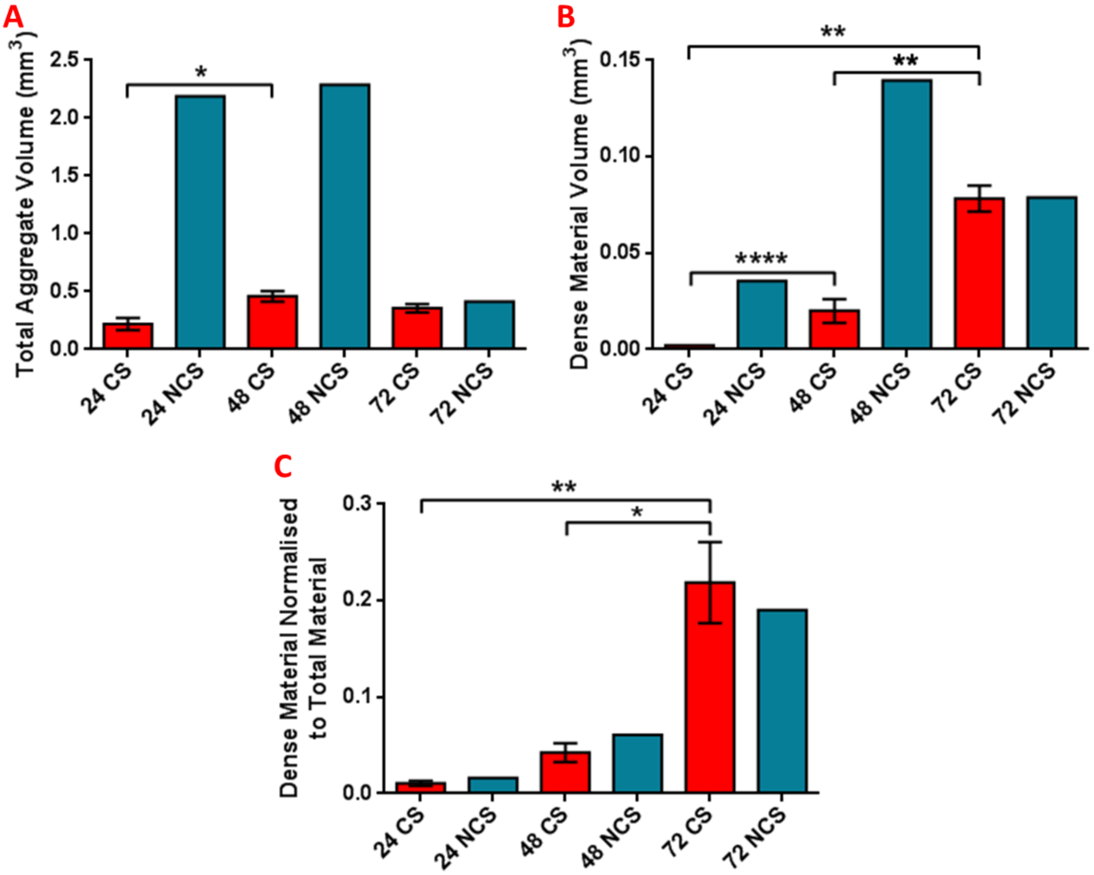

Figure 3.9: MLO-A5 cell aggregate volume measurements. Values were acquired from two thresholds: 60 (**A**) (total aggregate volume) and 120 (**B**) (dense material volume). Also shown is the ratio of both volume measurements (**C**) giving a dense material volume normalised to total material volume. Error bar represents standard error of the mean. * signifies $p < 0.05$, ** signifies $p < 0.01$ and **** signifies $p < 0.0001$.

3.5.2 MLO-A5 in vivo samples

Fig. 3.10 shows whole chamber scan images for the small and large MLO-A5 aggregate samples at a threshold of 130 alongside the average (mean ± standard error of the mean) density measurements for each variable. Fig. 3.11 shows the quantitative measurements acquired from the whole chamber scans. The volume of material found in each of the samples tested at a density threshold of 110 averaged (mean ± standard error of the mean) values of 0.426, 5.698 and 2.222 mm³ for the monolayer, small aggregate and large aggregate samples, respectively (one-way ANOVA, $p = 0.0391$). The volume of dense material found in the diffusion chambers at a density threshold of 170 was 0.036, 1.165 and 0.623 mm^3 for the monolayer, small aggregate and large aggregate samples, respectively. The volume of dense material was then normalised to the total volume of material found in the chambers giving values of 0.047, 0.197 and 0.088 mm^3 for the monolayer, small aggregate and large aggregate sample chambers, respectively (fig. 3.11). Also shown is a comparison between the normalised dense material values from each chamber variable and their equivalent values acquired from rat femur samples of various ages.

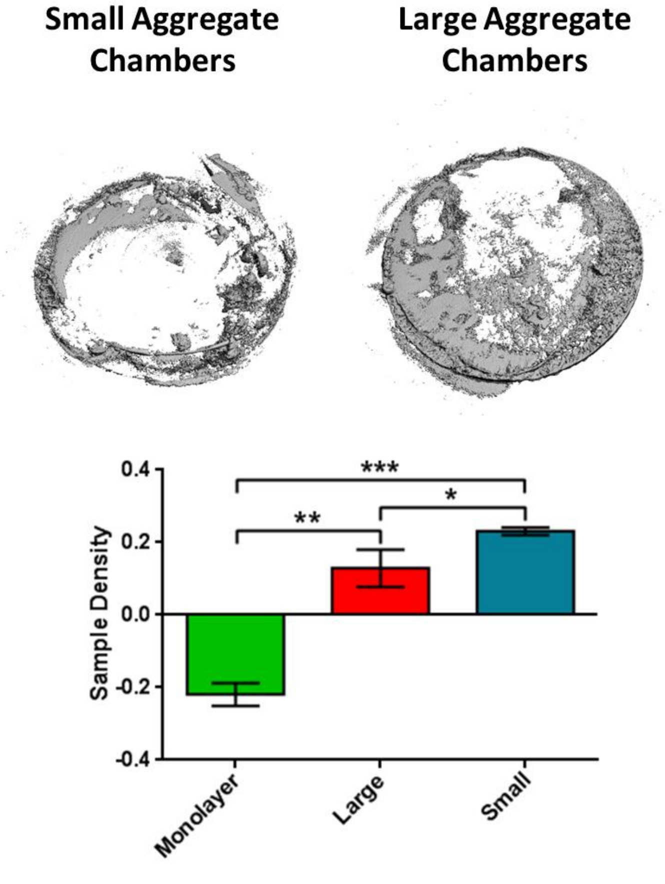

Figure 3.10: MicroCT scan images of whole MLO-A5 *in vivo* chambers. The chambers were fixed in formalin and contain both small and large MLO-A5 aggregate samples. No material was visible in the monolayer control chambers. The chamber contents are shown at a threshold of 130. Also shown is a graph displaying the density measurements of the chambers containing all three sample variables, small and large aggregates and the monolayer controls, at a threshold of 110. Error bar represents standard error of the mean. * signifies $p < 0.05$, ** signifies $p < 0.01$ and *** signifies $p < 0.001$.

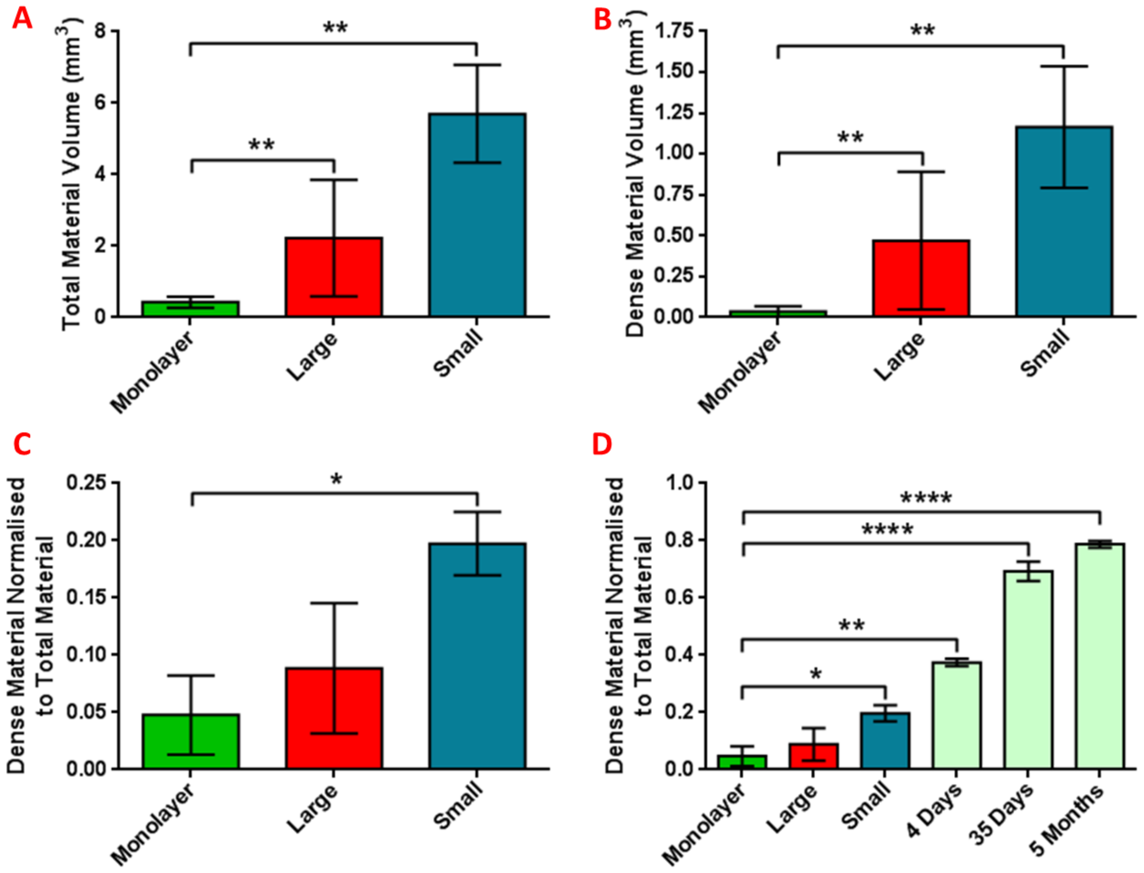

Figure 3.11: MLO-A5 *in vivo* chamber volume measurements. Values were acquired from two thresholds: 110 (**A**) (total material volume) and 170 (**B**) (dense material volume). Also shown is the ratio of both volume measurements (**C**) giving a dense material volume normalised to total material volume. In addition, the normalised material volume has also been compared to that of rat femur samples over three different ages: 4 days, 35 days and 5 months (**D**). Error bar represents standard error of the mean. * signifies $p < 0.05$, ** signifies $p < 0.01$ and **** signifies $p < 0.0001$.

3.6 Fourier transform infrared microspectroscopy

3.6.1 The effect of culture duration and aggregate size

MicroFTIR analysis of the *in vitro* aggregates has shown that culture duration has a substantial effect on mineralisation. Aggregates cultured over 24 and 72 hours have exhibited significant differences in spectral regions associated with mineralisation. Those aggregates cultured over 72 hours displayed considerably higher PO_4 peaks (960 – 1143 cm^{-1})[429] when compared to the aggregates cultured over just 24 hours (fig. 3.12). Considerable differences within particular spectral regions have also been observed between substrate types (aggregate size). The large aggregates have shown higher levels of mineralisation when compared to the small aggregates over the same 72 hour culture period (fig. 3.12).

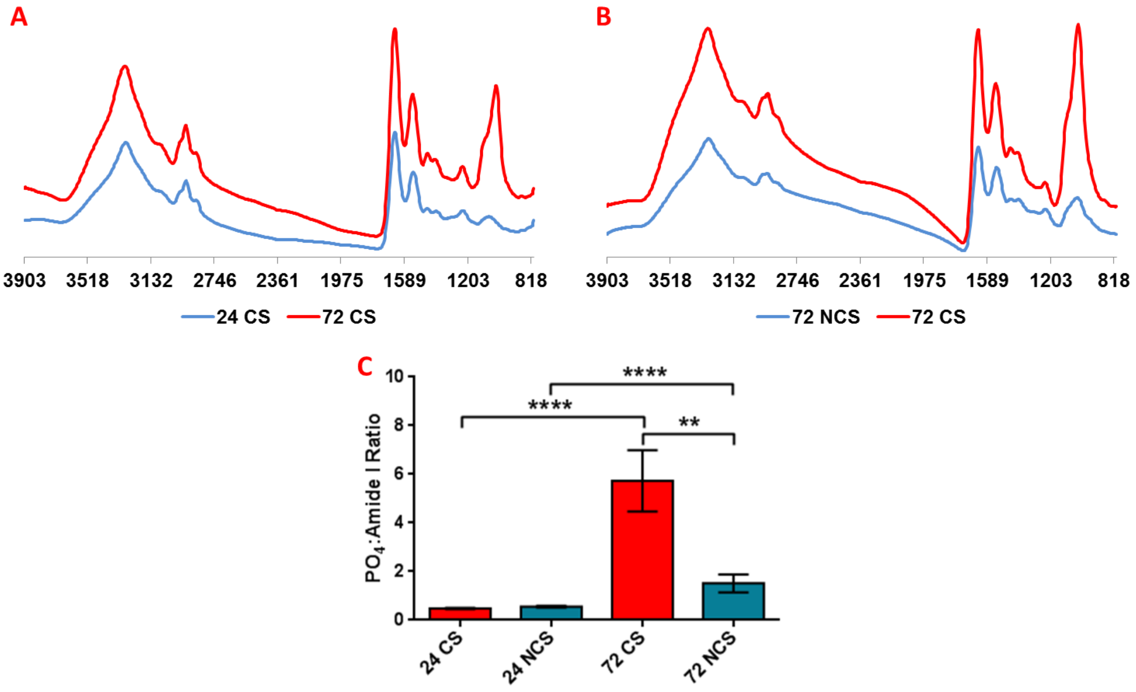

Figure 3.12: MicroFTIR spectra of MLO-A5 aggregates. Shown are the 24 hour and 72 hour coated suspension culture MLO-A5 aggregates (**A**) alongside microFTIR spectra of 72 hour non-coated suspension and coated suspension culture aggregates (**B**). Also shown is the PO_4:amide I ratios (**C**) of 24 hour and 72 hour coated and non-coated suspension culture aggregates. The MLO-A5 aggregate samples were prepared on MirrIR slides using 3 µm thick sections. Analysis was carried out in reflection mode using 128 scans per point at a resolution of 8 cm^{-1}. 24 and 72 denote hours in culture; CS and NCS denote coated suspension culture and non-coated suspension culture, respectively. Error bar represents standard error of the mean. ** signifies $p < 0.01$ and **** signifies $p < 0.0001$.

Taking PO_4:amide I ratios into account, the large and small aggregates displayed mineralisation levels of 0.48 and 0.55, respectively, after 24 hours in culture. After 72 hours in culture, these levels increased to 5.73 and 1.51, respectively (fig. 3.12) (t-test, $p = 0.0054$). After 72 hours of culturing, the levels of mineralisation within both types of aggregates increased significantly (one-way ANOVA, $p < 0.0001$) with the largest increase noted within the large aggregates compared to the small aggregates (t-test, $p = 0.001$ compared with $p = 0.0199$).

Scanning images and mapping analysis of both MLO-A5 aggregate sizes over 24 and 72 hours not only visually confirmed the presence of phosphate within the aggregates, but also offered an insight into the mineralisation development pattern (fig. 3.13). The concentrations of amide I (1625 – 1694 cm^{-1}) and PO_4 (960 – 1143 cm^{-1}) groups for the aggregates were mapped. After 24 hours in culture, the large aggregates displayed developing mineralisation that was more peripheral within the aggregates, whilst the initial areas of mineralisation within the small aggregates appeared to be more central. After 72 hours, mineralisation within both aggregate cultures, small and large, appeared to be more uniform and widespread throughout the aggregates.

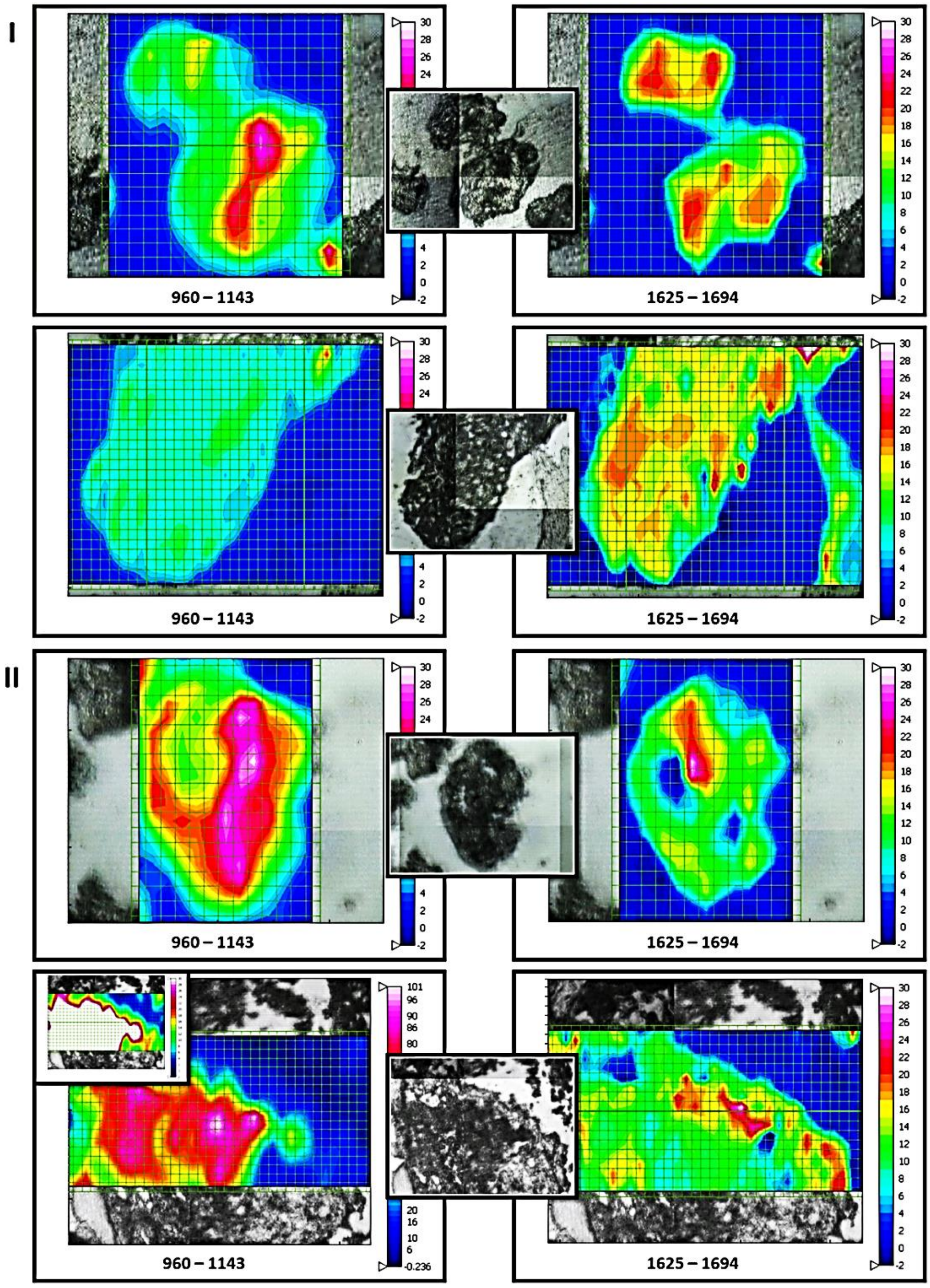

Figure 3.13: MicroFTIR mapping images of the MLO-A5 aggregates. **I**) Top: PO_4 and amide I regions of a 24 hour non-coated suspension MLO-A5 aggregate. Bottom: PO_4 and amide I regions of a 24 hour coated suspension MLO-A5 aggregate. **II**) Top: PO_4 and amide I regions of a 72 hour non-coated suspension MLO-A5 aggregate. Bottom: PO_4 and amide I regions of a 72 hour coated suspension MLO-A5 aggregate. The black and white images are corresponding visible images and the colour scale indicates spectral intensity. The PO_4 region of the 72 hour coated suspension aggregate was so intense (see insert in lower left image), the arbitrary unit (au) scale was heightened to lessen the intensity. The samples were prepared on MirrIR slides using 3 µm thick sections. Analysis was carried out in reflection mode with an 8 cm^{-1} resolution and 128 scans per point.

3.6.2 The effect of sample preparation

Analyses were carried out on 24 hour and 72 hour coated suspension aggregate sections cut to thicknesses of 3 and 5 µm using a synchrotron source in reflective mode. Visually, differences between the PO_4 regions of the spectra of the 24 hour aggregate sections were not overly impressive. The spectra of the 72 hour aggregates, however, clearly show considerable differences in PO_4 peak height (fig. 3.14). The 3 µm thick samples showed far higher PO_4 peaks indicating a higher sensitivity within that particular range.

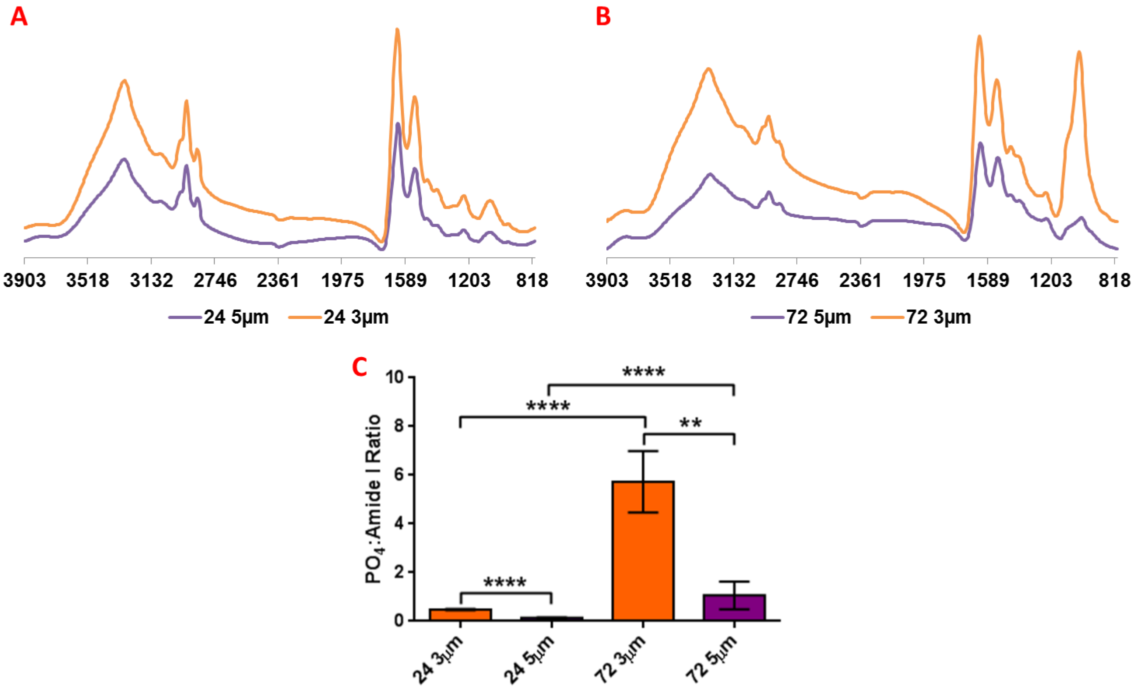

Figure 3.14: MicroFTIR spectra of MLO-A5 aggregates. Shown are the 24 hour (**A**) and 72 hour (**B**) coated suspension culture MLO-A5 aggregates. Also shown is the PO_4:amide I ratios (**C**) of 24 hour and 72 hour coated suspension MLO-A5 aggregates. Samples were prepared on MirrIR slides using 3 µm and 5 µm thick sections. Analysis was carried out in reflection mode with an 8 cm^{-1} resolution. The 3 µm thick sections used 128 scans per point and the 5 µm thick sections used 256 scans per point. 24 denotes 24 hours and 72 denotes 72 hours. Error bar represents standard error of the mean. ** signifies $p < 0.01$ and **** signifies $p < 0.0001$.

Using PO_4:amide I ratios has given a more in-depth look at how section thickness affects the obtained data. Even after just 24 hours in culture, significant differences were noted between the PO_4:amide I ratios of the 3 and 5 µm thick sections, 0.48 and 0.13, respectively (t-test, $p < 0.0001$) (fig. 3.14). Significant differences were again noted between the 72 hour aggregate sections, 5.732 and 1.062 for the 3 and 5 µm thick sections, respectively (t-test, $p = 0.0033$).

3.7 Scanning electron microscopy – energy-dispersive X-ray

The SEM imaging and EDX analysis was carried out for large and small MLO-A5 aggregates cultured over 24 and 72 hours. The spatial distribution of mineralised regions has clearly been identified within the aggregates with calcium and phosphorus regions also being shown to overlap for both time points, 24 and 72 hours (fig. 3.15). After 24 hours in culture, the only apparent difference between aggregate samples is in aggregate size; no significant differences can be identified in calcium and/or phosphorus levels between the two different-sized aggregates. After 72 hours, clear differences can be seen in both calcium and phosphorus levels between the aggregates of the coated and non-coated substrates (fig. 3.15).

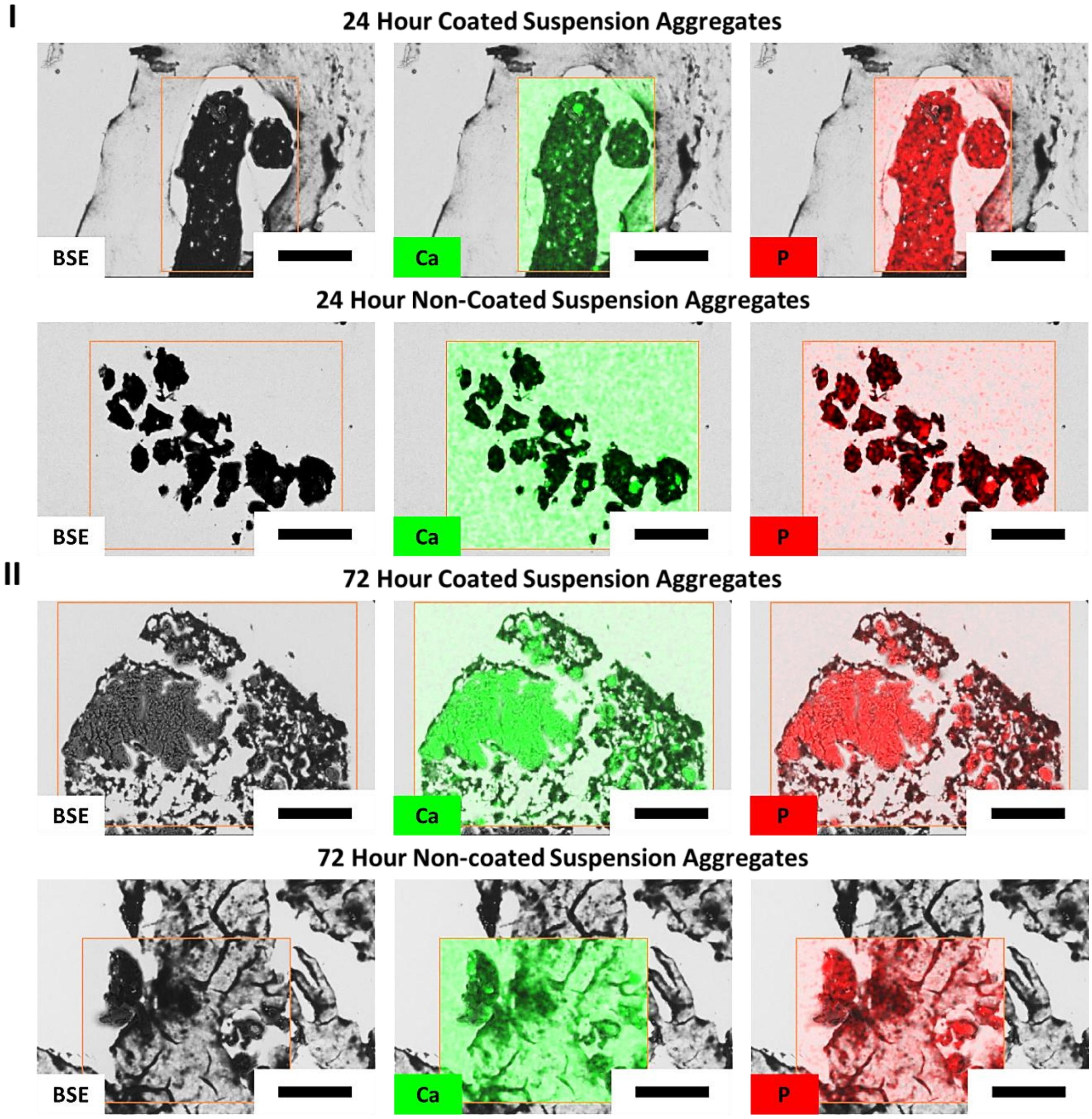

Figure 3.15: SEM images with combined EDX analysis of MLO-A5 aggregates. Shown is the calcium (green) and phosphorus (red) element distributions in MLO-A5 aggregates from both coated and non-coated suspension cultures after 24 hours (I) and 72 hours (II). BSE denotes base, Ca denotes calcium and P denotes phosphorus. Scale bar represents 80 µm.

Quantitatively, the total calcium levels from both MLO-A5 aggregate sizes at 72 hours increased from their 24 hour levels; however, only the increase in the large aggregates was significant (t-test, p = 0.0023) (fig. 3.16). The larger aggregates showed a 2.93 fold increase (95% CI 2.19 – 3.93) in calcium levels compared to their smaller aggregate counterparts at the same time point. The calcium-to-phosphorus ratio (Ca:P) is also represented (fig. 3.16). At 24 hours, the large and small aggregates had Ca:P ratios of 1.43 and 1.66, respectively. At 72 hours, the ratios had risen to 3.11 and 3.10 for the large and small aggregates, respectively. The large aggregates saw the most significant increase in ratio value, t-test, p = 0.0008 compared to 0.0361.

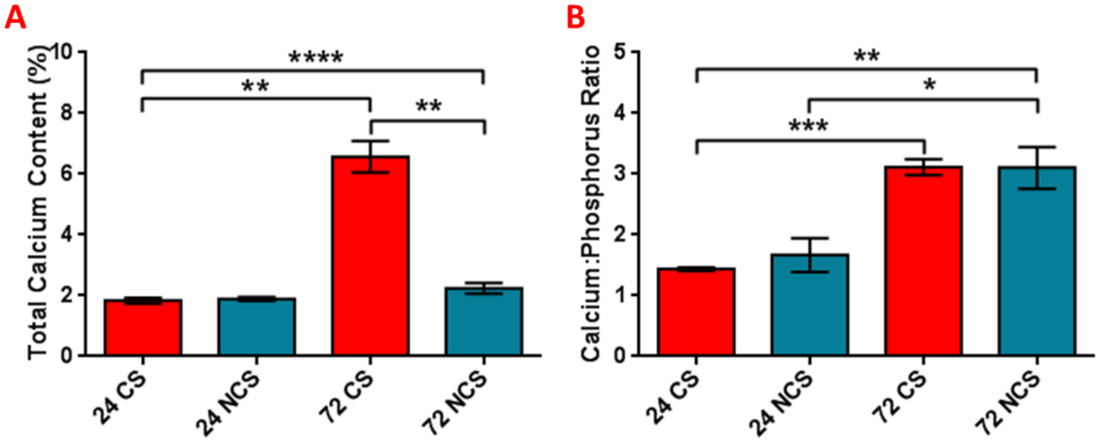

Figure 3.16: SEM-EDX measurements of MLO-A5 aggregates. Shown is the analysis of 24 hour and 72 hour coated and non-coated suspension MLO-A5 aggregates showing the total calcium content represented as a percentage (**A**). Also shown is the SEM-EDX analysis of 24 hour and 72 hour coated and non-coated suspension MLO-A5 aggregates showing the calcium and phosphorus contents represented as a ratio (**B**). 24 denotes 24 hours, 72 denotes 72 hours, CS denotes coated suspension culture and NCS denotes non-coated suspension culture. Error bar represents standard error of the mean. * signifies $p < 0.05$, ** signifies $p < 0.01$, *** signifies $p < 0.001$ and **** signifies $p < 0.0001$.

4. Discussion

In this study, we established a facile bone cell aggregation model by using a simple and convenient surface modification technique to promote the production of different-sized bone cell aggregates. We confirmed the acceleration effect of mineral formation in aggregates compared to a monolayer culture. Consistent with reports from other groups[153,415], our data demonstrated that culturing osteoblasts in an aggregate culture generates far more mineralised matrix under identical culture conditions, medium and duration, when compared to culturing them in a conventional monolayer culture, where little or no mineralised matrix was generated. The experimental results revealed that the gene expression of important ECM molecules for bone formation, COL 1, ALP, OPN and OCN, was temporally and spatially regulated, most likely influenced by cell – cell/cell – ECM interactions. In addition, the mineral content, composition and distribution within the bone cell aggregates depends on the culture substrate used (large aggregates formed on the coated substrate versus small aggregates formed on the non-coated substrate), evidenced by the histochemical staining, microCT analysis for both *in vitro* and *in vivo* components of the study, elemental quantification provided by microFTIR and SEM-EDX analyses, and phosphate distribution mapping, again provided by microFTIR. We postulate that aggregate culturing mimics the endogenous microenvironment, thus supporting osteoblast survival and full osteogenic differentiation[416]. An important effect of the culture substrate was on aggregate size. Aggregation pushes osteoblasts from a proliferation phase to a matrix synthesis, or maturation and mineralisation phase, whilst aggregate size determines how fast and how far these cells can be driven toward matrix mineralisation. Our data suggest that the large aggregates accelerate the onset and rate of mineralisation; most likely as a response to the more intense cell – cell contact experienced by those cells in the large aggregates compared to those in the small aggregates.

4.1 Substrate chemistry modification

Our study shows that altering the chemistry of cell culture substrates is a convenient and efficient technique to promote cell aggregation. Multiple aggregates can be formed within just a few hours without the requirement of a complicated mould or hanging drop culture. We used two different substrates to control aggregate size, i.e. a non-coated polystyrene surface and a Pluronic F127-coated polystyrene surface[7]. Pluronic F127 is polypropylene oxide (PPO) – polyethylene oxide (PEO) tri-block copolymer with two hydrophilic PEO side chains and a hydrophobic PPO chain in the centre[417], which endows Pluronic F127 with extremely flexible molecular chains and a high capacity to hydration. Coating substrates with F127 greatly suppresses protein adhesion[416,417], preventing seeded cells from adhering to the substrate and inducing them to form aggregates which then remain in suspension. The large aggregates found in the F127-coated plates were ascribed to the higher expulsion forces of F127 for proteins[430,431]. Our data reveal that aggregate size, controlled by substrate chemistry, affected the mineralisation rate. This finding is consistent with an earlier study on a spheroid culture system with different cell numbers in each aggregate[432]. In that study, higher cell numbers resulted in larger aggregates that produced higher calcium contents, a similar tendency to our results. Our microCT and SEM-EDX data indicate that the size of the aggregates may be a critical parameter in controlling mineralisation rate and mass. By tailoring the substrate composition, we can generate different-sized aggregates, enabling the study of different mineralisation stages.

4.2 Gene expression

In vivo bone formation is a prolonged process characterised by a series of reactions with osteoblasts playing a pivotal role in all stages. Osteoblasts are derived from osteoprogenitor cells, frequently from pluripotent mesenchymal stem cells (MSCs)[433]. The major role of osteoblasts is to produce ECM proteins and to regulate the mineralisation of the matrix. Gene expression patterns for these ECM proteins are similar between the *in vivo* developmental sequence and *in vitro* culture systems[9] except for one minor difference. It has been reported that OPN expression is slightly different *in vivo* when compared to *in vitro*; *in vivo* levels continue to increase after animal birth, whilst *in vitro* levels decrease when reaching the calcification stage. Nevertheless, osteoblast differentiation takes place in sequential steps. The rapid expression of ALP and COL 1 is followed by mineralisation[9,434] and fibronectin and COL 1 levels are high during proliferation but decline during the differentiation stage.

Lian and Stein[434] have depicted the temporal expression of cell growth and osteoblast phenotype related genes during a series of monolayer culture experiments and used them to define three distinct phases of osteoblast phenotype development eventually leading to bone formation, namely: I) proliferation and matrix synthesis, II) matrix development, maturation and organisation, and III) matrix mineralisation (fig. 3.17)[337,434,435]. Interestingly, when we plot the gene expression data from our three cell cultures under different culture durations on the same figure, a distinct separation between the aggregates and the monolayer culture method is suggested. The monolayer culture specimens appeared to stay in the late proliferation/early matrix maturation phase for the first time point tested and for the last two time points remained in matrix maturation, not mineralisation. The small aggregates seemed to be in the maturation phase for the first two time points and only moved to the mineralisation phase during the third time point. In contrast, the large aggregates seemed to be in the mineralisation phase for all three time points (fig. 3.17).

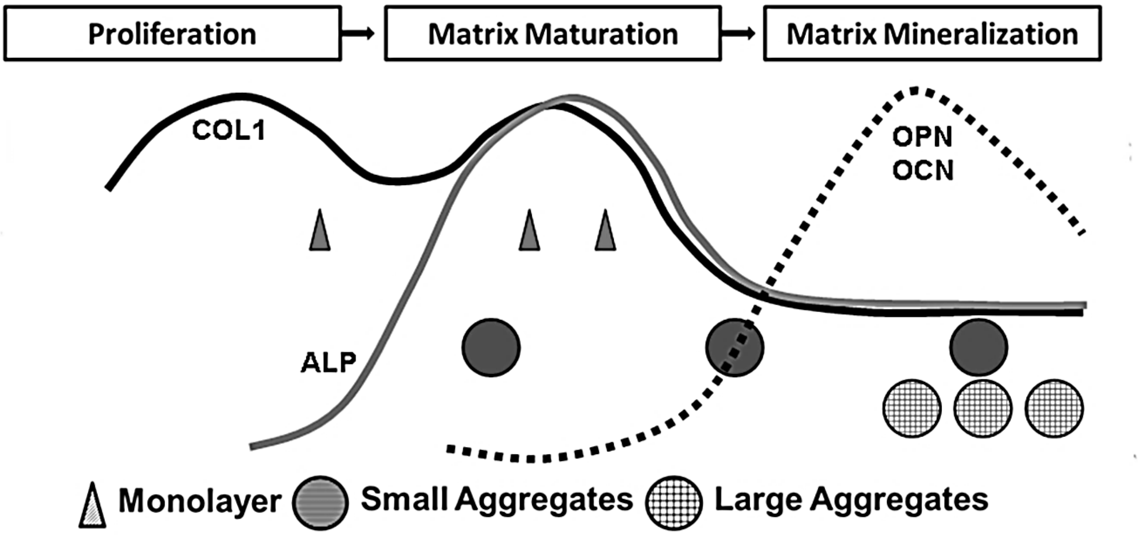

Figure 3.17: Prediction of the osteoblast development stages in MLO-A5 aggregates. Shown is the function of culture conditions and duration through depicting the temporal gene expression data (fig. 3.6) into the profile of marker gene expression produced by Lian and Stein[434], modification of fig. 4. Three symbols are used for each culture condition to represent three time points: 24 hours, 48 hours and 72 hours.

In this study, the monolayer culture exhibited the highest COL 1 expression for all three time points. A high COL 1 gene expression suggests that the monolayer culture specimens were in a late proliferation/matrix maturation phase (fig. 3.6)[45,434–438]. There are two peaks across the two phases implying that collagen production lasts for a prolonged period in the development pathway. The large aggregates demonstrated a low expression of COL 1 and ALP suggesting that they had left the maturation phase within just 24 hours of culturing and started transferring to the mineralisation phase (fig. 3.6). OPN expression in the monolayer culture continuously increased, further suggesting that they were in a late proliferation/maturation phase, whilst in both aggregate cultures, OPN expression was down-regulated by the 72 hour time point, reinforcing the suggestion that these cultures had entered the mineralisation stage (fig. 3.6). OCN has been classified as the last of the expression markers to be upregulated in mature osteoblasts[439]. Our OCN expression was similar in all culture specimens, suggesting all had at least reached a late osteoblast stage. From our study and those reported by other groups[440], it becomes clear that monolayer culture of even late osteoblasts under conditions of non-confluency maintains them in a proliferative state and could not drive them into matrix mineralisation for the duration of our experiments (3 days, see also Kato *et al.*[152]), whilst aggregate culturing can decisively drive this later proliferation/early maturation phase into the subsequent mineralisation phase.

A unique aspect of our study is the ability to finely control the stage of the osteoblast population along the osteoblast developmental sequence. If osteoblasts are cultured into aggregates of a large size by using a coated substrate, e.g. 500 – 100 µm, they have a high probability of quickly passing the late proliferation and maturation phase and entering the matrix mineralisation phase. Within such a culture environment, a large portion of the cell population has intense cell – cell contact, inhibiting further proliferation and causing a jump to the subsequent phase. In the smaller aggregates produced using a non-coated substrate, e.g. 80 – 300 µm, a large proportion of the cell population is lacking this intense cell – cell contact, particularly the cells on the periphery of the aggregates. These cells, therefore, remain in the matrix maturation phase for a longer period before eventually entering the matrix mineralisation phase at 72 hours. Further investigation is needed to define more accurately the aggregate size regions and determine which developmental phase is reached within a 72 hour culture period.

4.3 Mineralisation

Other outcomes of this study, including protein and mineral productions, support the above discussed phase mapping (proliferation, maturation and mineralisation). The histochemical staining, SEM-EDX and microFTIR all indicate that the large aggregates contained a higher quantity of minerals compared to the small aggregates.

4.3.1 Histochemical staining

The presence of minerals associated with bone formation, i.e. calcium and phosphate, was confirmed in both aggregate samples, i.e. small and large, after just 24 hours in culture, but not in the monolayer culture. This suggests that both aggregate types experienced enhanced mineralisation rates compared to their monolayer counterparts, whilst using the same supplemented medium and over the same culture period. Numerous previous studies have also used similar histochemical stains to confirm the onset of osteogenesis, i.e. ALP staining[4], and the presence of particular osteogenic-related minerals, i.e. calcium ions (through Alizarin red staining)[153,386] and phosphate salts (through von Kossa staining)[4,152], with the intention of showing enhanced osteogenesis and/or mineralisation rates.

4.3.2 Scanning electron microscopy – energy-dispersive X-ray

The combination of SEM imaging and EDX analysis accurately displayed the spatial distribution of developing calcification evidenced by the regions of calcium and phosphorus deposition which are believed to highlight regions of mineralisation. It is the quantitative elemental analysis that provided the most interesting data with this technique in the form of Ca:P ratios. In terms of what these ratios mean for bone nodule quality, some points of discussion can be raised. On one hand, one might consider higher ratios as being beneficial in terms of bone quality given that lower bone Ca:P ratios have been associated with bone loss[441] and a correlation has also been made between collagen fibril diameter and Ca:P ratios; in that, a decreased Ca:P ratio is an indication of a decreased collagen fibril diameter as well as bone loss[442]. Another aspect to be taken into account is that a ratio of 2.19 is typically used as a median reference value[443]. This value, however, is lower than those obtained from a study which found human ribs to contain ratios of 2.31 and 2.36 for women and men, respectively[444]. A ratio of < 2 is indicative of a hydroxyapatite (HA) dominant environment where bone hardening is occurring, whereas a ratio of > 2 is considered to be a calcium oxide (CaO) dominant phase which is indicative of bone formation due to osteoblast adhesion[445]. Whatever the true meaning of these ratios, the levels of calcium and phosphorus within both aggregate sizes, which are not evident in the monolayer culture, are promising indicators for developing bone but it is noted that further investigation is needed to evaluate the true significance of the figures discussed here.

4.3.3 Fourier transform infrared microspectroscopy

4.3.3.1 Temporal and spatial mineral distributions

The data obtained from the microFTIR not only corroborates with the data discussed above but also demonstrates that synchrotron-sourced microFTIR is advantageous in revealing dynamic mineralisation within immature tissue-engineered bone specimens. It would appear that the PO_4 region is very sensitive to the infrared source[7]. Our data has shown that both culture duration and aggregate size can affect the level and spatial distribution of minerals associated with bone formation. Mineral levels increased in conjunction with aggregate size and culture duration. This is most likely due to the larger aggregates entering the matrix mineralisation phase earlier and staying there for longer during the 72 hour culture period, compared to the smaller aggregates.

Interestingly, the mapping images have revealed different mineralisation patterns in the small and large aggregates. After 24 hours in culture, the large aggregates showed PO_4 regions developing around the outer edges of the aggregate, whilst the small aggregates showed signs of mineralisation centred within the aggregate. After 72 hours in culture, both the large and small aggregates displayed substantially increased and uniformly widespread PO_4 distributions. This suggests that the large aggregates mineralised from the periphery, whereas the small aggregates mineralised from the centre. Peripheral mineralisation was also observed by Schneider and colleagues[446]. These differing regions of initial mineral deposition could possibly be an indication of a region within the aggregates where an optimum balance exists between cell – cell and cell – matrix interactions and oxygen and nutrient diffusion. Given the size difference between the aggregates, these regions of optimum activity are located in different areas of the large and small aggregates.

4.3.3.2 Sample preparation and analysis

Another benefit to this study was the opportunity to refine sample preparation for use with microFTIR. Biological materials are predominantly probed in transmission- or reflection-mode; however, sample preparation becomes increasingly important when reflection mode is used because the incidence flux is reduced by almost 50%. This is so because the one objective has to both direct the beam onto the sample and also collect the reflected beam. Importantly, any inhomogeneities within the sample can cause oscillations in the IR spectra which can alter peak shapes, intensities, and frequencies[412]. In the case of this current study, those samples microtomed to 5 µm thick sections showed vastly differing inner-specimen thicknesses between the more dense mineralised regions and the thinner, non-mineralised regions. In a separate study, AFM analysis showed that even after just 24 hours of culturing, a 5 µm thick section of a large aggregate had a thickness range of 0 – 11.8 µm. Over the same culture period, a 5 µm thick section of a small aggregate had a thickness range of 0 – 6.7 µm. These data support the belief that considerable differences exist between culture method techniques. Given that the S:N ratio relies strongly on the collection of the reflected light back to the IR objective, the topography of the sample needs to be as smooth as possible.

4.4 MLO-A5 aggregate density and material volume

4.4.1 In vitro aggregates

Using two different thresholds to calculate material volumes of different densities derived from microCT analysis has been used with success in previous studies[285,386]. Therefore, the current study used two thresholds to determine total aggregate volume (lower threshold) and dense material volume within the aggregates (higher threshold) for mineralisation analysis (adapted from Henstock *et al*.[386]). In addition, the volume of dense material was normalised to the total material volume in the hope of eliminating any data misinterpretations as a result of scanning the non-coated suspension culture aggregates together. Whilst statistical analysis could not be carried out for the non-coated suspension samples, the coated suspension samples showed significantly increasing levels of dense material as culturing continued. The 72 hour samples had significantly higher volumes of dense material per unit volume of total material compared with the 24 and 48 hour samples, especially the 24 hour samples. The trend for the non-coated suspension aggregate samples followed that of the coated suspension culture but without statistical analysis it is difficult to determine how relevant this observation actually is. These data correlate with the above mentioned data sets confirming that aggregate mineralisation (dense material volume in this case) increases as culturing continues over the 72 hour period.

4.4.2 In vivo aggregates

Taking the material volume measurements into account, particularly the normalised volume measurements (fig. 3.11), it would appear as though the monolayer samples are not too dissimilar from the large aggregate samples. This may be for a number of reasons. Firstly, the monolayer samples are considerably more proliferative compared with the aggregate samples. It is, therefore, speculated that the control samples proliferated throughout the Neoveil mesh using it as a scaffold. Over the duration of the experiment, the once monolayer of cells created a self-assembled 3D structure of ECM. It is thought that, whilst very little of this material was actually formed, a similar proportion of normalised dense material to that of the large aggregates was developed. Secondly, a considerable proportion of the large aggregates disintegrated *in vivo*; thus, significantly reducing the amount of productive samples from this variable. Combined, these circumstances are believed to have significantly reduced the gap between the tissue formation potential of the monolayer control samples and the large aggregate samples.

With the initial *in vitro* investigation concentrating on aggregates being cultured over 72 hours, necrosis is not believed to be an issue. Although cell viability is a critical issue in aggregate culture, it is difficult to accurately evaluate cell viability within the aggregate centres. However, the histochemical staining, SEM analysis and outgrowth capacity (explained in further chapters) of the aggregates within this study, both large and small, showed no signs of necrosis or diminished osteogenic development within the aggregate centres after 72 hours which would suggest that high cell viability was maintained. Differences in cell – cell interactions are, thus, more likely to explain the differences in mineralisation levels between the different-sized aggregates of this short duration *in vitro* study[447]. However, over an 8-week period necrosis may become more of an influential factor given the findings of Rouwkema and colleagues who reported that necrosis is more prevalent in large aggregates exceeding 200 µm in diameter and who have been cultured for more than 7 days[323]. The small aggregates of both *in vitro* and *in vivo* experiments never exceeded this critical diameter size; however, the large aggregates of both the *in vitro* and *in vivo* experiments, in particular the *in vitro* experiments, did. It could therefore be argued that initial bone nodule development or osteoid mineralisation is largely dependent on cell – cell and cell – ECM contact but as development continues, oxygen and nutrient deficiency leading to necrosis could play a more influential role in determining a critical aggregate size limit.

5. Conclusions

In conclusion, by modifying culture substrates, this study generated a convenient and effective model to delineate some of the influential factors leading to mineralisation. Although aggregation is accepted to accelerate mineralisation, this study offers an insight into how aggregate size and culture duration affect mineralisation and the variation of mineral composition. The findings of this study have shown that the small aggregates are significantly more active for matrix synthesis, remaining in the early matrix formation phase for longer compared to the large aggregates. In comparison, the large aggregates mineralised earlier and became denser than their small aggregate counterparts. Additionally, the large aggregates also appeared to mineralise from the periphery, whilst the small aggregates mineralised from their centres. Interestingly, this study revealed that the effect of aggregate size and culture duration on the concentration of mineralising matrix within both *in vitro*- and *in vivo*-cultured bone tissue was different. When combined with the findings of other studies, it could be suggested that an aggregate size of 200 µm would offer the optimum level of cell – cell interaction, whilst also maintaining a diffusible construct for improved bone formation.

Chapter Four

Identification of Mesenchymal Stem Cell Subpopulations

Overview

This study investigated the heterogeneity of mesenchymal stem cells (MSC) isolated from human bone marrow mononuclear cells (MNC) and the possibility of donor-dependent heterogeneity (subpopulations) that may play a role in determining an individual's osteogenic capacity.

Using a substrate with particular characteristics that cannot be divulged at this time due to pending intellectual properties, substrate X, a new protocol was developed for the identification and isolation of possible subpopulations which encompasses a simple technique allowing the cells to self-sort and self-separate into identifiable cellular arrangements. The proportions of these specific cellular assemblies are thought to be donor specific and may correspond with an individual's bone formation potential. To investigate this, the quantification of such arrangements found within multiple cell populations provided by individual donors was attempted. The aggregation potential of several individual MSC populations was also evaluated using the aggregation of such cells into bone nodules. An aggregation model developed in a previous chapter (chapter 3) was used to assess this aggregation capacity. An *in vivo* investigation using MSCs was also carried out to investigate how aggregate size might influence eventual bone formation. The intention was to verify the MLO-A5 aggregate study using different-sized aggregates comprised of primary cells.

1. Introduction

MSCs possess a number of characteristics that render them a popular choice for research into tissue engineering and regenerative medicine, such as their homing ability following systemic injection[208,209], their non-immunogenic characteristics[182] and their ability to release paracrine factors thought to protect host cells, encourage cell proliferation and augment angiogenesis[179,180]. It is their extraordinary differentiation capacity that is of particular interest to this study, however. It is this capacity that has given rise to the belief that MSCs may contain numerous subpopulations. Unlike haematopoietic and neural stem cells, which typically only generate cells of the tissues from which they reside[357,358], MSCs have been shown to differentiate into cells of all three germ layers, mesodermal, ectodermal and endodermal[359–361]. It is not entirely clear how they perform this feat, however[362].

In an effort to explain this differentiation capacity, it has been suggested that MSCs may contain a mixture of phenotypically, biochemically and functionally different cells comprising subpopulations[211,363,364]. A number of adherent cell types have already been shown to exist within a population of bone marrow MNCs, i.e. embryonic-like stem cells, lineage-committed progenitor cells and mature cells, such as osteoblasts and fibroblasts[365–368]; so, the prospect that bone marrow-derived MSC cultures may contain numerous stem cell types with varying differentiation potentials has been put forward[369]. There are currently two theories on the subject. One hypothesis states that MSCs comprise a multitude of different stem cells making up a 'pluripotent-like' cell culture and the other suggests that amongst this multitude of different stem cells is a small proportion of true pluripotent stem cells. If a population of true pluripotent stem cells does exist within an MSC culture, it has been suggested that their numbers would be very small and dependent upon donor, and cell isolation and cultivation methods[370,371]. Numerous attempts have been made to isolate single bone marrow stem cell subpopulations using a variety of techniques, such as size sieving[372,373], long term culturing under specific conditions[367,374,375], fluorescence-activated cell sorting (FACS)[368,376,377] and counterflow centrifugal elutriation (CCE)[369], but few have claimed to have actually discovered pluripotent stem cells within bone marrow-derived MSCs. This study offers an alternate route for the identification of donor-dependent subpopulations through specific cellular arrangements alongside the ability to assess an individual's osteogenic potential. MSC subpopulation characterisation and differentiation potential has been the focus of numerous studies in the past[377,448–450] but none have used the specific strategy outlined in this study. This investigation is carried out with specific substrates, i.e. a substrate for subpopulation identification (denoted as substrate X) and a Pluronic F127-coated substrate (denoted simply as coated) used to create cellular aggregates. Both substrates are used alongside conventional monolayer controls.

2. Materials and Methods

Various tables have been used throughout this methods section to highlight the number of MNC donors used for MSC isolation, the age and gender information for donors and the various analyses each MSC population was subjected to. MSCs isolated from MNCs were the only cells used throughout this chapter; however, comparisons are made to data collected using the MLO-A5 cell line that was presented in the previous chapter, chapter 3, in sections 3.5.1.1 and 3.6.4.1.

2.1 Mesenchymal stem cell culturing and growth profile monitoring

Below is a table outlining the age and gender information for eight of the nine MNC donors used throughout this study (table 4.1). Additionally, table 4.2 highlights the nine MNC donors and the initial analyses carried out on each of their MSC populations.

Table 4.1: The age and gender of eight of the nine MNC donors used for MSC isolation. Information on the remaining donor, D3433B, was not available from the supply company.

Donor	Age	Gender
D3737A	30	M
D1908B	22	F
D3741A	37	M
D3120B	25	F
D3736A	23	M
D3549B	29	M
D3246B	23	M
D2884D	24	F

Table 4.2: MNC donors and initial analyses. Shown is each of the nine MNC donors used for MSC isolation and which of them were used for growth profile measurements, substrate X sample counts, subpopulation identification and proportion measurements and E-cadherin immunohistochemical staining. Two time points are represented for the latter two analyses: 96 and 168 hours.

MSC Culturing					Staining
Donor	**Growth Profiles**	**Sample Counts**	**Time**	**Subpopulations**	**E-Cadherin**
D3737A	X	X	96 hrs	X	-
			168 hrs	X	X
D1908B	X	X	96 hrs	X	X
			168 hrs	X	X
D3741A	X	X	96 hrs	X	X
			168 hrs	X	-
D3120B	X	X	96 hrs	X	X
			168 hrs	X	X
D3433B	X	-	96 hrs	X	-
			168 hrs	X	X
D3736A	X	X	96 hrs	X	-
			168 hrs	X	-
D3549B	X	X	96 hrs	X	X
			168 hrs	X	X
D3246B	X	X	96 hrs	X	X
			168 hrs	-	-
D2884D	X	X	96 hrs	X	X
			168 hrs	X	X

MSCs were isolated from populations of commercially acquired MNCs (Lonza, Belgium) which were acquired from the bone marrow of nine individual human donors (table 4.1). Only donor number was recorded and used to identify and track the evaluation of different MSC populations. The MSCs were isolated and cultured using protocols described in chapter 2, section 1.2. Both culturing and experimental media are described in full. During cell expansion, a basal medium was used, chapter 2, section 1.2. The cells were passage three when used for experimenting, passage four for tri-lineage differentiation and passage five for flow cytometry analysis.

Detailed records were kept during the culturing phase of this study taking into account the number of days between each time a cell population reached 80% confluency. This gave rise to growth profiles which could then be used to compare growth rates between each donor.

2.2 Subpopulation identification and quantification

Possible subpopulations were identified for each MSC population obtained from the donors outlined in table 4.1 using a minimum of three samples per time point. During the subpopulation identification process, an osteogenic-supplemented medium was used, chapter 2, section 1.4.3. MSCs were seeded onto substrate X as described in chapter 2, section 4.2. They were then allowed to self-sort and form specific cellular arrangements for up to 7 days. These cellular arrangements were optically imaged using software and equipment outlined in chapter 2, section 9.1. Identification and quantification of the cellular arrangements was made from optical images as explained in chapter 2, section 11. Quantification was carried out using a minimum of three images per MSC population per time point. The substrate X samples were terminated after 4 (96 hours) and 7 days (168 hours). Termination involved fixing in situ with an appropriate fixative. Those samples intended for alkaline phosphatase (ALP) staining were fixed with 4% paraformaldehyde (PFA) for 2 minutes, those intended for all other histochemical and immunohistochemical staining were fixed with formalin for 20 minutes.

2.3 Aggregate formation

Table 4.3: MNC donors and MSC aggregation assessment. A table showing each of the MNC donors used for MSC isolation and which were then used for aggregation. Also shown are those samples that were used for aggregate size and aspect ratio measurements alongside those that were used for microCT scanning. Two culture durations are represented: 96 and 168 hours.

MSC Aggregation				
Donor	**Time**	**Size**	**Aspect Ratio**	**MicroCT**
D3737A	96 hrs	X	X	-
	168 hrs	X	X	X
D1908B	96 hrs	X	X	-
	168 hrs	X	X	X
D3741A	168 hrs	-	-	X
D3120B	96 hrs	X	X	-
	168 hrs	X	X	X
D3433B	96 hrs	X	X	-
	168 hrs	X	X	X
D3736A	96 hrs	X	X	-
	168 hrs	X	X	X
D3549B	96 hrs	X	X	-
	168 hrs	X	X	X
D3246B	168 hrs	-	-	X
D2884D	96 hrs	X	X	-
	168 hrs	X	X	X

A minimum of three aggregates were formed from each MSC population outlined in table 4.2, per time point. During the MSC aggregation process, an osteogenic-supplemented medium was used, chapter 2, section 1.4.3. Aggregation was used to evaluate donor-dependent variabilities and followed the same principals outlined in the MLO-A5 study (chapter 3). The technique used for aggregate formation, the F127-coated suspension culture, is explained in detail in chapter 2, section 4.1.1. Cells were seeded at a density of 3 x 10^5 cells per well in 1 ml osteogenic-supplemented medium and were cultured for 4 days (96 hours) and 7 days (168 hours). Culture medium was not changed throughout this culture period. The samples were terminated in the same way as the substrate X samples described in the previous section. The only difference being, the aggregates were not fixed in situ but were first transferred to micro-centrifuge tubes. Once fixed, the aggregate samples were stored in phosphate buffer saline (PBS) at 4 °C (except for those intended for ALP staining which were processed immediately).

2.4 Aggregate measurements

The aggregates were imaged via optical microscopy (chapter 2, section 9.1). Measurements were taken from a minimum of three separate samples per variable to give aggregate size and aspect ratio values as discussed in chapter 2, section 10.

2.5 Histology

Table 4.4: MNC donors and aggregate analyses. A table showing each of the MNC donors used for MSC isolation and which MSC populations were then subjected to histochemical staining. Both subpopulation and aggregate section staining are represented with two time points: 96 and 168 hours.

Subpopulation Staining					**Aggregate Staining**		
Donor	**Time**	**ALP**	**Alizarin Red**	**von Kossa**	**ALP**	**Alizarin Red**	**von Kossa**
D3737A	96 hrs	X	X	X	-	X	-
	168 hrs	X	X	X	-	X	X
D1908B	96 hrs	X	X	X	X	X	-
	168 hrs	X	X	X	X	X	X
D3120B	96 hrs	-	-	-	-	X	X
	168 hrs	-	-	-	-	X	X
D3736A	96 hrs	X	X	X	X	X	X
	168 hrs	X	X	X	X	X	X
D3549B	96 hrs	X	X	X	X	X	-
	168 hrs	X	X	X	X	X	X
D3246B	96 hrs	-	-	-	X	X	X
	168 hrs	-	-	-	X	X	-
D2884D	96 hrs	X	X	X	X	X	X
	168 hrs	X	X	X	X	X	X

Histochemical staining was carried out on a minimum of two separate samples per variable. Staining was carried out for the identification of markers associated with osteogenic differentiation and mineralisation. All samples used for subpopulation evaluation were stained in situ, whilst most, but not all, aggregate samples used for osteogenic evaluation were cryosectioned prior to staining. Those aggregates intended for ALP staining were not cryosectioned prior to staining.

2.5.1 Alkaline phosphatase staining

ALP staining for subpopulation evaluation was carried out in situ at the time of termination because ALP activity is very sensitive and diminishes quickly after fixation. The aggregates stained for ALP activity too were stained immediately upon fixation and so were stained whole (without sectioning) in micro-centrifuge tubes. A full protocol outlining the procedures used is described in chapter 2, section 12.2. The stained aggregates were placed onto standard glass slides and imaged immediately post-staining.

2.5.2 Alizarin red staining

Alizarin red staining was used for the identification of calcium, thus, indicating the presence of minerals. This staining, for subpopulation evaluation, was carried out in situ following the protocol outlined in chapter 2, section 12.3. Aggregate samples stained for Alizarin red were cryosectioned prior to staining following the protocol outlined in chapter 2, section 8.3. Staining of the aggregate sections then followed the protocol outlined in chapter 2, section 12.3.

2.5.3 von Kossa staining

von Kossa staining was used to identify the presence of phosphate salts, again indicating the presence of minerals. For subpopulation evaluation, staining was carried out in situ following the protocol outlined in chapter 2, section 12.4. Aggregate samples stained for von Kossa were cryosectioned prior to staining following the protocol outlined in chapter 2, section 8.3. Staining of the aggregate sections then followed the protocol outlined in chapter 2, section 12.4.

2.6 E-cadherin staining

E-cadherin staining was used to evaluate the cadherin levels of the cellular subpopulations and to compare them between multiple donors. The staining was carried out using the manufacturer's protocols outlined in chapter 2, section 13.2. Samples from multiple donors over two culture time points, 96 hours and 168 hours, were selected. Epifluorescent imaging and the quantification of fluorescence intensity followed the protocols described in chapter 2, section 9.2.

2.7 Flow cytometry

Table 4.5: MNC donors and MSC validation. A table showing each of the MNC donors used for MSC isolation and which donors were subjected for flow cytometry and tri-lineage differentiation.

Flow cytometry			**Tri-Lineage**		
Donor	**All Antibodies**	**CD324**	**Alizarin Red**	**Alcian Blue**	**Oil Red O**
D3737A	X	X	X	X	X
D1908B	X	X	X	X	X
D3741A	X	X	X	X	X
D3120B	X	-	X	X	X
D3433B	X	X	X	X	X
D3736A	X	X	X	X	X
D3549B	X	X	X	X	X
D3246B	X	X	X	X	X
D2884D	X	X	X	X	X

Flow cytometry was used to test for the presence of multiple surface markers to confirm the use of MSCs. Three positive markers (CD73, CD90 and CD105) and five negative markers (CD14, CD19, CD34, CD45 and HLA) were evaluated. An additional surface marker (CD324) was used with the intention of quantifying the levels of E-cadherin within multiple donor samples. Flow cytometry was carried out on nine donors (passage five) and analysed using the protocols outlined in chapter 2, section 18.

2.8 Tri-lineage differentiation

Tri-lineage differentiation was intended to confirm the use of MSCs through positive differentiation down multiple lineages: adipogenic, chondrogenic and osteogenic. A minimum of three separate samples were used per variable. The MSCs used were passage four. Each lineage required particular supplementation; therefore, all three media are described in chapter 2, section 1.4. MSC culturing for differentiation is explained in chapter 2, section 2.1. The same methods were used for all three lineages and all donors tested. To confirm positive differentiation, the cells were optically imaged, histochemically-stained and imaged again, as described in chapter 2, section 2.2. Each differentiation required a different stain, the protocols for which can be found in chapter 2, section 12.

2.9 Microcomputerised tomography of *in vitro* aggregates

Microcomputerised tomography (microCT/µCT) was intended to compare the aggregate volumes and densities of multiple donor samples. A minimum of three samples per variable were scanned. Scanning was carried out on the aggregates of numerous donors after 168 hours in culture (table 4.2) using the protocol discussed in chapter 2, section 15.1.2. Two thresholds were used for the analysis, 110 and 130. The first, 110, was chosen to represent the volume of dense collagenous material within the aggregates; the second, 130, was chosen because this was the highest threshold where all of the samples scanned still registered a volume measurement.

2.10 *In vivo* investigation

An *in vivo* study was carried out to demonstrate how different-sized aggregates from a single donor (D3591A – selected at random) react to long term *in vivo* culturing. A monolayer control seeded on a Neoveil mesh was used as a control for comparative purposes. The intention of this element of the study was to confirm the observations made during the MLO-A5 *in vivo* study (chapter 3).

2.10.1 Diffusion chamber construction, seeding, implantation and termination

A complete protocol for the *in vivo* experiment is described in chapter 2, section 5. Five separate samples were used per variable.

2.10.2 Optical imaging

Optical imaging was used to monitor chamber integrity post-implantation, possible engraftment and contents immediately following *in vivo* experiment termination and sample fixation. Equipment and software used are outlined in chapter 2, section 9.1.

2.10.3 Microcomputerised tomography of the in vivo diffusion chambers

MicroCT scanning followed the protocols outlined in chapter 2, section 15.2. The samples were scanned whilst still in their chambers so as not to disturb any of the material that had formed over the course of the experiment. All five samples per variable were scanned in this way. To maintain consistency with the MLO-A5 *in vivo* study, a threshold of 110 was used to show the total volume of material within each of the chambers and a threshold of 170 was used to show the volume of dense material within each of the chambers.

2.11 Statistical analysis

Sample groups were compared using independent t-tests alongside one-way and two-way analysis of variance (ANOVA). A p-value below 0.05 was taken to indicate statistical significance. Graphically, statistical significance is indicated at four levels: * $p \leq 0.05$, ** $p \leq 0.01$, *** $p \leq 0.001$ and **** $p \leq 0.0001$.

3. Results

The MNCs from the bone marrow of nine individual donors were used for various experiments throughout this study. The cells were commercially acquired and labelled with donor numbers for identification (e.g. D1908B) prior to our procurement. Those same donor numbers were used throughout this study to track the specific MSC populations as investigations continued.

3.1 Stemness verification

The cell populations of nine donors were evaluated for stemness verification through the use of flow cytometry and tri-lineage differentiation.

3.1.1 Flow cytometry

Nine surface markers were measured in each of the nine donor cell populations evaluated for stemness using flow cytometry: three positive (CD73, CD90 and CD105), five negative (CD14, CD19, CD34, CD45 and HLA) and one additional marker explained later (CD324) (table 4.4 and 4.5).

Table 4.6: MSC flow cytometry data. Shown is the percentage of positive events from nine MSC populations. Eight markers are represented: three positive (the first three rows) and five negative (the remaining five rows).

Marker	D3737A	D1908B	D3741A	D3120B	D3433B	D3736A	D3549B	D3246B	D2884D
CD73	89.31	86.36	92.17	96.59	52.05	46.03	60.53	75.35	62.55
CD90	9.86	8.65	51.24	16.99	44.36	3.71	9.72	7.52	9.38
CD105	17.92	35.85	18.15	70.49	15.22	17.16	39.73	13.69	9.57
CD14	6.16	3.32	13.22	5.96	7.68	5.9	63.44	5.33	6.47
CD19	7.5	9.07	5.01	5.12	5.24	5.67	3.18	5.02	3.94
CD34	5.21	4.5	5.97	4.8	5.71	4.74	19.14	4.13	3.85
CD45	6.23	3.46	5.03	4.19	5.28	4.72	5.61	4.34	3.97
HLA	5.79	4.67	5.55	13.85	5.6	8.37	61.41	4.45	5.25

Fig. 4.1 shows the flow cytometry Overlay Histogram Plots of each surface marker with their particular isotype control. Each donor cell population depicted in this figure was selected to represent a particular marker because it most closely represents the average (mean ± standard error of the mean) percentage of positive events amongst all cell populations evaluated.

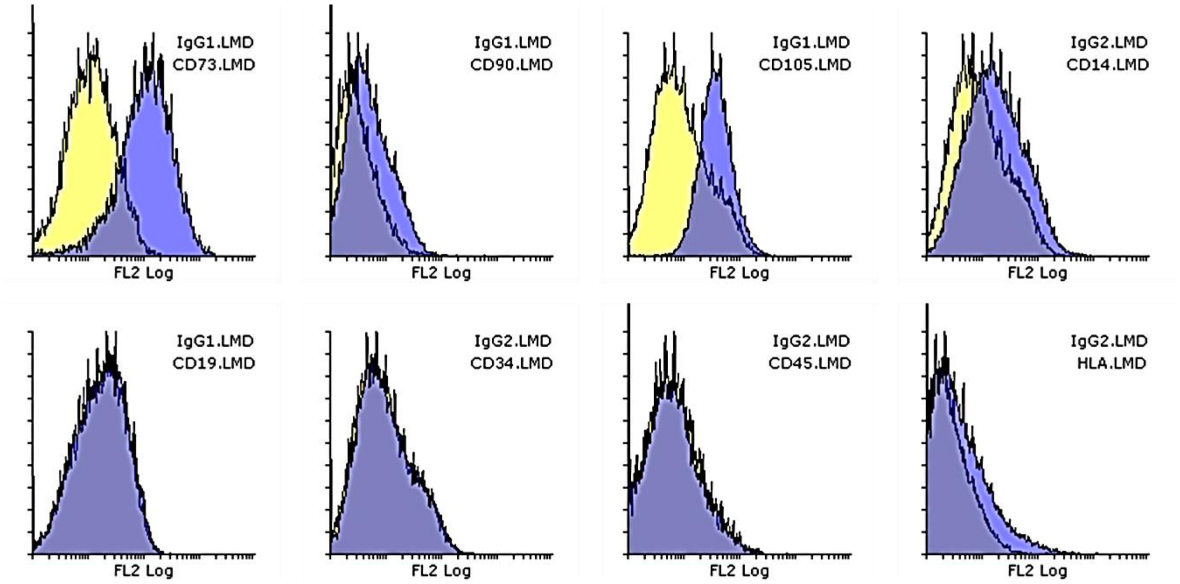

Figure 4.1: MSC flow cytometry Histograms. Shown are the Overlay Histograms of eight surface markers and their respective isotype controls: CD73, CD90, CD105, CD14, CD19, CD34, CD45 and HLA, alongside IgG1 and IgG2.

3.1.2 Tri-lineage differentiation

Nine separate cell populations were evaluated for stemness capacity through their ability to differentiate down three separate lineages, i.e. adipogenesis, chondrogenesis and osteogenesis. All nine cell populations were positively confirmed as having differentiated down all three lineages. Fig. 4.2 shows examples of the different cellular morphologies resulting from the differentiation processes alongside examples of positive staining used to confirm differentiation. Oil red O staining was used to confirm adipogenesis, Alcian blue staining was used to confirm chondrogenesis and Alizarin red staining was used to confirm osteogenesis.

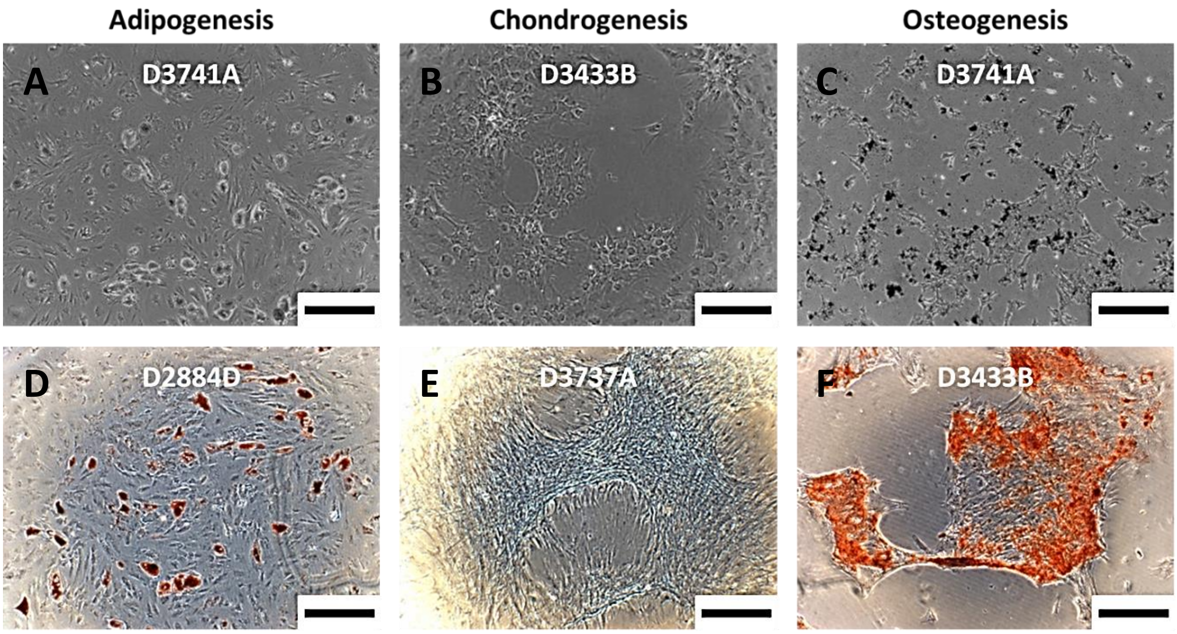

Figure 4.2: MSC tri-lineage differentiation. Optical images showing three different MSC morphologies following 30 days of culturing under three different differentiation conditions: adipogenesis (**A**), chondrogenesis (**B**) and osteogenesis (**C**). Also shown are the stains used to confirm differentiation: Oil red O to confirm adipogenesis (**D**), Alcian blue to confirm chondrogenesis (**E**) and Alizarin red to confirm osteogenesis (**F**). Scale bar represents 400 µm.

3.1.2.1 Adipogenesis

Morphologically, those cells encouraged down an adipogenic lineage now comprised clearly visible globules. The presence of such globules was confirmed with the use of Oil red O staining (fig. 4.2). Subsequently, the presence of such globules confirms differentiation down the adipogenic lineage.

3.1.2.2 Chondrogenesis

Fig. 4.2 shows the MSCs with a more fibroblastic morphology and increased extracellular matrix (ECM) production post-chondrogenic differentiation. Alcian blue staining confirmed the presence of ECM proteins associated with cartilage (fig. 4.2), thus, confirming differentiation down the chondrogenic lineage.

3.1.2.3 Osteogenesis

Osteogenic differentiation was apparent because the presence of dark mineral deposits post-differentiation (fig. 4.2). Alizarin red staining confirmed the presence of calcium ions which in turn confirmed the onset of mineralisation and, thus, differentiation down the osteogenic lineage (fig. 4.2).

3.2 Cell population heterogeneity

3.2.1 Mesenchymal stem cell isolation and expansion

Prior to any subpopulation experimentation being carried out, a sufficient cell number/population had to be acquired. This resulted in the cells being expanded to 16 x T75 flasks at passage two. Additionally, this expansion stage allowed for further cell heterogeneity assessment through the monitoring of proliferation profiles and cell morphologies.

3.2.1.1 Initial mesenchymal stem cell attachment and culturing

An example of the initial MSC isolation through attachment of two donor cell populations is documented showing differences in terms of cell number relative to culture duration (fig. 4.3). At given time points, i.e. 7 or 14 days, the faster proliferating cells resulted in higher cell numbers which subsequently led to the formation of larger colonies at said time points. It was also noted immediately prior to the use of each MSC population that cellular morphology and size differed considerably between each population. Those cells that were slower to proliferate remained in culture for longer and so were larger and more fibroblastic in shape compared to the faster proliferating cells which were smaller and more elongated in shape. These differences did not become apparent until the cells were in their second passage. Fig. 4.4 shows cells from two donors, one fast proliferating and one slow proliferating, over three time points, 7 days, 14 days and 21 days, at passage three.

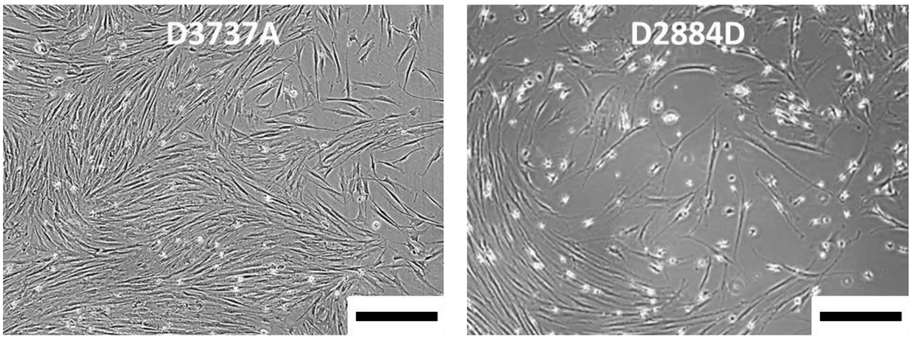

Figure 4.3: Initial MSC attachment. Optical images showing initial MSC attachment from two donors, D3737A and D2884D, after 14 days in culture. Scale bar represents 400 µm.

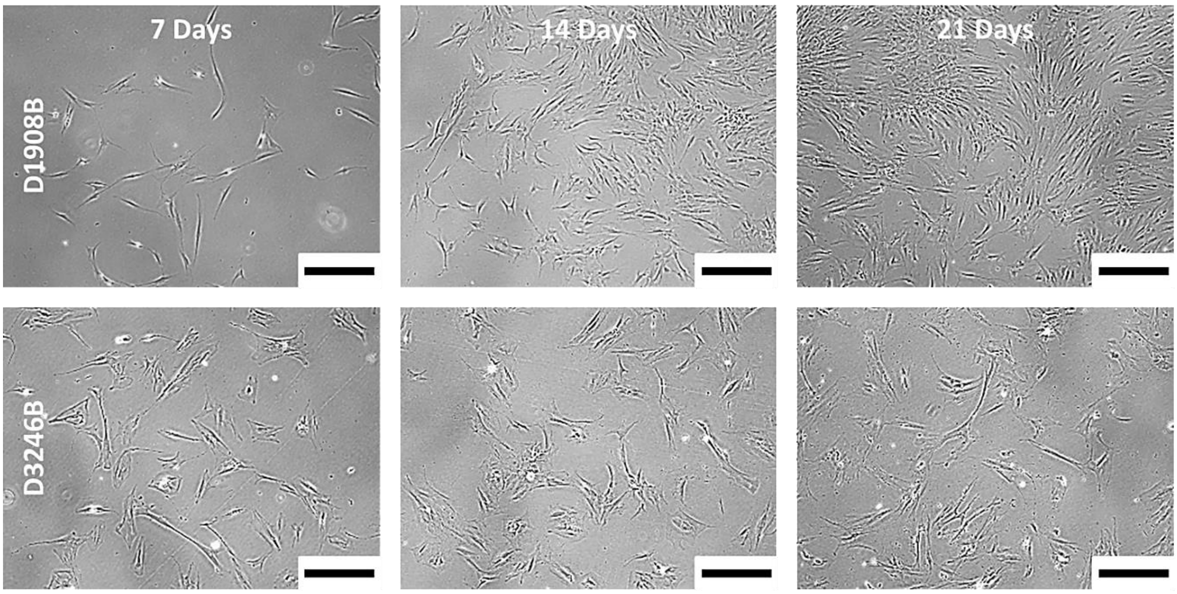

Figure 4.4: MSC culturing over time. Optical images showing MSCs from two donors covering three time points, 7 days, 14 days and 21 days, at passage three. The images show different cell morphologies, with D3246B (the slower proliferating cell population) having a larger and more fibroblastic cell size and shape. Scale bar represents 400 µm.

3.2.1.2 Growth profiles

The growth profiles of the MSCs over three passages (0 – 2) are shown in fig. 4.5. The total culture time in days ranged from 33 to 64 days. Whilst differences could be seen over the three passages, the largest culture time gap was between passages one and two where culture duration ranged from 5 to 35 days (fig. 4.5).

In addition, the growth profiles affected the number of available cells for use in each experiment (fig. 4.5). As noted, a decreased growth rate was observed to correspond with an increase in cell size. This subsequently meant that, whilst all of the MSC populations were cultured to 80% confluency, passage two, before being used in each experiment, available cell numbers differed between each population. The faster proliferating cells produced approximately 16 x 10^6 cells in total, whilst the slower proliferating cells produced approximately 12 x 10^6 cells in total, a 25% decrease. This decrease in cell numbers resulted in a subsequent decrease in substrate X sample numbers (fig. 4.5).

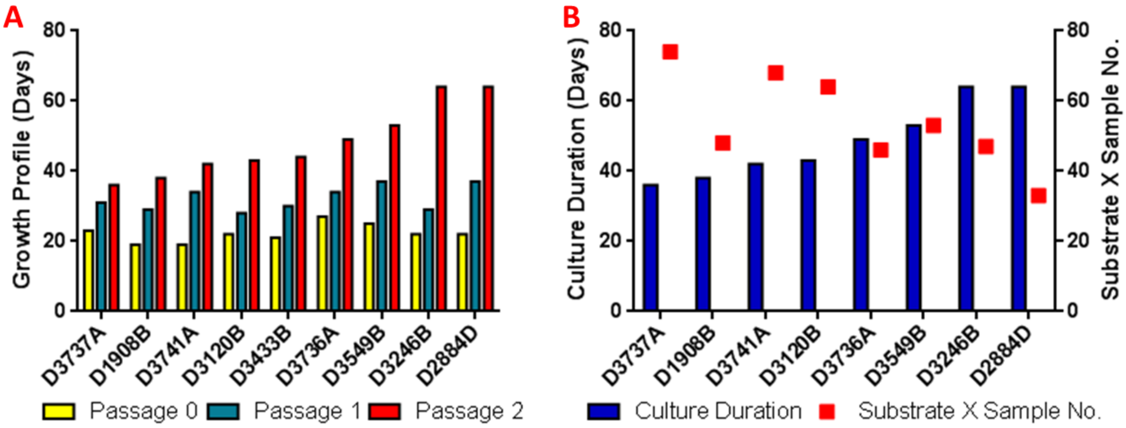

Figure 4.5: Quantitative growth profile data from MSC culturing. Growth profiles (**A**) of individual donors from initial MNC seeding and MSC isolation (revival) through to use in subpopulation experiments (passage three). Also shown is the total culture duration correlating to the total substrate X sample number acquired (**B**). Growth profile refers to the time required by each cell population to reach 80% confluency following each treatment/passage (passage 0 covers culture duration from MSC isolation through to 80% confluency, passage 1 covers first passage to 80% confluency and passage 2 covers second passage to 80% confluency). Total culture duration refers to the length of time (in days) required to culture an MSC population from initial isolation to 16 x T75 flasks at 80% confluency. Substrate X sample number refers to the number of samples acquired from each donor using substrate X and is used to convey cell numbers.

3.2.2 Subpopulation separation and identification

Once the appropriate cell number/population had been acquired (16 x T75 flasks at 80% confluency), the next phase was to seed the cells on substrate X for subpopulation separation and identification. Tissue culture polystyrene (TCP) was also used alongside substrate X for control purposes. The cells were cultured on both substrates, substrate X and TCP, and terminated after 96 hours and 168 hours.

3.2.2.1 Attachment arrangements

Nine donor cell populations were identified as having multiple subpopulations through differing attachment arrangements (fig. 4.6). Under TCP control culture conditions, little difference could be seen in terms of cellular arrangements between any of the cell populations examined over both time points. A considerable difference, however, could be seen with cellular arrangements between each of the donors after just hours under substrate X culture conditions. Three distinct cellular arrangements became apparent within each donor MSC population examined under the same culture conditions: a monolayer arrangement, a sunflower-like arrangement and an aggregate-like arrangement (fig. 4.6).

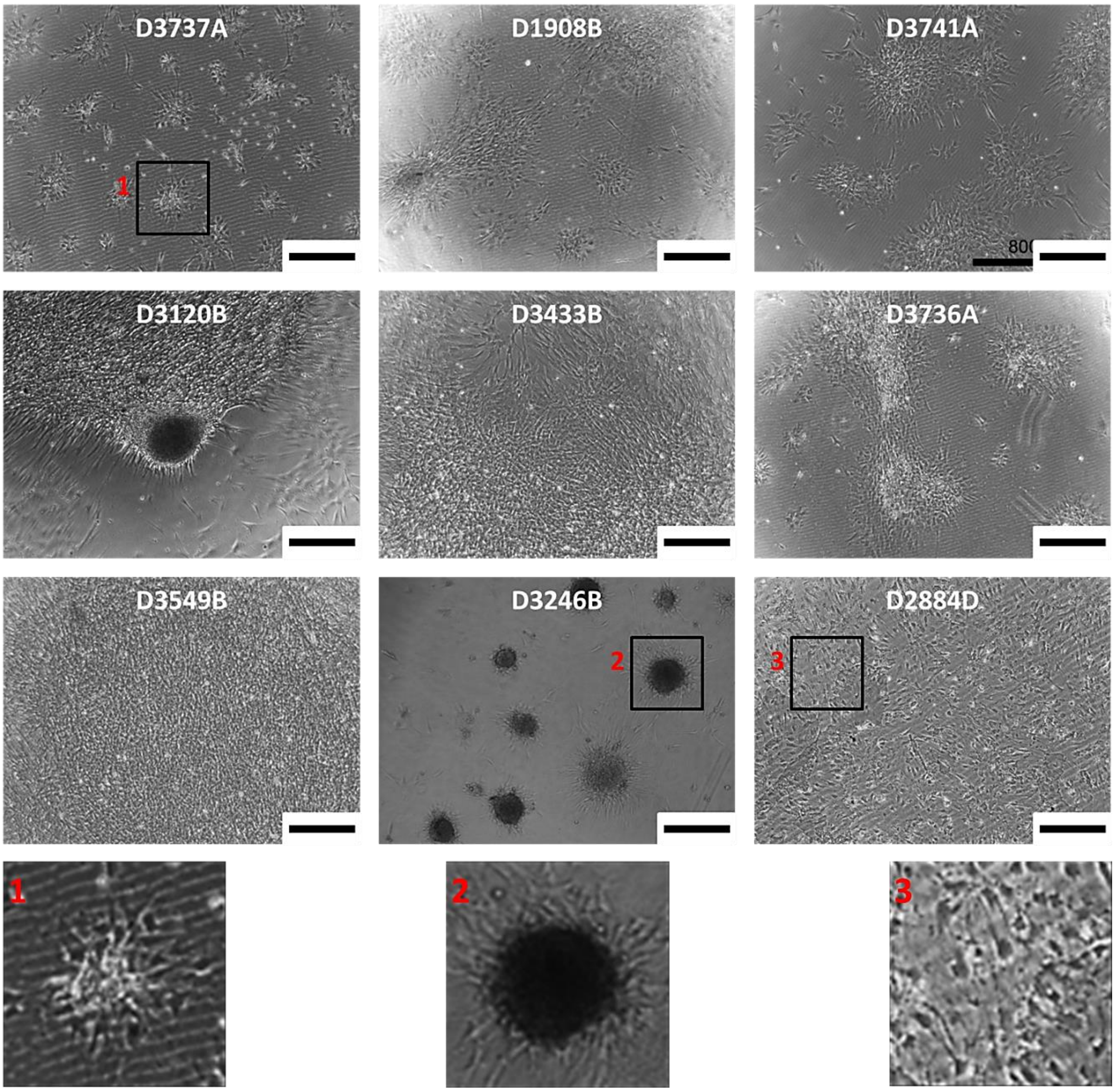

Figure 4.6: MSC attachment arrangements on substrate X. Optical images showing how the MSCs from each donor reacted to substrate X. The images were taken after 96 hours in culture with osteogenic-supplemented medium. Scale bar represents 400 µm. The three images on the bottom row labelled 1 – 3 represent magnified examples of three subpopulations highlighted by black squares in the upper three rows of images: a sunflower-like arrangement (**1**), an aggregate-like arrangement (**2**) and a monolayer arrangement (**3**).

In addition, the proportions of each subpopulation were measured within each of the MSC populations assessed (fig. 4.7). An aggregate-like arrangement was the rarest with only three of the eight populations showing this arrangement. The donors are also arranged in order of ascending growth profiles, i.e. the fastest proliferating population to the front and slowest to the back.

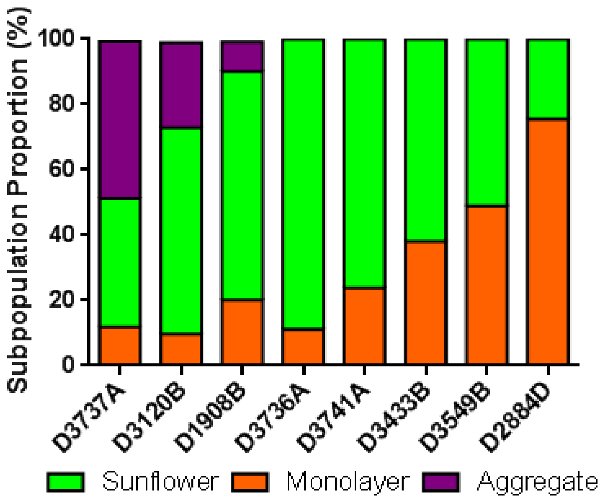

Figure 4.7: Quantitative data showing donor variations in subpopulation proportions. The subpopulation proportions of each donor are represented as a percentage of total cell population. Three subpopulations correspond to three cellular arrangements: sunflower, monolayer and aggregate.

3.2.2.2 E-cadherin

In addition to the morphological assessment identifying three distinct subpopulations, E-cadherin was measured from two different angles to confirm the presence of subpopulations and to explain why the subpopulations are identifiable on substrate X. E-cadherin staining was carried out on multiple substrate X cell samples after 96 hours and 168 hours in culture (fig. 4.8 and 4.9, respectively). After just 96 hours, clear differences could be seen with the stain intensity depending upon the arrangement of the cells. Those cells with a more monolayer or featureless cellular arrangement were poorly stained (D2884D for example), whilst those with a more sunflower-like or aggregated arrangement were stained more positively (D3120B for example). Fluorescence intensity was also measured giving figures of 9.101 and 21.412 for D2884D and D3120B, respectively (fig. 4.10). This trend continued for those samples stained after 168 hours in culture albeit with slightly less dramatic differences between donors. Fluorescence intensity ranged from 9.101 – 21.412 at 96 hours and 23.12 – 36.849 at 168 hours. That is a 235% difference in comparison to a 159% difference, respectively.

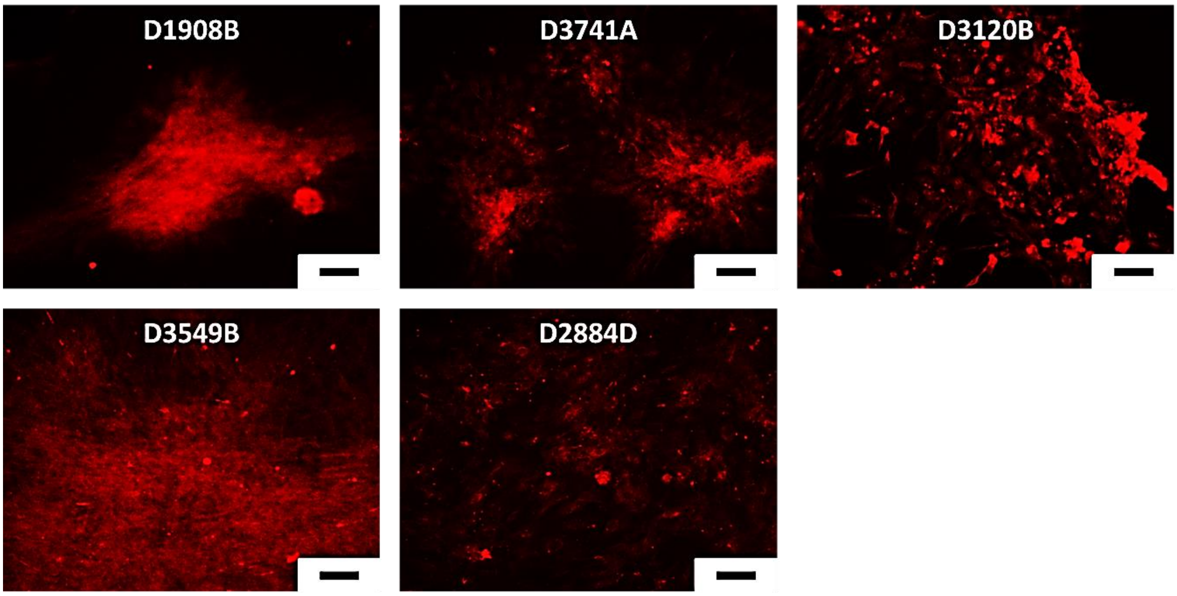

Figure 4.8: Subpopulations immunohistochemically stained for E-cadherin. Epifluorescent images showing E-cadherin staining carried out on MSCs which were cultured on substrate X for 96 hours. Red colouration indicates positive staining for E-cadherin. Scale bar represents 250 µm.

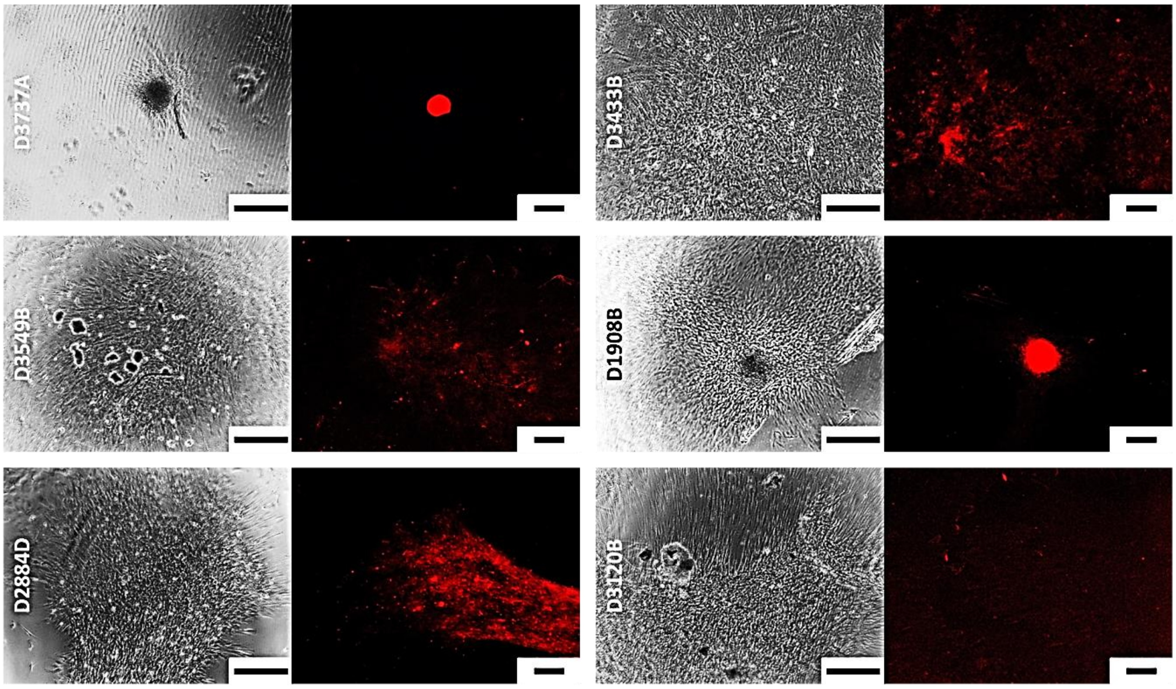

Figure 4.9: Subpopulations immunohistochemically stained for E-cadherin. Brightfield and corresponding epifluorescent images showing E-cadherin staining carried out on MSCs which were cultured on substrate X for 168 hours. Red colouration indicates positive staining for E-cadherin. Brightfield images scale bar represents 400 µm, fluorescent images scale bar represents 250 µm.

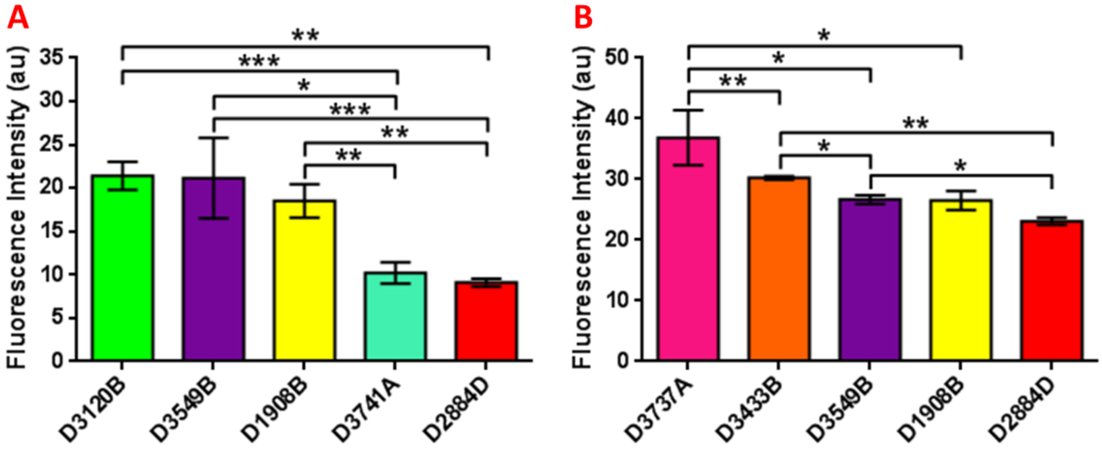

Figure 4.10: Quantitative data derived from E-cadherin staining. Fluorescence intensity of E-cadherin staining carried out on MSCs cultured on substrate X. Samples were culture for 96 hours (**A**) and 168 hours (**B**). Error bar represents standard error of the mean. * signifies $p < 0.05$, ** signifies $p < 0.01$ and *** signifies $p < 0.001$.

In addition to fluorescently staining and measuring the intensity of such fluorescence on cell samples cultured on substrate X, donor cells were assessed for E-cadherin using flow cytometry (fig. 4.11). In conjunction with the eight markers being assessed for stemness verification, one additional marker was also measured, CD324 (E-cadherin). CD324 levels were evaluated for eight cell populations and with levels of positive events ranging from 0.69% to 10.29% (fig. 4.11); this corroborates previous findings suggesting the populations of MSCs have measurable levels of heterogeneity.

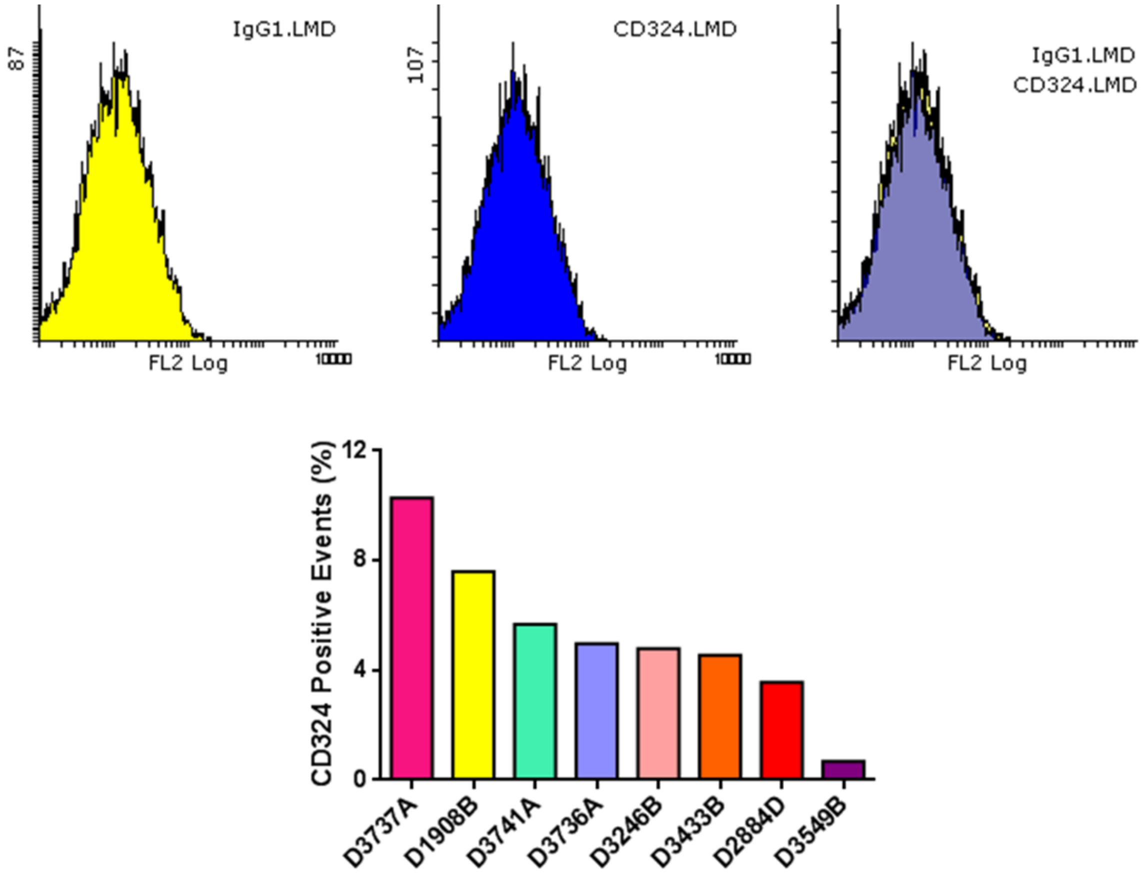

Figure 4.11: Flow cytometry data showing CD324 (E-cadherin) analysis on multiple MSC populations. Represented are the IgG1 control and CD324 antibody Histograms alongside an Overlay Histogram. Also shown is a chart demonstrating the percentage of CD324 positive events within MSC populations acquired from multiple donors.

3.3 Subpopulation osteogenic capacity evaluation

Alongside identifying possible subpopulations, the osteogenic capacity of such was also assessed. This was carried out through the histochemical staining of cell samples cultured on substrate X in the hope of identifying differing levels of markers associated with osteogenic potential.

3.3.1 Histology

Histochemical staining has shown that all three subpopulations achieved different osteogenic and mineralisation levels under the same culture conditions and over the same culture period (fig. 4.12 and 4.13).

3.3.1.1 Alkaline phosphatase staining

After just 96 hours in culture, ALP staining was strongest in the samples with more self-organising cellular arrangements, i.e. sunflower-like or aggregate-like arranged cells (fig. 4.12). Whilst positive staining was seen in a number of control and monolayer dominant cultures, it is the substrate X cultures containing obvious sunflower-like or aggregate-like cellular arrangements that were stained most vividly.

After 168 hours in culture, the same trait was observed as with the 96 hour samples (fig. 4.13). Also, after 168 hours, those samples with the highest cellular mass appeared to become loosened and/or lift from substrate X during the fixing and staining process. These more organised cellular arrangements stained more positively than their monolayer-arranged and/or control counterparts.

3.3.1.2 Alizarin red staining

As was the case with the ALP staining, substrate X cultures with a higher degree of cellular arrangement stained more positively for Alizarin red compared to their monolayer counterparts at both 96 and 168 hours culturing (fig. 4.12 and 4.13, respectively).

3.3.1.3 von Kossa staining

von Kossa staining correlates well with the observations noted during Alizarin red staining (fig. 4.12 and 4.13, respectively). The more organised cellular arrangements again stained more positively compared to their monolayer-like or monolayer control counterparts for both time points tested.

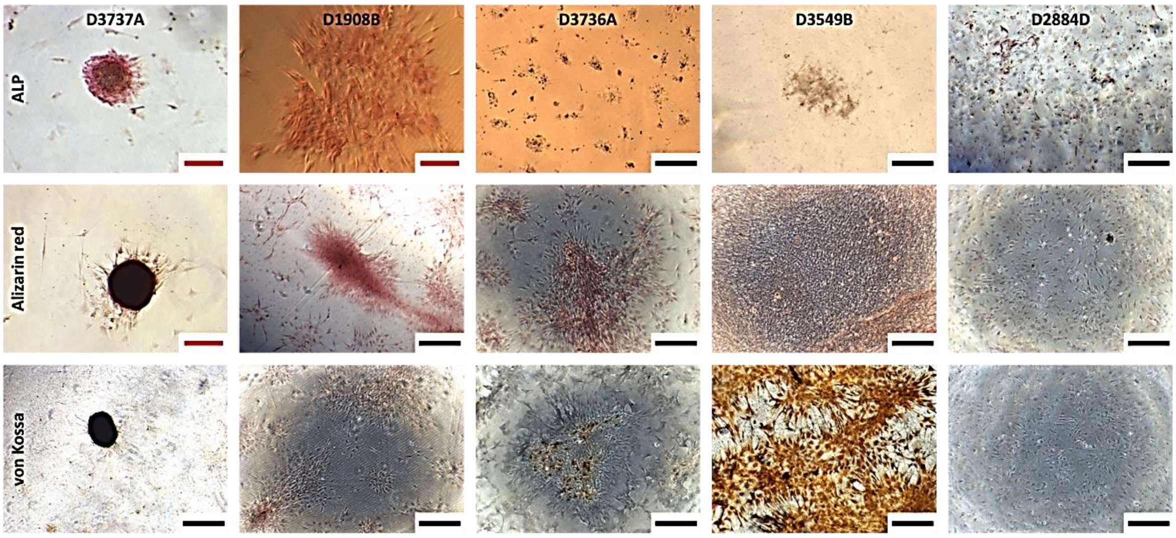

Figure 4.12: Histochemical staining of MSCs seeded on substrate X. Optical images of ALP, Alizarin red and von Kossa staining carried out on MSCs acquired from multiple donors cultured on substrate X for 96 hours. Positive staining for ALP and Alizarin red is indicated with red colouration and positive staining for von Kossa is indicated with brown to black colouration. Red scale bar represents 150 µm, black scale bar represents 400 µm.

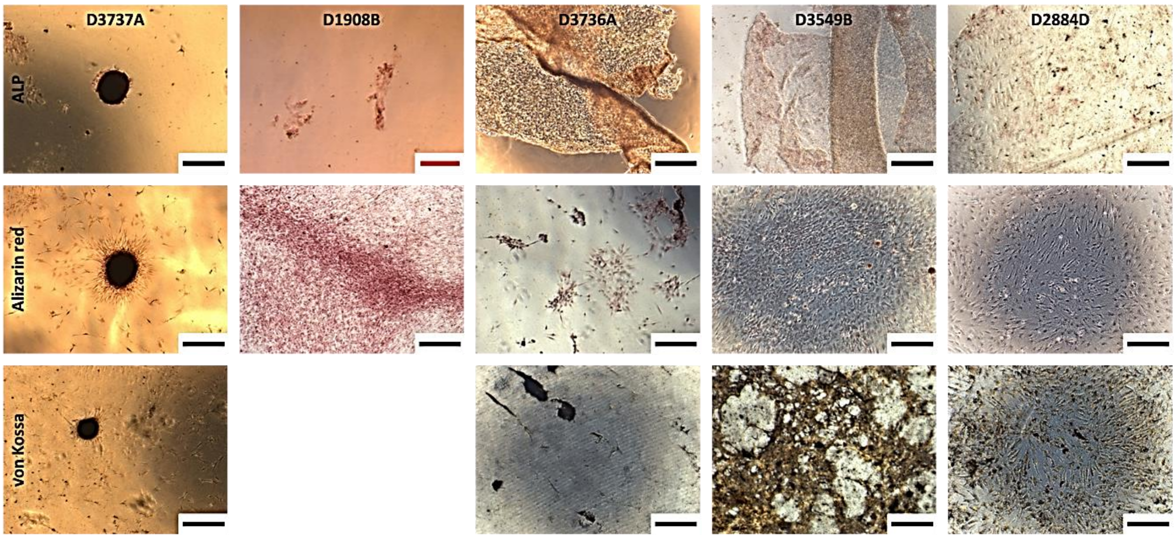

Figure 4.13: Histochemical staining of MSCs seeded on substrate X. Optical images of ALP, Alizarin red and von Kossa staining carried out on MSCs acquired from multiple donors cultured on substrate X for 168 hours. Positive staining for ALP and Alizarin red is indicated with red colouration and positive staining for von Kossa is indicated with brown to black colouration. Red scale bar represents 150 µm, black scale bar represents 400 µm.

3.4 Donor-dependent variability

Given that multiple subpopulations have been identified from individual MSC donors corroborating the long-held theory that MSC populations are heterogeneous and that each of the three subpopulations have been shown to hold differing osteogenic potentials, logic would dictate that varying subpopulation proportions between the MSC populations of different donors would result in varying osteogenic capacities between those different donors. Of the nine MSC populations (donors) cultured, four underwent sufficient analyses allowing for growth profile assessment, subpopulation separation and identification, and subsequent subpopulation osteogenic assessment. These four MSC populations all came from individual donors allowing for the assessment of possible donor-dependent variabilities. The four donors were not purposefully selected. Additional donors would have been used ideally but time and sample constraints have restricted our comparisons to four.

3.4.1 Culture duration, osteogenic markers, cell size and E-cadherin levels

Each of the donors had different proliferation rates and subsequent culture durations. This resulted in a cell culture duration ranging from 36 to 64 days, a 78% difference between the slowest (D2884D) and fastest (D3737A) proliferating cells.

In terms of osteogenic markers, the faster proliferating cell population provided by D3737A displayed a higher affinity to histochemical staining when compared to the slower proliferating cell population provided by D2884D (fig. 4.12 and 4.13). D3737A exhibited more positive staining for all three markers assessed, i.e. ALP, calcium ions (Alizarin red) and phosphate (von Kossa), when compared to D2884D. This suggests that D3737A had a higher capacity for osteogenic differentiation compared with D2884D. Both cell populations provided by D1908B and D3549B again provided similar histochemical staining results for all three markers.

These differing proliferation rates also resulted in varying sample number availability as a result of differing cell sizes. D2884D for example, provided 33 samples cultured on substrate X, whilst D3737A provided 74; that is more than a 120% increase, indicating a considerable difference in cell size resulting from expansion duration. The other two cell populations provided by D1908B and D3549B, which have fast and moderate cell growth profiles, respectively, provided similar substrate X sample numbers, 48 and 53, respectively, indicating a similar cell size post-expansion (fig. 4.14).

The proportions of the subpopulations within each cell population cultured on substrate X has also been quantified for each of the four donors (fig. 4.14). The fastest proliferating cell population (D3737A) displayed the highest proportion of self-organising cellular arrangements, most notably the aggregate-like-arranged cells, whilst the slowest proliferating cell population (D2884D) displayed the lowest proportion of self-organising cellular arrangements with no aggregate-like cellular arrangements at all. D2884D consisted mainly of monolayer-arranged cells. The cells provided by D1908B had the highest proportion of sunflower-like-arranged cells with a small fraction of aggregate-like-arranged cells, whilst the cells provided by D3549B had no aggregate-like-arranged cells but an almost even mix of sunflower-like-arranged cells and monolayer-arranged cells.

In parallel, E-cadherin levels determined via fluorescence intensity post-substrate X culturing was also used to compare all four donors (fig. 4.14). After 168 hours in culture, the cells provided by D3737A displayed the highest fluorescence intensity, 36.849, indicating the highest presence of E-cadherin, whilst the cells provided by D2884D displayed the lowest fluorescence intensity, 23.115, indicating the lowest E-cadherin levels amongst the four donors evaluated. Both cell populations provided by D1908B and D3549B again displayed very similar levels of fluorescence intensity, 26.525 and 26.675, respectively. These data strongly corroborate previously noted observations suggesting that the faster proliferating cells, D3737A for example, contained a higher proportion of subpopulations with a higher degree of self-organising once cultured on substrate X when compared to the slower proliferating cells, D2884D for example.

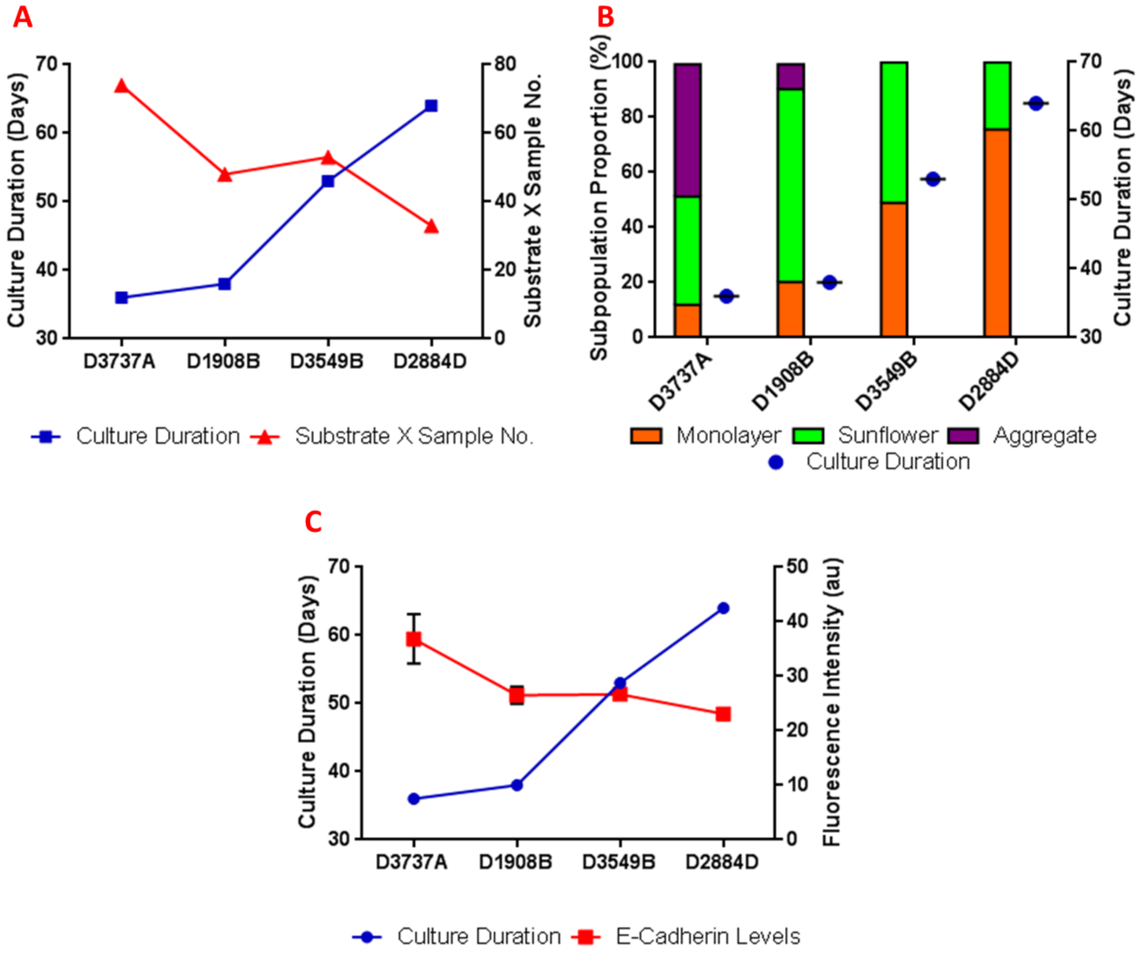

Figure 4.14: Various correlations derived from MSC culturing, substrate X seeding and immunohistochemical staining. Shown are the correlations between MSC culture duration and substrate X sample number (**A**), culture duration and subpopulation proportions (**B**) and culture duration and E-cadherin fluorescence intensity levels from substrate X samples cultured for 168 hours (**C**). MSC populations from four individual donors contributed to these data sets. Error bar represents standard error of the mean.

3.5 Cellular aggregation and osteogenic potential

Using a previously developed aggregation technique, an F127-coated suspension culture substrate, the MSCs from multiple individual donors were aggregated and assessed for donor-dependent variabilities. This phase of the study intended to show that individual donors possess different aggregation capabilities.

3.5.1 Aggregate size and morphology

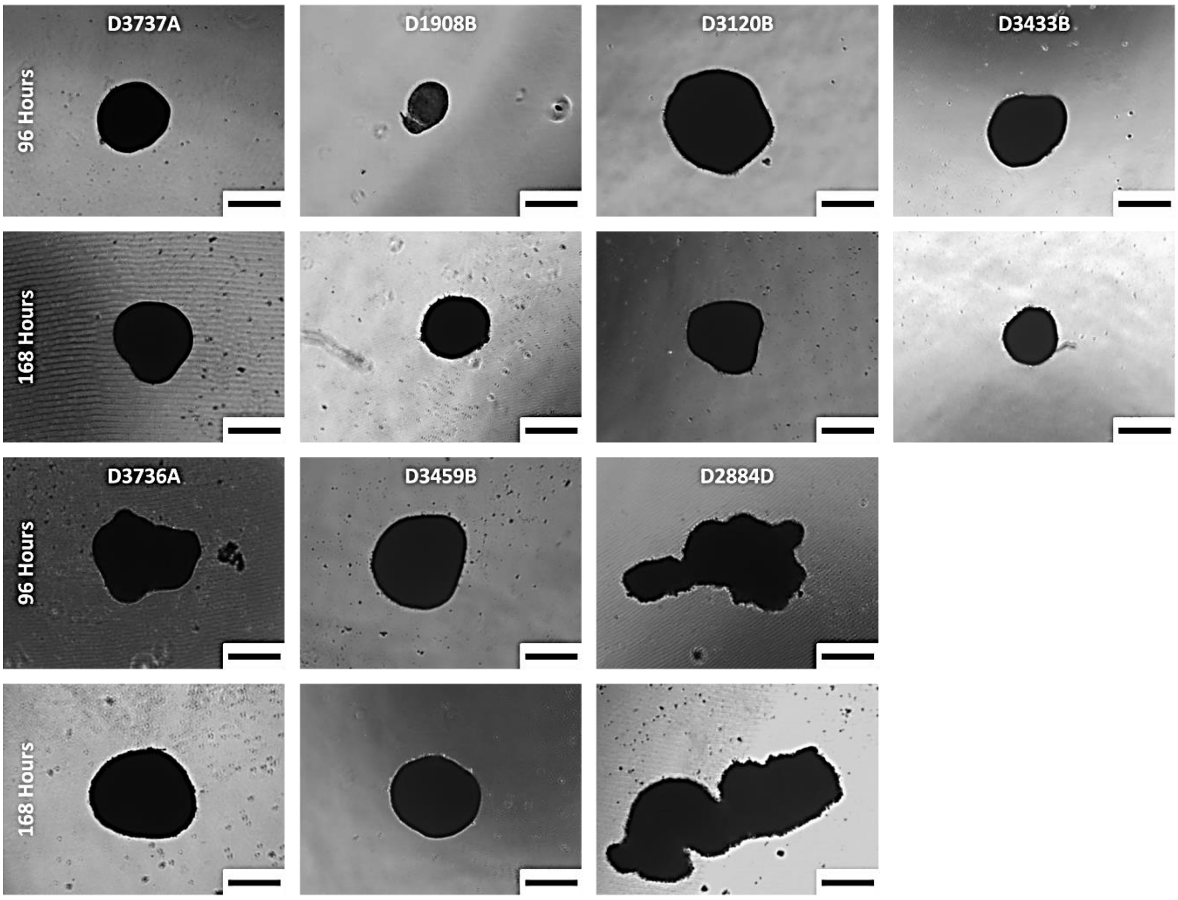

Figure 4.15: MSC aggregates from numerous donors. Optical images showing the aggregates formed using MSCs from multiple donors over two time points: 96 and 168 hours. Scale bar represents 400 µm.

The aggregates were optically imaged (fig. 4.15) and dimensions measured over two time points, 96 and 168 hours (fig. 4.16 and 4.17, respectively). Significant differences could be seen between aggregate sizes over both time points between multiple donors especially after just 96 hours in culture. After 96 hours of culturing, the aggregates ranged from 370 µm to 820 µm approximately, a 120% difference. After 168 hours of culturing, the aggregates ranged from 465 µm to 985 µm approximately, a 112% difference (fig. 4.16). The aspect ratios of the aggregates are also shown in fig. 4.17. After 96 hours in culture, the aspect ratios ranged from 1.08 – 2.14 and after 168 hours, the aspect ratios dropped to a range of 1.02 – 2.02.

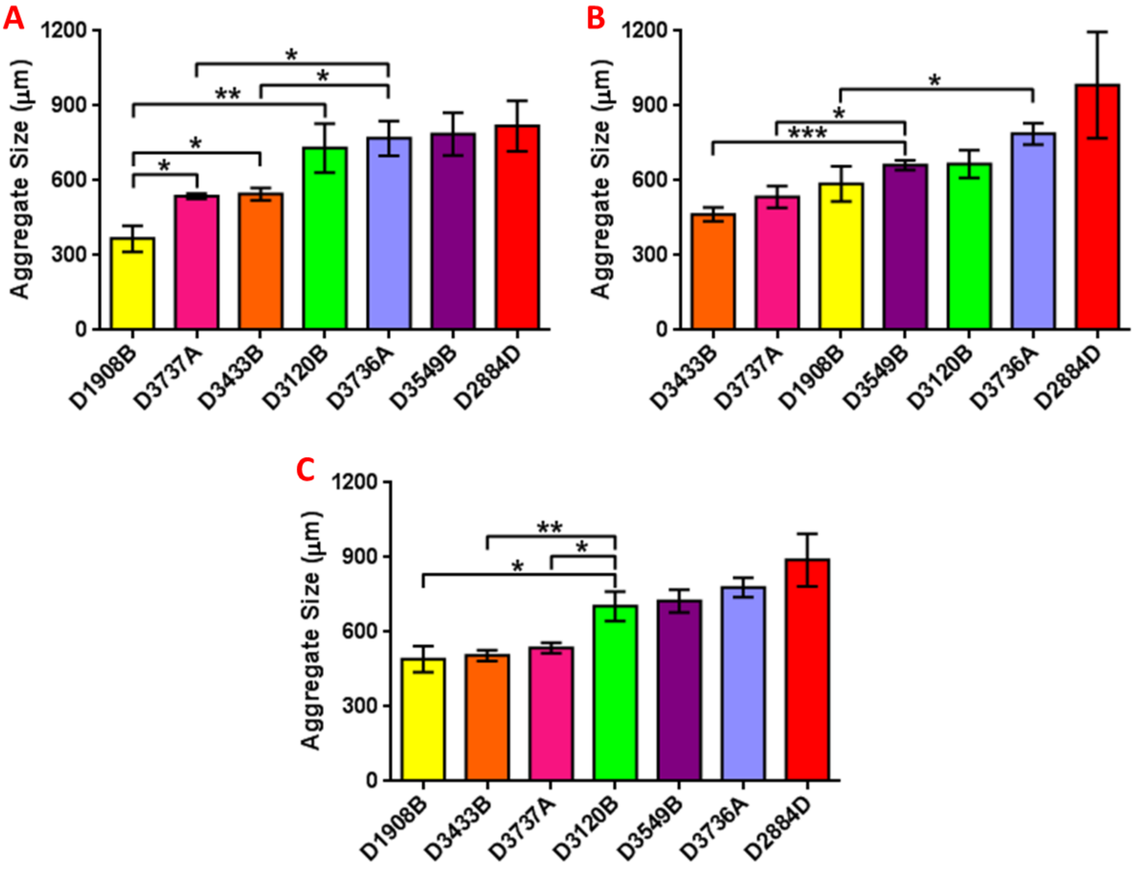

Figure 4.16: MSC aggregate size measurements. Values cover two time points, 96 hours (**A**) and 168 hours (**B**), and the average (mean) aggregate size from both time points (**C**). Error bar represents standard error of the mean. * signifies $p < 0.05$, ** signifies $p < 0.01$ and *** signifies $p < 0.001$.

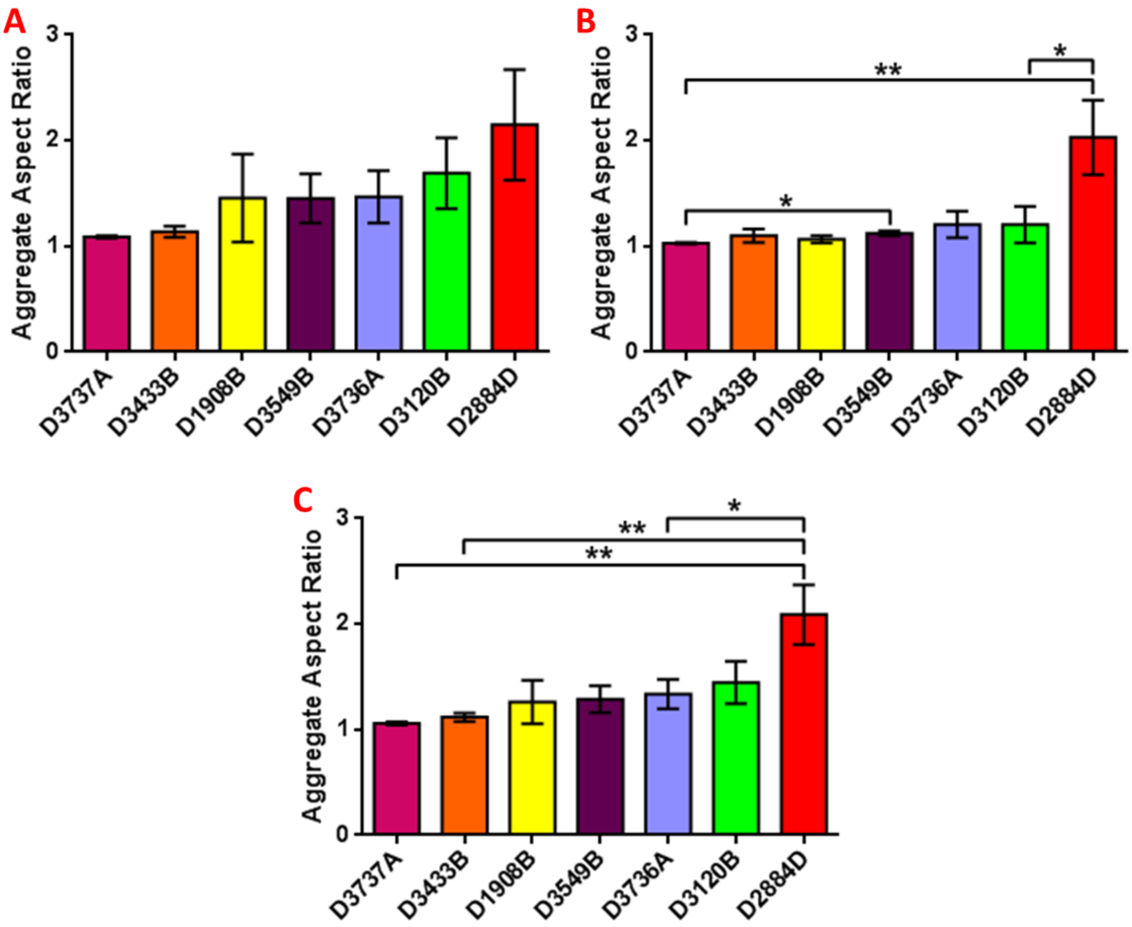

Figure 4.17: MSC aggregate aspect ratio measurements. Shown are the aspect ratios of multiple MSC aggregates over two time points: 96 hours (**A**) and 168 hours (**B**). Also shown are the average (mean) aggregate aspect ratio measurements from both time points (**C**). A value of 1 represents a perfect circle with circularity decreasing with increasing values. Error bar represents standard error of the mean. * signifies $p < 0.05$ and ** signifies $p < 0.01$.

In addition, aggregate size has been correlated with E-cadherin fluorescence intensity levels (fig. 4.18). Whilst just five donor cell populations underwent both aggregation and E-cadherin immunohistochemical staining, a strong correlation appears to exist between both data sets with the smaller aggregates having the highest E-cadherin levels and the larger aggregates having the lowest E-cadherin levels (two-way ANOVA, $p < 0.0001$).

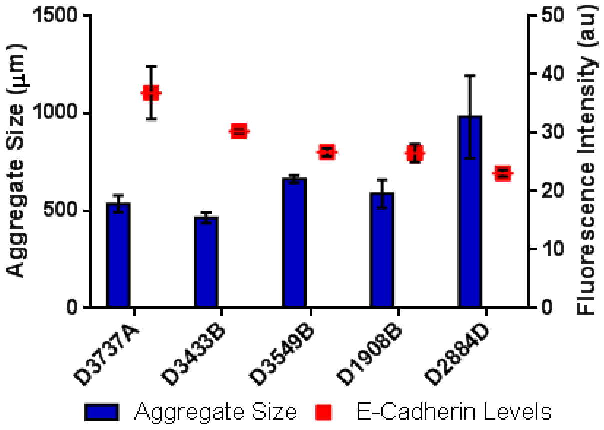

Figure 4.18: E-cadherin fluorescence intensity levels compared with aggregate size. Samples were cultured for 168 hours (two-way ANOVA, p < 0.0001). Error bar represents standard error of the mean.

3.5.1.1 Aggregate circularity and cell source

As an interesting observation, comparisons between cell sources can be made at this point. In terms of the average (mean ± standard error of the mean) aggregate circularity, as determined by aspect ratio measurements, the fastest proliferating MSC population, D3737A, the slowest proliferating MSC population, D2884D, and the MLO-A5 cell line were compared (fig. 4.19 and 4.20). Neither of the MSC aggregates differed significantly from one another; however, the faster proliferating MSC population, D3737A, did differ from the MLO-A5 cell line (t-test, p = 0.0441). The slower proliferating MSC population, D2884D, did not (fig. 4.20).

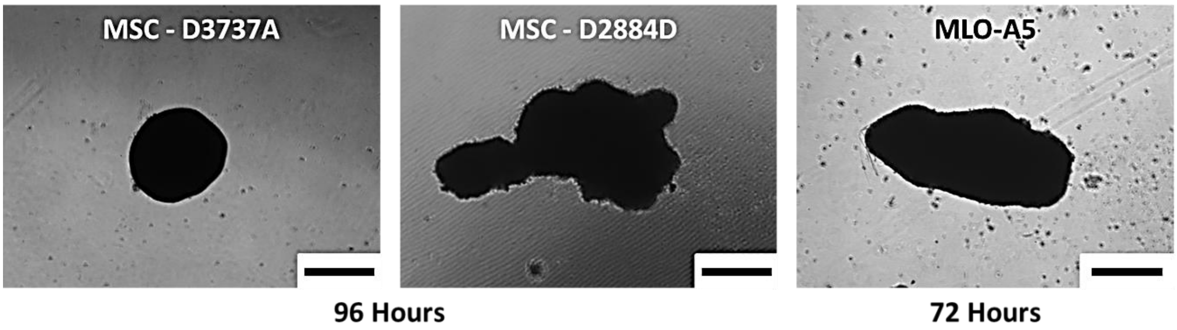

Figure 4.19: Comparisons between MSC and MLO-A5 aggregates. Optical images showing cellular aggregates formed on the F127-coated suspension substrate. The left and centre images show aggregates produced from two MSC populations acquired from two different donors: one fast proliferating (D3737A) and one slow proliferating (D2884D). The image on the right shows an aggregate produced from the MLO-A5 cell line. Both MSC aggregates were imaged after 96 hours in culture and the MLO-A5 aggregate was imaged after 72 hours in culture. Scale bar represents 400 µm.

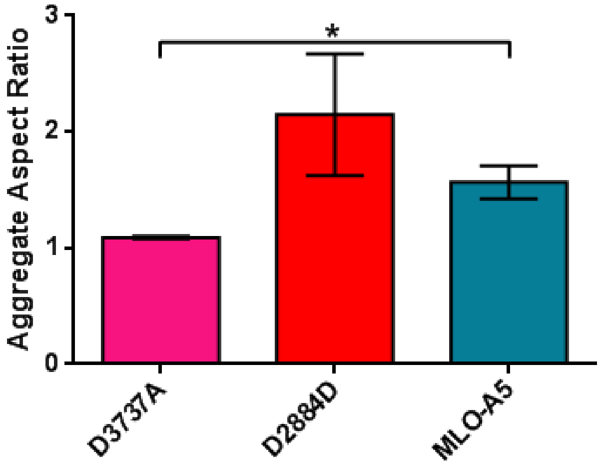

Figure 4.20: Aggregate measurements comparing MSC and MLO-A5 aggregates. A graph showing the average (mean) aspect ratios of the aggregates formed from both MSC populations and the MLO-A5 cell line. The measurements were taken from the MSC aggregates after 96 hours in culture and the MLO-A5 aggregates after 72 hours in culture. Error bar represents standard error of the mean. * signifies $p < 0.05$.

In addition, the standard error of the mean aggregate aspect ratio also differed in areas. If we take the standard error of the mean as being an indication of the variation from average (mean), the slower proliferating MSCs, D2884D, had a significantly higher variation compared to the faster proliferating MSCs, D3737A, (f-test, $p = 0.0008$) but did not differ from the MLO-A5 cell line. The

MLO-A5 cell line was also seen to have a significantly higher standard error of the mean compared to the faster proliferating MSCs, D3737A, (f-test, p = 0.0082). These observations are discussed in chapter 6.

3.5.2 Histology

Histochemical staining was also carried out on the aggregates obtained from multiple donors to assess possible osteogenic potential. The aggregates were sectioned prior to staining. Both Alizarin red and von Kossa stains confirmed the presence of minerals associated with bone formation after just 96 hours of culturing.

In addition, the levels of such minerals differed between donors. After 168 hours of culturing, both Alizarin red and von Kossa staining was stronger than that noted in the 96 hour samples. Aggregate integrity was also noted to differ between donors during histological processing. Those aggregates that stained more positively for Alizarin red and von Kossa appeared to better maintain their aggregate structures whilst being sectioned. This meant that after 96 hours, the majority of the aggregates sectioned lost their aggregate shape and structure, whereas after 168 hours, the majority of the aggregates sectioned maintained their aggregate shape and structure.

3.5.2.1 Alizarin red staining

Aggregate sections stained for Alizarin red showed differences between donor aggregates after just 96 hours (fig. 4.21). Clear differences can be seen between aggregate samples in terms of the number of small pockets of positively-stained minerals. Fig. 4.21 shows the 96 hour aggregates of seven donors that were stained for Alizarin red. One of the seven donors stained positively for Alizarin red indicating the presence of calcium ions at this early time point.

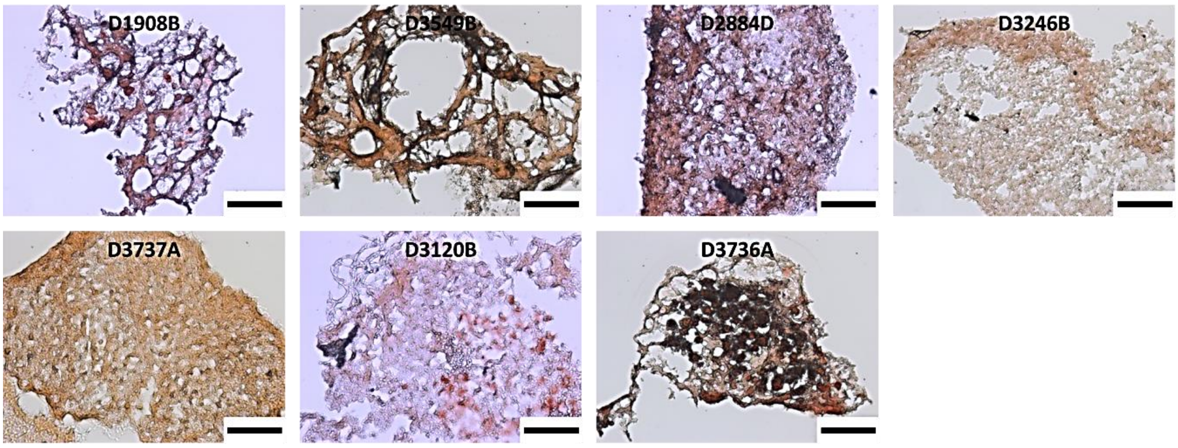

Figure 4.21: Alizarin red staining of MSC aggregate sections. Optical images of Alizarin red staining carried out on MSC aggregate sections after 96 hours in culture. Scale bar represents 80 µm. Images are arranged in no particular order.

After 168 hours in culture, differences in stain intensity are more apparent between donor aggregates (fig. 4.22). Four of the seven donors assessed with Alizarin red stained positively. A significant increase in mineral quantity when compared to the 96 hour samples was evident. Additionally, the differences between donor samples are more apparent when compared to the 96 hour samples indicating that certain donor samples progressed further along the osteogenic lineage when compared to the others.

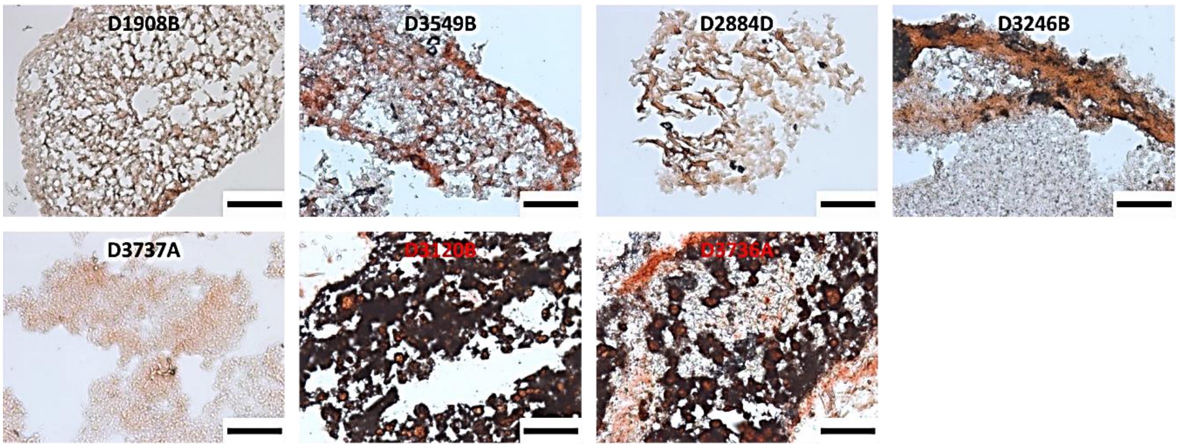

Figure 4.22: Alizarin red staining of MSC aggregate sections. Optical images of Alizarin red staining carried out on sections of MSC aggregates after 168 hours in culture. The MSCs were obtained from multiple donors. Scale bar represents 80 µm.

3.5.2.2 von Kossa staining

Again, aggregate sections were stained for von Kossa with differences being visible between donor aggregates after just 96 hours (fig. 4.23). von Kossa staining highlighted the presence of small phosphate deposits within one of the donors after 96 hours. After 168 hours in culture, differences in stain intensity are again more apparent between donor samples further suggesting that certain donors progressed further down the osteogenic lineage when compared to others (fig. 4.24). Three of the six donors assessed with von Kossa stained positively.

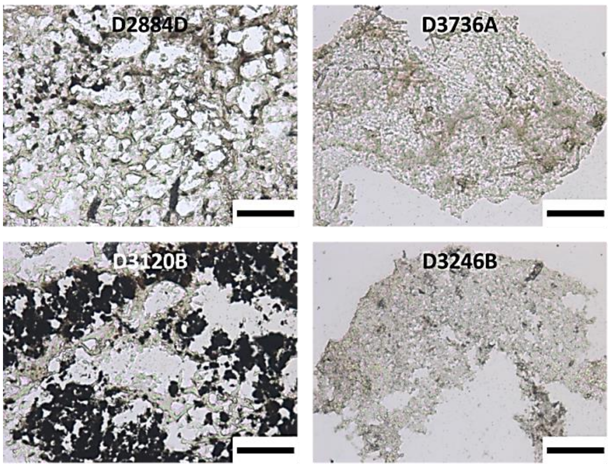

Figure 4.23: von Kossa staining of MSC aggregate sections. Optical images of von Kossa staining carried out on sections of MSC aggregates after 96 hours in culture. Scale bar represents 80 µm.

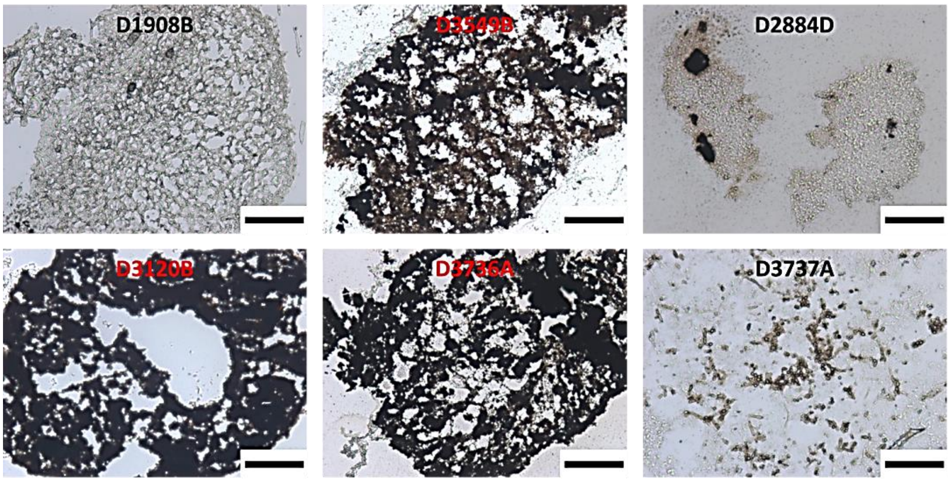

Figure 4.24: von Kossa staining of MSC aggregate sections. Optical images of von Kossa staining carried out on sections of MSC aggregates cultured for 168 hours. Scale bar represents 80 µm.

3.5.3 Microcomputerised tomography

MicroCT scanning and analysis was carried out on aggregate samples acquired from multiple MSC populations, each provided by individual donors. Fig. 4.25 shows a number of microCT scan images of several aggregates from different donors at a threshold of 110 after 168 hours in culture. The difference in aggregate density has been quantified and shows significant differences between a number of the donor aggregates. The average (mean ± standard error of the mean) aggregate density obtained from multiple donors ranged from 1.093 to 1.805 at a threshold of 110. Interestingly, these data appeared to produce a trend, albeit a surprising one. That is to say, the 3 smallest aggregates mentioned previously (fig. 4.16) appeared the least dense, whilst the largest aggregates previously mentioned (fig. 4.16) appeared to have the highest densities at a threshold of 110.

The volume of the aggregates was also measured at a number of thresholds (fig. 4.26). At a threshold of 110, significant differences in aggregate volume could already be seen between several of the aggregate samples, values ranged from 0.013 mm^3 to 0.068 mm^3. At a threshold of 130, the same trend was noted and volume measurements ranged from 0.001 mm^3 to 0.056 mm^3. With volume measurements taken from two thresholds, a ratio was obtained to determine the volume of dense material per unit total aggregate volume. Using this method of analysis, only one donor differed significantly from the remaining donors assessed. The volume of dense material per unit total aggregate volume of the different aggregates was also compared with those same measurements taken from rat femurs of different ages with the majority of the donor samples appearing to fall directly between 4 day old femurs and 35 day old femurs.

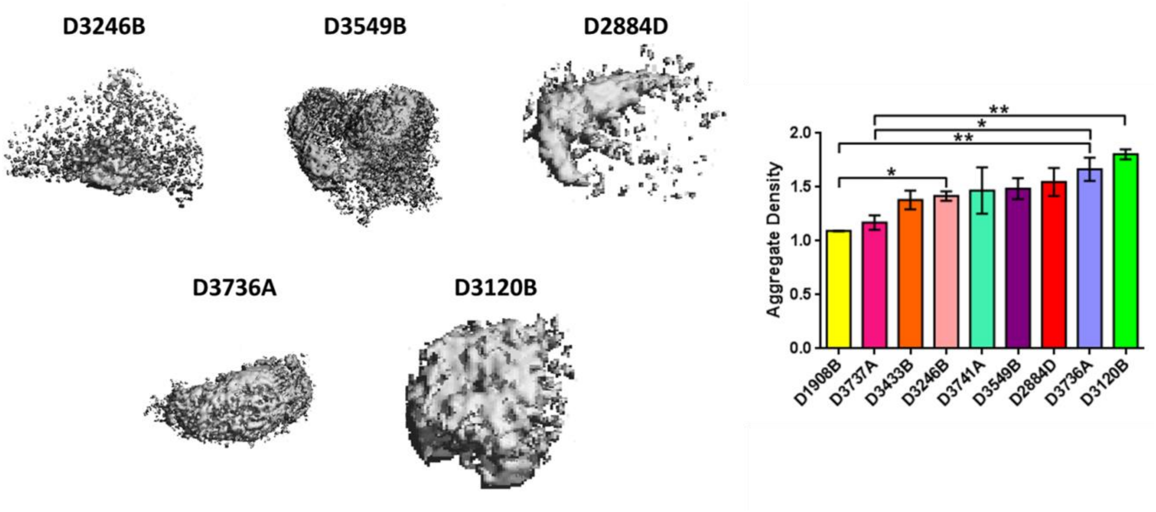

Figure 4.25: MicroCT scan images and density measurements of MSC aggregates. The aggregates were obtained from multiple donor cell populations after 168 hours in culture at a threshold of 110. Also shown are the aggregate density measurements at a threshold of 110. Error bar represents standard error of the mean. * signifies $p < 0.05$ and ** signifies $p < 0.01$.

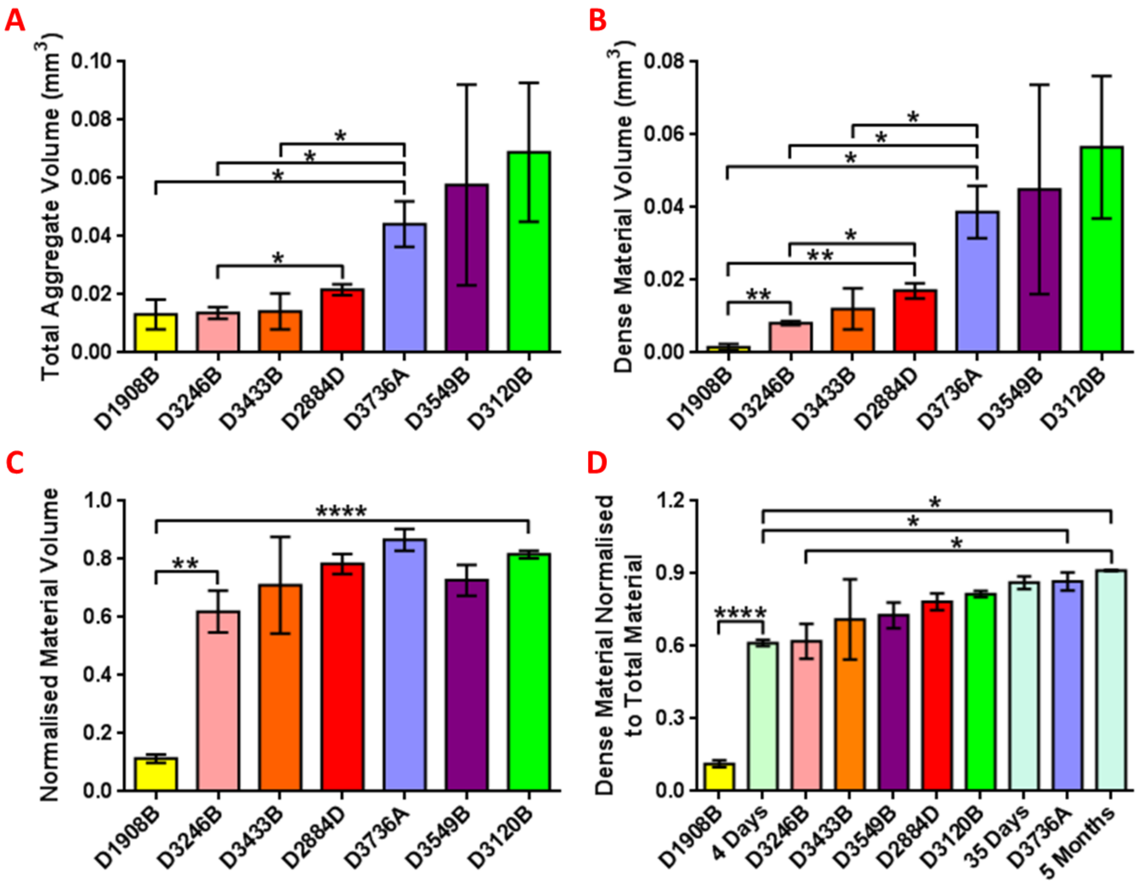

Figure 4.26: MSC aggregate material volume measurements. The average (mean) volume of MSC aggregates obtained from multiple donors after 168 hours in culture at a threshold of 110 (**A**). Also, the average (mean) dense material volumes from the same aggregates at a threshold of 130 (**B**) are shown. Both volumes were used to give normalised dense material volumes to total aggregate volumes (**C**). In addition, normalised dense material volumes were compared to those of rat femurs from three different ages: 4 days, 35 days and 5 months (**D**). Error bar represents standard error of the mean. * signifies $p < 0.05$, ** signifies $p < 0.01$ and **** signifies $p < 0.0001$.

3.6 *In vivo* study

3.6.1 Monolayer controls

Alongside the contents of a monolayer control sample chamber, fig. 4.27 shows H & E staining carried out on Neoveil mesh sections post-termination. The presence of cells was confirmed by dark speckled colouration.

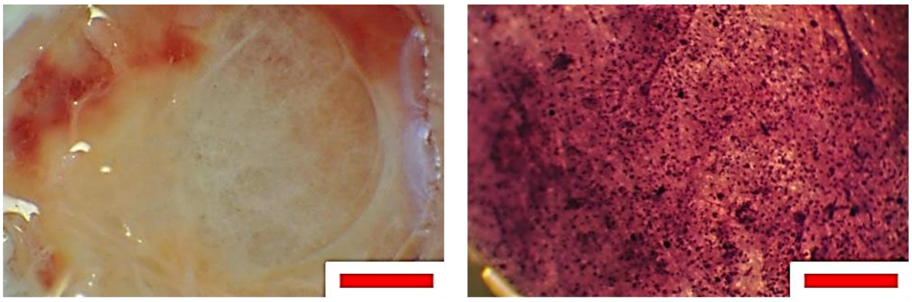

Figure 4.27: MSC monolayer samples pre and post-*in vivo* termination. Optical images showing a monolayer sample of MSCs within its chamber (left). Also shown is H & E staining carried out on a section of Neoveil mesh taken from a fixed monolayer sample pre-implantation (right). Scale bar represents 200 µm.

3.6.2 Aggregate size post-termination

Post-termination, the small MSC aggregates had an average (mean ± standard error of the mean) diameter of 81 µm (± 5 µm), whilst the large MSC aggregates had an average (mean ± standard error of the mean) diameter of 218 µm (± 18 µm). No pre-experiment aggregate measurements were taken.

3.6.3 Termination observations

Whilst removing the chambers it was noted that each one had remained sealed throughout the course of the experiment thus preventing the unwanted infiltration of any host cells and/or materials. The level at which the chambers were enveloped within the body and their subsequent vascularisation varied from sample to sample with no obvious pattern being noted. The monolayer samples had in several cases developed extracellular material further confirming the presence of cellular activity within the chambers (fig. 4.28).

In terms of the aggregates, many of the large aggregates appeared to disintegrate over the course of the experiment, whilst many of the small aggregates remained intact and in many cases appeared to have created more extracellular material *in vivo* which often also had stronger colouration compared to the material found in the large aggregate chambers. Fig. 4.28 shows optical images taken of the contents of both small and large aggregate sample chambers. Each of the small aggregate chambers show intact aggregates surrounded by considerable extracellular material growth. The large aggregate chambers, however, show very few intact aggregates, a large amount of debris and little extracellular material.

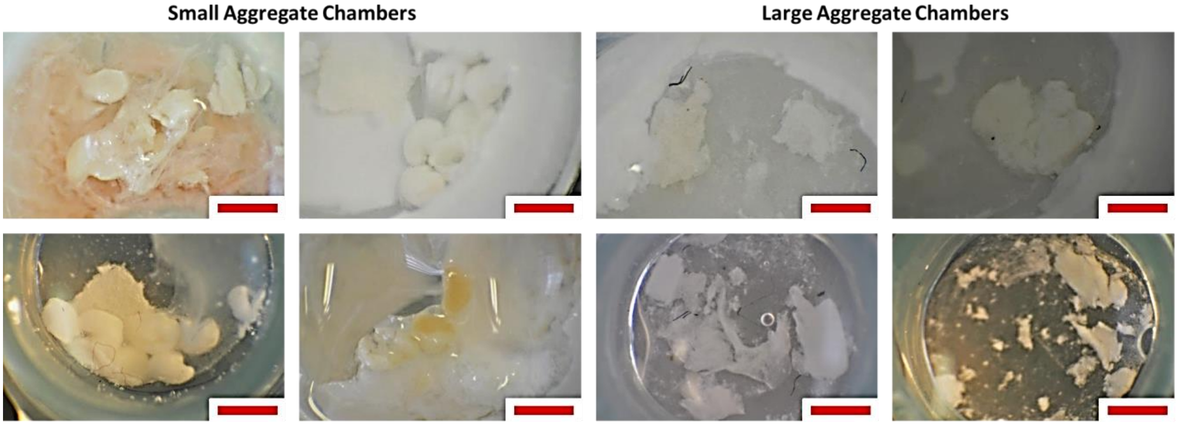

Figure 4.28: MSC sample chambers post-*in vivo* termination. Optical images showing the contents of the chambers with small aggregates (left) and large aggregates (right). Scale bar represents 200 µm.

3.6.4 Chamber content assessment

MicroCT analysis was carried out in such a way so as to evaluate the contents of the whole chamber and also the individual aggregates themselves. Fig. 4.29 shows the microCT scan images of both small and large aggregates. The small aggregates appear more uniform in size and shape, whilst the large aggregates appear to be more irregularly-shaped. Fig. 4.30 shows microCT density gradient map images of both small and large aggregates. The small aggregates again appeared more regular in size and shape and although the level of dense material varied from aggregate to aggregate, they all had their most dense material located around their peripheries. The large aggregates were again more irregular in size and shape making the spatial distribution of dense material more difficult to determine.

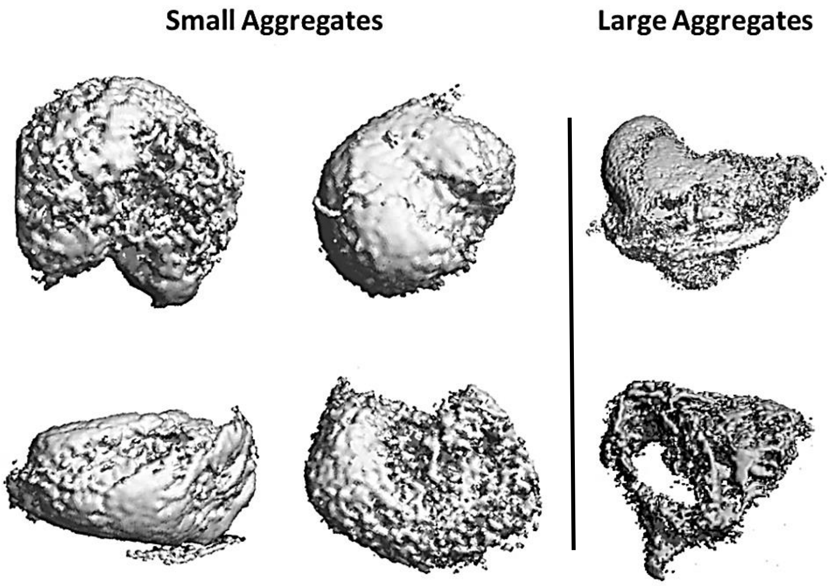

Figure 4.29: MicroCT scan images of MSC aggregates post-*in vivo* termination. Shown are small MSC aggregates (left) and large MSC aggregates (right) at a threshold of 130.

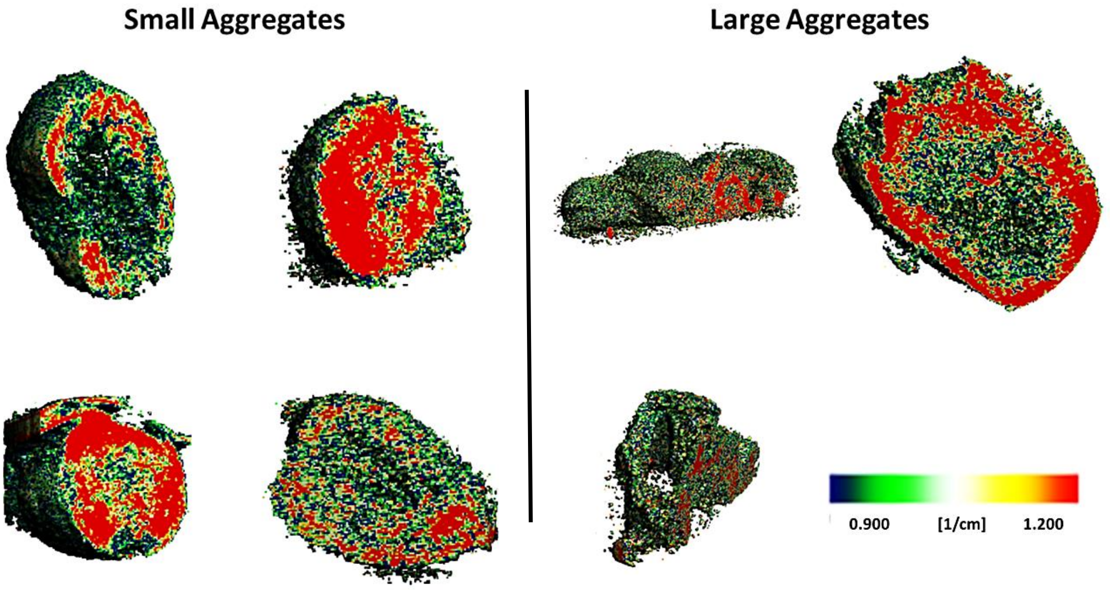

Figure 4.30: MicroCT density gradient map images of MSC aggregates post-*in vivo* termination. Shown are small MSC aggregate (left) and large MSC aggregates (right) at a threshold of 110. Density gradient ranges from 0.9 – 1.2 1/cm with the red end of the spectrum indicating areas of higher densities and the blue end of the spectrum indicating areas of lower densities.

The microCT scans of the chambers containing the MSCs showed total material volumes of 1.963 mm³, 4.832 mm³ and 10.187 mm³ for the monolayer, large aggregate and small aggregate samples, respectively, at a threshold of 110 (fig. 4.31).

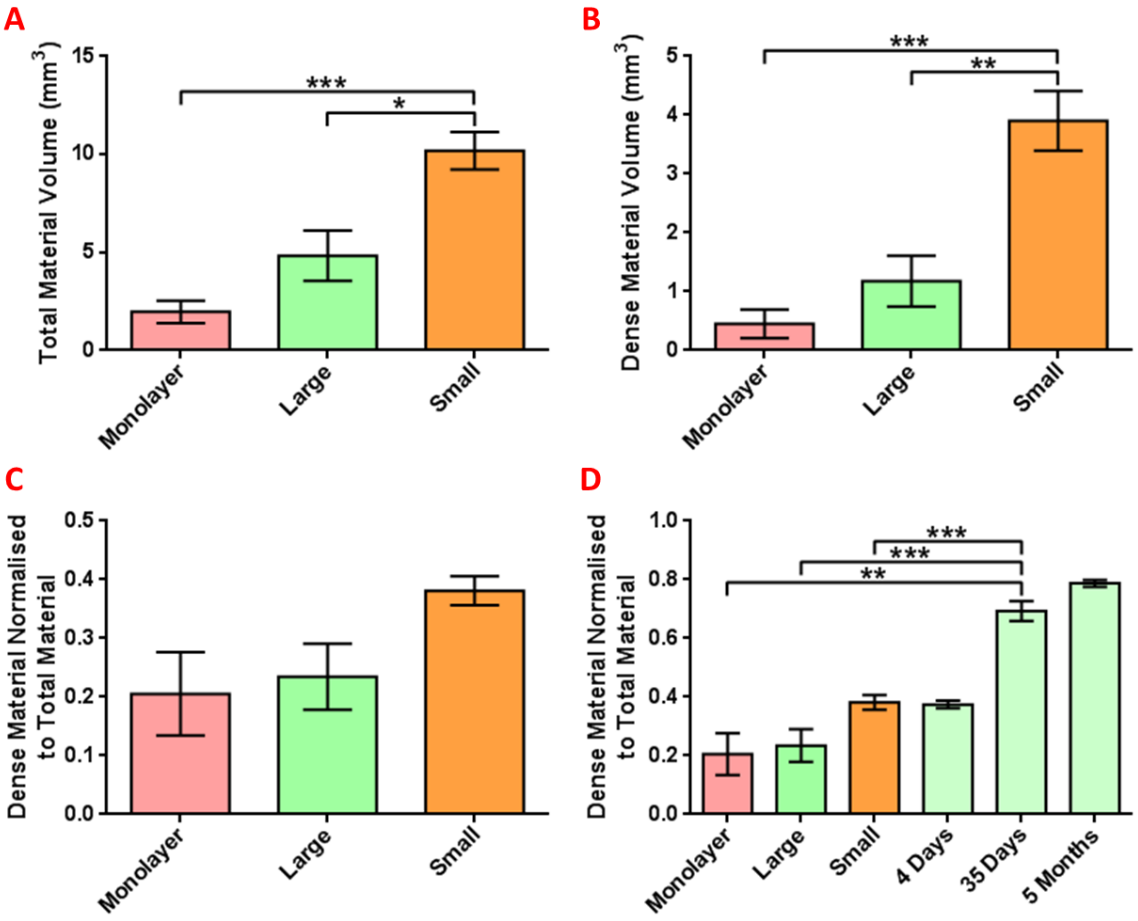

Figure 4.31: MSC *in vivo* chamber material volume measurements. Graphs showing the total material volume within the chambers at a threshold of 110 (**A**), the volume of dense material per chamber at a threshold of 170 (**B**) and the volume of dense material normalised to the total volume per chamber (**C**). Also shown is the normalised dense material volume compared to the equivalent values derived from rat femur samples of various ages (**D**). Error bar represents standard error of the mean. * signifies $p < 0.05$, ** signifies $p < 0.01$ and *** signifies $p < 0.001$.

The small aggregate samples had significantly higher volumes at this threshold compared to both the monolayer and large aggregate samples. Using a threshold of 170, the volume of dense material per sample was also measured giving values of 0.45 mm³, 1.179 mm³ and 3.902 mm³ for the monolayer, large aggregate and small aggregate samples, respectively.

The small aggregate samples again had significantly higher volumes at this threshold compared to both the monolayer and large aggregate samples. Using the 110 and 170 thresholds, a volume of dense material normalised to unit total chamber material volume was obtained. Figures of 0.205, 0.234 and 0.381 were obtained for the monolayer, large aggregate and small aggregate samples, respectively. The volume of dense material normalised to unit total chamber material volume was also compared with the equivalent measurements taken from rat femurs of different ages. All three *in vivo* samples showed similar values to that of 4 day old femur samples but were significantly lower than both the 35 day old and 5 month old femur samples.

When assessing the total volume of the individual samples rather than the whole chambers, the monolayer samples and individual aggregates for instance, significant differences can be seen (fig. 4.32). At the lowest threshold used for assessment, 110, the monolayer samples did not register a volume, whilst both large and small aggregate samples had average (mean ± standard error of the mean) individual aggregate volumes of 1.716 mm^3 and 0.516 mm^3, respectively. The average (mean ± standard error of the mean) volume of the large aggregate samples was significantly higher than those of the small aggregate samples. Given the nil value acquired from the individual sample analysis for the monolayer samples, all continued measurements refer to the large aggregates and small aggregates only. Using a threshold of 170 a volume of dense material per aggregate was obtained and averaged (mean ± standard error of the mean) giving values of 0.18 mm^3 and 0.063 mm^3 for the large and small aggregate samples, respectively. Using both data sets, the volume of dense material was normalised to the total aggregate volumes giving figures of 0.104 and 0.114 for the large and small aggregate samples, respectively. The normalised dense material volumes were again compared to those of rat femur samples of differing ages. Both the large and small aggregate samples were significantly lower than the femurs of all ages.

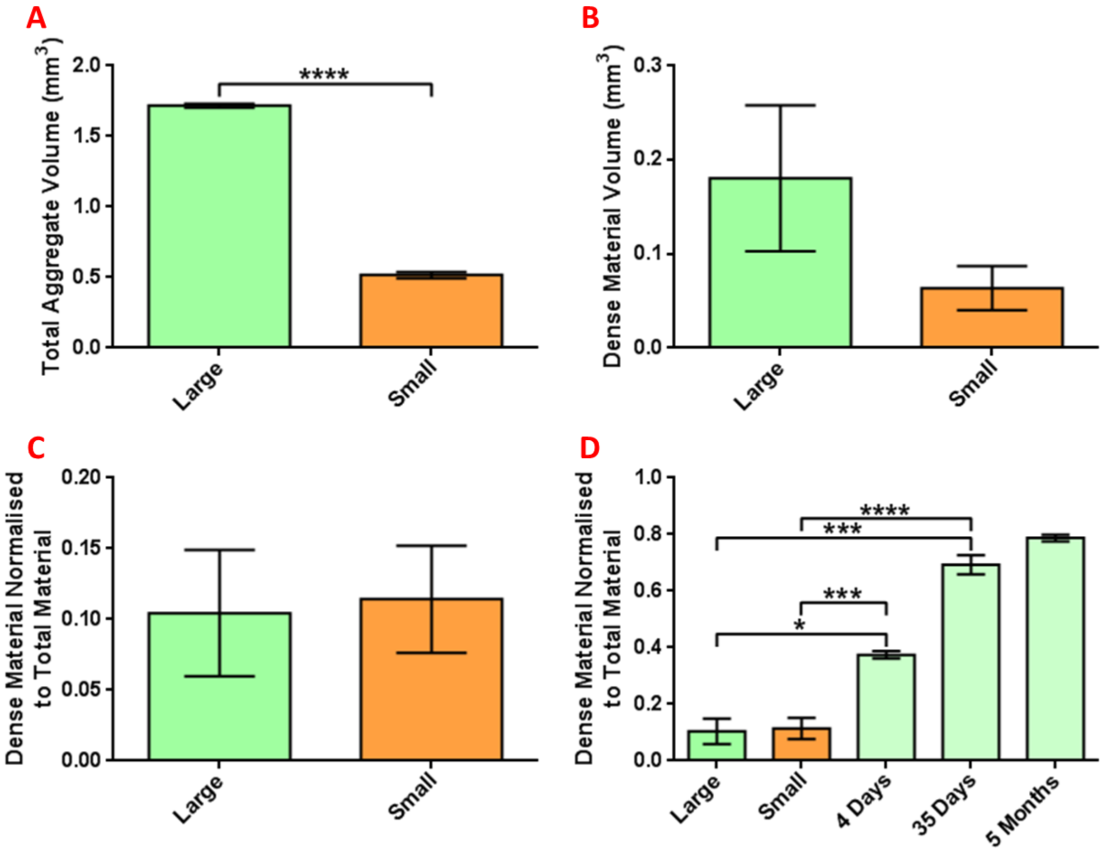

Figure 4.32: MSC *in vivo* chamber aggregate volume measurements. Graphs showing the total material volume per MSC aggregate at a threshold of 110 (**A**), the volume of dense material per aggregate at a threshold of 170 (**B**) and the volume of dense material normalised to the total material volume (**C**). Also shown is the normalised dense material volume compared to the equivalent values derived from rat femur samples of various ages (**D**). Error bar represents standard error of the mean. * signifies $p < 0.05$, *** signifies $p < 0.001$ and **** signifies $p < 0.0001$.

3.6.4.1 In vivo sample observations and cell source

If we take the *in vivo* data obtained from the MLO-A5 cell line and compared it to that of the MSC data, some interesting additional observations can be made from the *in vivo* study. Whilst significant differences cannot be seen directly between either of the monolayer samples or either of the large aggregate samples, significant differences can be seen between the small aggregate samples of both cell types. The small aggregates formed using MSCs produced a significantly higher volume of dense material normalised to total sample volume (t-test, $p = 0.002$).

Additionally, both data sets were compared to their equivalent data set obtained from rat femur samples of various ages (fig. 4.33). Whilst none of the MSC samples differed significantly from the youngest of the rat femur samples, all of the MLO-A5 samples did (t-test, p = 0.0011, 0.0128, and 0.0036 for the monolayer, large aggregate and small aggregate samples, respectively). Whilst there were no direct significant differences between the first two of the three sample variables from either cell type; indirectly, differences can be seen with the MSCs producing more similar levels of dense material to natural bone compared to the MLO-A5 cell line.

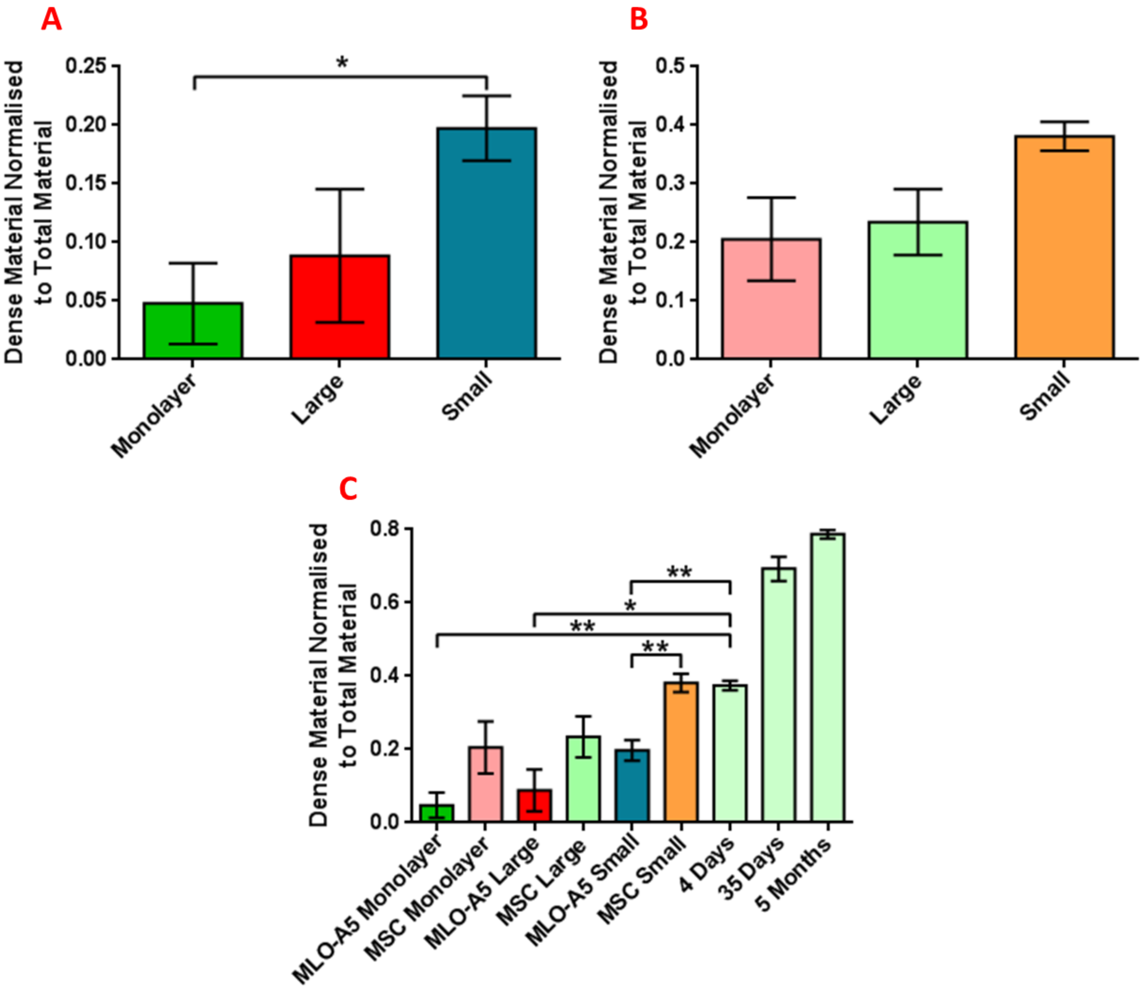

Figure 4.33: MicroCT material measurements comparing MLO-A5 and MSC *in vivo* chambers. Shown are the normalised dense material volumes acquired from whole chamber scans of both MLO-A5 (**A**) and MSC (**B**) *in vivo* samples post-termination. Also shown is a comparison between both cell types and rat femur samples of various ages (**C**). Error bar represents standard error of the mean. * signifies $p < 0.05$ and ** signifies $p < 0.01$.

4. Discussion

This study used a newly developed substrate, substrate X, to identify, quantify and assess the bone formation potential of donor-dependent MSC subpopulations. MSCs were isolated from MNC populations obtained from nine individual donors and cultured under previously established proliferative conditions until a sufficient cell number was acquired, 16 x 80% confluent T75 flasks at passage two. Monitoring growth profiles afforded us the opportunity to compare this new subpopulation identification technique with previously established growth rate studies. Once a specific culture point was reached and using substrate X, three subpopulations were identified based on their cellular attachment arrangements, a monolayer arrangement, a sunflower-like arrangement and an aggregate-like arrangement. Each subpopulation was subsequently assessed for osteogenic potential using a well-established osteogenic assay, histochemical staining, under the speculation that each subpopulation will hold a different capacity for osteogenic differentiation. The varying subpopulation-dependent osteogenic potentials are thought to ally with varying donor-dependent subpopulation proportions which could aid in assessing an individual's osteogenic capacity.

4.1 Mesenchymal stem cell verification

There are a minimum of three validation techniques required to confirm the use of MSCs in any study: isolation through plastic adherence, flow cytometry measurements of at least eight surface markers and tri-lineage differentiation down three lineages, i.e. adipogenic, chondrogenic and osteogenic[158]. Whilst two techniques have been successfully completed throughout this study, i.e. isolation through plastic adherence and tri-lineage differentiation, the third requirement, i.e. flow cytometry analysis of eight surface markers, did not provide evidence to a satisfactory degree to conclude that MSCs were used here. This is thought to be due, in part, to the way in which the flow cytometry assessment was carried out. The manufacturer's protocol recommended a specific volume of antibody to be used, 10 µl; however, this was for a far greater cell number, 1 x 10^7, than those intended for use in this element of this study, 1 – 3 x 10^4 approximately. Therefore, the volume used was reduced to one tenth of that recommended. Whilst the supply company assured that this was perfectly safe and would not affect the results, it is the opinion of the author that this may have hindered the acquisition of reliable data. Given the limited availability of cells and in the interest of maintaining consistency throughout the study, the true impact of the volume reduction on the results was not thoroughly investigated and the volume used was not altered by the author. The author is of the belief, however, that should repeated flow cytometry analyses be possible, the use of MSCs would be satisfactorily verified.

4.2 Mesenchymal stem cell heterogeneity

MSC heterogeneity was investigated and evaluated from two primary points, differences in growth profile characteristics during initial cellular expansion and the identification and quantification of multiple subpopulations.

4.2.1 Mesenchymal stem cell isolation and expansion

Using common isolation techniques, MSCs were isolated from MNC cultures taken from multiple donors. The growth profile of each MSC population differed considerably once the cells had been cultured beyond their second passage. This is thought to be the earliest point at which one can start to identify possible bone formation potential as growth rate has been linked with osteogenic capacity in previous studies[451]. It is thought that the quicker the growth rate, the higher the potential for bone formation. Morphologically speaking, the MSCs within our study that were cultured for longer periods, the slower proliferating cells, demonstrated different cell shapes and sizes to those MSCs with shorter culture periods, the faster proliferating cells. The faster proliferating cells were smaller overall than their slower proliferating counterparts. The evidence for this is, whilst at 80% confluency and passage two, the acquired cell numbers differed between MSC populations indicating cells of differing sizes and/or qualities. The faster proliferating cells had approximately 1 x 10^6 cells per T75 culture flask, whilst the slower proliferating cells had approximately 0.75 x 10^6 cells per T75 culture flask. The lowering of the cell counts with increasing culture duration was also observed through sample number records (fig. 4.5). Additionally, previous studies have suggested that subpopulations of different sizes, proliferation rates and differentiation capacities may exist[368,376]. Majore and colleagues attempted to isolate two MSC subpopulations from human umbilical cord using CCE[369]. Their results demonstrated that the smaller cells (11 µm) had a higher proliferative capacity compared to the larger cells (19 µm) which correlates with the data presented in this study. Interestingly, a flattened and enlarged cell shape similar to that noted for the slower proliferating cells in this study is also characteristic of MSC senescence[452]. Taken together, these data would suggest that an increased proliferation duration or decreased growth rate correlates with an increased level of possible senescence within an MSC population which results in an altered fibroblastic morphology and a subsequent reduction in bone formation potential.

Whilst age and gender are two commonly used parameters for donor-dependent comparisons, they were not included in this study. The age range of the cohort used in this study is fairly narrow (age range of 22 – 30 with one outlier of 37) (table 4.1). Several other groups have examined age-related donor differences in bone marrow-derived MSCs with much wider age ranges than that noted here, as reviewed by Stolzing *et al.*[453]. Furthermore, a cohort of nine with information for eight, five males and three females, is thought to be too small a sample size to be further divided into gender subcategories. For example, Leonardi *et al*. used 20 donors and reported cell recovery and osteogenic potential to be independent of donor gender[454], Yoo *et al*. used 72 donors and again reported no significant differences dependent upon donor age or gender[455], Payne *et al*. used 41 donors with no gender-related differences in cumulative population doublings being reported[456] and Siegel *et al*. used 53 donors[250]. With a larger cohort and wider age range, such donor comparisons could have been possible within the current study.

4.2.2 Subpopulation identification

Subpopulation identification has been achieved on two levels, initial identification and quantification through a cellular arrangement study followed by verification and possible reasoning via immunostaining.

4.2.2.1 Cell attachment arrangements

During each of the donor-dependent experiments, the MSCs were seeded on both TCP and substrate X, for monolayer/control culturing and subpopulation identification, respectively. When the MSCs were seeded onto substrate X, they attached and formed three specific cellular arrangements, i.e. a monolayer arrangement, a sunflower-like arrangement and an aggregate-like arrangement. Using multiple optical images of each MSC population from multiple donors over two time points, 96 and 168 hours, the proportions of these cellular arrangements have been quantified (fig. 4.7) with each donor being seen to produce differing proportions of these supposed subpopulations. Interestingly, for the donors that completed the full array of assessments, the proportions of the three subpopulations appeared to correlate with growth rates (fig. 4.14). Those cell populations with faster proliferation rates subsequently produced more organising cellular arrangements, i.e. sunflower-like- and/or aggregate-like-arranged cells, when cultured on substrate X compared to the cell populations with slower proliferation rates.

4.2.2.2 E-cadherin levels

In an effort to ascertain if E-cadherin expression might be the reason behind these apparent cellular arrangements, E-cadherin staining was carried out on the MSC samples cultured on substrate X (fig. 4.8 and 4.9) in the hope of identifying and quantifying cadherin expression levels within each of the subpopulations. The colony-like arrangements observed on substrate X are thought to be more indicative of embryonic stem cell (ESC) cultures, rather than MSC cultures. Whilst typical *in vitro* cultures grow in a two-dimensional (2D) -monolayered fashion, ESC cultures have been shown to be morphologically distinct from such cultures whilst being grown on the same substrate. Such cells have been seen to form three-dimensional (3D) colonies under standard tissue culture conditions[155,457]. The distinct cellular arrangements observed with the MSC cultures grown on substrate X are thought to possibly represent varying degrees of ESC-like subpopulations within the MSC population.

Much of the self-organising carried out by cells is mediated through the expression of particular surface molecules called cadherins[458]. Cadherins are of interest to this study because they encompass a group of transmembrane or membrane-associated glycoproteins responsible for mediating specific cell – cell adhesions. These molecules function in a calcium-dependent manner controlling the morphogenesis of a number of tissues and organs[459–461]. Whilst there have been many different cadherins identified, E-cadherin-mediated cell – cell contact is particularly relevant because it maintains colony formation within ESC cultures[462] and is, therefore, thought to also be responsible for the cellular arrangements noted in this study.

During the early stages of mammalian development, cell – cell contact mediated by E-cadherin is required for embryonic blastocyst integrity[463] and has also been shown to control the processes of early differentiation[464]. Whilst E-cadherin is expressed in all cell types during early mouse embryonic development, its inactivation first becomes apparent in mesodermal cells during the gastrulation phase[465–467]. Those mesodermal cells then express mesoderm-specific genes[468]. Interestingly, cadherin-11 is initially detected in mesodermal cells at the gastrulation phase with a particularly high expression being noted in MSCs surrounding developing organs[469]. It has been suggested that E-cadherin expression during early embryonic development is essential for the further development of tissue-specific structures during the gastrulation phase. As E-cadherin expression decreases, the expression of other cadherins increases.

The expression of other cadherins and subsequent tissue formation is dependent upon the initial foundations laid down by the expression of E-cadherin. E-cadherin is required for early cell condensation which might be a prerequisite for subsequent inductive events leading to controlled cell patterning and the generation of differentiated structures[464]. The expression patterns of cadherins have been shown to correlate with distinct morphogenetic events. For example, E-cadherin is expressed during mouse gastrulation and in epithelial tissues[465,467], N-cadherin is expressed in neuroepithelium, myocardium and osteoblasts[470,471], and R-cadherin displays a clear expression pattern in the developing nervous system[472].

The varied fluorescence intensities measured in this study suggest that the more organisation-capable the cellular arrangement, i.e. the higher the proportion of sunflower-like and aggregate-like cells, the higher the degree of E-cadherin expression. These data not only confirm the presence of distinguishable subpopulations but also suggests that E-cadherin plays a part in the subpopulations' self-organising properties, if not controlling them entirely.

When comparing E-cadherin levels between the individual MSC populations that were subjected to the complete series of analyses, a correlation appears between E-cadherin levels and growth rates (fig. 4.14). E-cadherin levels appear to decrease as growth durations increase. This observation correlates with previous data sets suggesting that the faster proliferating cell populations not only contain higher proportions of subpopulations with higher self-organising capabilities but also that these subpopulations possess higher levels of E-cadherin.

4.3 Subpopulation assessment

Given the links noted between donor-dependent growth profiles, differing cell sizes and subpopulation proportions, it was speculated that the different subpopulations may also hold different osteogenic capacities; which, because of the varying donor-dependent subpopulation proportions, may in turn influence an individual's bone formation potential. Whilst it was clear three distinct cellular arrangements of differing proportions were present in all MSC populations examined and differing osteogenic potentials could be speculated upon based on previously conducted research from different laboratories[361], the osteogenic potential of each subpopulation needed to be identified.

To investigate this, the cellular arrangements, along with the TCP-produced monolayer controls, were histochemically stained for osteogenic markers (fig. 4.12 and 4.13). These data suggest that the subpopulations with more organisational traits correspondingly have a higher osteogenic capacity. As mentioned earlier, cell – cell contact mediated by E-cadherin is important during the early stages of embryonic development[463] but it has also been shown to control the processes of early differentiation[464]. E-cadherin expression during early embryonic development is essential for further cadherin-11 expression following E-cadherin decline which is subsequently important for the further development of tissue-specific structures during the gastrulation phase[464]. Cadherin-11 has also been shown to be specifically involved in osteoblast differentiation[473–475]. Whilst several *in vitro* studies have shown that the expression of cadherins can change during osteoblast differentiation, the most common cadherins expressed by osteoblasts are E-cadherin, N-cadherin and cadherin-11[474,475]. N-cadherin and cadherin-11 have both been shown to influence bone formation and mass[476]. Low N-cadherin levels have also been shown to correlate with adipogenic differentiation[477]. It can, therefore, be postulated that the expression of E-cadherin within certain subpopulations may have possibly increased the levels of other osteogenic-related cadherins during the differentiation processes resulting in the increased osteogenic capacity of those same subpopulations.

With particular cellular arrangements appearing to have a higher differentiation capacity, logic would dictate that those donors with a higher percentage of sunflower-like- or aggregate-like-arranged cells would correspondingly have a higher osteogenic capacity.

4.4 Mesenchymal stem cell aggregation

4.4.1 Aggregate size and shape

Each MSC population expectedly produced single aggregates when seeded in the wells of the F127-coated suspension culture but the size and shape of the aggregates differed. Whilst a number of the MSC populations produced spherical aggregates of a uniform size and shape, other populations produced irregularly-shaped aggregates of non-uniform sizes.

When looking at the size of the aggregates, especially the combined average (mean ± standard error of the mean) aggregate size from both 96 hour and 168 hour cultures (fig. 4.16), a distinct junction becomes apparent. The three smallest aggregates did not differ in size from one another, nor did the four largest aggregates. Rather, they formed two distinct groups which ultimately differed in size from one another. Interestingly, these two distinct groups also correlated with growth rate. The smaller aggregates on average (mean ± standard error of the mean) had faster proliferation rates compared to the larger aggregates. Additionally, the aspect ratio measurements provided for some noteworthy data. After 96 hours in culture, many of the aggregate samples had considerable inner-variances in aggregate size ultimately diluting any mean aspect ratio differences from one donor to the next. This rendered any possible differences insignificant. After 168 hours, however, the majority of aggregate samples appeared to tighten and reduce their overall aspect ratio. This led to significant differences becoming apparent between a number of the aggregate samples reiterating the speculation that certain donors had a higher capacity for aggregation compared to others. These data suggest that each of the MSC populations evaluated possessed different aggregation capacities. Possible reasons behind these donor-dependent variabilities are discussed later.

4.4.2 Aggregate osteogenic potential

Given that aggregate culturing has been shown to enhance osteogenesis (chapter 3), assessing the nodule formation capacity of multiple donors should include an evaluation of minerals associated with osteogenesis. Histochemical staining for Alizarin red and von Kossa allowed for the comparison of calcium ions and phosphate salts, respectively, indicating the deposition of minerals, over time. These data suggest that there are donor-dependent differences in aggregation capacity and possible subsequent osteogenic potential.

4.4.3 Aggregate material assessment

The aggregates formed using the F127-coated suspension cultures have also been microCT scanned for material evaluation. An increased aggregate density or volume of dense material is thought to indicate increased mineralisation and potential for bone formation. The aggregates from nine donors were microCT scanned after 168 hours in culture. Density measurements were taken for all nine donors; however, due to the lack of available higher threshold volume measurements, total volume measurements were taken for seven donors.

A tentative explanation for the data described in fig. 4.16 and 4.25, which show the smallest aggregates had the lowest densities and the largest aggregates had the highest densities, could include two possible reasons. Firstly, the high E-cadherin expressive donor samples formed smaller and denser cellular aggregates which may have led to a low oxygen and nutrient exchange for the centrally located cells with subsequent lowered cell viability. Secondly, the donor samples with more densely packed cell populations may have been induced earlier into osteogenic differentiation (the phenomenon discussed in detail in chapter 3) with lower proliferation compared to the more loosely packed cell populations, the lower E-cadherin expressive donor samples. Over the following culture period, the loosely packed aggregates formed from the poor

E-cadherin expressive donor cells gained an advantage with higher cell numbers and a higher concentration of mineralising matrix.

Encouragingly, however, the aggregate volumes confirm previous data suggesting that the aggregates formed from the MSCs of multiple donors produced aggregates of different sizes despite being formed using the same cell numbers, culture conditions and duration. This further compounds the observation that each MSC population possesses a different aggregation capacity. Given that the minerals required for bone formation are denser than the cellular or collagenous extracellular material of the aggregates, a more dense aggregate is thought to be indicative of an increased mineral content and subsequent bone formation potential. The considerable differences between the aggregate densities of individual donors suggest that those donors with higher densities would also have a correspondingly higher bone formation potential. The volume of dense material, material still present above a threshold of 130, correlates well with the previously discussed histochemical staining. That is to say, the three donors that were shown to possess the highest volumes of dense material also had the strongest staining for calcium and phosphate deposits after 168 hours in culture.

4.4.4 Aggregation and donor-dependent E-cadherin levels

A correlation appears to exist between E-cadherin fluorescence levels and aggregate size measurements after 168 hours in culture (two-way analysis of variance (ANOVA), $p < 0.0001$) (fig. 4.18). This correlation does help to relate donor-dependent subpopulations with aggregation potential through E-cadherin levels. E-cadherin expression has previously been shown to be an indicator of subpopulation proportions and to be donor-variable but apparently also has links to aggregate size and shape. This study has demonstrated that MSC cultures contain differing quantities of cells expressing E-cadherin and, as mentioned, E-cadherin is required for embryonic blastocyst integrity[463]. Taken together and given that E-cadherin was found to be involved in forming cellular aggregates[478], it was conjectured that the different E-cadherin levels found in each MSC population of this study would result in different aggregation capacities.

The correlation between aggregation and E-cadherin levels thus validates the hypothesis that a possible relationship exists between an individual's subpopulation proportions and their aggregation capacities. It is noted, however, that no further correlations have been made between donor-dependent aggregation and donor-dependent osteogenic potential and further investigations are required if a more tangible link is to be conclusively proven.

4.5 *In vivo* experiment

4.5.1 Experiment observations

The *in vivo* element of this study has provided some interesting results. H & E staining combined with post-termination imaging have shown that the monolayer samples were biologically active *in vivo*. Contrary to the *in vitro* examinations, the monolayer samples produced more material over the course of the experiment than expected. The aggregates also delivered some remarkable results. Whilst the majority of the small aggregates were still visible upon termination, many of the large aggregates appeared to disintegrate over the course of the experiment. Additionally, the chambers containing the small aggregates had more extracellular material after 8 weeks when compared to their large aggregate counterparts. The post-experiment aggregates on average (mean ± standard error of the mean) measured an approximate size of 80 µm and 220 µm for the small and large samples, respectively. With so many of the large aggregates being lost throughout the experiment, it is thought that all of the aggregates lost were possibly larger than 220 µm. This would suggest that the smaller the aggregate samples, the more biologically active they are over an 8-week period and that a size approaching 220 µm may be a critical cut off point for possible bone formation through aggregation. It has been suggested that the diffusion limit of oxygen is only 100 – 200 µm and so any tissue larger than this would require vascularisation[479].

4.5.2 Microcomputerised tomography of post-in vivo samples

Fig. 4.31 shows the measured volumes of two different thresholds acquired from whole chamber scans. At the lower threshold, the small aggregates were the best performing group in terms of material volume. The lower than expected volume of the large aggregate samples is thought to be as a result of the apparent disintegration of many of the aggregates. Conversely, the larger than expected volume of the monolayer controls is thought to be the result of a comparatively enhanced proliferation rate. The Neoveil mesh used to house the monolayer of cells could possibly have acted as a scaffold over the course of 8 weeks allowing for the cells to spread throughout the mesh, creating a volume of extracellular material. A similar trend was noted at a higher threshold of 170. These data would suggest that the small aggregates were more active in terms of creating extracellular material but also in creating dense, possibly mineralised, material.

Previous *in vitro* studies have suggested that the large aggregates mineralised at a faster rate compared to their smaller counterparts over a short culture duration, but, whilst this is true, without an appropriate diffusion of oxygen and nutrients over a considerably longer culture duration, this accelerated mineralisation rate is rendered pointless, as indicated by the assumed disintegration of any aggregates larger than 220 µm. The smaller aggregates appeared in this case to outmanoeuvre the other test groups by remaining active and producing more material overall. In a comparative study, these data were also plotted against data acquired from rat femurs of different ages. Encouragingly, the material produced within this experiment was statistically similar in terms of specific density threshold volumes to that of 4 day old femurs.

The individual samples were also assessed in the hope of confirming the observations discussed above (fig. 4.32). When attempting to measure the inner-chamber material, i.e. the original samples only minus the additional material produced throughout the experiment, several interesting observations became apparent. The monolayer controls alone did not produce a measurable volume at a threshold of 110 and were, therefore, excluded from further analysis.

When assessing the aggregate samples, perhaps unsurprisingly, the large aggregates had a larger total volume when compared to the small aggregates. The large aggregates also initially appeared to have a higher volume of dense material; however, such considerable errors of the mean rendered any possible mean differences insignificant. This subsequently led to both aggregate samples being statistically similar in terms of dense material per unit total volume. Given the compromised integrity of the large aggregates and the difficulty associated with trying to assess individual aggregates buried within considerable extracellular material, these individual data are not considered reliable enough to provide a concrete conclusion.

In terms of eventual bone formation, the small aggregates appeared in this study to be most successful; although, the increased mineralisation rates of the large aggregates cannot be overlooked. Perhaps the ultimate solution would be to combine the attributes of both aggregate sizes; the increased mineralisation rates of the large aggregates with the diffusion capabilities and sustainability of the small aggregates. Perhaps the answer lies in vascularisation of the large aggregates.

5. Conclusion

MSC subpopulations were identified through different cellular arrangements, i.e. a monolayer arrangement, a sunflower-like arrangement and an aggregate-like arrangement, using a specific substrate, substrate X. The more organised arrangements, i.e. sunflower-like and aggregate-like arrangements, were shown to have higher E-cadherin expression levels and, therefore, a higher capacity for cell – cell interactions. Using histochemical staining, the more organised arrangements, i.e. sunflower-like and aggregate-like arrangements, were also shown to possess a higher aptitude for indicators associated with mineralisation. These data suggest that the proportions of these supposed subpopulations are donor-dependent and allow for the hypothesis that a donor with a higher proportion of sunflower-like or aggregate-like cells would correspondingly have a higher capacity for osteogenic development. Aggregation capacity was also shown to differ between donors with a correlation being noted between aggregation and E-cadherin levels which corroborates previously conducted studies suggesting that E-cadherin plays a role in aggregation.

An additional element to this study has shown that aggregate size affects the mineralised matrix content and aggregate survival, similar to that of the MLO-A5 *in vivo* outcomes (previous chapter). Therefore, it is speculated that a combination of the chief characteristics of both aggregate sizes, i.e. increased mineralisation rates with sufficient diffusion capabilities, would most effective for potential bone formation. Taken together, our data suggest that donor-dependent growth profiles correlate with specific subpopulation proportions with differing osteogenic capacities which may be the result of E-cadherin expression levels. Logic, therefore, would tell us that quantifying an individual’s subpopulation proportions may help us to assess an individual’s bone formation capacity.

Chapter Five

Promotion of Vascularisation via Co-Cultured Aggregation

Overview

The vascularisation and potential bone formation of co-cultured cellular aggregates under mechanical loading was the primary focus of this study. We proposed to investigate the influences imparted by cellular aggregation and mechanical loading on inner-aggregate cellular arrangements and potential pre-vascularisation within mesenchymal stem cell (MSC) and human umbilical vein endothelial cell (HUVEC) aggregate co-cultures. In conjunction with cellular arrangements, this study intended to ascertain what effects such culturing techniques might have on mineralisation levels and prospective bone formation. In addition, aggregate formation technique was theorised as being influential with regards to construct vascularisation and bone formation; so, cellular aggregates were developed using two aggregate formation techniques, pellet culture aggregation and suspension culture aggregation, to ascertain if this parameter has significance.

MSCs alone and MSCs co-cultured with HUVECs were aggregated and cultured under static and dynamically loaded culture conditions. Following aggregation, static culturing encompassed a standard cell culture approach, whilst hydrostatic loading was used to impart mechanical strain in a specifically designed chamber. Cellular arrangements and potential pre-vascularisation was assessed by monitoring inner-aggregate HUVEC arrangements to compare the static and loaded culture conditions, the aggregate formation techniques under both culture conditions, and the cellular composition of the aggregates from both aggregation techniques and under static and loaded culture conditions. Potential bone formation was assessed using microcomputerised tomography (microCT/µCT), again comparing the static and loaded culture conditions, and aggregate composition and formation technique under both culture conditions.

1. Introduction

Large tissue-engineered bone grafts often suffer from poor core cell viability which subsequently leads to compromised graft integration and possible graft failure[25]. Uneven cell integration, cellular necrosis and eventual graft failure are the result of an inadequate supply of oxygen and nutrients[323,347,348]. Such an inhibition to the viability of implants poses a major obstacle to the progression and translation of tissue engineering[349]. In response to this, research is currently ongoing to both refine and enhance bone tissue engineering techniques and also to vascularise the resulting tissue-engineered constructs[323,350].

Naturally, the most effective bone regeneration techniques will replicate the *in vivo* processes known to develop and regenerate bone. Therefore, numerous cell types, biomaterials, culture conditions and combinations of such, have been rigorously investigated and documented. Various cell types have been used for tissue engineering bone grafts: bone marrow aspirates, lineage-specific osteoblasts and differentiated stem cells[145,146]. When using bone marrow aspirates, bone tissue engineering has experimented with directly implanted aspirate as well as culture-expanded MSCs that were pre-differentiated prior to implantation[228]. MSCs are a logical choice for tissue engineering for a number of reasons. Chiefly, they have multipotent capabilities allowing them to differentiate into numerous cell types, e.g. bone, muscle, fat and others[480], they can be easily isolated via plastic adherence from a number of different sources, such as umbilical cord blood, liver and amniotic fluid, adipose tissue and bone marrow[156,359], they can be separated and expanded whilst also maintaining a good level of stemness[224,480], they have a stable phenotype in culture[156] and exhibit low immunogenic characteristics which could allow for possible allergenic use[146,481]. The potential for MSCs to enhance bone fracture healing has been demonstrated in numerous preclinical animal models[183,185,186,266] and clinical trials[146], and are also known to encouragingly influence cohabiting cells derived from other tissues, such as skin, muscle, endothelial and renal epithelial layers[175].

As previously mentioned, the vascularisation of bone tissue-engineered constructs becomes increasingly important if large grafts are required for substantial bone defects or injuries. For this reason, exploration into tissue vascularisation, and bone tissue vascularisation in particular, is being carried out with some very interesting theories and hypotheses being investigated.

The co-culturing of cells is one method being explored for the vascularisation of tissue-engineered constructs. Endothelial cells (EC) for example, are being co-cultured with various other cell types in an attempt to achieve *in vitro* pre-vascularisation within scaffold constructs[351–354]. MSCs and ECs would appear to be a sensible combination for co-cultured constructs with the interactions between both cell types being a highly regulated process. Paying close attention to, and mimicking where possible, the *in vivo* bone vascularisation processes is as important as ever when co-culturing. It is thought that the most successful microvasculature formation to date was achieved with the delayed addition of MSCs to ECs encapsulated in collagen[355]. Such an experimental procedure was carried out because this arrangement was thought to better mimic the natural *in vivo* environment where MSCs are only recruited to the site of vascularisation after ECs have begun vascular construction[355].

Three-dimensional (3D) microenvironments offer an ideal environment for improved cell – cell communication enhancing cell – cell signalling, proliferation, differentiation and survival. Because of this, attempts have been made previously to use such constructs for the study of vascularisation. Taking advantage of such effects, a previous study seeded MSC aggregates onto porous polyurethane scaffolds and when compared with non-seeded scaffolds and scaffolds seeded with individual MSCs, an improved vascularisation and micro-vessel functionality was noted within the aggregate-seeded scaffolds[482]. In another series of *in vitro* and *in vivo* experiments, MSC aggregates were noted to have heightened cell survival and subsequent vascularisation. The aggregates, produced by a hanging-drop method, were compared to an MSC monolayer. Improved cell viability, amplified micro-vessel formation and lessened necrosis and limb loss in ischemic mice were noted[483]. Whilst the aggregate culturing in that study may have augmented paracrine signalling and function in the cells, it was also noted that the aggregate structure itself may have helped to prolong the length of time the MSCs were present at the graft site through entrapment.

Implanting MSCs in aggregate form would appear to enhance the stimulation of angiogenesis and neovascularisation with such a technique seemingly working well for implants of a smaller size or when used as a supportive role for osteogenesis. However, unmodified MSCs alone may not be sufficient for supporting vascularisation in large grafts[349]. Additional environmental conditions may help to further enhance the positive results seen thus far.

The use of bioreactors may offer the environmental conditions required to enhance both the mineralisation of bone tissue-engineered constructs and also the vascularisation of such. Numerous studies have shown that bioreactors could provide the necessary growth environments for advanced tissue engineering and may also allow for the investigation of physical forces on cells and cell/scaffold constructs[285]. Under physiological conditions, loading placed on the bone through compression and/or tension via movement drives interstitial fluid flow through the lacunae of the bone resulting in the application of fluid sheer stresses[257]. This creates hydrostatic and dynamic shear forces detectable by the cells[258–261]. Such mechanical stimuli are known to influence embryonic bone formation[262,263] as well as post-embryonic bone regeneration[265]. Therefore, replicating such physiological conditions should enhance or encourage bone tissue engineering and/or the vascularisation of such grafts. Given that dynamic culturing has been demonstrated to improve cell survival and mineralisation in both *in vitro* and *in vivo* studies[266,267], numerous different types of bioreactors have been developed for bone tissue engineering, including perfusion bioreactors[271–273], magnetic bioreactors[274] and spinner flasks[275], all with positive results. Bone formation and vascularisation is also well documented under such dynamic conditions[277–283] and it is, therefore, proposed that the mechanical stimulation of a co-culture system will encourage both osteogenic[484,485] and endothelial[486] differentiation for more healthy bone and vasculature.

A hydrostatic bioreactor was used in this particular study because numerous previous studies have shown that hydrostatic loading is an important mechanical stimulus influencing the direction of cell fate in various tissues, such as the intervertebral disc, the vascular system, articular cartilage and bone[276,284,285]. The use of a hydrostatic bioreactor is interesting because the application of hydrostatic loading to a tissue-engineered construct is thought to not only provide physical forces but to also increase the transfer of small molecules, such as O_2 and CO_2, into the tissue matrix[286]. When using hydrostatic loading to pressurise a closed chamber containing a gas-liquid interface, as is the case with the bioreactor used in this study, the solubility of O_2 and CO_2 is increased resulting in higher concentrations of dissolved gases in the medium[284,287]. pH levels and dissolved O_2 concentrations have been shown in numerous studies to influence cellular mechanisms, such as inter-cellular signalling, cell proliferation and differentiation[288,289], as well as the cell cycle, apoptosis and protein synthesis[290–295]. Culturing osteoblasts *in vitro* under hyperbaric oxygen conditions has been shown to not only boost cell proliferation and differentiation but also to improve alkaline phosphatase (ALP) activity and collagen type I (COL 1) production leading to enhanced osteogenesis[296]. The use of such a bioreactor was, therefore, hoped to improve both mineralisation and vascularisation of the cellular aggregates studied here.

With the advantages of 3D microenvironments being discussed in previous chapters, we decided to explore the vascularisation of such for large graft construction. The combination of cellular aggregation, cellular co-culturing and hydrostatic loading is thought to best represent the bone formation and regeneration processes observed *in vivo* and, thus, offers the best opportunity to study such process *in vitro* with the hope of creating viable large bone tissue-engineered grafts for possible implantation.

2. Materials and Methods

This co-culture experiment was carried out on a total of six separate occasions with a minimum of three samples per variable each time. The parameters assessed in this chapter are outlined below in fig. 5.1. On all six occasions, aggregates containing MSCs alone were compared to MSC/HUVEC co-cultured aggregates under both loaded and static culture conditions. On three of the six occasions, the aggregation technique was also evaluated.

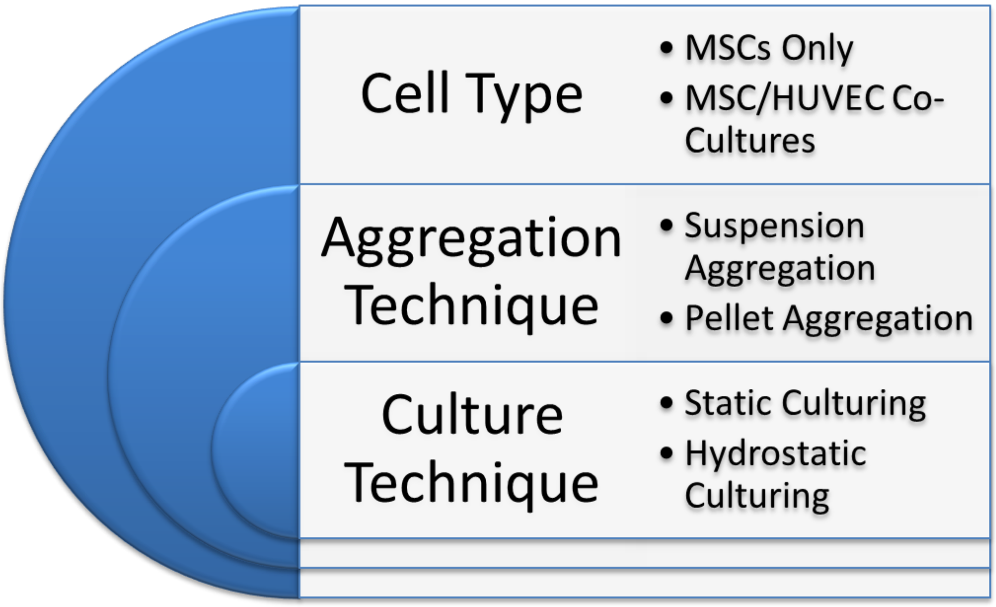

Figure 5.1: A basic overview of the parameters investigated throughout the vascularisation chapter.

2.1 Cell culturing

There are two cell types used in this chapter: MSCs and HUVECs.

2.1.1 Mesenchymal stem cells

MSCs were isolated from MNCs and cultured following the protocols outlined in chapter 2, section 1.2. The proliferative medium used during MSC culturing is also described in the same section. The MSCs were cultured to passage three and used for the experiments described in this chapter at passage four.

2.1.2 Human umbilical vein endothelial cells

One vial of HUVECs was acquired from a commercial source and cultured as described in chapter 2, section 1.3. The specific HUVEC medium used for culturing is also described in the same section. HUVECs were cultured to passage three and used for the experiments illustrated in this chapter at passage four.

2.2 Cell tracking

Cell tracking was carried out in four separate experiments. On all four occasions, the HUVECs were tracked with a FITC-conjugated dye. On one occasion, the MSCs were also tracked, but with a TRITC-conjugated dye. Continued tracking of the MSCs in further experiments was not attempted because it was deemed unnecessary and unfruitful. The addition and use of cell tracking membrane dyes is described in full in chapter 2, section 3.

2.3 Cell aggregation

The ratio of MSCs to HUVECs (90 – 95% MSCs and 5 – 10% HUVECS) was chosen because Rouwkema and colleagues had previously demonstrated that a HUVEC proportion as low as 5% of the total cell number was capable of forming tube-like structures resembling vascularisation within the main aggregate body[323]. When a HUVEC proportion of more than 10% was used, structures appeared less elongated and more HUVECs could be seen in clumps rather than vessel-like structures. The HUVEC proportion was decreased from 10% to 5% when 10% was deemed unnecessary.

2.3.1 Aggregate formation

The F127-coated suspension culture method for aggregate formation is described in full in chapter 2, section 4.1.1. The pellet culture method for aggregate formation is described in full in chapter 2, section 4.1.2. Both aggregation techniques used 1 x 10^5 cells/aggregate. Aggregates were made up of 100% MSCs or a co-culture of 90 – 95% MSCs and 5 – 10% HUVECs. Regardless of aggregation technique, the MSC only aggregates were formed using MSC proliferative/basal medium (chapter 2, section 1.2) and the MSC/HUVEC aggregates were formed using MSC proliferative/basal medium (chapter 2, section 1.2) and HUVEC basal medium (chapter 2, section 1.3) at a ratio of 1:1 (adapted from Saleh *et al.*[487]). All aggregates were formed undisturbed for 48 hours prior to use in any experiments. After 48 hours, the aggregates were encapsulated in collagen hydrogel before any further experiments were carried out. If any of the cells were fluorescently tagged, they were protected from light throughout the aggregation process.

2.3.2 Aggregate measurements

The dimensions of the aggregates, i.e. size and aspect ratio, were determined from a minimum of three samples per variable from one MSC population using the protocols described in chapter 2, section 10.

2.4 Collagen encapsulation

Collagen encapsulation was used to house the aggregates during the hydrostatic loading and static culturing phase of the experiments. Post-aggregation, the individual aggregates were placed into individual wells of a standard 24-well tissue culture polystyrene (TCP) plate. The aggregates were centred within the wells and any remaining media was removed immediately prior to encapsulation. The collagen gel was then formed with a concentration of 3 mg/ml using the protocol outlined in chapter 2, section 6. One ml collagen gel was added to each well. The gel/aggregate constructs were then placed into an incubator (37 °C and 5% CO_2) for 24 hours.

2.5 Further aggregate culturing

The next phase of the experiment involved two different culture environments: static and loaded. Culture duration (7 – 10 days) was adapted from Rouwkema *et al.*[401]. The culture duration was increased from 7 days to 10 days with all samples having been cultured for 7 or 10 days.

2.5.1 Static culturing

The gel/aggregate constructs intended for static culturing were kept in an incubator at 37 °C and 5% CO_2 for the remainder of the experiment (7 – 10 days).

2.5.2 Hydrostatic loading

The gel/aggregate constructs intended for hydrostatic loading were kept in the same incubator as their statically cultured counterparts. After the initial 24 hour period immediately following collagen encapsulation, the loaded samples were subjected to their first loading session. This was carried out using the protocol described in chapter 2, section 7. For 1 hour/day, these samples were hydrostatically loaded over the following 7 – 10 days.

2.6 Aggregate termination

After 7 – 10 days of loaded or static culturing, the aggregate samples were terminated. Those samples intended for microCT scanning were fixed with formalin for 1 hour; after such time, the formalin was removed and the samples covered with 1 ml phosphate buffered saline (PBS) to prevent them from drying out. Those samples intended for whole aggregate immunohistochemical staining were fixed with 4% paraformaldehyde (PFA) for 1 hour; after which, the fixative was removed and the samples stored in 1 ml PBS. Those samples intended for cryosectioning and immunohistochemical staining were not fixed until after they were sectioned. This meant that those samples intended for section staining were cryosectioned on the day of termination.

2.7 Imaging

2.7.1 Light microscopy

Optical imaging for the monitoring of aggregate size, colour intensity and cellular outgrowth was carried out on a minimum of three samples per variable using the protocols and equipment outlined in chapter 2, section 9.1. Pre-collagen encapsulation, imaging was carried out on the MSC only and MSC/HUVEC co-cultured suspension aggregates after 8 and 48 hours post-suspension culture seeding to monitor aggregate formation. Post-collagen encapsulation, imaging took place every 3 – 4 days to monitor cellular outgrowth from pellet and suspension aggregates under static and loaded culture condition. Over imaging of the samples was avoided so as to prevent photo bleaching of the fluorescently tagged cells.

2.7.2 Epifluorescent imaging

Epifluorescent imaging for cellular tracking and arrangement monitoring was carried out using the protocols described in chapter 2, section 9.2. Epifluorescent imaging was carried out immediately post-collagen encapsulation and again after 3 and 7 days of loaded and/or static culturing. Again, over imaging of the samples was avoided.

2.7.3 Confocal imaging

Confocal z-stacking was intended to monitor inner-aggregate cellular arrangement through the imaging of membrane dye-tagged cells. Confocal z-stacking was carried out using the protocols described in chapter 2, section 9.3. Z-stack imaging was carried out every 24 hours post-collagen encapsulation and immediately prior to each loading session.

2.8 Microcomputerised tomography

MicroCT was carried out in one experiment using a minimum of three samples per variable from one MSC population. It was used to quantify aggregate volume (mm^3) and volume of dense material normalised to total aggregate volume. MicroCT scanning was carried out on the individual aggregates following the termination of each experiment using the protocol outlined in chapter 2, section 15.1.2. To allow for volume measurements to be acquired without interference from background collagen, the aggregated samples were carefully removed from their encapsulating collagen with a scalpel prior to scanning. The aggregates were placed in a polystyrene holder, as described in chapter 2, section 15.1.2, immediately prior to scanning and were scanned as individual aggregates. The microCT scans were then evaluated using thresholds of 110 and 130. These thresholds were chosen because 110 would ensure that no background collagen could distort the results and 130 was the highest threshold where volume measurements were still obtainable from each sample tested.

2.9 Cryosectioning

Given the 3D nature of the aggregates, they were cryosectioned into 8 µm thick slices to allow for staining. Staining was intended to highlight the inner-aggregate structure and cellular arrangement. Cryosectioning was carried out on three separate occasions with a minimum of two samples per variable using the protocols outlined in chapter 2, section 8.3. Initially, the surrounding collagen gel was removed from around the aggregates prior to sectioning but this was later thought to hinder or lessen the obtainable data. Further samples retained enough of their surrounding collagen gel so as to house any cellular outgrowth. Because these samples were not fixed prior to sectioning, they were snap-frozen in liquid nitrogen immediately prior to cryosectioning.

2.10 Immunostaining

CD31 staining was used to identify the presence and spatial distribution of HUVECs located in and/or possibly around the aggregates. CD31 staining was carried out using the protocol described in chapter 2, section 13.1. Staining was conducted on two separate experiments using both whole aggregates and aggregate sections. Whole aggregates and aggregate sections were stained using this same protocol.

2.11 Statistical analysis

For aggregate measurements and microCT analysis, sample groups acquired from one experiment using single populations of MSCs and HUVECs were compared using independent t-tests and f-tests. A p-value below 0.05 was taken to indicate statistical significance. Graphically, statistical significance is indicated at four levels: * $p \leq 0.05$, ** $p \leq 0.01$, *** $p \leq 0.001$ and **** $p \leq 0.0001$.

3. Results

3.1 Aggregate formation

Both aggregation techniques formed aggregates of different sizes and shapes despite both techniques using the same cell numbers. Optical imaging has shown aggregate formation within the F127-coated suspension cultures over a period of 48 hours (fig. 5.2). After 8 hours in culture, multiple small aggregates were formed which subsequently joined together forming one large aggregate in each well. The shape of the final aggregates would lead one to believe that the multiple structures of the initial small aggregates were still present in the final aggregate form in many cases (fig. 5.2).

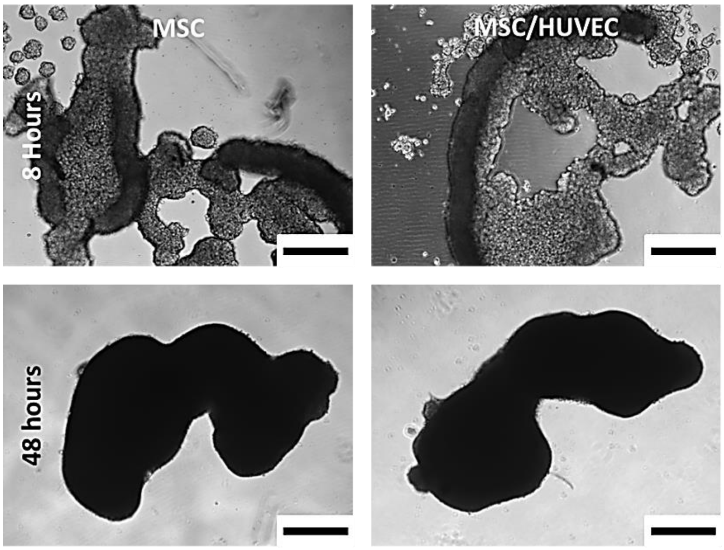

Figure 5.2: Suspension culture aggregate formation. Optical images showing aggregates forming on a 1% F127-coated suspension culture after 8 hours and 48 hours in culture. The aggregates on the left contain MSCs only, whilst the aggregates on the right contain a co-culture of 97.5% MSCs and 2.5% HUVECs. Scale bar represents 400 µm.

Fig. 5.3 shows the average (mean ± standard error or the mean) size of the aggregates immediately post-collagen encapsulation. The average (mean ± standard error of the mean) suspension culture aggregate was 885 µm and the average (mean ± standard error of the mean) pellet culture aggregate was 497 µm (t-test, p = 0.0133).

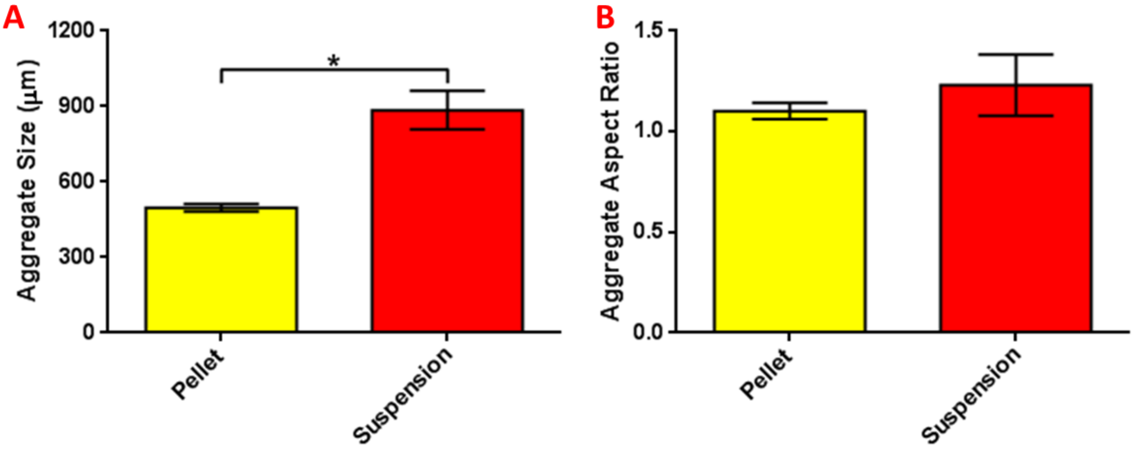

Figure 5.3: Aggregate measurements comparing both aggregation techniques. Shown is the average (mean) aggregate size (**A**) and aspect ratio (**B**) of the samples formed from both aggregation techniques immediately post-collagen encapsulation. Error bar represents standard error of the mean. * signifies $p < 0.05$.

The formation of the pellet culture aggregates was not imaged over the initial 48 hour culture period due to the difficulty of imaging within a centrifuge tube. Fig. 5.3 shows the average (mean ± standard error of the mean) aspect ratio of the aggregates immediately post-collagen encapsulation. The suspension culture aggregates had an average (mean ± standard error of the mean) aspect ratio of 1.23 and the pellet culture aggregates had an average (mean ± standard error of the mean) aspect ratio of 1.102).

Considerable cellular outgrowth was also visible from the optical images. Such outgrowth could be seen from the static samples from the early stages of the experiment with a smaller amount of outgrowth being witnessed from the loaded samples (fig. 5.4 and 5.5). Measurements would suggest that the average (mean ± standard error of the mean) cellular outgrowth experienced by the aggregates under loaded conditions was approximately 10% of the original aggregate size regardless of the aggregation technique used to initially develop the aggregates. Whilst the average (mean ± standard error of the mean) cellular outgrowth experienced by the aggregates under static conditions was difficult to accurately measure, it was thought to exceed 40% of the original aggregate size (data not shown).

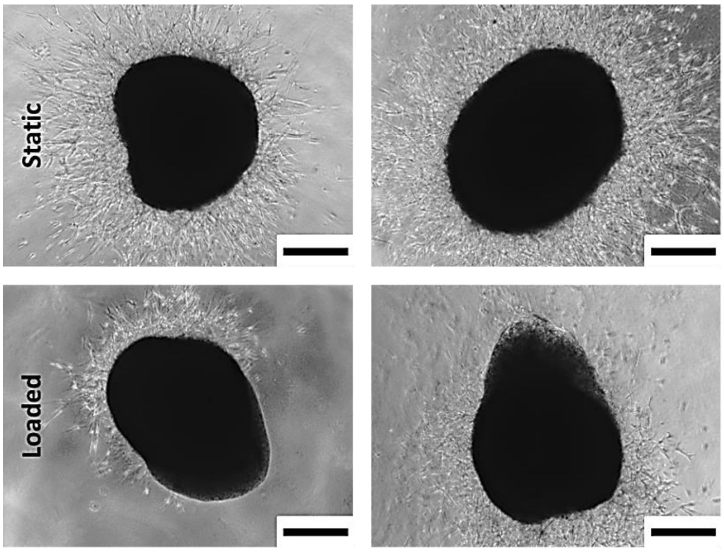

Figure 5.4: Suspension culture aggregates following 4 days of culturing. Optical images of aggregates following 4 days of culturing in collagen gel. The aggregates were formed in a 1% F127-coated suspension culture plate and contained a co-culture of 90% MSCs and 10% HUVECs. Scale bar represents 400 µm.

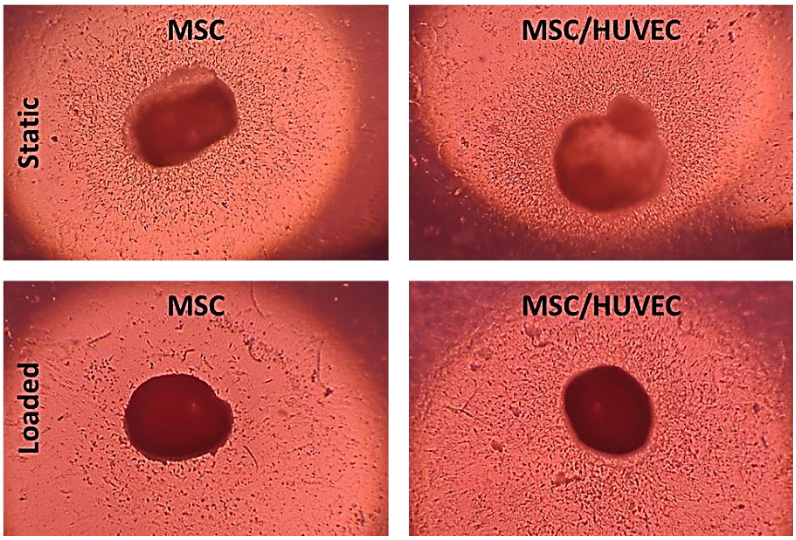

Figure 5.5: Pellet culture aggregates following 10 days of culturing. Optical images of MSC and MSC/HUVEC co-cultured aggregates following 10 days of culturing in collagen gel. The aggregates were formed from a pellet culture. This figure shows aggregates after both static (top) and loaded (bottom) culturing. The aggregates on the left contain MSCs only, whilst the aggregates on the right contain a co-culture of 95% MSCs and 5% HUVECs.

3.2 Cell tracking

HUVEC arrangement, as monitored by the cell tracking dye, was difficult to evaluate via epifluorescent imaging given the 3D nature of the aggregates (fig. 5.6 and 5.7). That is to say, any particular cellular arrangement, tubular or otherwise, could not be accurately identified. Confocal z-stacking has given an insight into the cellular arrangement taking place within the whole aggregate samples that epifluorescent imaging could not (fig. 5.8, 5.9, 5.10, 5.11 and 5.12).

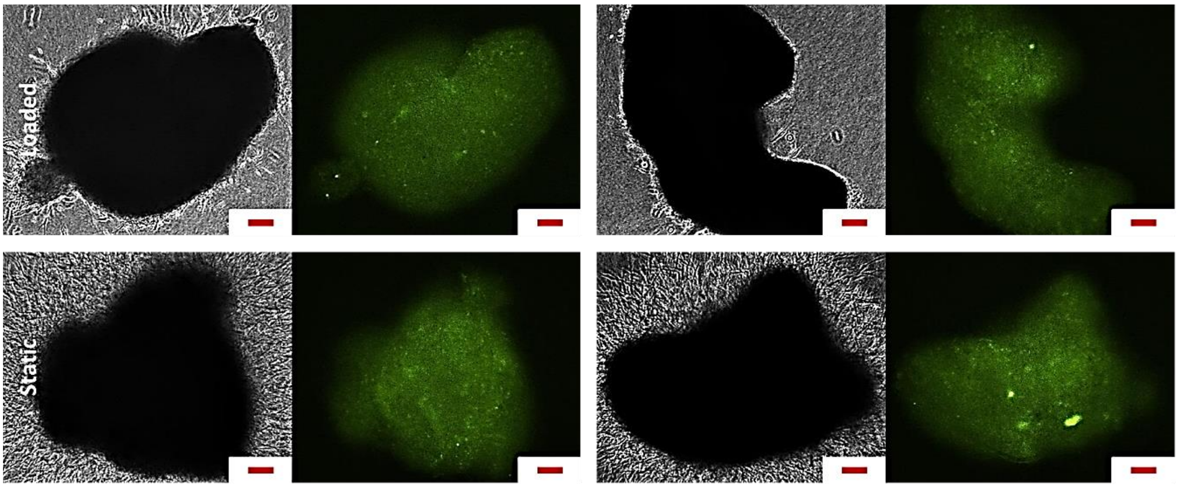

Figure 5.6: Epifluorescent images of fluorescently-tagged HUVECs in MSC/HUVEC co-cultured suspension aggregates. Brightfield and corresponding epifluorescent images of aggregates following 3 days of static and loaded culturing. The aggregates were formed via suspension aggregation and contained a co-culture of 95% MSCs and 5% HUVECs. The fluorescence is emitted by the fluorescently-tagged HUVECs. The MSCs were not fluorescently-tagged. Scale bar represents 100 µm.

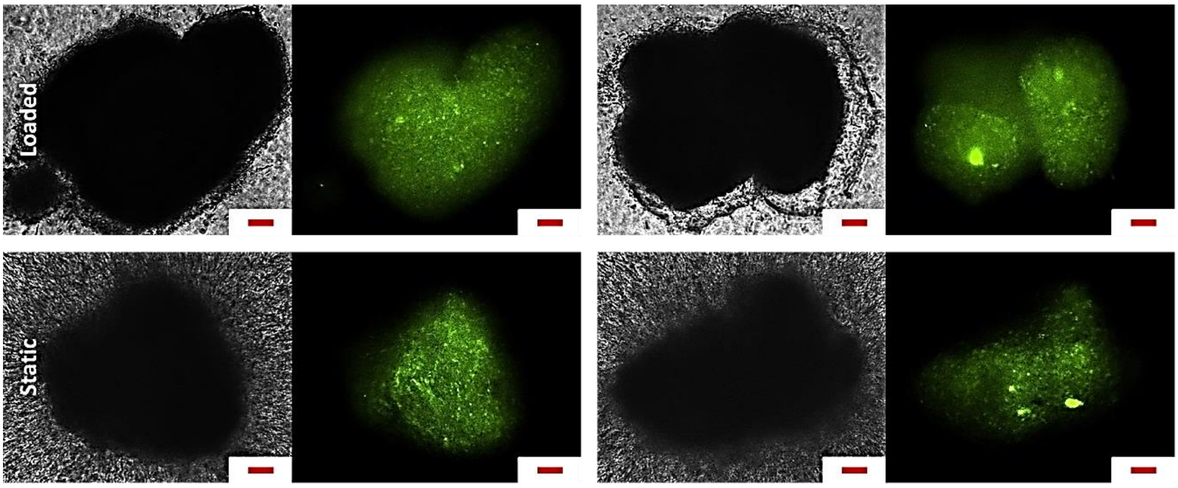

Figure 5.7: Epifluorescent images of fluorescently tagged HUVECs in MSC/HUVEC co-cultured suspension aggregates. Brightfield and corresponding epifluorescent images of aggregates following 7 days of static and loaded culturing. The aggregates were formed via suspension aggregation and contained a co-culture of 95% MSCs and 5% HUVECs. The fluorescence is emitted by the fluorescently-tagged HUVECs. The MSCs were not fluorescently-tagged. Scale bar represents 100 µm.

Confocal z-stacks of HUVECs in both suspension culture and pellet culture aggregates taken immediately post-collagen encapsulation have shown that HUVEC arrangement within the suspension culture aggregates appeared to be arranged to the peripheries of the multiple small aggregates making up the final aggregate form. The HUVECs present in the pellet culture aggregates are thought to be more uniformly distributed throughout the aggregate bodies (fig. 5.8).

Suspension Culture Aggregates

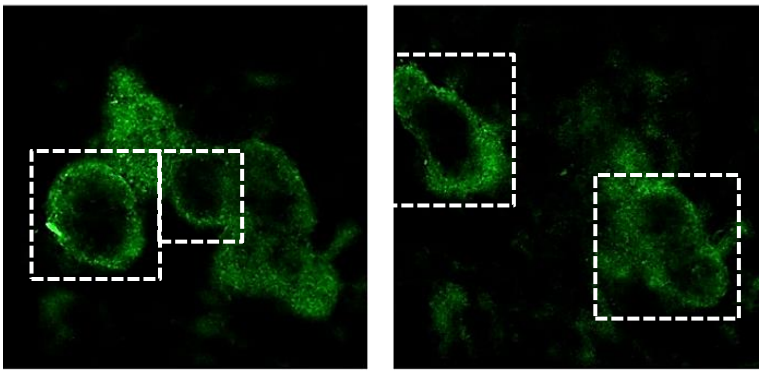

Pellet Culture Aggregates

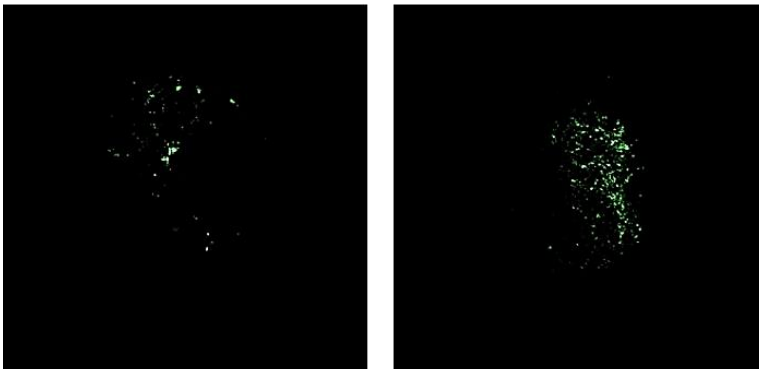

Figure 5.8: Confocal images of fluorescently-tagged HUVECs in MSC/HUVEC co-cultured aggregates. Images were taken immediately following collagen encapsulation (pre-loading). The aggregates were formed using 95% MSCs and 5% HUVECs with both suspension culture and pellet culture techniques. The MSCs were not fluorescently-tagged. White boxes highlight areas of compartmentalisation within the suspension culture aggregates.

As culturing continued, increased HUVEC arrangement was noted in both aggregate types, suspension culture and pellet culture alike; however, more so within the samples cultured under hydrostatic loading (fig. 5.9, 5.10, 5.11 and 5.12).

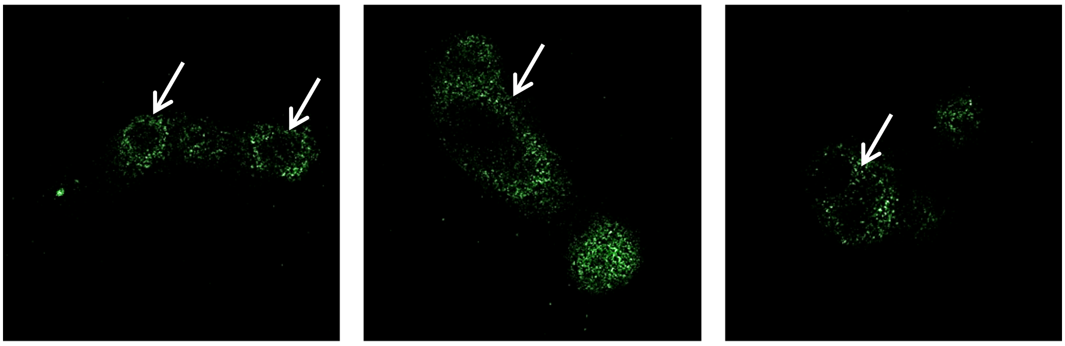

Suspension Culture Aggregates

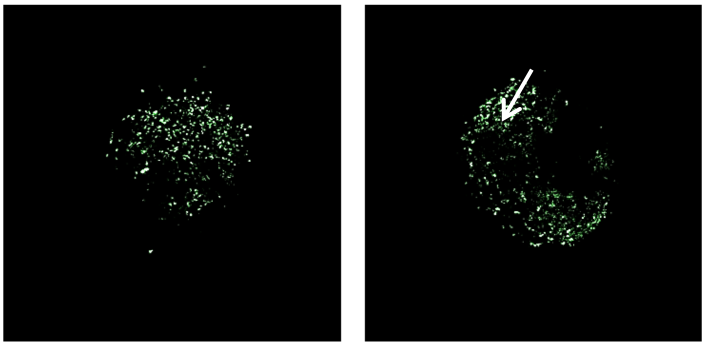

Pellet Culture Aggregates

Figure 5.9: Confocal images of fluorescently-tagged HUVECs in MSC/HUVEC co-cultured aggregates. Images were taken following 3 days of hydrostatic loading. The aggregates were formed using 95% MSCs and 5% HUVECs with both suspension culture and pellet culture techniques. The MSCs were not fluorescently-tagged. White arrows indicate areas of tubular cellular arrangements.

Suspension Culture Aggregates

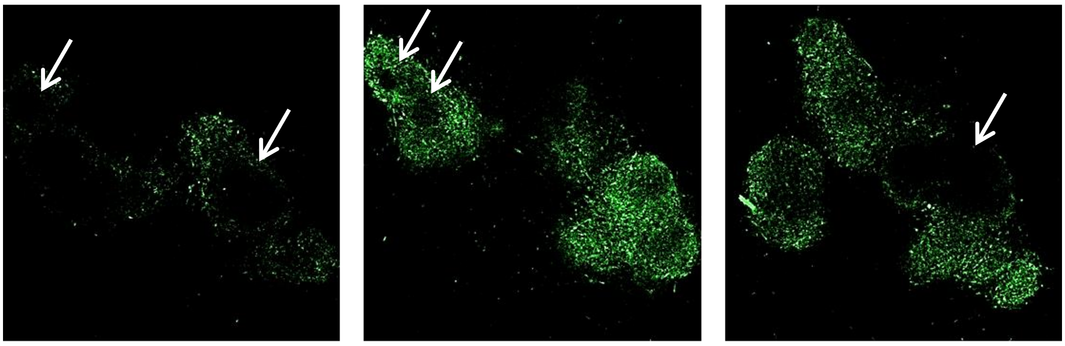

Pellet Culture Aggregates

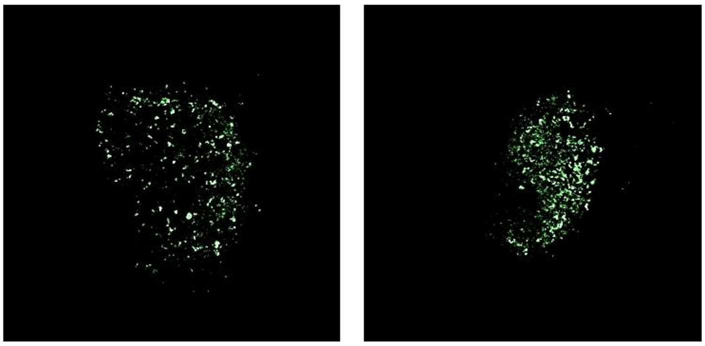

Figure 5.10: Confocal images of fluorescently-tagged HUVECs in MSC/HUVEC co-cultured aggregates. Images were taken following 3 days of static culturing. The aggregates were formed using 95% MSCs and 5% HUVECs with both suspension culture and pellet culture techniques. The MSCs were not fluorescently-tagged. White arrows indicate areas of tubular cellular arrangements.

After 7 days of culturing under loaded and static conditions, obvious differences were noted between the loaded and static samples (fig. 5.11). The loaded samples had significantly more tubular HUVEC arrangements when compared to the static samples. After 10 days of culturing, the samples undergoing loading were still showing increased HUVEC arrangement when compared to statically cultured samples for both aggregate formation techniques (fig. 5.12). The loaded suspension culture aggregates have shown the most obvious cellular arrangements followed closely by the loaded pellet culture aggregates.

The static suspension culture aggregates were also showing slightly more cellular arrangement when compared to the static pellet culture aggregates, which were showing no arrangement at all (fig. 5.12). That is to say, the loaded suspension culture aggregates were showing the most HUVEC arrangement, followed by the loaded pellet culture aggregates, the static suspension culture aggregates and finally the static pellet culture aggregates.

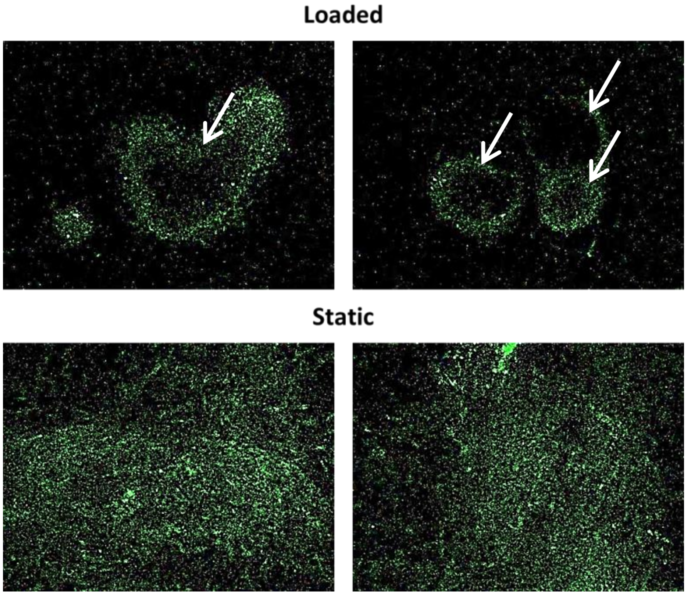

Figure 5.11: Confocal images of fluorescently-tagged HUVECs in MSC/HUVEC co-cultured aggregates. Images were taken following 7 days under loaded and static culture conditions. The aggregates were formed via suspension aggregation using 95% MSCs and 5% HUVECs. The MSCs were not fluorescently-tagged. White arrows indicate areas of tubular cellular arrangements.

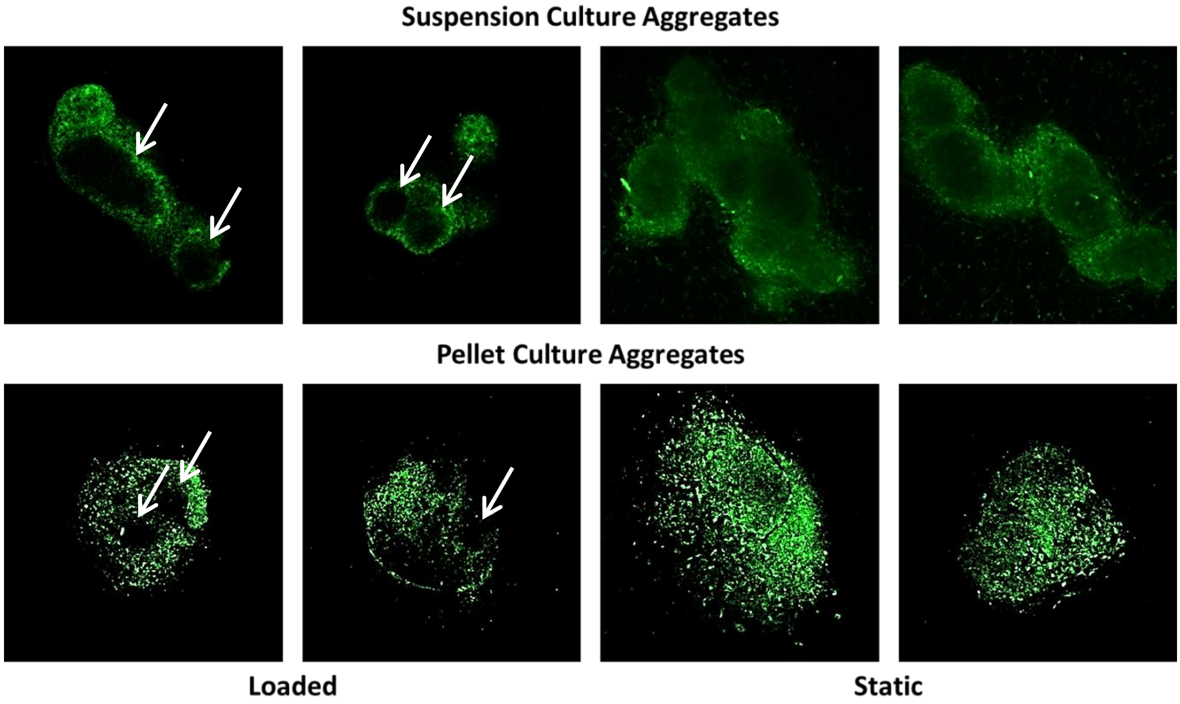

Figure 5.12: Confocal images of fluorescently-tagged HUVECs in MSC/HUVEC co-cultured aggregates. Images were taken following 10 days of loaded and static culturing. The aggregates were formed via both suspension and pellet aggregation techniques using 95% MSCs and 5% HUVECs. The MSCs were not fluorescently-tagged. White arrows indicate areas of tubular cellular arrangements.

3.3 Immunostaining

CD31 staining of aggregate sections corroborated previously conducted HUVEC tracking and confocal imaging. The loaded samples appeared to better maintain their initial spheroidal shape over the duration of the study, more so in the pellet culture aggregates. The static samples experienced sizeable cellular outgrowth and altered aggregate size and shape as a result (fig. 5.13). Particular HUVEC arrangements appear far more distinct also. The HUVECs would appear to be most organised in the loaded samples.

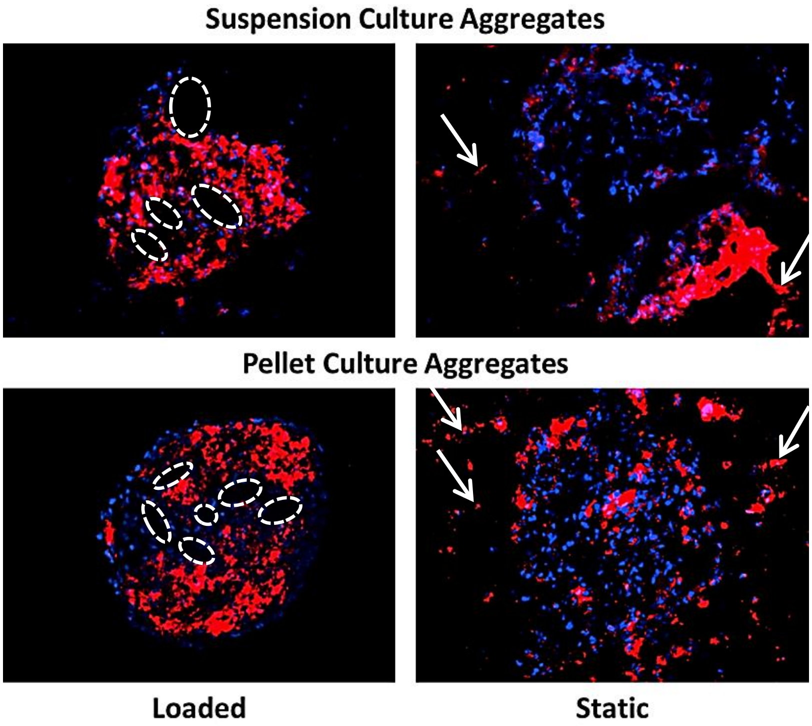

Figure 5.13: Epifluorescent images of CD31-stained MSC/HUVEC co-cultured aggregate sections. Images were taken following 7 days under loaded and static culture conditions. The aggregates were formed via both suspension and pellet aggregation techniques using 95% MSCs and 5% HUVECs. The aggregate sections were stained for CD31 and Dapi. White dotted lines highlight possible tubular structures and white arrows highlight cellular outgrowth from the aggregate body.

3.4 Aggregate density and material volume

Aggregate density and volume were evaluated using microCT scanning after 10 days of culturing for the assessment of mineralisation (fig. 5.14). Three variables were compared for aggregate volume, dense material volume and volume of dense material normalised to total aggregate volume: suspension culture aggregation versus pellet culture aggregation (fig. 5.15), loaded versus static culturing conditions (fig. 5.16) and MSC aggregates versus MSC/HUVEC co-cultured aggregates (fig. 5.17).

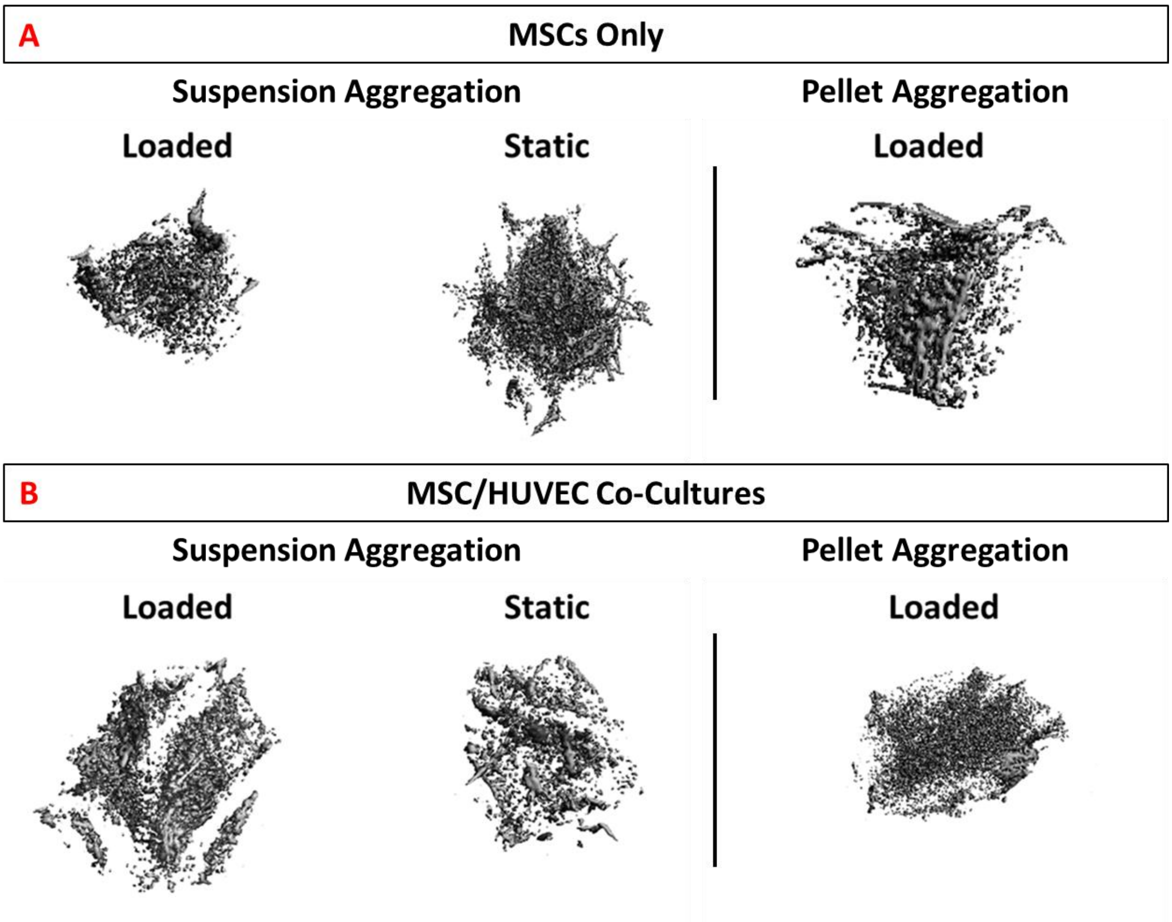

Figure 5.14: MicroCT scan images showing suspension and pellet culture aggregates. Samples were produced from MSCs only (**A**) and MSC/HUVEC co-cultures (**B**). The suspension aggregate samples of MSCs only and MSC/HUVEC co-cultures are shown under loaded and static culture conditions, whilst the pellet aggregate samples of MSCs only and MSC/HUVEC co-cultures are shown under loaded culture conditions only.

3.4.1 Suspension culture aggregation versus pellet culture aggregation

When evaluating the aggregate formation techniques, both culture aggregates had similar material volumes at a threshold of 110, 0.03 mm^3 and 0.03 mm^3 for the pellet and suspension cultures, respectively. At a threshold of 130, the suspension culture aggregates and pellet culture aggregates had dense material volumes of 0.002 mm^3 and 0.001 mm^3, respectively (fig. 5.15). Taking these values into account, it was possible to compare the volume of dense material normalised to total aggregate volume. The suspension culture aggregates and their pellet culture counterparts had normalised dense material volumes of 0.071 mm^3 and 0.047 mm^3, respectively (fig. 5.15).

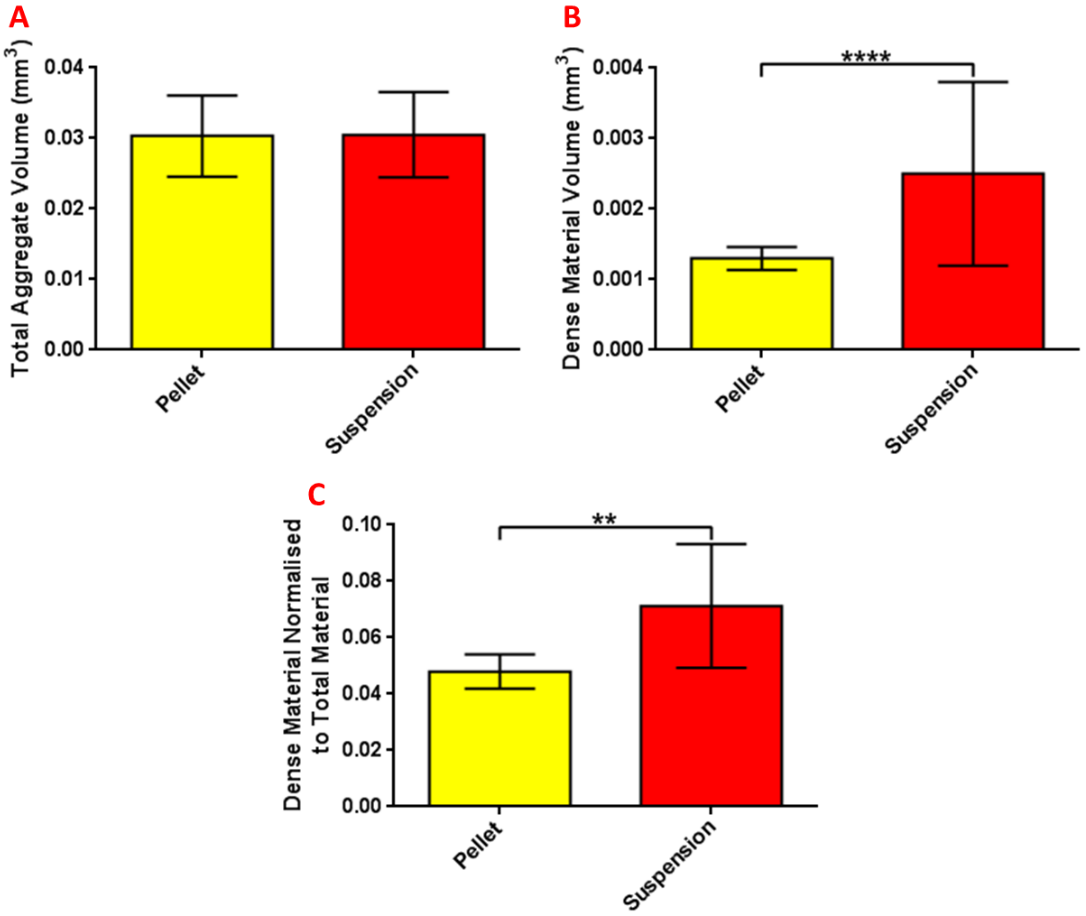

Figure 5.15: MicroCT data comparing aggregate volume measurements. The average (mean) volumes of aggregates formed using suspension and pellet culture techniques at thresholds of 110 (**A**) and 130 (**B**). Also shown is the volume of dense material normalised to total sample volume (**C**). Data was collected using aggregates formed from MSCs only and MSC/HUVEC co-cultures (95% MSCs and 5% HUVECs) and cultured under loaded and static conditions. Error bar represents standard error of the mean. ** signifies $p < 0.01$ and **** signifies $p < 0.0001$.

3.4.2 Loaded versus static culture conditions

At a threshold of 110, the loaded and statically-cultured samples had material volumes of 0.031 mm^3 and 0.028 mm^3, respectively (fig. 5.16). At a threshold of 130, the loaded and statically-cultured samples had dense material volumes of 0.002 and 0.001 mm^3, respectively (fig. 5.16).

The volume of dense material normalised to total aggregate volume values were 0.07 and 0.04 mm³ for the loaded and statically-cultured samples, respectively (fig. 5.16).

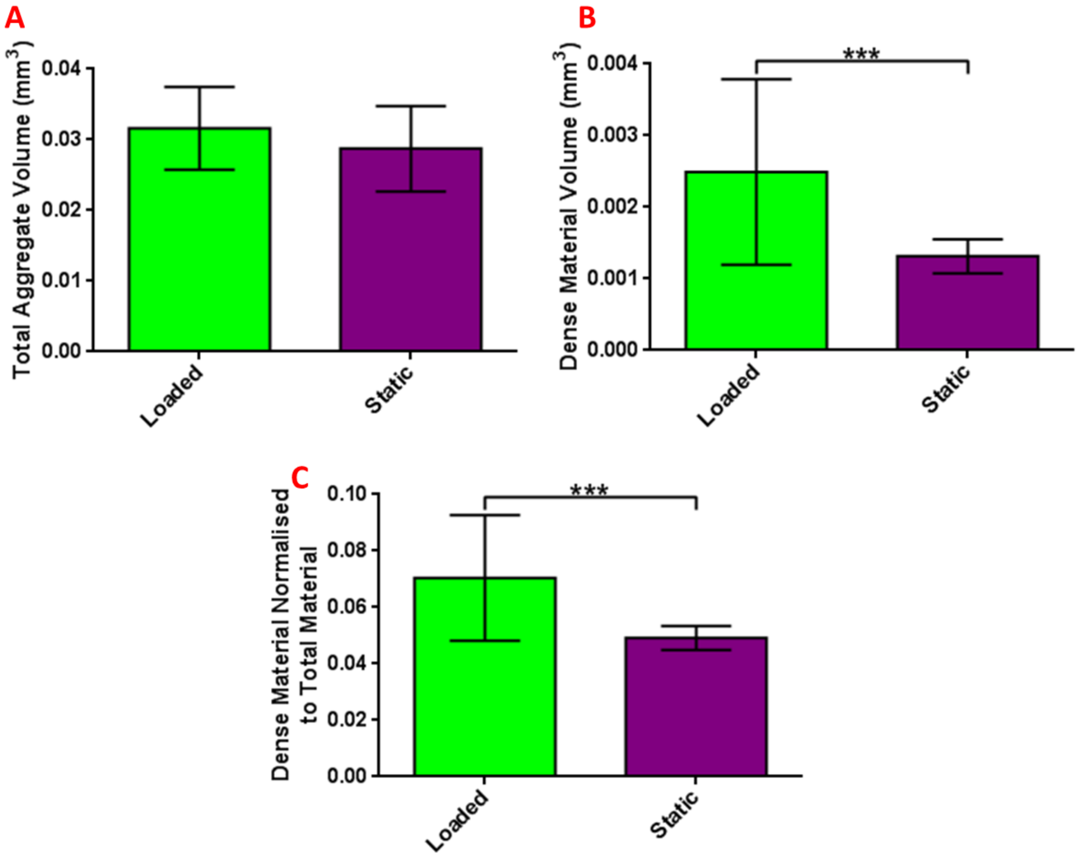

Figure 5.16: MicroCT data comparing aggregate volume measurements. The average (mean) sample volumes cultured under loaded and static conditions at thresholds of 110 (**A**) and 130 (**B**). Also shown is the dense material volume normalised to total sample volume (**C**). Data was collected using aggregates formed from MSCs only and MSC/HUVEC co-cultures in suspension and pellet aggregation cultures. Error bar represents standard error of the mean. *** signifies $p < 0.001$.

3.4.3 Mesenchymal stem cell only aggregates versus co-cultured aggregates

At a threshold of 110, the MSC only aggregates and MSC/HUVEC co-cultured aggregates had material volumes of 0.025 mm³ and 0.034 mm³, respectively (fig. 5.17). When comparing the volume of dense material at a threshold of 130, the MSC only aggregates had a volume of 0.002 mm³ compared to a volume of 0.001 mm³ for the MSC/HUVEC co-cultured aggregates (fig. 5.17).

When normalised to total aggregate volume, the volume of dense material then read 0.079 mm^3 and 0.045 mm^3 for the MSC only controls and the MSC/HUVEC co-cultures, respectively (fig. 5.17).

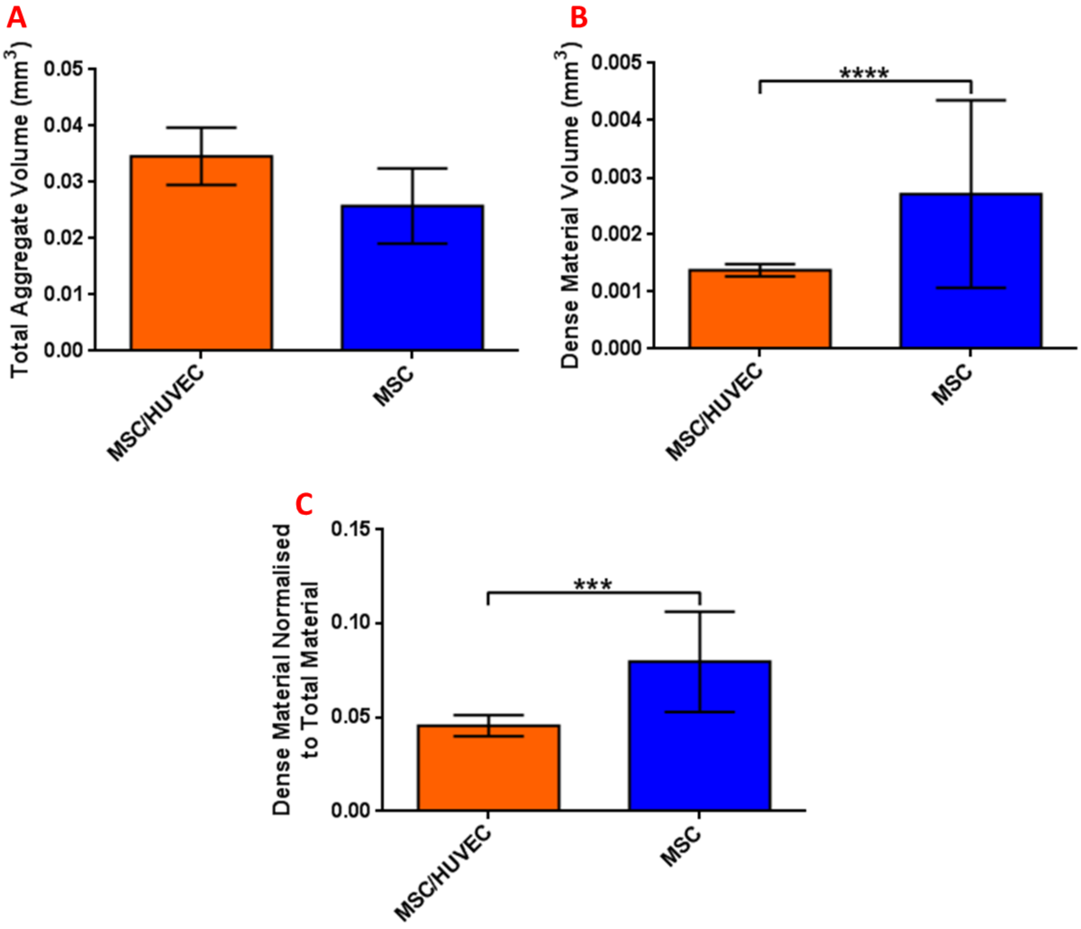

Figure 5.17: MicroCT data comparing aggregate volume measurements. The volumes of MSC only and MSC/HUVEC co-cultured aggregates at thresholds of 110 (**A**) and 130 (**B**). Also shown is the volume of dense material normalised to total sample volume (**C**). Data was collected using suspension and pellet culture aggregates cultured under loaded and static conditions. Error bar represents standard error of the mean. *** signifies $p < 0.001$ and **** signifies $p < 0.0001$.

3.4.4 In vitro aggregates versus rat femur models

The normalised volumes of dense material for each of the aggregate variables were compared to one another and also to rat femurs of various ages (fig. 5.18). Three variables stood out as being most influential in terms of dense material accumulation: aggregates composed of MSCs only, formed on a suspension culture substrate and cultured under loaded conditions. Whilst none of the upper three variables differed from one another and none of the lower three variables differed from one another, both groups were deemed statistically similar. All of the *in vitro* aggregate samples were significantly lower, in terms of normalised dense material volume, than even the youngest of the rat femurs.

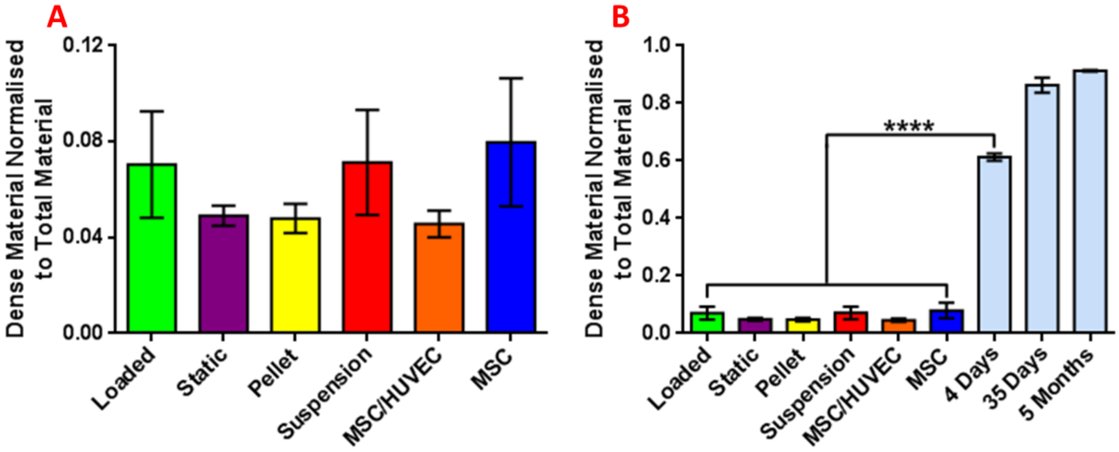

Figure 5.18: Aggregate material measurements compared to rat femur material measurements. Shown is the normalised dense material volume of each experimental variable (**A**). These normalised values are also compared to the equivalent values derived from rat femurs of various ages (**B**). Data comparing loaded and static culture conditions were compiled from suspension and pellet culture aggregates formed using MSCs only and MSC/HUVEC co-cultured aggregates. Data comparing suspension and pellet aggregation techniques were compiled using MSC only and MSC/HUVEC co-cultured aggregates cultured under loaded and static conditions. Data comparing MSC only and MSC/HUVEC co-cultured aggregates were compiled using suspension and pellet aggregates cultured under loaded and static conditions. Error bar represents standard error of the mean. **** signifies $p < 0.0001$.

3.5 Difficulties of imaging stained/tracked whole aggregates

It should be documented that some interesting and possibly contradicting data sets were also obtained throughout this study. CD31 staining of the intact aggregates did not offer any insight into the inner aggregate HUVEC arrangement; rather, it failed to show any arrangement at all (fig. 5.19 and 5.20).

Thankfully, however, some corroborating data can be obtained. Antibody penetration differed depending upon both aggregation technique and culture condition, suggesting that both initial aggregate density and the maintenance of such are highly influenced by the techniques discussed here. Penetration of the antibodies was less extensive in the pellet culture aggregates when compared to the suspension culture aggregates suggesting a higher aggregate density in the pellet culture samples. The antibody penetration was also lower in the loaded samples compared to the static samples, again suggesting a higher aggregate density through loading. Live/dead staining was also carried on whole aggregate samples but experienced similar dye penetration issues and so was not included in the results of this experiment. These data, at best, corroborate with the microCT density measurements noted previously.

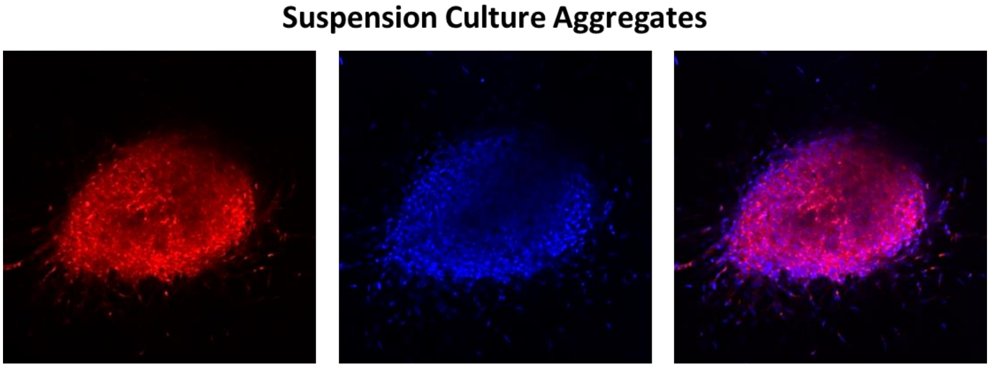

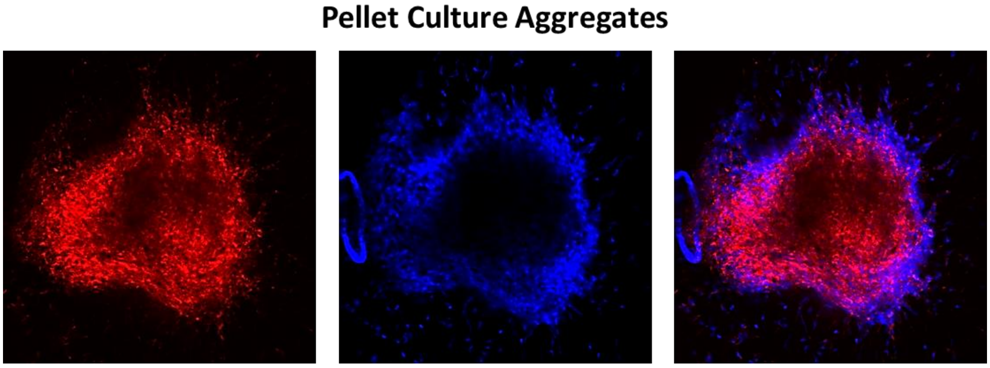

Figure 5.19: Confocal images of CD31-stained MSC/HUVEC co-cultured aggregates. Images were taken following 7 days under loaded culturing conditions. The aggregates contained 95% MSCs and 5% HUVECs and were formed using suspension and pellet aggregation techniques. The whole aggregates were stained for CD31 and mounted with a Dapi-conjugated mounting medium.

Suspension Culture Aggregates

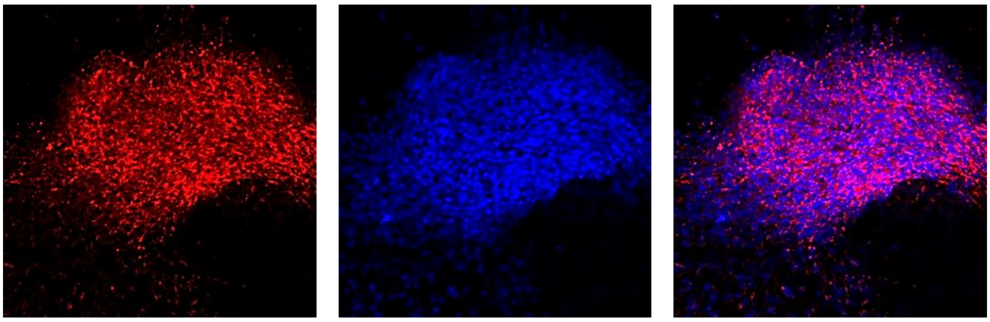

Pellet Culture Aggregates

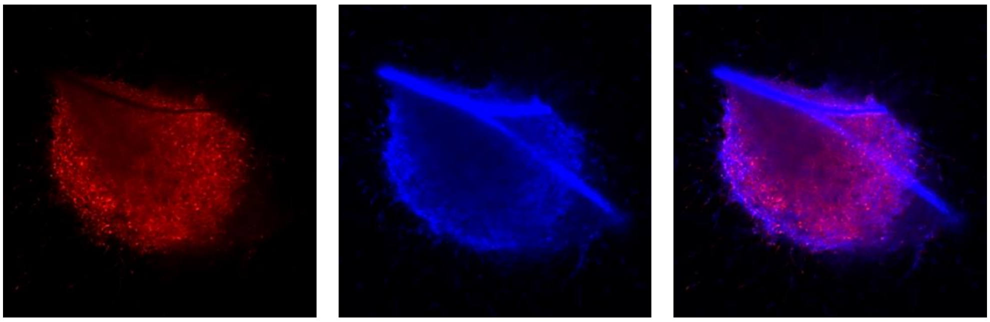

Figure 5.20: Confocal images of CD31-stained MSC/HUVEC co-cultured aggregates. Images were taken following 7 days under static culturing conditions. The aggregate contained 95% MSCs and 5% HUVECs and were formed using suspension and pellet aggregation techniques. The whole aggregates were stained for CD31 and mounted with a Dapi-conjugated mounting medium.

Also, when both HUVECs and MSCs were tracked in both suspension- and pellet-cultured aggregates, HUVEC arrangement into any discernible pattern was more difficult to visualise (fig. 5.21, 5.22, 5.23 and 5.24). The experimental set-up was the same as that used for previous experiments with the only difference being the MSCs were also fluorescently-tagged. There is no obvious reason for the data obtained from this particular experiment. The software used for the confocal z-stacking analysis had sequential settings enabled to prevent any “bleed through” between the two fluorescent markers, FITC and TRITC, so cross-contamination between images cannot be the issue. The precise reason for this observation is unknown. Again, however, these data corroborate previously noted observations suggesting that the main aggregate body was better maintained under loaded conditions compared to static conditions.

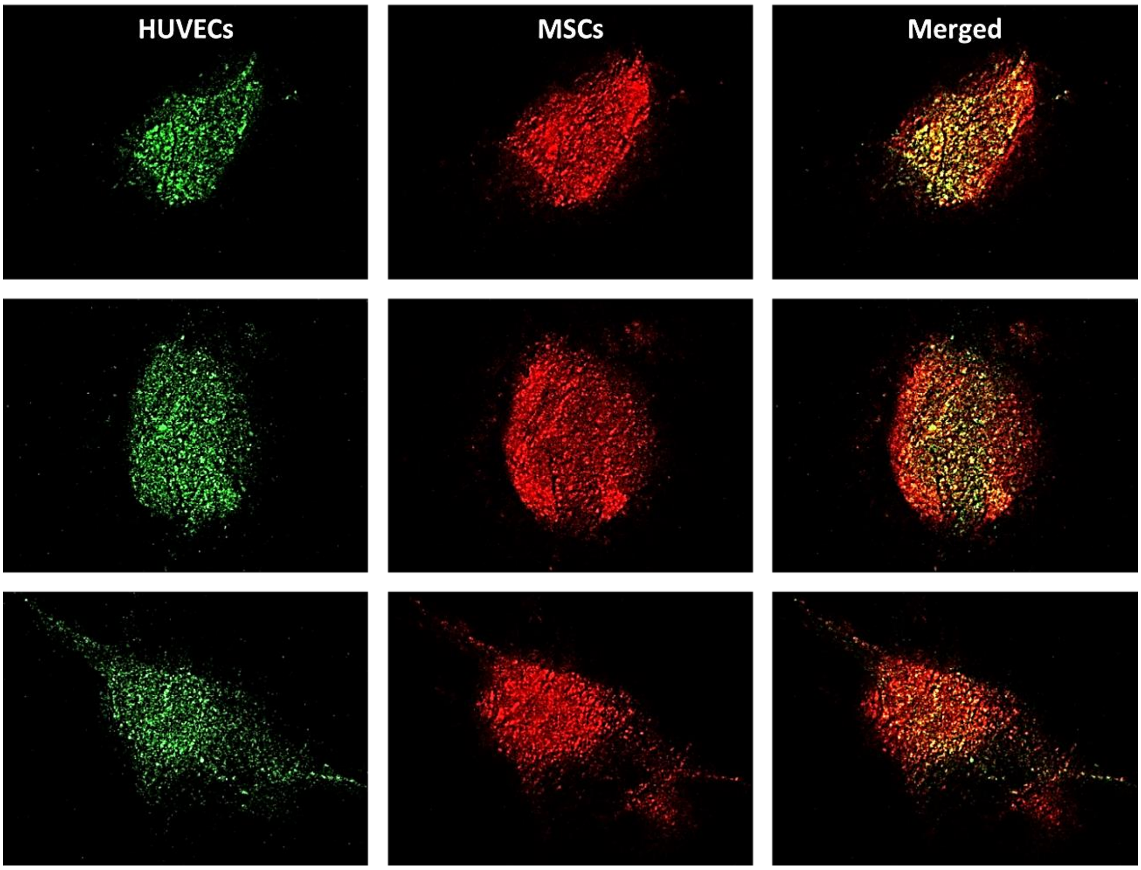

Figure 5.21: Confocal images of aggregates containing fluorescently-tagged MSCs and HUVECs. Images were taken following 7 days under loaded culturing conditions. MSCs were tagged with a TRITC-conjugated membrane dye, whilst HUVECs were tagged with a FITC-conjugated membrane dye. The aggregates contain 95% MSCs and 5% HUVECs and were formed using the suspension aggregation technique.

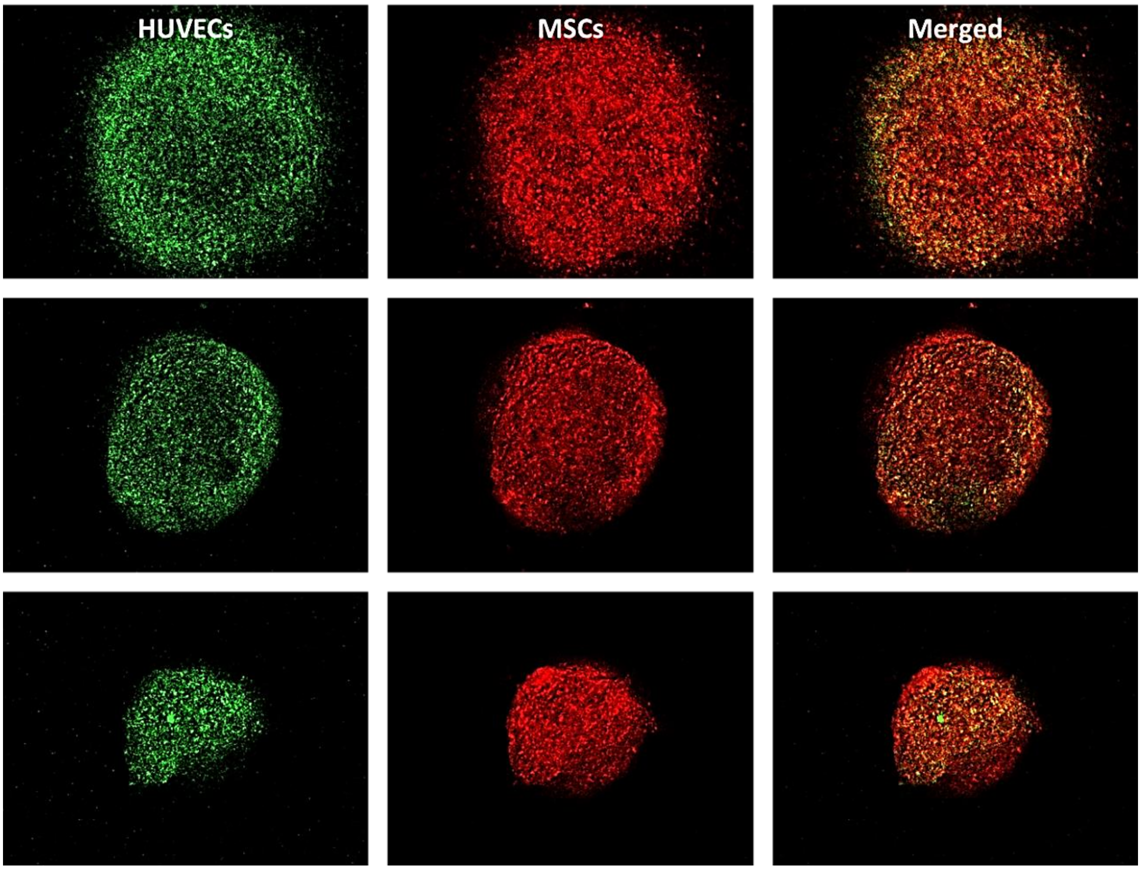

Figure 5.22: Confocal images of aggregates containing fluorescently-tagged MSCs and HUVECs. Images were taken following 7 days under loaded culturing conditions. MSCs were tagged with a TRITC-conjugated membrane dye, whilst HUVECs were tagged with a FITC-conjugated membrane dye. The aggregates contained 95% MSCs and 5% HUVECs and were formed using the pellet aggregation technique.

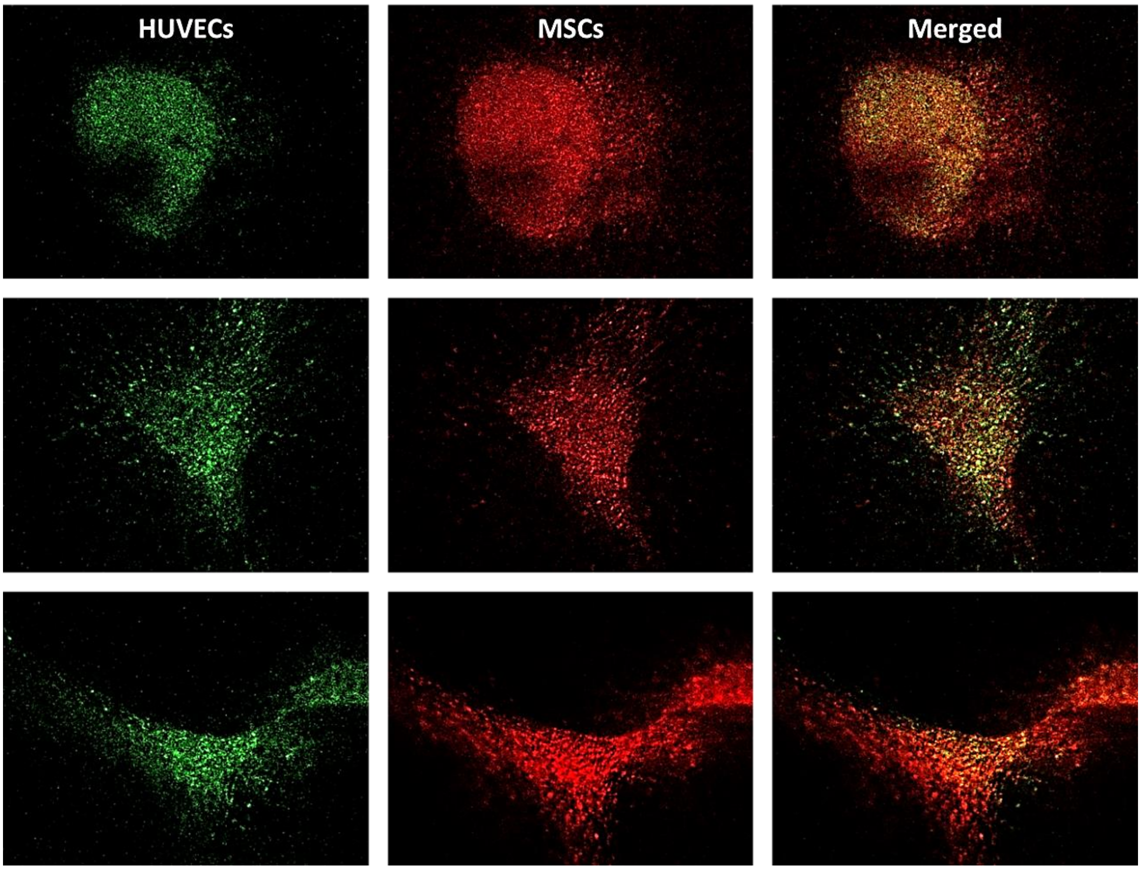

Figure 5.23: Confocal images of aggregates containing fluorescently-tagged MSCs and HUVECs. Images were taken following 7 days under static culturing conditions. MSCs were tagged with a TRITC-conjugated membrane dye, whilst HUVECs were tagged with a FITC-conjugated membrane dye. The aggregates contain 95% MSCs and 5% HUVECs and were formed using the suspension aggregation technique.

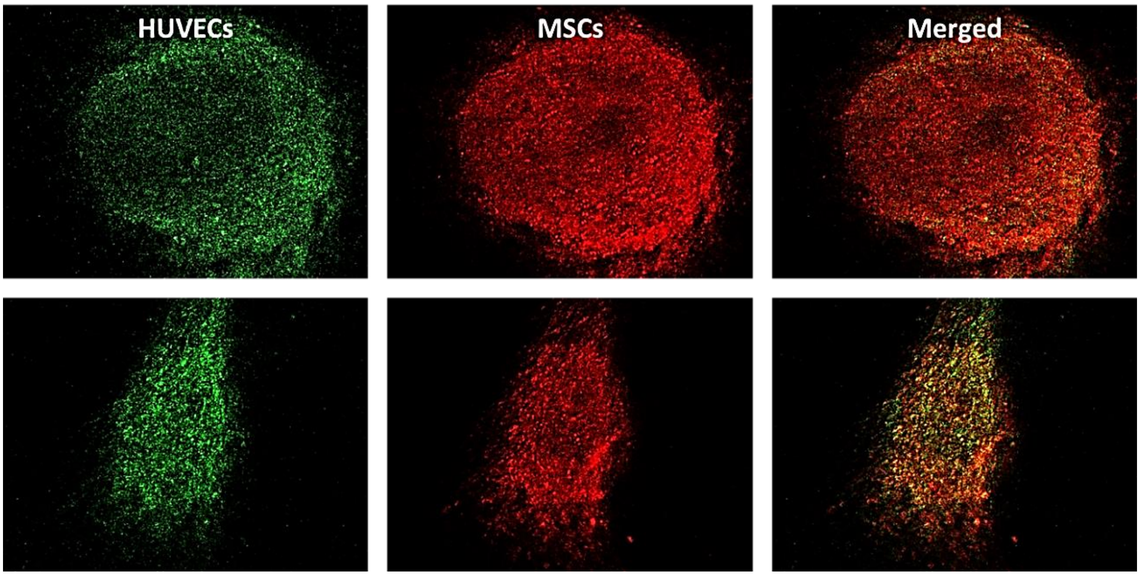

Figure 5.24: Confocal images of aggregates containing fluorescently-tagged MSCs and HUVECs. Images were taken following 7 days under static culturing conditions. MSCs were tagged with a TRITC-conjugated membrane dye, whilst HUVECs were tagged with a FITC-conjugated membrane dye. The aggregates contain 95% MSCs and 5% HUVECs and were formed using the pellet aggregation technique.

4. Discussion

The advantages of using 3D microenvironments (cellular aggregates) for tissue engineering has been discussed in previous chapters; therefore, using such environments for the study of vascularisation and mineralisation of constructs makes for sound experimental reasoning. This study intended to evaluate the enhancement effects of culture environments, e.g. hydrostatic loading, on vascularisation and mineralisation with the use of 3D cellular aggregates. The aggregates consisted of MSCs only and MSC/HUVEC co-cultures that were formed using two different methods: pellet culture aggregation and suspension culture aggregation. The suspension culture method comprised a simple F127-coated hydrophilic environment that encouraged the cells to remain in suspension (described in detail in chapter 3). Once suspended, the cells were free to aggregate and self-assemble into spheroidal structures. The pellet culture method, on the other hand, forced the cells into a cell pellet that subsequently became spheroidal. The suspension culture method was considered to be a less severe method for aggregation with the cells aggregating or self-assembling of their own accord over a 48 hour period. The pellet culture method was less forgiving and forced the cells into a pellet through centrifugation. The aggregates were comprised mostly of MSCs (90 – 95%) which formed the main body of the constructs. The HUVECs were far fewer in number (5 – 10%) but their role was no less important. The intention was for the HUVECs to form vascular or tubular structures within the aggregate body.

4.1 Aggregate formation, size and shape

The first observation made was with regards to the structure of the aggregates depending upon which aggregate formation technique was used. The suspension culture method initially created multiple small aggregates that eventually joined together to form a single aggregate per well. Similar occurrences were noted when forming suspension culture aggregates using an MLO-A5 cell line (chapter 3). The sometimes elongated and irregular shape of the aggregates formed using this technique suggested that the inner structure of the final aggregates still comprised the initial small aggregates. The pellet culture method, however, formed a single cell pellet immediately upon centrifugation with, what is suspected to be, a more uniform inner-aggregate structure.

4.2 HUVEC arrangements and aggregate vascularisation

If one considers the development of a viable vascular network a key component of bone formation, as is the case for *in vivo* bone regeneration, then the measurement of vascularisation through cellular arrangements becomes a crucial element for evaluating bone formation.

4.2.1 Whole aggregate monitoring

The initial aggregate structure appeared to influence cellular arrangement even prior to any further cultural conditions, i.e. loaded or static culturing. Confocal z-stacking has shown suspension culture aggregates with an enhanced HUVEC arrangement compared to the pellet culture aggregates. The small aggregates making up the final large aggregate of the suspension culture offered an inner-aggregate structure that was lacking in the aggregates of the pellet culture method which is believed to aid HUVEC arrangement and subsequent vascularisation. Saleh and colleagues demonstrated a similar cellular arrangement to our own[488]. Their study too used a non-adherent or suspension culture to allow for the self-assembly of aggregates which were smaller than our own (3 x 10^5 cells in total) but contained a larger proportion of HUVECs (50% of the total cell count). After 7 days in culture, the majority of the HUVECs were seen to be located around the periphery of the aggregates. These findings corroborate our own in the sense that the HUVECs in our study were predominantly located around the periphery of the smaller aggregates making up the inner structure of the large aggregates. A similar phenomenon was noted by Stahl *et al*. who cultured primary osteoblasts with human ECs[489]. One theory put forward to explain this cellular self-assembly is the differential adhesion hypothesis (DAH)[490]. The theory simply states that cells will aggregate to maximise adhesion and minimise energy with different cell types segregating according to cell – cell adhesion capabilities; those cells of a higher cohesion form the aggregate centre and those with a lower cohesion form the aggregate periphery.

Culture conditions have also been seen to influence cellular arrangement. Within the suspension-cultured aggregates, extensive HUVEC arrangement into tubular structures was clearly visible within the loaded samples, even within the early stages of the experiment. The pellet culture aggregates did not have the same level of HUVEC arrangement from the onset, but with continued loading, HUVEC arrangement into possible tubular structures did improve. Cyclic hydrostatic loading, therefore, positively influenced cellular arrangements in both aggregate types. Although the inner aggregate structure of the suspension culture aggregates allowed for minor initial HUVEC arrangement within the statically-cultured samples, this arrangement did not improve over the course of the experiment. Taking both aggregation techniques and culture conditions into account, it can be said that the suspension culture method allowed for a greater initial HUVEC arrangement compared to the pellet culture method and both techniques benefited from loaded culturing. The statically-cultured aggregates did not appear to develop tubular structures to the same degree. This may, in part, be due to VE-cadherin expression. VE-cadherin is present at endothelial adherens junctions and has been reported to play an important role in the intercellular adhesion, differentiation, growth and migration of ECs[278]. The expression of such has also been shown to be upregulated under shear stress conditions[491] making its increased expression under hydrostatic loading a likely contributor to the increased cellular arrangements noted in this study.

4.2.2 Aggregate sections

Aggregate sectioning and staining has offered a valuable insight for this study with even the sectioning itself offering some corroborative observations. The loaded samples appeared to better maintain their initial spheroidal structures throughout the study when compared to the static samples. This was largely due to the extensive cellular outgrowth noted from the statically-cultured aggregates that was considerably less severe from the hydrostatically-loaded samples.

Inner-aggregate cellular arrangements also differed between culture conditions. The hydrostatically-cultured aggregates appeared to have a more distinctive cellular arrangement compared to the statically-cultured aggregates. Tubular structuring of the HUVECs was notably more apparent in the loaded samples. The CD31-stained sections suggest that the pellet culture method of aggregation resulted in enhanced HUVEC arrangements into tube-like structures, and whilst this is entirely possible, it is the opinion of the author that the increased density of the pellet culture aggregates allowed for more intact sectioning and should the suspension culture aggregates have experienced as high quality sectioning, they too would have increased tubular arrangements.

4.2.3 Combined interpretations

Regardless of what criteria one uses for evaluating *in vitro* bone formation, it is clear that cellular aggregation combined with hydrostatic loading offers an invaluable model for the continued research into developing large bone tissue-engineered constructs. Cellular aggregation has been discussed in depth in previous chapters; thus, its use here is considered advantageous. What is interesting, however, is how different aggregation techniques influenced levels of cellular arrangement and mineralisation. Which technique is better for graft development and subsequent implantation has yet to be conclusively shown but what this study has demonstrated is that in the quest for large implantable bone grafts, one should not only consider cellular aggregation but also the method of aggregation. In addition, mechanical loading has been shown to hold some influence over the production of dense material. Hydrostatic loading has been shown by previous studies to enhance mineralisation and bone formation[386] but this study has shown some interesting results that allow for some thought provoking discussions. Increased cellular arrangements and varied levels of mineralisation were observed for samples cultured under mechanically-loaded conditions.

4.3 Aggregate material volumes

4.3.1 Aggregate formation technique

At a threshold of 110, neither aggregate formation technique had a significantly higher aggregate volume in comparison to the other. At a threshold of 130, both aggregate cultures, again, had similar material volumes. However, the standard error of the mean for both aggregate samples was significantly different with the suspension culture aggregates having a far higher standard error (f-test, $p < 0.0001$). This notable difference is likely due to the way the aggregates were formed. The pellet culture aggregates were forcibly aggregated producing uniform aggregates, whilst the suspension culture allowed the aggregates to form of their own accord, thus, producing aggregates of a less uniform nature. This considerable variation in standard error is thought to have diluted the magnitude of the overall mean value differences, rendering them insignificant. Using both thresholds, 110 and 130, we were able to normalise the volume of dense material to total volume of collagenous material. In doing so, we saw that the suspension culture aggregates again contained a statistically similar percentage of dense material but a significantly higher standard error of the mean (f-test, p = 0.002). All of the data, thus far, would suggest that, whilst both aggregation techniques were statistically similar in terms of dense material production, perhaps with a higher cohort this standard error could have been reduced and the difference between aggregation methods may have been seen.

4.3.2 Culture environment

Subsequent culturing conditions are thought to build upon these initial observations. When measuring the volume of dense material via microCT, the hydrostatically-loaded aggregates had a statistically similar volume of material compared to the statically-cultured samples. As was the case with the suspension culture aggregates, however, the loaded aggregates had a significantly higher standard error of the mean compared to the statically-cultured aggregates (f-test, p = 0.0002). Whilst there are a number of occurrences believed to be responsible for these observations, the loading parameters were carefully selected and are thought to not have obstructed the acquired data in any way. Henstock *et al.*[276] noted that bone formation was directly proportional to stimulation frequency and was independent of the degree of pressure applied. Therefore, the cyclic application of pressure is thought to be more relevant than the magnitude of the pressure itself. Airing on the side of caution, however, the pressure and frequency rate were still carefully chosen. The pressure used most closely replicates the pressure experienced by osteocytes in the canaliculi-lacuna system of load-bearing bones (270 kPa)[474] and the frequency rate used is similar to many physiological processes, such as the human pulse rate (1 – 2 Hz) and bone/joint compression (0.3 – 3 Hz) under normal conditions[276].

Rather, the hydrostatic chamber itself and the position of the aggregate samples within such are thought to play more of a hindering role in the data mentioned above. It was noted by Reinwald and colleagues that when hydrostatically loading a hydrogel construct within a chamber, such as the one used in this study, the centre of the hydrogel experiences considerably lower fluid flow and stress levels when compared to the peripheries of the gel[285]. Given that all of the aggregate samples for this study were placed centrally in their hydrogel housings, this observation could explain the lower than expected differences in dense material production between the loaded and statically-cultured aggregates.

Another possibly influential observation made during the use of the hydrostatic bioreactor was that during the loading of the samples, substantial medium evaporation was experienced. This evaporation was noted to be unevenly distributed across the well plate. Those wells closest to the air inlet port suffered the most severe medium loss with evaporation lessening across the plate towards the air outlet port. Given the non-uniform distribution of fluid loss, evaporation was, therefore, most likely due to gas shear flow across the medium surface[492]; which can induce additional surface stresses in the medium[493]. In addition, given that the samples were encapsulated in collagen gel and that this collagen was never directly exposed to the flow of gas, it is difficult to say what effect shear flow might have had on the data sets discussed above. It is noted that this element of the discussion is speculative and no experiments have been carried out by the author to investigate the extent of these observations but this could explain the considerable standard error of the mean values acquired for the loaded samples.

4.3.3 Aggregate constituents

The microCT data has shown that the MSC/HUVEC co-cultured aggregates had a similar volume of material at a threshold of 110 compared to the MSC only aggregates. At a threshold of 130, both aggregate samples, again, had statistically similar material volumes but the MSC only aggregates had a significantly higher standard error of the mean (f-test, $p < 0.0001$). The normalised values followed a similar trend (f-test, $p = 0.0003$). Given that previous studies have demonstrated when ECs are cultured in contact with bone marrow stromal cells, they promote *in vitro* osteogenesis through the expression of several factors, such as bone morphogenetic protein 2 (BMP-2)[494], and the intercommunication with osteoblast-like cell gap junctions (connexin 43)[281,495], this data might initially seem contradictory. However, in a study conducted by Bidara and colleagues, significant

ALP upregulation was only recorded in the final week of this 21 day co-culture monolayer study which was conducted using a minimal HUVEC concentration of 25%[496].

In comparison, our study was only 10 – 12 days in duration and used only 5 – 10% HUVEC concentration. In another co-culture study, Saleh and colleagues noted increased osteogenesis through ALP activity after just 7 days in culture which significantly increased after 14 days in culture compared with non-HUVEC-containing controls[488]. This study too used MSC/HUVEC co-cultured aggregates but with a 50% HUVEC concentration. The promotion of osteogenesis was noted by Bidara and colleagues to be cell ratio-dependent so it is entirely possible that the HUVEC concentration used in our study had not yet had enough time to significantly enhance osteogenesis. In terms of *in vivo* bone formation, the phenomenon noted in our study is perhaps not surprising. As mentioned previously, natural bone formation or regeneration follows vascular formation at the site of injury or defect. If we consider our model as an *in vitro* replica of *in vivo* bone regeneration, MSC differentiation would have been initially delayed by the surrounding environment which would have coincided with a shift from mineralisation to vascularisation within the aggregates. Also, the MSC/HUVEC co-cultured aggregates were cultured in only 50% of the osteogenic supplements that were enjoyed by the MSC only aggregates due to the 1:1 ratio of MSC osteogenic medium and HUVEC medium. This may have limited the availability of agents and minerals required for mineralisation but it is considered by the author that the presence and subsequent focus on the arrangement of HUVECs was a more limiting factor for initial mineralisation than the reduced availability of osteogenic supplements. Although speculative, it is believed that if our study duration was extended, the presence of HUVECs would most-likely have enhanced the mineralisation of the co-cultured aggregates over the MSC only aggregates.

5. Conclusions

In conclusion, whilst bone formation cannot be decisively concluded upon for a number of reasons, cellular arrangements and possible vascularisation can be. How the aggregates were formed appears to affect the inner-aggregate architecture. This, in turn, affects levels of HUVEC arrangement. The suspension culture aggregates are thought to have had a more compartmentalised inner structure compared to the more homogeneous inner-structure of the pellet culture aggregates. This increase in self-assembled structural interest allowed for a higher degree of cellular arrangement within the aggregates. In addition, the aggregates cultured under hydrostatically-loaded conditions, regardless of aggregate formation technique, experienced a considerably higher level of cellular arrangement compared to those cultured under static conditions. Taking both aggregation method and culture conditions together for the evaluation of vascularisation, it would appear that the suspension culture aggregates cultured under hydrostatic loading offered the best environment for vascularisation, closely followed by the pellet culture aggregates cultured under hydrostatic loading, the suspension culture aggregates cultured under static conditions and the pellet culture aggregates cultured under static conditions.

Chapter Six

Discussion and Conclusions

Overview

This study attempted to develop novel tissue engineering approaches to enhance natural bone formation. Induction and control of various cell – cell interactions are the central basis of these approaches, including the initiation of early onset mineralisation, the maintenance of prolonged aggregate culturing, the self-sorting of mixed stem cell subpopulations and the promotion of simultaneous vascularisation and mineralisation. To do this, an aggregation model was first developed and mineralisation rates and patterns verified and studied. Secondly, an *in vivo* study was conducted using two cell types to confirm the observations noted during *in vitro* examinations and also to evaluate how the said observations would affect long term cell aggregate survival and possible bone formation *in vivo*. Thirdly, a technique was developed to investigate the segregation of mesenchymal stem cell (MSC) subpopulations and their possible influences on an individual's osteogenic capacity. In addition, tissue vascularisation was also investigated using a co-culture aggregation model and mechanical loading.

1. Discussion

1.1 Cellular aggregate model

It was hypothesised that cellular condensation and aggregate formation could greatly enhance bone tissue development through mimicking of the intramembranous ossification pathway. It was believed that bone cell aggregates could become the ossification centres for nodule development which would greatly reduce the time required for mineralisation. It has already been reported that aggregate culturing of MSCs can induce osteogenic differentiation[3] through the mediation of specific cellular integrin interactions[340]; so, an aggregate model was investigated here.

The modification of substrate chemistry can influence cellular aggregation allowing for greater control over aggregate size, number, gene expression and mineralisation rate[4]. Such a simple technique is thought to offer a deeper understanding of the mechanisms involved in natural bone growth and regeneration which will allow for the refinement of current tissue engineering techniques or the development of new approaches to better mimic such *in vivo* processes for improved patient care.

Two substrates were used in the first phase of this study to develop an aggregate model. The first was a commercially-available hydrophobic substrate (denoted as non-coated) and the second involved using the same commercially-available hydrophobic substrate coated with a Pluronic solution (F127) (denoted as coated) (adapted from Aydin *et al.*[7]). This coating created an extremely hydrophilic substrate. Each substrate, coated and non-coated, discouraged cell attachment and maintained the cell populations in suspension. In doing so, the cells attached to one another creating cellular aggregates. How the coated and non-coated substrates differed from one another is in the magnitude by which they repel cell attachment, thus, creating aggregates of different sizes, denoted as small and large.

An MLO-A5 cell line was used with the aforementioned substrate modification technique to successfully develop an *in vitro* aggregate model to replicate the *in vivo* intramembranous ossification pathway for the study of developing mineralisation over time. Several modes of analyses are used to evaluate and compare the potential for bone development with some interesting observations being made. As was the case for previously conducted studies, mineralisation rates were influenced by aggregate size[432]. Ultimately, the large aggregates were seen to mineralise faster than their smaller counterparts and progress further down the bone formation pathway over just 72 hours (chapter 3). The size of the aggregate was also seen to influence where minerals were initially deposited within the aggregates themselves. That is to say, the smaller aggregates appeared to initially deposit minerals within the aggregate centre, whilst the larger aggregates deposited minerals on the aggregate periphery. As mentioned, peripheral mineral deposition was also noted by Schneider and colleagues[446] suggesting regions of optimal cell – cell and cell – extracellular matrix (ECM) interactions differ depending upon aggregate size.

The F127-coated suspension culture was also used to form aggregates from multiple MSC populations acquired from different donors (chapter 4). Each cell population produced a single large aggregate as expected, the results of which are described in detail in chapter 4. What is interesting, however, is what observations can be made when we compare how each cell type, MLO-A5 cells and MSCs, compare to one another when seeded on the same substrate. Both cell types used the very same cells numbers per aggregate, 3 x 10^5 cells, but formed aggregates of differing circularities. This would suggest that the slower proliferating MSCs reacted in a more similar way to the differentiated cell line compared to the faster proliferating MSCs. In that, the faster proliferating MSCs produced aggregates that were more spherical in shape and the slower proliferating MSCs, along with the cell line, produced more irregularly-shaped aggregates. In addition, the differences between the standard error of the mean aggregate aspect ratio would suggest that the slower proliferating MSCs were, again, more similar to the cell line in terms of variation in aggregate shape compared to the faster proliferating MSCs.

Taking both observations into account, it would appear as though the MSCs and MLO-A5 cell line reacted differently to the coated suspension culture. In addition, differences between the MSC populations themselves were also noted. The faster proliferating MSCs produced spherical aggregates of a standard circularity with little variation. The slower proliferating MSCs produced aggregates with an average (mean ± standard error of the mean) circularity more similar to that of the MLO-A5 cell line and also with a significantly higher variation in terms of reproducible circularity.

There are a number of possible explanations for this phenomenon, chiefly among which are cadherins. Cadherins have been discussed in detail in chapter 4; therefore, it is speculated that the different cell types may express varying levels of different cadherins. E-cadherin expression has been shown previously to precede cadherin-11 expression[464], and whilst several *in vitro* studies have shown that the expression of cadherins can change during osteoblast differentiation, the most common cadherins expressed by osteoblasts are E-cadherin, N-cadherin and cadherin-11[474,475]. Osteoblasts have been shown to mainly express N-cadherin and cadherin-11, however, which have both been shown to influence bone formation and mass[476]. In addition, E-cadherin has been noted previously to be an influential factor in forming cellular aggregates[478]. It is, therefore, thought that MSCs may express more E-cadherin, whereas the MLO-A5 cell line may express more N-cadherin and/or cadherin-11. Additionally, the faster proliferating MSCs, D3737A, have been shown to express significantly higher E-cadherin levels compared with the slower proliferating MSCs, D2884D (chapter 4).

1.2 *In vivo* examinations

Whilst the observations made during the development of the aforementioned model were certainly interesting, they were only relative to the onset of mineralisation or the initial stages of mineralisation. A key question remained at this point and that was how aggregate size would affect long term aggregate survival, mineralisation and/or bone formation. An 8-week *in vivo* investigation was, therefore, carried out with the hope of shedding light on the potential for long term aggregate survival and bone formation using two different cell types. Both cell types, MLO-A5 cells and MSCs, were used for this study with similar observations being noted for both. The initial observations made post-termination are described in detail in chapters 3 and 4. Comparisons between data obtained from both cell types are also made in chapter 4.

1.3 Mesenchymal stem cell subpopulations

The use of modified substrates may also offer a route for further investigations into individual-specific cellular biology, thus, allowing for more accurate patient assessment and personalised treatment strategies. This study investigated the possibility that MSCs isolated from human bone marrow mononuclear cells (MNCs) contain donor-dependent subpopulations that may play a role in determining an individual’s osteogenic capacity. Using a novel substrate, substrate X, a new protocol was developed for the identification of suspected subpopulations which encompasses a simple technique allowing the cells to self-sort into identifiable cellular arrangements, denoted as a monolayer arrangement, a sunflower-like arrangement and an aggregate-like arrangement. Each arrangement is thought to represent a separate subpopulation.

The proportions of these specific cellular assemblies are thought to be donor specific and may correspond with an individual's bone formation potential. The different arrangements were assessed for E-cadherin levels indicating that the more organised arrangements, i.e. sunflower-like and aggregate-like arrangements, had higher E-cadherin expression levels and, therefore, a higher capacity for cell – cell interactions.

The osteogenic potential of each cellular subpopulation was also assessed using histochemical staining and showed that those subpopulations with a higher aptitude for self-organisation, again, had a higher aptitude for indicators associated with mineralisation. Multiple analyses suggest that the proportions of these supposed subpopulations are donor-dependent allowing for correlations to be made between growth profiles, cell sizes, E-cadherin levels and osteogenic capacities. These data allow for the hypothesis that a donor with a higher proportion of sunflower-like or aggregate-like cells would correspondingly have a higher capacity for osteogenic development.

1.4 Aggregate vascularisation

The vascularisation and mineralisation of cellular aggregates was also investigated within this project. We explored the influences imparted by aggregate formation techniques and mechanical loading on inner aggregate cellular arrangements (construct pre-vascularisation) and mineralisation levels (potential bone formation) within MSC and human umbilical vein endothelial cell (HUVEC) aggregate co-cultures. The aggregate samples were formed using two different aggregation techniques, suspension culture aggregation and pellet culture aggregation, and were cultured under two different culturing conditions, hydrostatically-loaded culturing and static culturing. Clear differences could be seen when comparing both the aggregate formation techniques and culture conditions for possible effects on cellular arrangements for construct pre-vascularisation and mineralisation levels for bone formation.

How the aggregates were formed influences the inner aggregate architecture which, in turn, affects levels of HUVEC arrangement. Taking both aggregation methods and culture conditions together, it would appear that the suspension culture aggregates cultured under hydrostatic loading offered the best environment for vascularisation and mineralisation, closely followed by the pellet culture aggregates cultured under hydrostatic loading, the suspension culture aggregates cultured under static conditions and the pellet culture aggregates cultured under static conditions.

2. Conclusions

In conclusion, using simple yet novel substrate chemistry modifications has allowed for the development of a number of models for the assessment of various parameters intended for refined bone tissue engineering. A cellular aggregate model was established using a murine cell line and found that larger aggregates mineralised at a faster rate and initially deposited minerals towards the periphery of the aggregates, whilst smaller aggregates mineralised at a slower rate and deposited minerals within the aggregate centres. Gene expression patterns also differed depending upon aggregate size suggesting cellular maturation was influenced by cell – cell interactions. In conjunction, an *in vivo* study was carried out using the same cell line alongside a primary cell culture, MSCs, to evaluate how aggregate size would affect possible bone formation post-long term implantation. As with the *in vitro* studies, the data obtained suggested aggregate size strongly influenced aggregate survival rate with larger aggregates appearing to disintegrate over the course of the experiment. The reasons behind these data are thought to be focused on oxygen and nutrient supply giving rise to the concept of an optimal aggregate size for smaller grafts or implants, or the need for enhanced perfusion within larger grafts or implants. In addition to aggregation, substrate chemistry modification was used to identify possible MSC subpopulations. Three subpopulations are thought to have been identified through distinct cell attachment arrangements. Each of these subpopulations was shown to possess different differentiation potentials and E-cadherin levels. The proportions of the subpopulations were quantified in numerous individual donors and were shown to correlate with aggregation potential. These data suggest that subpopulation proportions are donor-dependent and could correlate with an individual’s bone formation capacity. Another study undertaken throughout this project involved the simultaneous assessment of vascularisation through cellular arrangements, and mineralisation. This study found that aggregation technique strongly influenced the level of cellular arrangements as did culturing technique. That is, the model developed as part of this project created aggregates with enhanced cellular arrangements compared to the conventional aggregation technique, and hydrostatic loading enhanced cellular arrangements more so than the static equivalents. A conclusion was difficult to draw for levels mineralisation given the short duration of the study.

Chapter Seven

Future Work

Overview

Numerous novel techniques have been developed throughout this project but, whilst the preliminary research has been fruitful, continued investigations are required to refine current protocols and ensure progression.

1. Further mesenchymal stem cell investigations

The current subpopulation identification protocols should be investigated further to advance this novel technique. The current study required a large number of mesenchymal stem cells (MSCs) which meant a correspondingly high passage number, passage three. Whilst this allowed us to compare and correlate our assessment technique with previously conducted research, the next step would be to refine our current protocols. To do this, MSCs would be used from multiple donors as before but with a dramatically reduced cell number. If we can obtain the same level of validation from a minimum number of cells, 0.5×10^6 for example, and a lower passage number, passage one for example, this would significantly reduce the time required to culture a functional cell population. In addition, with cellular arrangements on substrate X being noted to have fully formed within just hours of seeding, reducing the time required to identify and quantify the subpopulations and their proportions, to just 24 hours for example, would allow for the assessment of the osteogenic potential within an MSC population to be conducted at a much faster rate. Also, a more objective and reproducible identification and quantification technique needs to be developed. Whilst the current technique was sufficient to develop the initial protocols and validate our preliminary research, a more robust and accurate identification and quantification technique is required to reduce the time required for patient assessment whilst simultaneously increasing reproducibility and decreasing inter-institute variabilities. This would initially require an accurate definition of what the three cellular arrangements look like which will allow for their accurate identification. Perhaps, an imaging technique alongside software programming would be the next step in accurately measuring the subpopulation proportions. All in all, these refinements would dramatically reduce the time require for patient assessment whilst also increasing the accuracy and reproducibility of the assay. This would ultimately allow for this technique to be used within a clinical setting as a cheap, but effective, diagnostic tool. The assessment of an individual's bone formation or regeneration capacity would allow for patient specific treatments to be used, improving a patient's ability or likelihood to recover from acute bone loss or injury.

In addition, isolation and further enrichment of specific subpopulations identified using our current technique would be beneficial to both clinicians and companies dedicated to the mass production of MSCs for cellular therapy purposes. An isolation technique could be developed to separate those subpopulations identified as being most osteogenic in capacity. This would require an investigation into enzymatic, non-enzymatic and physical cleaving agents and techniques that would allow for the very specific division of particular cells from a population of multiple subpopulations. Once isolated, however, those cells could be further cultured to give a patient the best possible treatment; or within a commercial setting, it can be used to increase the therapeutic potential of mass-produced MSCs. Isolated cell populations should be evaluated *in vivo* to not only validate their therapeutic capacities but also the isolation process itself.

2. Aggregate vascularisation

Another interesting area that deserves further investigation is the prospect of pre-vascularised aggregates. How vascularised aggregates compare to their non-vascularised equivalents once implanted *in vivo* for example, would be a beneficial study for the continued development of large tissue constructs. The aggregation techniques established throughout this project could be used to create both vascularised and non-vascularised aggregates that can then be evaluated and compared for their bone formation potentials.

References

1. Kaiser, L. R. The future of multihospital systems. *Top. Health Care Financ.* **18,** 32–45 (1992).
2. Ehnert, S. *et al.* The possible use of stem cells in regenerative medicine: dream or reality? *Langenbecks Arch. Surg. Dtsch. Ges. Für Chir.* **394,** 985–997 (2009).
3. Wang, W. *et al.* 3D spheroid culture system on micropatterned substrates for improved differentiation efficiency of multipotent mesenchymal stem cells. *Biomaterials* **30,** 2705–2715 (2009).
4. Hildebrandt, C., Büth, H. & Thielecke, H. A scaffold-free in vitro model for osteogenesis of human mesenchymal stem cells. *Tissue Cell* **43,** 91–100 (2011).
5. Vacanti, J. P., Otte, J.-B. & Wertheim, J. A. in *Regenerative Medicine Applications in Organ Transplantation* (eds. Lerut, J., Soker, S. & Stratta, R. J.) 1–15 (Academic Press, 2014).
6. Amini, A. R., Laurencin, C. T. & Nukavarapu, S. P. Bone tissue engineering: recent advances and challenges. *Crit. Rev. Biomed. Eng.* **40,** 363–408 (2012).
7. Aydin, H. M., Hu, B., Sulé Suso, J., El Haj, A. & Yang, Y. Study of Tissue Engineered Bone Nodules by Fourier Transform Infrared Spectroscopy. *The Analyst* **136,** 775 (2011).
8. Rodan, G. A. Introduction to bone biology. *Bone* **13 Suppl 1,** S3–6 (1992).
9. Cowles, E. A., DeRome, M. E., Pastizzo, G., Brailey, L. L. & Gronowicz, G. A. Mineralization and the Expression of Matrix Proteins During In Vivo Bone Development. *Calcif. Tissue Int.* **62,** 74–82 (1998).
10. Eriksen, E. F., Axelrod, D. W. & Melsen, F. in *Bone Histomorphometry*. 1–12 (Raven Press, 1994).
11. Clarke, B. Normal Bone Anatomy and Physiology. *Clin. J. Am. Soc. Nephrol. CJASN* **3,** S131–S139 (2008).
12. Brodsky, B. & Persikov, A. V. Molecular structure of the collagen triple helix. *Adv. Protein Chem.* **70,** 301–339 (2005).
13. Nudelman, F., Lausch, A. J., Sommerdijk, N. A. J. M. & Sone, E. D. In vitro models of collagen biomineralization. *J. Struct. Biol.* **183,** 258–269 (2013).
14. Whyte, M. P. Hypophosphatasia and the role of alkaline phosphatase in skeletal mineralization. *Endocr. Rev.* **15,** 439–461 (1994).
15. Heinrichs, A. A. *et al.* Proximal promoter binding protein contributes to developmental, tissue-restricted expression of the rat osteocalcin gene. *J. Cell. Biochem.* **57,** 90–100 (1995).
16. Glowacki, J., Rey, C., Glimcher, M. J., Cox, K. A. & Lian, J. A role for osteocalcin in osteoclast differentiation. *J. Cell. Biochem.* **45,** 292–302 (1991).

17. Liggett, W. H., Jr, Lian, J. B., Greenberger, J. S. & Glowacki, J. Osteocalcin promotes differentiation of osteoclast progenitors from murine long-term bone marrow cultures. *J. Cell. Biochem.* **55,** 190–199 (1994).

18. Weiss, R. E. & Reddi, A. H. Synthesis and localization of fibronectin during collagenous matrix-mesenchymal cell interaction and differentiation of cartilage and bone in vivo. *Proc. Natl. Acad. Sci. U. S. A.* **77,** 2074–2078 (1980).

19. Nordahl, J., Mengarelli-Widholm, S., Hultenby, K. & Reinholt, F. P. Ultrastructural immunolocalization of fibronectin in epiphyseal and metaphyseal bone of young rats. *Calcif. Tissue Int.* **57,** 442–449 (1995).

20. George, E. L., Georges-Labouesse, E. N., Patel-King, R. S., Rayburn, H. & Hynes, R. O. Defects in mesoderm, neural tube and vascular development in mouse embryos lacking fibronectin. *Dev. Camb. Engl.* **119,** 1079–1091 (1993).

21. Hunter, G. K., Kyle, C. L. & Goldberg, H. A. Modulation of crystal formation by bone phosphoproteins: structural specificity of the osteopontin-mediated inhibition of hydroxyapatite formation. *Biochem. J.* **300,** 723–728 (1994).

22. Chellaiah, M. A. *et al.* Osteopontin deficiency produces osteoclast dysfunction due to reduced CD44 surface expression. *Mol. Biol. Cell* **14,** 173–189 (2003).

23. Kini, U. & Nandeesh, B. N. in *Radionuclide and Hybrid Bone Imaging* (eds. Fogelman, I., Gnanasegaran, G. & Wall, H. van der) 29–57 (Springer Berlin Heidelberg, 2012).

24. Mackie, E. J., Tatarczuch, L. & Mirams, M. The skeleton: a multi-functional complex organ. The growth plate chondrocyte and endochondral ossification. *J. Endocrinol.* **211,** 109–121 (2011).

25. Liu, Y., Chan, J. K. Y. & Teoh, S.-H. Review of vascularised bone tissue-engineering strategies with a focus on co-culture systems. *J. Tissue Eng. Regen. Med.* **9,** 85–105 (2015).

26. Shapiro, F. Bone development and its relation to fracture repair. The role of mesenchymal osteoblasts and surface osteoblasts. *Eur. Cell. Mater.* **15,** 53–76 (2008).

27. Teixeira, C. C., Agoston, H. & Beier, F. Nitric oxide, C-type natriuretic peptide and cGMP as regulators of endochondral ossification. *Dev. Biol.* **319,** 171–178 (2008).

28. Browner, B. D. *et al*. in *Skeletal Trauma: Basic Science, Management, and Reconstruction*. Chapter 2 (Elsevier Health Sciences, 2003).

29. Bradley, E. W., McGee-Lawrence, M. E. & Westendorf, J. J. Hdac-mediated control of endochondral and intramembranous ossification. *Crit. Rev. Eukaryot. Gene Expr.* **21,** 101–113 (2011).

30. Winet, H., Bao, J. Y. & Moffat, R. A control model for tibial cortex neovascularization in the bone chamber. *J. Bone Miner. Res. Off. J. Am. Soc. Bone Miner. Res.* **5,** 19–30 (1990).

31. Shapiro, I. M. *et al.* Linkage between energy status of perivascular cells and mineralization of the chick growth cartilage. *Dev. Biol.* **129,** 372–379 (1988).

32. Olusola, O. A., Dearing, O. S. & Pringle, S. in *Bone Circulation and Vascularization in Normal and Pathological Conditions* (eds. Schoutens, A., Arlet, J., Gardeniers, J. W. & Hughes, S. P. F.) 43–48 (Springer Science & Business Media, 2012).

33. Thompson, T. J., Owens, P. D. & Wilson, D. J. Intramembranous osteogenesis and angiogenesis in the chick embryo. *J. Anat.* **166,** 55–65 (1989).

34. Florencio-Silva, R., Sasso, G. R. da S., Sasso-Cerri, E., Simões, M. J. & Cerri, P. S. Biology of Bone Tissue: Structure, Function, and Factors That Influence Bone Cells. *BioMed Res. Int.* **2015,** (2015).

35. Nguyen Hoai Nam, N. K. Bone Cell Function: A Review. *Thai J. Vet. Med.* **43(3)**, 329–336 (2013).

36. Landis, W. J. The strength of a calcified tissue depends in part on the molecular structure and organization of its constituent mineral crystals in their organic matrix. *Bone* **16,** 533–544 (1995).

37. Anderson, H. C. Matrix vesicles and calcification. *Curr. Rheumatol. Rep.* **5,** 222–226 (2003).

38. Kwan Tat, S., Padrines, M., Théoleyre, S., Heymann, D. & Fortun, Y. IL-6, RANKL, TNF-alpha/IL-1: interrelations in bone resorption pathophysiology. *Cytokine Growth Factor Rev.* **15,** 49–60 (2004).

39. Nakamura, H. Morphology, Function, and Differentiation of Bone Cells. *J. Hard Tissue Biol.* **16,** 15–22 (2007).

40. Phan, T. C. A., Xu, J. & Zheng, M. H. Interaction between osteoblast and osteoclast: impact in bone disease. *Histol. Histopathol.* **19,** 1325–1344 (2004).

41. Karsdal, M. A. & Henriksen, K. Osteoclasts control osteoblast activity. *BoneKEy-Osteovision* **4,** 19–24 (2007).

42. Bonewald, L. F. The amazing osteocyte. *J. Bone Miner. Res. Off. J. Am. Soc. Bone Miner. Res.* **26,** 229–238 (2011).

43. Idris, A. I. Cannabinoid Receptors as Target for Treatment of Osteoporosis: A Tale of Two Therapies. *Curr. Neuropharmacol.* **8,** 243–253 (2010).

44. Nakamura, H., Sato, G., Hirata, A. & Yamamoto, T. Immunolocalization of matrix metalloproteinase-13 on bone surface under osteoclasts in rat tibia. *Bone* **34,** 48–56 (2004).

45. Franz-Odendaal, T. A., Hall, B. K. & Witten, P. E. Buried alive: how osteoblasts become osteocytes. *Dev. Dyn. Off. Publ. Am. Assoc. Anat.* **235,** 176–190 (2006).

46. Aubin, J. E., Liu, F., Malaval, L. & Gupta, A. K. Osteoblast and chondroblast differentiation. *Bone* **17,** S77–S83 (1995).

47. Lian, J. B. & Stein, G. S. Concepts of osteoblast growth and differentiation: basis for modulation of bone cell development and tissue formation. *Crit. Rev. Oral Biol. Med. Off. Publ. Am. Assoc. Oral Biol.* **3,** 269–305 (1992).

48. Liu, F., Malaval, L., Gupta, A. K. & Aubin, J. E. Simultaneous detection of multiple bone-related mRNAs and protein expression during osteoblast differentiation: polymerase chain reaction and immunocytochemical studies at the single cell level. *Dev. Biol.* **166,** 220–234 (1994).

49. Aubin, J. E. & Turksen, K. Monoclonal antibodies as tools for studying the osteoblast lineage. *Microsc. Res. Tech.* **33,** 128–140 (1996).

50. Lorenzo, J., Horowitz, M., Choi, Y. & Takayanagi, H. *Osteoimmunology: Interactions of the Immune and Skeletal Systems*. 1–5 (Academic Press, 2010).

51. Lacey, D. L. *et al.* Bench to bedside: elucidation of the OPG-RANK-RANKL pathway and the development of denosumab. *Nat. Rev. Drug Discov.* **11,** 401–419 (2012).

52. Saltel, F., Destaing, O., Bard, F., Eichert, D. & Jurdic, P. Apatite-mediated actin dynamics in resorbing osteoclasts. *Mol. Biol. Cell* **15,** 5231–5241 (2004).

53. Bonewald, L. F. Establishment and characterization of an osteocyte-like cell line, MLO-Y4. *J. Bone Miner. Metab.* **17,** 61–65 (1999).

54. Barragan-Adjemian, C. *et al.* Mechanism by which MLO-A5 late osteoblasts/early osteocytes mineralize in culture: similarities with mineralization of lamellar bone. *Calcif. Tissue Int.* **79,** 340–353 (2006).

55. Kamioka, H., Sugawara, Y., Honjo, T., Yamashiro, T. & Takano-Yamamoto, T. Terminal differentiation of osteoblasts to osteocytes is accompanied by dramatic changes in the distribution of actin-binding proteins. *J. Bone Miner. Res. Off. J. Am. Soc. Bone Miner. Res.* **19,** 471–478 (2004).

56. Guo, D. *et al.* Identification of osteocyte-selective proteins. *Proteomics* **10,** 3688–3698 (2010).

57. Mikuni-Takagaki, Y. *et al.* Matrix mineralization and the differentiation of osteocyte-like cells in culture. *J. Bone Miner. Res. Off. J. Am. Soc. Bone Miner. Res.* **10,** 231–242 (1995).

58. Dallas, S. L., Prideaux, M. & Bonewald, L. F. The Osteocyte: An Endocrine Cell … and More. *Endocr. Rev.* **34,** 658–690 (2013).

59. Ferguson, C., Alpern, E., Miclau, T. & Helms, J. A. Does adult fracture repair recapitulate embryonic skeletal formation? *Mech. Dev.* **87,** 57–66 (1999).

60. Gerstenfeld, L. C., Cullinane, D. M., Barnes, G. L., Graves, D. T. & Einhorn, T. A. Fracture healing as a post-natal developmental process: molecular, spatial, and temporal aspects of its regulation. *J. Cell. Biochem.* **88,** 873–884 (2003).

61. Bais, M. *et al.* Transcriptional analysis of fracture healing and the induction of embryonic stem cell-related genes. *PloS One* **4,** e5393 (2009).

62. Ozaki, A., Tsunoda, M., Kinoshita, S. & Saura, R. Role of fracture hematoma and periosteum during fracture healing in rats: interaction of fracture hematoma and the periosteum in the initial step of the healing process. *J. Orthop. Sci. Off. J. Jpn. Orthop. Assoc.* **5,** 64–70 (2000).

63. Kon, T. *et al.* Expression of osteoprotegerin, receptor activator of NF-kappaB ligand (osteoprotegerin ligand) and related proinflammatory cytokines during fracture healing. *J. Bone Miner. Res. Off. J. Am. Soc. Bone Miner. Res.* **16,** 1004–1014 (2001).

64. Timlin, M. *et al.* Fracture hematoma is a potent proinflammatory mediator of neutrophil function. *J. Trauma* **58,** 1223–1229 (2005).

65. Park, S.-H., Silva, M., Bahk, W.-J., McKellop, H. & Lieberman, J. R. Effect of repeated irrigation and debridement on fracture healing in an animal model. *J. Orthop. Res. Off. Publ. Orthop. Res. Soc.* **20,** 1197–1204 (2002).

66. Wray, J. B. ACUTE CHANGES IN FEMORAL ARTERIAL BLOOD FLOW AFTER CLOSED TIBIAL FRACTURE IN DOGS. *J. Bone Joint Surg. Am.* **46,** 1262–1268 (1964).

67. Xing, Z., Lu, C., Hu, D., Miclau, T. & Marcucio, R. S. Rejuvenation of the inflammatory system stimulates fracture repair in aged mice. *J. Orthop. Res. Off. Publ. Orthop. Res. Soc.* **28,** 1000–1006 (2010).

68. Lange, J. *et al.* Action of IL-1beta during fracture healing. *J. Orthop. Res. Off. Publ. Orthop. Res. Soc.* **28,** 778–784 (2010).

69. Takayama, S. *et al.* Expression of receptors for basic fibroblast growth factor on human periodontal ligament cells. *J. Periodontal Res.* **33,** 315–322 (1998).

70. Wang, X. *et al.* MMP9 regulates the cellular response to inflammation after skeletal injury. *Bone* **52,** 111–119 (2013).

71. Cheng, H. *et al.* Osteogenic activity of the fourteen types of human bone morphogenetic proteins (BMPs). *J. Bone Joint Surg. Am.* **85–A,** 1544–1552 (2003).

72. Jensen, J. A., Hunt, T. K., Scheuenstuhl, H. & Banda, M. J. Effect of lactate, pyruvate, and pH on secretion of angiogenesis and mitogenesis factors by macrophages. *Lab. Investig. J. Tech. Methods Pathol.* **54,** 574–578 (1986).

73. Zabel, D. D., Feng, J. J., Scheuenstuhl, H., Hunt, T. K. & Hussain, M. Z. Lactate stimulation of macrophage-derived angiogenic activity is associated with inhibition of Poly(ADP-ribose) synthesis. *Lab. Investig. J. Tech. Methods Pathol.* **74,** 644–649 (1996).

74. Trabold, O. *et al.* Lactate and oxygen constitute a fundamental regulatory mechanism in wound healing. *Wound Repair Regen. Off. Publ. Wound Heal. Soc. Eur. Tissue Repair Soc.* **11,** 504–509 (2003).

75. Hunt, T. K., Aslam, R., Hussain, Z. & Beckert, S. Lactate, with oxygen, incites angiogenesis. *Adv. Exp. Med. Biol.* **614,** 73–80 (2008).

76. Kumar, V. B. S., Binu, S., Soumya, S. J., K, H. & Sudhakaran, P. R. Regulation of vascular endothelial growth factor by metabolic context of the cell. *Glycoconj. J.* **31,** 427–434 (2014).

77. Lehmann, W. *et al.* Tumor necrosis factor alpha (TNF-alpha) coordinately regulates the expression of specific matrix metalloproteinases (MMPS) and angiogenic factors during fracture healing. *Bone* **36,** 300–310 (2005).

78. Lu, K. V. & Bergers, G. Mechanisms of evasive resistance to anti-VEGF therapy in glioblastoma. *CNS Oncol.* **2,** 49–65 (2013).

79. Laskin, D. L. Macrophages and inflammatory mediators in chemical toxicity: a battle of forces. *Chem. Res. Toxicol.* **22,** 1376–1385 (2009).

80. Nauta, A. J. & Fibbe, W. E. Immunomodulatory properties of mesenchymal stromal cells. *Blood* **110,** 3499–3506 (2007).

81. Morandi, F. *et al.* Immunogenicity of human mesenchymal stem cells in HLA-class I-restricted T-cell responses against viral or tumor-associated antigens. *Stem Cells Dayt. Ohio* **26,** 1275–1287 (2008).

82. Rizzo, R. *et al.* A functional role for soluble HLA-G antigens in immune modulation mediated by mesenchymal stromal cells. *Cytotherapy* **10,** 364–375 (2008).

83. Montespan, F., Deschaseaux, F., Sensébé, L., Carosella, E. D. & Rouas-Freiss, N. Osteodifferentiated mesenchymal stem cells from bone marrow and adipose tissue express HLA-G and display immunomodulatory properties in HLA-mismatched settings: implications in bone repair therapy. *J. Immunol. Res.* **2014,** 230346 (2014).

84. Uccelli, A., Pistoia, V. & Moretta, L. Mesenchymal stem cells: a new strategy for immunosuppression? *Trends Immunol.* **28,** 219–226 (2007).

85. Najar, M. *et al.* Immune-related antigens, surface molecules and regulatory factors in human-derived mesenchymal stromal cells: the expression and impact of inflammatory priming. *Stem Cell Rev.* **8,** 1188–1198 (2012).

86. Al-Sebaei, M. O. *et al.* Role of Fas and Treg cells in fracture healing as characterized in the fas-deficient (lpr) mouse model of lupus. *J. Bone Miner. Res. Off. J. Am. Soc. Bone Miner. Res.* **29,** 1478–1491 (2014).

87. Dickson, K. F., Katzman, S. & Paiement, G. The importance of the blood supply in the healing of tibial fractures. *Contemp. Orthop.* **30,** 489–493 (1995).

88. Lu, C., Miclau, T., Hu, D. & Marcucio, R. S. Ischemia leads to delayed union during fracture healing: a mouse model. *J. Orthop. Res. Off. Publ. Orthop. Res. Soc.* **25,** 51–61 (2007).

89. Germain, S. & Eichmann, A. VEGF and ephrin-B2: a bloody duo. *Nat. Med.* **16,** 752–754 (2010).

90. Coulon, C. *et al.* From Vessel Sprouting to Normalization Role of the Prolyl Hydroxylase Domain Protein/Hypoxia-Inducible Factor Oxygen-Sensing Machinery. *Arterioscler. Thromb. Vasc. Biol.* **30,** 2331–2336 (2010).

91. Hynes, R. O. & Lander, A. D. Contact and adhesive specificities in the associations, migrations, and targeting of cells and axons. *Cell* **68,** 303–322 (1992).

92. Clark, R. A. Potential roles of fibronectin in cutaneous wound repair. *Arch. Dermatol.* **124,** 201–206 (1988).

93. Ffrench-Constant, C., Water, L. V. de, Dvorak, H. F. & Hynes, R. O. Reappearance of an embryonic pattern of fibronectin splicing during wound healing in the adult rat. *J. Cell Biol.* **109,** 903–914 (1989).

94. Potier, E. *et al.* Hypoxia affects mesenchymal stromal cell osteogenic differentiation and angiogenic factor expression. *Bone* **40,** 1078–1087 (2007).

95. Rochefort, G. Y. *et al.* Multipotential Mesenchymal Stem Cells Are Mobilized into Peripheral Blood by Hypoxia. *STEM CELLS* **24,** 2202–2208 (2006).

96. Zwezdaryk, K. J. *et al.* Erythropoietin, a hypoxia-regulated factor, elicits a pro-angiogenic program in human mesenchymal stem cells. *Exp. Hematol.* **35,** 640–652 (2007).

97. Einhorn, T. A. The cell and molecular biology of fracture healing. *Clin. Orthop.* S7-21 (1998).

98. Barnes, G. L., Kostenuik, P. J., Gerstenfeld, L. C. & Einhorn, T. A. Growth factor regulation of fracture repair. *J. Bone Miner. Res. Off. J. Am. Soc. Bone Miner. Res.* **14,** 1805–1815 (1999).

99. Vortkamp, A. *et al.* Recapitulation of signals regulating embryonic bone formation during postnatal growth and in fracture repair. *Mech. Dev.* **71,** 65–76 (1998).

100. Hadjiargyrou, M. & O'Keefe, R. J. The Convergence of Fracture Repair and Stem Cells: Interplay of Genes, Aging, Environmental Factors and Disease. *J. Bone Miner. Res. Off. J. Am. Soc. Bone Miner. Res.* **29,** 2307–2322 (2014).

101. Schmitt, A., van Griensven, M., Imhoff, A. B. & Buchmann, S. Application of Stem Cells in Orthopedics. *Stem Cells Int.* **2012,** 1–11 (2012).

102. Brooks, P. J., Walker, P. S. & Scott, R. D. Tibial component fixation in deficient tibial bone stock. *Clin. Orthop.* 302–308 (1984).

103. Toms, A. D. *et al.* Repair of defects and containment in revision total knee replacement: a comparative biomechanical analysis. *J. Bone Joint Surg. Br.* **91,** 271–277 (2009).

104. Persson, B. M. & Wouters, H. W. Curettage and acrylic cementation in surgery of giant cell tumors of bone. *Clin. Orthop.* 125–133 (1976).

105. Persson, B. M., Ekelund, L., Lövdahl, R. & Gunterberg, B. Favourable results of acrylic cementation for giant cell tumors. *Acta Orthop. Scand.* **55,** 209–214 (1984).

106. Qiu, Y. Y., Yan, C. H., Chiu, K. Y. & Ng, F. Y. Review article: Treatments for bone loss in revision total knee arthroplasty. *J. Orthop. Surg. Hong Kong* **20,** 78–86 (2012).

107. Gross, A. E. Revision total knee arthroplasty of bone grafts versus implant supplementation. *Orthopedics* **20,** 843–844 (1997).

108. Ritter, M. A. Screw and cement fixation of large defects in total knee arthroplasty. *J. Arthroplasty* **1,** 125–129 (1986).

109. Engh, G. A. & Ammeen, D. J. CLASSIFICATION AND PREOPERATIVE RADIOGRAPHIC EVALUATION: KNEE. *Orthop. Clin. North Am.* **29,** 205–217 (1998).

110. Radnay, C. S. & Scuderi, G. R. Management of bone loss: augments, cones, offset stems. *Clin. Orthop.* **446,** 83–92 (2006).

111. Werle, J. R., Goodman, S. B. & Imrie, S. N. Revision total knee arthroplasty using large distal femoral augments for severe metaphyseal bone deficiency: a preliminary study. *Orthopedics* **25,** 325–327 (2002).

112. Gofton, W. T. *et al.* Revision total knee arthroplasty: fixation with modular stems. *Clin. Orthop.* 158–168 (2002).

113. Poultsides, L. A. & Sculco, T. P. Bone Loss Management in Revision Total Knee Replacement: *Tech. Orthop.* **26,** 84–93 (2011).

114. Patel, J. V., Masonis, J. L., Guerin, J., Bourne, R. B. & Rorabeck, C. H. The fate of augments to treat type-2 bone defects in revision knee arthroplasty. *J. Bone Joint Surg. Br.* **86,** 195–199 (2004).

115. Brand, M. G., Daley, R. J., Ewald, F. C. & Scott, R. D. Tibial tray augmentation with modular metal wedges for tibial bone stock deficiency. *Clin. Orthop.* 71–79 (1989).

116. Cypher, T. J. & Grossman, J. P. Biological principles of bone graft healing. *J. Foot Ankle Surg. Off. Publ. Am. Coll. Foot Ankle Surg.* **35,** 413–417 (1996).

117. Finkemeier, C. G. Bone-Grafting and Bone-Graft Substitutes. *J. Bone Jt. Surg.* **84,** 454–464 (2002).

118. Bahney, C. S., Hu, D. P., Miclau, T. & Marcucio, R. S. The Multifaceted Role of the Vasculature in Endochondral Fracture Repair. *Front. Endocrinol.* **6,** (2015).

119. Jager, M. *et al.* Bone Marrow Concentrate: A Novel Strategy for Bone Defect Treatment. *Curr. Stem Cell Res. Ther.* **4,** 34–43 (2009).

120. Chamberlain, G., Fox, J., Ashton, B. & Middleton, J. Concise review: mesenchymal stem cells: their phenotype, differentiation capacity, immunological features, and potential for homing. *Stem Cells Dayt. Ohio* **25,** 2739–2749 (2007).

121. Pelissier, P., Boireau, P., Martin, D. & Baudet, J. Bone reconstruction of the lower extremity: complications and outcomes. *Plast. Reconstr. Surg.* **111,** 2223–2229 (2003).

122. Gladstone, J. N., Bishop, J. Y., Lo, I. K. Y. & Flatow, E. L. Fatty Infiltration and Atrophy of the Rotator Cuff Do Not Improve After Rotator Cuff Repair and Correlate With Poor Functional Outcome. *Am. J. Sports Med.* **35,** 719–728 (2007).

123. Forriol, F. *et al.* Platelet-rich plasma, rhOP-1 (rhBMP-7) and frozen rib allograft for the reconstruction of bony mandibular defects in sheep. A pilot experimental study. *Injury* **40 Suppl 3,** S44-49 (2009).

124. Maffulli, N., Longo, U. G. & Denaro, V. Novel approaches for the management of tendinopathy. *J. Bone Joint Surg. Am.* **92,** 2604–2613 (2010).

125. Castricini, R. *et al.* Platelet-Rich Plasma Augmentation for Arthroscopic Rotator Cuff Repair A Randomized Controlled Trial. *Am. J. Sports Med.* **39,** 258–265 (2011).

126. Kokkonen, A., Ikävalko, M., Tiihonen, R., Kautiainen, H. & Belt, E. A. High rate of osteolytic lesions in medium-term followup after the AES total ankle replacement. *Foot Ankle Int. Am. Orthop. Foot Ankle Soc. Swiss Foot Ankle Soc.* **32,** 168–175 (2011).

127. Longo, U. G. *et al.* Biological resurfacing for early osteoarthritis of the shoulder. *Sports Med. Arthrosc. Rev.* **19,** 380–394 (2011).

128. Longo, U. G., Lamberti, A., Khan, W. S., Maffulli, N. & Denaro, V. Synthetic augmentation for massive rotator cuff tears. *Sports Med. Arthrosc. Rev.* **19,** 360–365 (2011).

129. Luginbuehl, V., Meinel, L., Merkle, H. P. & Gander, B. Localized delivery of growth factors for bone repair. *Eur. J. Pharm. Biopharm. Off. J. Arbeitsgemeinschaft Für Pharm. Verfahrenstechnik EV* **58,** 197–208 (2004).

130. Devescovi, V., Leonardi, E., Ciapetti, G. & Cenni, E. Growth factors in bone repair. *Chir. Organi Mov.* **92,** 161–168 (2008).

131. Peres, J. A. & Lamano, T. Strategies for stimulation of new bone formation: a critical review. *Braz. Dent. J.* **22,** 443–448 (2011).

132. Giannoudis, P. V., Einhorn, T. A. & Marsh, D. Fracture healing: the diamond concept. *Injury* **38 Suppl 4,** S3-6 (2007).

133. Venkatesan, J., Nithya, R., Sudha, P. N. & Kim, S.-K. Role of alginate in bone tissue engineering. *Adv. Food Nutr. Res.* **73,** 45–57 (2014).

134. Khan, Y., Yaszemski, M. J., Mikos, A. G. & Laurencin, C. T. Tissue engineering of bone: material and matrix considerations. *J. Bone Joint Surg. Am.* **90 Suppl 1,** 36–42 (2008).

135. Meinel, L. *et al.* Bone tissue engineering using human mesenchymal stem cells: effects of scaffold material and medium flow. *Ann. Biomed. Eng.* **32,** 112–122 (2004).

136. Yoshikawa, H. & Myoui, A. Bone tissue engineering with porous hydroxyapatite ceramics. *J. Artif. Organs* **8,** 131–136 (2005).

137. Zhou, H. & Lee, J. Nanoscale hydroxyapatite particles for bone tissue engineering. *Acta Biomater.* **7,** 2769–2781 (2011).

138. Villa, M. M., Wang, L., Huang, J., Rowe, D. W. & Wei, M. Bone tissue engineering with a collagen–hydroxyapatite scaffold and culture expanded bone marrow stromal cells. *J. Biomed. Mater. Res. B Appl. Biomater.* **103,** 243–253 (2015).

139. Moore, W. R., Graves, S. E. & Bain, G. I. Synthetic bone graft substitutes. *ANZ J. Surg.* **71,** 354–361 (2001).

140. Liu, X., Won, Y. & Ma, P. X. Surface modification of interconnected porous scaffolds. *J. Biomed. Mater. Res. A* **74,** 84–91 (2005).

141. Bosetti, M. *et al.* Cell behaviour on phospholipids-coated surfaces. *J. Mater. Sci. Mater. Med.* **18,** 611–617 (2007).

142. Zhang, H., Lin, C.-Y. & Hollister, S. J. The interaction between bone marrow stromal cells and RGD-modified three-dimensional porous polycaprolactone scaffolds. *Biomaterials* **30,** 4063–4069 (2009).

143. Tachibana, A. *et al.* Modified keratin sponge: binding of bone morphogenetic protein-2 and osteoblast differentiation. *J. Biosci. Bioeng.* **102,** 425–429 (2006).

144. Ueblacker, P. *et al.* In vivo analysis of retroviral gene transfer to chondrocytes within collagen scaffolds for the treatment of osteochondral defects. *Biomaterials* **28,** 4480–4487 (2007).

145. Szpalski, C., Barbaro, M., Sagebin, F. & Warren, S. M. Bone tissue engineering: current strategies and techniques--part II: Cell types. *Tissue Eng. Part B Rev.* **18,** 258–269 (2012).

146. Zhang, Y., Khan, D., Delling, J. & Tobiasch, E. Mechanisms Underlying the Osteo- and Adipo-Differentiation of Human Mesenchymal Stem Cells. *Sci. World J.* **2012,** (2012).

147. Hayes, J. S., Khan, I. M., Archer, C. W. & Richards, R. G. The role of surface microtopography in the modulation of osteoblast differentiation. *Eur. Cell. Mater.* **20,** 98–108 (2010).

148. Kartsogiannis, V. & Ng, K. W. Cell lines and primary cell cultures in the study of bone cell biology. *Mol. Cell. Endocrinol.* **228,** 79–102 (2004).

149. Aubin, J. E., Turksen, K. & Heersche, J. N. M. in *Cellular and Molecular Biology of Bone* (ed. Noda, M.) 1–45 (Academic Press, 2014).

150. Billiau, A. *et al.* Human Interferon: Mass Production in a Newly Established Cell Line, MG-63. *Antimicrob. Agents Chemother.* **12,** 11–15 (1977).

151. Czekanska, E. M., Stoddart, M. J., Richards, R. G. & Hayes, J. S. In search of an osteoblast cell model for in vitro research. *Eur. Cell. Mater.* **24,** 1–17 (2012).

152. Kato, Y. *et al.* Establishment of an Osteoid Preosteocyte-like Cell MLO-A5 That Spontaneously Mineralizes in Culture. *J. Bone Miner. Res.* **16,** 1622–1633 (2001).

153. Jähn, K. Pellet culture model for human primary osteoblasts. *Eur. Cell. Mater.* **20,** 149 (2010).

154. Ogawa, M. Differentiation and proliferation of hematopoietic stem cells. *Blood* **81,** 2844–2853 (1993).

155. Thomson, J. A. *et al.* Embryonic Stem Cell Lines Derived from Human Blastocysts. *Science* **282,** 1145–1147 (1998).

156. Pittenger, M. F. *et al.* Multilineage potential of adult human mesenchymal stem cells. *Science* **284,** 143–147 (1999).

157. Mafi, R., Hindocha, S., Mafi, P., Griffin, M. & Khan, W. S. Sources of adult mesenchymal stem cells applicable for musculoskeletal applications - a systematic review of the literature. *Open Orthop. J.* **5 Suppl 2,** 242–248 (2011).

158. Dominici, M. Minimal criteria for defining multipotent mesenchymal stromal cells. The International Society for Cellular Therapy position statement. *Cytotherapy* **8,** 315 (2006).

159. Fukuda, K. Reprogramming of bone marrow mesenchymal stem cells into cardiomyocytes. *C. R. Biol.* **325,** 1027–1038 (2002).

160. Schwartz, R. E. *et al.* Multipotent adult progenitor cells from bone marrow differentiate into functional hepatocyte-like cells. *J. Clin. Invest.* **109,** 1291–1302 (2002).

161. Bossolasco, P. *et al.* Neuro-glial differentiation of human bone marrow stem cells in vitro. *Exp. Neurol.* **193,** 312–325 (2005).

162. Cao, Y. *et al.* Human adipose tissue-derived stem cells differentiate into endothelial cells in vitro and improve postnatal neovascularization in vivo. *Biochem. Biophys. Res. Commun.* **332,** 370–379 (2005).

163. Porada, C. D. & Almeida-Porada, G. Mesenchymal stem cells as therapeutics and vehicles for gene and drug delivery. *Adv. Drug Deliv. Rev.* **62,** 1156–1166 (2010).

164. Zippel, N., Schulze, M. & Tobiasch, E. Biomaterials and mesenchymal stem cells for regenerative medicine. *Recent Pat. Biotechnol.* **4,** 1–22 (2010).

165. Zippel, N. *et al.* Purinergic receptors influence the differentiation of human mesenchymal stem cells. *Stem Cells Dev.* **21,** 884–900 (2012).

166. Hass, R., Kasper, C., Böhm, S. & Jacobs, R. Different populations and sources of human mesenchymal stem cells (MSC): A comparison of adult and neonatal tissue-derived MSC. *Cell Commun. Signal.* **9,** 12 (2011).

167. Wang, L., Tran, I., Seshareddy, K., Weiss, M. L. & Detamore, M. S. A comparison of human bone marrow-derived mesenchymal stem cells and human umbilical cord-derived mesenchymal stromal cells for cartilage tissue engineering. *Tissue Eng. Part A* **15,** 2259–2266 (2009).

168. Barlow, S. *et al.* Comparison of human placenta- and bone marrow-derived multipotent mesenchymal stem cells. *Stem Cells Dev.* **17,** 1095–1107 (2008).

169. Brooke, G., Tong, H., Levesque, J.-P. & Atkinson, K. Molecular trafficking mechanisms of multipotent mesenchymal stem cells derived from human bone marrow and placenta. *Stem Cells Dev.* **17,** 929–940 (2008).

170. Baksh, D., Song, L. & Tuan, R. S. Adult mesenchymal stem cells: characterization, differentiation, and application in cell and gene therapy. *J. Cell. Mol. Med.* **8,** 301–316 (2004).

171. Lu, L. L. *et al.* Isolation and characterization of human umbilical cord mesenchymal stem cells with hematopoiesis-supportive function and other potentials. *Haematologica* **91,** 1017–1026 (2006).

172. Van Harmelen, V., Röhrig, K. & Hauner, H. Comparison of proliferation and differentiation capacity of human adipocyte precursor cells from the omental and subcutaneous adipose tissue depot of obese subjects. *Metabolism.* **53,** 632–637 (2004).

173. Shi, Y.-Y., Nacamuli, R. P., Salim, A. & Longaker, M. T. The osteogenic potential of adipose-derived mesenchymal cells is maintained with aging. *Plast. Reconstr. Surg.* **116,** 1686–1696 (2005).

174. Schipper, B. M., Marra, K. G., Zhang, W., Donnenberg, A. D. & Rubin, J. P. Regional anatomic and age effects on cell function of human adipose-derived stem cells. *Ann. Plast. Surg.* **60,** 538–544 (2008).

175. Thiede, M. A., Pittenger, M. F. & Mbalaviele, G. Vitro maintenance of hematopoietic stem cells. (2000).

176. Zhang, T. *et al.* Bone marrow-derived mesenchymal stem cells promote growth and angiogenesis of breast and prostate tumors. *Stem Cell Res. Ther.* **4,** 70 (2013).

177. Gnecchi, M. *et al.* Paracrine action accounts for marked protection of ischemic heart by Akt-modified mesenchymal stem cells. *Nat. Med.* **11,** 367–368 (2005).

178. Dai, W., Hale, S. L. & Kloner, R. A. Role of a paracrine action of mesenchymal stem cells in the improvement of left ventricular function after coronary artery occlusion in rats. *Regen. Med.* **2,** 63–68 (2007).

179. Yu, X.-Y. *et al.* The effects of mesenchymal stem cells on c-kit up-regulation and cell-cycle re-entry of neonatal cardiomyocytes are mediated by activation of insulin-like growth factor 1 receptor. *Mol. Cell. Biochem.* **332,** 25–32 (2009).

180. Chen, T. S. *et al.* Mesenchymal stem cell secretes microparticles enriched in pre-microRNAs. *Nucleic Acids Res.* **38,** 215–224 (2010).

181. Lee, J. W., Fang, X., Krasnodembskaya, A., Howard, J. P. & Matthay, M. A. Concise review: Mesenchymal stem cells for acute lung injury: role of paracrine soluble factors. *Stem Cells Dayt. Ohio* **29,** 913–919 (2011).

182. Devine, S. M. *et al.* Mesenchymal stem cells are capable of homing to the bone marrow of non-human primates following systemic infusion. *Exp. Hematol.* **29,** 244–255 (2001).

183. Bruder, S. P. *et al.* Bone regeneration by implantation of purified, culture-expanded human mesenchymal stem cells. *J. Orthop. Res. Off. Publ. Orthop. Res. Soc.* **16,** 155–162 (1998).

184. Bruder, S. P., Kraus, K. H., Goldberg, V. M. & Kadiyala, S. The effect of implants loaded with autologous mesenchymal stem cells on the healing of canine segmental bone defects. *J. Bone Joint Surg. Am.* **80,** 985–996 (1998).

185. Kruyt, M. C. *et al.* Optimization of bone-tissue engineering in goats. *J. Biomed. Mater. Res. B Appl. Biomater.* **69B,** 113–120 (2004).

186. Bensaïd, W. *et al.* De novo reconstruction of functional bone by tissue engineering in the metatarsal sheep model. *Tissue Eng.* **11,** 814–824 (2005).

187. Frank, O. *et al.* Real-time quantitative RT-PCR analysis of human bone marrow stromal cells during osteogenic differentiation in vitro. *J. Cell. Biochem.* **85,** 737–746 (2002).

188. Ducy, P. & Karsenty, G. Genetic control of cell differentiation in the skeleton. *Curr. Opin. Cell Biol.* **10,** 614–619 (1998).

189. Lee, K.-S. *et al.* Runx2 Is a Common Target of Transforming Growth Factor β1 and Bone Morphogenetic Protein 2, and Cooperation between Runx2 and Smad5 Induces Osteoblast-Specific Gene Expression in the Pluripotent Mesenchymal Precursor Cell Line C2C12. *Mol. Cell. Biol.* **20,** 8783–8792 (2000).

190. Lee, M.-H. *et al.* BMP-2-induced Runx2 expression is mediated by Dlx5, and TGF-beta 1 opposes the BMP-2-induced osteoblast differentiation by suppression of Dlx5 expression. *J. Biol. Chem.* **278,** 34387–34394 (2003).

191. Lee, M.-H., Kwon, T.-G., Park, H.-S., Wozney, J. M. & Ryoo, H.-M. BMP-2-induced Osterix expression is mediated by Dlx5 but is independent of Runx2. *Biochem. Biophys. Res. Commun.* **309,** 689–694 (2003).

192. Gaur, T. *et al.* Canonical WNT signaling promotes osteogenesis by directly stimulating Runx2 gene expression. *J. Biol. Chem.* **280,** 33132–33140 (2005).

193. Enomoto, H. *et al.* Runx2 deficiency in chondrocytes causes adipogenic changes in vitro. *J. Cell Sci.* **117,** 417–425 (2004).

194. Harada, S. & Rodan, G. A. Control of osteoblast function and regulation of bone mass. *Nature* **423,** 349–355 (2003).

195. Matsubara, T. *et al.* BMP2 regulates Osterix through Msx2 and Runx2 during osteoblast differentiation. *J. Biol. Chem.* **283,** 29119–29125 (2008).

196. Liu, W. *et al.* Overexpression of Cbfa1 in osteoblasts inhibits osteoblast maturation and causes osteopenia with multiple fractures. *J. Cell Biol.* **155,** 157–166 (2001).

197. Nakashima, K. *et al.* The Novel Zinc Finger-Containing Transcription Factor Osterix Is Required for Osteoblast Differentiation and Bone Formation. *Cell* **108,** 17–29 (2002).

198. Oldberg, A., Franzén, A. & Heinegård, D. Cloning and sequence analysis of rat bone sialoprotein (osteopontin) cDNA reveals an Arg-Gly-Asp cell-binding sequence. *Proc. Natl. Acad. Sci. U. S. A.* **83,** 8819–8823 (1986).

199. Hauschka, P. V., Lian, J. B., Cole, D. E. & Gundberg, C. M. Osteocalcin and matrix Gla protein: vitamin K-dependent proteins in bone. *Physiol. Rev.* **69,** 990–1047 (1989).

200. Pavlin, D., Dove, S. B., Zadro, R. & Gluhak-Heinrich, J. Mechanical loading stimulates differentiation of periodontal osteoblasts in a mouse osteoinduction model: effect on type I collagen and alkaline phosphatase genes. *Calcif. Tissue Int.* **67,** 163–172 (2000).

201. Pavlin, D., Zadro, R. & Gluhak-Heinrich, J. Temporal pattern of stimulation of osteoblast-associated genes during mechanically-induced osteogenesis in vivo: early responses of osteocalcin and type I collagen. *Connect. Tissue Res.* **42,** 135–148 (2001).

202. Petit, I. *et al.* G-CSF induces stem cell mobilization by decreasing bone marrow SDF-1 and up-regulating CXCR4. *Nat. Immunol.* **3,** 687–694 (2002).

203. Lévesque, J.-P., Hendy, J., Takamatsu, Y., Simmons, P. J. & Bendall, L. J. Disruption of the CXCR4/CXCL12 chemotactic interaction during hematopoietic stem cell mobilization induced by GCSF or cyclophosphamide. *J. Clin. Invest.* **111,** 187–196 (2003).

204. Lévesque, J.-P., Hendy, J., Winkler, I. G., Takamatsu, Y. & Simmons, P. J. Granulocyte colony-stimulating factor induces the release in the bone marrow of proteases that cleave c-KIT receptor (CD117) from the surface of hematopoietic progenitor cells. *Exp. Hematol.* **31,** 109–117 (2003).

205. Kawada, H. *et al.* Nonhematopoietic mesenchymal stem cells can be mobilized and differentiate into cardiomyocytes after myocardial infarction. *Blood* **104,** 3581–3587 (2004).

206. Zhao, D.-C. *et al.* Bone marrow-derived mesenchymal stem cells protect against experimental liver fibrosis in rats. *World J. Gastroenterol. WJG* **11,** 3431–3440 (2005).

207. Rubart, M. & Field, L. J. Cardiac repair by embryonic stem-derived cells. *Handb. Exp. Pharmacol.* 73–100 (2006).

208. Horwitz, E. M. *et al.* Isolated allogeneic bone marrow-derived mesenchymal cells engraft and stimulate growth in children with osteogenesis imperfecta: Implications for cell therapy of bone. *Proc. Natl. Acad. Sci. U. S. A.* **99,** 8932–8937 (2002).

209. Lazarus, H. M. *et al.* Cotransplantation of HLA-identical sibling culture-expanded mesenchymal stem cells and hematopoietic stem cells in hematologic malignancy patients. *Biol. Blood Marrow Transplant. J. Am. Soc. Blood Marrow Transplant.* **11,** 389–398 (2005).

210. Granero-Moltó, F. *et al.* Regenerative effects of transplanted mesenchymal stem cells in fracture healing. *Stem Cells Dayt. Ohio* **27,** 1887–1898 (2009).

211. Jones, E. & McGonagle, D. Human bone marrow mesenchymal stem cells in vivo. *Rheumatology* **47,** 126–131 (2008).

212. Bernardo, M. E., Locatelli, F. & Fibbe, W. E. Mesenchymal Stromal Cells. *Ann. N. Y. Acad. Sci.* **1176,** 101–117 (2009).

213. Liu, J.-F., Wang, B.-W., Hung, H.-F., Chang, H. & Shyu, K.-G. Human mesenchymal stem cells improve myocardial performance in a splenectomized rat model of chronic myocardial infarction. *J. Formos. Med. Assoc. Taiwan Yi Zhi* **107,** 165–174 (2008).

214. Hare, J. M. *et al.* A randomized, double-blind, placebo-controlled, dose-escalation study of intravenous adult human mesenchymal stem cells (prochymal) after acute myocardial infarction. *J. Am. Coll. Cardiol.* **54,** 2277–2286 (2009).

215. Mizuno, H. Adipose-derived stem and stromal cells for cell-based therapy: current status of preclinical studies and clinical trials. *Curr. Opin. Mol. Ther.* **12,** 442–449 (2010).

216. Bullens, P. H. J., Schreuder, H. W. B., Malefijt, M. C. de W., Verdonschot, N. & Buma, P. The presence of periosteum is essential for the healing of large diaphyseal segmental bone defects reconstructed with trabecular metal: A study in the femur of goats. *J. Biomed. Mater. Res. B Appl. Biomater.* **92B,** 24–31 (2010).

217. Tran Van, P. T., Vignery, A. & Baron, R. Cellular kinetics of the bone remodeling sequence in the rat. *Anat. Rec.* **202,** 445–451 (1982).

218. De Bari, C. *et al.* Mesenchymal multipotency of adult human periosteal cells demonstrated by single-cell lineage analysis. *Arthritis Rheum.* **54,** 1209–1221 (2006).

219. Soltan, M., Smiler, D. & Soltan, C. The inverted periosteal flap: a source of stem cells enhancing bone regeneration. *Implant Dent.* **18,** 373–379 (2009).

220. Jacobsen, F. S. Periosteum: its relation to pediatric fractures. *J. Pediatr. Orthop. Part B* **6,** 84–90 (1997).

221. Melcher, A. H. & Accursi, G. E. Osteogenic capacity of periosteal and osteoperiosteal flaps elevated from the parietal bone of the rat. *Arch. Oral Biol.* **16,** 573–580 (1971).

222. Lemperle, S. M., Calhoun, C. J., Curran, R. W. & Holmes, R. E. Bony healing of large cranial and mandibular defects protected from soft-tissue interposition: A comparative study of spontaneous bone regeneration, osteoconduction, and cancellous autografting in dogs. *Plast. Reconstr. Surg.* **101,** 660–672 (1998).

223. Runyan, C. M. *et al.* Porcine allograft mandible revitalization using autologous adipose-derived stem cells, bone morphogenetic protein-2, and periosteum. *Plast. Reconstr. Surg.* **125,** 1372–1382 (2010).

224. Bruder, S. P., Jaiswal, N. & Haynesworth, S. E. Growth kinetics, self-renewal, and the osteogenic potential of purified human mesenchymal stem cells during extensive subcultivation and following cryopreservation. *J. Cell. Biochem.* **64,** 278–294 (1997).

225. Bruder, S. P., Horowitz, M. C., Mosca, J. D. & Haynesworth, S. E. Monoclonal antibodies reactive with human osteogenic cell surface antigens. *Bone* **21,** 225–235 (1997).

226. Benayahu, D., Fried, A., Zipori, D. & Wientroub, S. Subpopulations of marrow stromal cells share a variety of osteoblastic markers. *Calcif. Tissue Int.* **49,** 202–207 (1991).

227. Xiao, Y., Mareddy, S. & Crawford, R. Clonal characterization of bone marrow derived stem cells and their application for bone regeneration. *Int. J. Oral Sci.* **2,** 127–135 (2010).

228. Salter, E. *et al.* Bone tissue engineering bioreactors: a role in the clinic? *Tissue Eng. Part B Rev.* **18,** 62–75 (2012).

229. Barry, F. P., Boynton, R. E., Haynesworth, S., Murphy, J. M. & Zaia, J. The monoclonal antibody SH-2, raised against human mesenchymal stem cells, recognizes an epitope on endoglin (CD105). *Biochem. Biophys. Res. Commun.* **265,** 134–139 (1999).

230. Minguell, J. J., Erices, A. & Conget, P. Mesenchymal Stem Cells. *Exp. Biol. Med.* **226,** 507–520 (2001).

231. Luria, E. A., Panasyuk, A. F. & Friedenstein, A. Y. Fibroblast colony formation from monolayer cultures of blood cells. *Transfusion (Paris)* **11,** 345–349 (1971).

232. Kassem, M., Mosekilde, L. & Eriksen, E. F. 1,25-dihydroxyvitamin D3 potentiates fluoride-stimulated collagen type I production in cultures of human bone marrow stromal osteoblast-like cells. *J. Bone Miner. Res. Off. J. Am. Soc. Bone Miner. Res.* **8,** 1453–1458 (1993).

233. Abdallah, B. M. & Kassem, M. The use of mesenchymal (skeletal) stem cells for treatment of degenerative diseases: current status and future perspectives. *J. Cell. Physiol.* **218,** 9–12 (2009).

234. Bruder, S. P., Fink, D. J. & Caplan, A. I. Mesenchymal stem cells in bone development, bone repair, and skeletal regeneration therapy. *J. Cell. Biochem.* **56,** 283–294 (1994).

235. Campagnoli, C. *et al.* Identification of mesenchymal stem/progenitor cells in human first-trimester fetal blood, liver, and bone marrow. *Blood* **98,** 2396–2402 (2001).

236. Hernigou, P., Poignard, A., Manicom, O., Mathieu, G. & Rouard, H. The use of percutaneous autologous bone marrow transplantation in nonunion and avascular necrosis of bone. *J. Bone Joint Surg. Br.* **87,** 896–902 (2005).

237. Kuznetsov, S. A. *et al.* Single-colony derived strains of human marrow stromal fibroblasts form bone after transplantation in vivo. *J. Bone Miner. Res. Off. J. Am. Soc. Bone Miner. Res.* **12,** 1335–1347 (1997).

238. Bianchi, G. *et al.* Ex vivo enrichment of mesenchymal cell progenitors by fibroblast growth factor 2. *Exp. Cell Res.* **287,** 98–105 (2003).

239. Asatrian, G., Pham, D., Hardy, W. R., James, A. W. & Peault, B. Stem cell technology for bone regeneration: current status and potential applications. *Stem Cells Cloning Adv. Appl.* **8,** 39–48 (2015).

240. Bruder, S. P. & Fox, B. S. Tissue engineering of bone. Cell based strategies. *Clin. Orthop.* S68-83 (1999).

241. Shim, W. S. N. *et al.* Ex vivo differentiation of human adult bone marrow stem cells into cardiomyocyte-like cells. *Biochem. Biophys. Res. Commun.* **324,** 481–488 (2004).

242. McLain, R. F., Boehm, C. A., Rufo-Smith, C. & Muschler, G. F. Transpedicular aspiration of osteoprogenitor cells from the vertebral body: progenitor cell concentrations affected by serial aspiration. *Spine J. Off. J. North Am. Spine Soc.* **9,** 995–1002 (2009).

243. Mazzocca, A. D. *et al.* Rapid isolation of human stem cells (connective tissue progenitor cells) from the proximal humerus during arthroscopic rotator cuff surgery. *Am. J. Sports Med.* **38,** 1438–1447 (2010).

244. Mazzocca, A. D. *et al.* Bone marrow-derived mesenchymal stem cells obtained during arthroscopic rotator cuff repair surgery show potential for tendon cell differentiation after treatment with insulin. *Arthrosc. J. Arthrosc. Relat. Surg. Off. Publ. Arthrosc. Assoc. N. Am. Int. Arthrosc. Assoc.* **27,** 1459–1471 (2011).

245. Narbona-Carceles, J., Vaquero, J., Suárez-Sancho, S. B. S., Forriol, F. & Fernández-Santos, M. E. Bone marrow mesenchymal stem cell aspirates from alternative sources: is the knee as good as the iliac crest? *Injury* **45 Suppl 4,** S42-47 (2014).

246. Guilak, F. *et al.* Clonal analysis of the differentiation potential of human adipose-derived adult stem cells. *J. Cell. Physiol.* **206,** 229–237 (2006).

247. Russell, K. C. *et al.* Clonal analysis of the proliferation potential of human bone marrow mesenchymal stem cells as a function of potency. *Biotechnol. Bioeng.* **108,** 2716–2726 (2011).

248. Gentili, C. *et al.* Cell proliferation, extracellular matrix mineralization, and ovotransferrin transient expression during in vitro differentiation of chick hypertrophic chondrocytes into osteoblast-like cells. *J. Cell Biol.* **122,** 703–712 (1993).

249. Galotto, M. *et al.* Hypertrophic chondrocytes undergo further differentiation to osteoblast-like cells and participate in the initial bone formation in developing chick embryo. *J. Bone Miner. Res. Off. J. Am. Soc. Bone Miner. Res.* **9,** 1239–1249 (1994).

250. Siegel, G. *et al.* Phenotype, donor age and gender affect function of human bone marrow-derived mesenchymal stromal cells. *BMC Med.* **11,** 146 (2013).

251. Phinney, D. G. *et al.* Donor variation in the growth properties and osteogenic potential of human marrow stromal cells. *J. Cell. Biochem.* **75,** 424–436 (1999).

252. Russell, K. C. *et al.* In vitro high-capacity assay to quantify the clonal heterogeneity in trilineage potential of mesenchymal stem cells reveals a complex hierarchy of lineage commitment. *Stem Cells Dayt. Ohio* **28,** 788–798 (2010).

253. Quirici, N. *et al.* Isolation of bone marrow mesenchymal stem cells by anti-nerve growth factor receptor antibodies. *Exp. Hematol.* **30,** 783–791 (2002).

254. Schäfer, R. *et al.* Basic research and clinical applications of non-hematopoietic stem cells, 4-5 April 2008, Tubingen, Germany. *Cytotherapy* **11,** 245–255 (2009).

255. Schäfer, R. *et al.* Expression of blood group genes by mesenchymal stem cells. *Br. J. Haematol.* **153,** 520–528 (2011).

256. Siddappa, R., Licht, R., van Blitterswijk, C. & de Boer, J. Donor variation and loss of multipotency during in vitro expansion of human mesenchymal stem cells for bone tissue engineering. *J. Orthop. Res. Off. Publ. Orthop. Res. Soc.* **25,** 1029–1041 (2007).

257. McCoy, R. J. & O’Brien, F. J. Influence of shear stress in perfusion bioreactor cultures for the development of three-dimensional bone tissue constructs: a review. *Tissue Eng. Part B Rev.* **16,** 587–601 (2010).

258. Burger, E. H., Klein-Nulend, J. & Veldhuijzen, J. P. Mechanical stress and osteogenesis in vitro. *J. Bone Miner. Res.* **7,** S397–S401 (1992).

259. Burger, E. H. & Klein-Nulend, J. Mechanotransduction in bone--role of the lacuno-canalicular network. *FASEB J. Off. Publ. Fed. Am. Soc. Exp. Biol.* **13 Suppl,** S101-112 (1999).

260. Macdonald, A. G. & Fraser, P. J. The transduction of very small hydrostatic pressures. *Comp. Biochem. Physiol. A. Mol. Integr. Physiol.* **122,** 13–36 (1999).

261. Mullender, D. M. *et al.* Mechanotransduction of bone cellsin vitro: Mechanobiology of bone tissue. *Med. Biol. Eng. Comput.* **42,** 14–21 (2004).

262. Lelkes, G. Experiments in vitro on the role of movement in the development of joints. *J. Embryol. Exp. Morphol.* **6,** 183–186 (1958).

263. Hosseini, A. & Hogg, D. A. The effects of paralysis on skeletal development in the chick embryo. I. General effects. *J. Anat.* **177,** 159–168 (1991).

264. Hosseini, A. & Hogg, D. A. The effects of paralysis on skeletal development in the chick embryo. II. Effects on histogenesis of the tibia. *J. Anat.* **177,** 169–178 (1991).

265. Carter, D. R., Beaupré, G. S., Giori, N. J. & Helms, J. A. Mechanobiology of skeletal regeneration. *Clin. Orthop.* S41-55 (1998).

266. Meinel, L. *et al.* Silk implants for the healing of critical size bone defects. *Bone* **37,** 688–698 (2005).

267. Zhang, Z.-Y. *et al.* A biaxial rotating bioreactor for the culture of fetal mesenchymal stem cells for bone tissue engineering. *Biomaterials* **30,** 2694–2704 (2009).

268. Yourek, G., McCormick, S. M., Mao, J. J. & Reilly, G. C. Shear stress induces osteogenic differentiation of human mesenchymal stem cells. *Regen. Med.* **5,** 713–724 (2010).

269. Jansen, J. H. *et al.* Stimulation of osteogenic differentiation in human osteoprogenitor cells by pulsed electromagnetic fields: an in vitro study. *BMC Musculoskelet. Disord.* **11,** 188 (2010).

270. Hess, R. *et al.* Hydrostatic pressure stimulation of human mesenchymal stem cells seeded on collagen-based artificial extracellular matrices. *J. Biomech. Eng.* **132,** 21001 (2010).

271. Sellgren, K. L. & Ma, T. Effects of flow configuration on bone tissue engineering using human mesenchymal stem cells in 3D chitosan composite scaffolds. *J. Biomed. Mater. Res. A* **103(8)**, 2509–2520 (2014).

272. Kleinhans, C. *et al.* A perfusion bioreactor system efficiently generates cell-loaded bone substitute materials for addressing critical size bone defects. *Biotechnol. J.* 10(11), 1727–1738 (2015).

273. Porta, G. D., Nguyen, B.-N. B., Campardelli, R., Reverchon, E. & Fisher, J. P. Synergistic effect of sustained release of growth factors and dynamic culture on osteoblastic differentiation of mesenchymal stem cells. *J. Biomed. Mater. Res. A* **103,** 2161–2171 (2015).

274. Rotherham, M. & El Haj, A. J. Remote activation of the Wnt/β-catenin signalling pathway using functionalised magnetic particles. *PloS One* **10,** e0121761 (2015).

275. Woloszyk, A. *et al.* Influence of the mechanical environment on the engineering of mineralised tissues using human dental pulp stem cells and silk fibroin scaffolds. *PloS One* **9,** e111010 (2014).

276. Henstock, J. R., Rotherham, M., Rose, J. B. & El Haj, A. J. Cyclic hydrostatic pressure stimulates enhanced bone development in the foetal chick femur in vitro. *Bone* **53,** 468–477 (2013).

277. Ehrlich, P. J. & Lanyon, L. E. Mechanical strain and bone cell function: a review. *Osteoporos. Int. J. Establ. Result Coop. Eur. Found. Osteoporos. Natl. Osteoporos. Found. USA* **13,** 688–700 (2002).

278. Yamamoto, K. *et al.* Proliferation, differentiation, and tube formation by endothelial progenitor cells in response to shear stress. *J. Appl. Physiol. Bethesda Md 1985* **95,** 2081–2088 (2003).

279. Yamamoto, K. *et al.* Fluid shear stress induces differentiation of Flk-1-positive embryonic stem cells into vascular endothelial cells in vitro. *Am. J. Physiol. Heart Circ. Physiol.* **288,** H1915-1924 (2005).

280. McCloskey, K. E., Smith, D. A., Jo, H. & Nerem, R. M. Embryonic stem cell-derived endothelial cells may lack complete functional maturation in vitro. *J. Vasc. Res.* **43,** 411–421 (2006).

281. Grellier, M., Bareille, R., Bourget, C. & Amédée, J. Responsiveness of human bone marrow stromal cells to shear stress. *J. Tissue Eng. Regen. Med.* **3,** 302–309 (2009).

282. Stolberg, S. & McCloskey, K. E. Can shear stress direct stem cell fate? *Biotechnol. Prog.* **25,** 10–19 (2009).

283. Kimelman-Bleich, N. *et al.* The effect of ex vivo dynamic loading on the osteogenic differentiation of genetically engineered mesenchymal stem cell model. *J. Tissue Eng. Regen. Med.* **5,** 384–393 (2011).

284. Frieboes, L. R. & Gupta, R. An in-vitro traumatic model to evaluate the response of myelinated cultures to sustained hydrostatic compression injury. *J. Neurotrauma* **26,** 2245–2256 (2009).

285. Reinwald, Y. *et al.* Evaluation of the growth environment of a hydrostatic force bioreactor for preconditioning of tissue-engineered constructs. *Tissue Eng. Part C Methods* **21,** 1–14 (2015).

286. Pörtner, R., Nagel-Heyer, S., Goepfert, C., Adamietz, P. & Meenen, N. M. Bioreactor design for tissue engineering. *J. Biosci. Bioeng.* **100,** 235–245 (2005).

287. Darling, E. M. & Athanasiou, K. A. Articular cartilage bioreactors and bioprocesses. *Tissue Eng.* **9,** 9–26 (2003).

288. Hanson, M. A. *et al.* Comparisons of optical pH and dissolved oxygen sensors with traditional electrochemical probes during mammalian cell culture. *Biotechnol. Bioeng.* **97,** 833–841 (2007).

289. V. M. Nock, R. J. B. Micro-patterning of polymer-based optical oxygen sensors for lab-on-chip applications. *Proc. SPIE 6799 BioMEMS and Nanotechnol III* **6799Y** (2007).

290. Metzen, E., Wolff, M., Fandrey, J. & Jelkmann, W. Pericellular PO2 and O2 consumption in monolayer cell cultures. *Respir. Physiol.* **100,** 101–106 (1995).

291. Xu, X., Smith, S., Urban, J. & Cui, Z. An in line non-invasive optical system to monitor pH in cell and tissue culture. *Med. Eng. Phys.* **28,** 468–474 (2006).

292. Malda, J., Klein, T. J. & Upton, Z. The roles of hypoxia in the in vitro engineering of tissues. *Tissue Eng.* **13,** 2153–2162 (2007).

293. Wang, Y. *et al.* The hypoxia-inducible factor alpha pathway couples angiogenesis to osteogenesis during skeletal development. *J. Clin. Invest.* **117,** 1616–1626 (2007).

294. Volkmer, E. *et al.* Hypoxia in static and dynamic 3D culture systems for tissue engineering of bone. *Tissue Eng. Part A* **14,** 1331–1340 (2008).

295. Zhou, H., Purdie, J., Wang, T. & Ouyang, A. pH measurement and a rational and practical pH control strategy for high throughput cell culture system. *Biotechnol. Prog.* **26,** 872–880 (2010).

296. Al Hadi, H., Smerdon, G. R. & Fox, S. W. Hyperbaric oxygen therapy accelerates osteoblast differentiation and promotes bone formation. *J. Dent.* **43,** 382–388 (2015).

297. Langenbach, F. & Handschel, J. Effects of dexamethasone, ascorbic acid and β-glycerophosphate on the osteogenic differentiation of stem cells in vitro. *Stem Cell Res. Ther.* **4,** 117 (2013).

298. Vater, C., Kasten, P. & Stiehler, M. Culture media for the differentiation of mesenchymal stromal cells. *Acta Biomater.* **7,** 463–477 (2011).

299. Fatherazi, S. *et al.* Phosphate regulates osteopontin gene transcription. *J. Dent. Res.* **88,** 39–44 (2009).

300. Tada, H., Nemoto, E., Foster, B. L., Somerman, M. J. & Shimauchi, H. Phosphate increases bone morphogenetic protein-2 expression through cAMP-dependent protein kinase and ERK1/2 pathways in human dental pulp cells. *Bone* **48,** 1409–1416 (2011).

301. Seong, J. M. *et al.* Stem cells in bone tissue engineering. *Biomed. Mater. Bristol Engl.* **5,** 62001 (2010).

302. Igarashi, M. *et al.* Inductive effects of dexamethasone on the gene expression of Cbfa1, Osterix and bone matrix proteins during differentiation of cultured primary rat osteoblasts. *J. Mol. Histol.* **35,** 3–10 (2004).

303. Hamidouche, Z. *et al.* FHL2 mediates dexamethasone-induced mesenchymal cell differentiation into osteoblasts by activating Wnt/beta-catenin signaling-dependent Runx2 expression. *FASEB J. Off. Publ. Fed. Am. Soc. Exp. Biol.* **22,** 3813–3822 (2008).

304. Hong, D. *et al.* Osteoblastogenic effects of dexamethasone through upregulation of TAZ expression in rat mesenchymal stem cells. *J. Steroid Biochem. Mol. Biol.* **116,** 86–92 (2009).

305. Beresford, J. N., Joyner, C. J., Devlin, C. & Triffitt, J. T. The effects of dexamethasone and 1,25-dihydroxyvitamin D3 on osteogenic differentiation of human marrow stromal cells in vitro. *Arch. Oral Biol.* **39,** 941–947 (1994).

306. Fromigué, O., Marie, P. J. & Lomri, A. Differential effects of transforming growth factor beta2, dexamethasone and 1,25-dihydroxyvitamin D on human bone marrow stromal cells. *Cytokine* **9,** 613–623 (1997).

307. D'Ippolito, G., Schiller, P. C., Ricordi, C., Roos, B. A. & Howard, G. A. Age-related osteogenic potential of mesenchymal stromal stem cells from human vertebral bone marrow. *J. Bone Miner. Res. Off. J. Am. Soc. Bone Miner. Res.* **14,** 1115–1122 (1999).

308. Coelho, M. J. & Fernandes, M. H. Human bone cell cultures in biocompatibility testing. Part II: effect of ascorbic acid, beta-glycerophosphate and dexamethasone on osteoblastic differentiation. *Biomaterials* **21,** 1095–1102 (2000).

309. Yamanouchi, K. *et al.* Bone formation by transplanted human osteoblasts cultured within collagen sponge with dexamethasone in vitro. *J. Bone Miner. Res. Off. J. Am. Soc. Bone Miner. Res.* **16,** 857–867 (2001).

310. Cheng, S. L., Yang, J. W., Rifas, L., Zhang, S. F. & Avioli, L. V. Differentiation of human bone marrow osteogenic stromal cells in vitro: induction of the osteoblast phenotype by dexamethasone. *Endocrinology* **134,** 277–286 (1994).

311. Canalis, E., Economides, A. N. & Gazzerro, E. Bone morphogenetic proteins, their antagonists, and the skeleton. *Endocr. Rev.* **24,** 218–235 (2003).

312. Yoon, B. S. & Lyons, K. M. Multiple functions of BMPs in chondrogenesis. *J. Cell. Biochem.* **93,** 93–103 (2004).

313. Wan, M. & Cao, X. BMP signaling in skeletal development. *Biochem. Biophys. Res. Commun.* **328,** 651–657 (2005).

314. Chen, G., Deng, C. & Li, Y.-P. TGF-β and BMP Signaling in Osteoblast Differentiation and Bone Formation. *Int. J. Biol. Sci.* **8,** 272–288 (2012).

315. Geiger, M., Li, R. . & Friess, W. Collagen sponges for bone regeneration with rhBMP-2. *Adv. Drug Deliv. Rev.* **55,** 1613–1629 (2003).

316. Dimitriou, R. & Giannoudis, P. V. Discovery and development of BMPs. *Injury* **36,** S28–S33 (2005).

317. Caplan, A. I. & Correa, D. PDGF in bone formation and regeneration: new insights into a novel mechanism involving MSCs. *J. Orthop. Res. Off. Publ. Orthop. Res. Soc.* **29,** 1795–1803 (2011).

318. Kempen, D. H. R. *et al.* Effect of local sequential VEGF and BMP-2 delivery on ectopic and orthotopic bone regeneration. *Biomaterials* **30,** 2816–2825 (2009).

319. Yang, Y.-Q. *et al.* The role of vascular endothelial growth factor in ossification. *Int. J. Oral Sci.* **4,** 64–68 (2012).

320. Kigami, R. *et al.* FGF-2 angiogenesis in bone regeneration within critical-sized bone defects in rat calvaria. *Implant Dent.* **22,** 422–427 (2013).

321. Tang, Y. *et al.* TGF-β1-induced Migration of Bone Mesenchymal Stem Cells Couples Bone Resorption and Formation. *Nat. Med.* **15,** 757–765 (2009).

322. Caplan, A. I. Review: mesenchymal stem cells: cell-based reconstructive therapy in orthopedics. *Tissue Eng.* **11,** 1198–1211 (2005).

323. Rouwkema, J., Rivron, N. C. & van Blitterswijk, C. A. Vascularization in tissue engineering. *Trends Biotechnol.* **26,** 434–441 (2008).

324. Mitra, J., Tripathi, G., Sharma, A. & Basu, B. Scaffolds for bone tissue engineering: role of surface patterning on osteoblast response. *RSC Adv.* **3,** 11073–11094 (2013).

325. Rentsch, B. *et al.* Embroidered and surface coated polycaprolactone-co-lactide scaffolds. *Biomatter* **2,** 158–165 (2012).

326. Bacakova, L., Filova, E., Parizek, M., Ruml, T. & Svorcik, V. Modulation of cell adhesion, proliferation and differentiation on materials designed for body implants. *Biotechnol. Adv.* **29,** 739–767 (2011).

327. Abagnale, G. *et al.* Surface topography enhances differentiation of mesenchymal stem cells towards osteogenic and adipogenic lineages. *Biomaterials* **61,** 316–326 (2015).

328. Griffin, M. F., Palgrave, R. G., Seifalian, A. M., Butler, P. E. & Kalaskar, D. M. Enhancing tissue integration and angiogenesis of a novel nanocomposite polymer using plasma surface polymerisation, an in vitro and in vivo study. *Biomater Sci* **4,** 145–158 (2016).

329. Zhou, G., Niepel, M. S., Saretia, S. & Groth, T. Reducing the inflammatory responses of biomaterials by surface modification with glycosaminoglycan multilayers. *J. Biomed. Mater. Res. A* **104,** 493–502 (2016).

330. Salasznyk, R. M., Williams, W. A., Boskey, A., Batorsky, A. & Plopper, G. E. Adhesion to Vitronectin and Collagen I Promotes Osteogenic Differentiation of Human Mesenchymal Stem Cells. *J. Biomed. Biotechnol.* **2004,** 24–34 (2004).

331. Mizuno, M. & Kuboki, Y. Osteoblast-related gene expression of bone marrow cells during the osteoblastic differentiation induced by type I collagen. *J. Biochem. (Tokyo)* **129,** 133–138 (2001).

332. Kundu, A. K. & Putnam, A. J. Vitronectin and collagen I differentially regulate osteogenesis in mesenchymal stem cells. *Biochem. Biophys. Res. Commun.* **347,** 347–357 (2006).

333. Vukicevic, S. *et al.* Identification of multiple active growth factors in basement membrane Matrigel suggests caution in interpretation of cellular activity related to extracellular matrix components. *Exp. Cell Res.* **202,** 1–8 (1992).

334. Handschel, J. G. *et al.* Prospects of micromass culture technology in tissue engineering. *Head Face Med.* **3,** 4 (2007).

335. Hall, B. K. & Miyake, T. Divide, accumulate, differentiate: cell condensation in skeletal development revisited. *Int. J. Dev. Biol.* **39,** 881–893 (1995).

336. Rozario, T. & DeSimone, D. W. The extracellular matrix in development and morphogenesis: a dynamic view. *Dev. Biol.* **341,** 126–140 (2010).

337. Owen, T. A. *et al.* Progressive development of the rat osteoblast phenotype in vitro: reciprocal relationships in expression of genes associated with osteoblast proliferation and differentiation during formation of the bone extracellular matrix. *J. Cell. Physiol.* **143,** 420–430 (1990).

338. Rossi, M. I. D. *et al.* Multicellular spheroids of bone marrow stromal cells: a three-dimensional in vitro culture system for the study of hematopoietic cell migration. *Braz. J. Med. Biol. Res.* **38,** 1455–1462 (2005).

339. Berrier, A. L. & Yamada, K. M. Cell–matrix adhesion. *J. Cell. Physiol.* **213,** 565–573 (2007).

340. Kale, S. *et al.* Three-dimensional cellular development is essential for ex vivo formation of human bone. *Nat. Biotechnol.* **18,** 954–958 (2000).

341. Martino, M. M. *et al.* Controlling integrin specificity and stem cell differentiation in 2D and 3D environments through regulation of fibronectin domain stability. *Biomaterials* **30,** 1089–1097 (2009).

342. Ma, D. *et al.* Engineering Injectable Bone Using Bone Marrow Stromal Cell Aggregates. *Stem Cells Dev.* **20,** 989–999 (2011).

343. Temenoff, J. S. & Mikos, A. G. Injectable biodegradable materials for orthopedic tissue engineering. *Biomaterials* **21,** 2405–2412 (2000).

344. Griffith, L. G. & Naughton, G. Tissue Engineering--Current Challenges and Expanding Opportunities. *Science* **295,** 1009–1014 (2002).

345. Xu, X. L. *et al.* Evaluation of different scaffolds for BMP-2 genetic orthopedic tissue engineering. *J. Biomed. Mater. Res. B Appl. Biomater.* **75,** 289–303 (2005).

346. Logeart-Avramoglou, D., Anagnostou, F., Bizios, R. & Petite, H. Engineering bone: challenges and obstacles. *J. Cell. Mol. Med.* **9,** 72–84 (2005).

347. Ko, H. C. H., Milthorpe, B. K. & McFarland, C. D. Engineering thick tissues--the vascularisation problem. *Eur. Cell. Mater.* **14,** 1-18-19 (2007).

348. Kanczler, J. M. & Oreffo, R. O. C. Osteogenesis and angiogenesis: the potential for engineering bone. *Eur. Cell. Mater.* **15,** 100–114 (2008).

349. Melchiorri, A. J., Nguyen, B.-N. B. & Fisher, J. P. Mesenchymal Stem Cells: Roles and Relationships in Vascularization. *Tissue Eng. Part B Rev.* **20,** 218–228 (2014).

350. Lovett, M., Lee, K., Edwards, A. & Kaplan, D. L. Vascularization strategies for tissue engineering. *Tissue Eng. Part B Rev.* **15,** 353–370 (2009).

351. Fuchs, S., Hofmann, A. & Kirkpatrick, C. J. Microvessel-like structures from outgrowth endothelial cells from human peripheral blood in 2-dimensional and 3-dimensional co-cultures with osteoblastic lineage cells. *Tissue Eng.* **13,** 2577–2588 (2007).

352. Melero-Martin, J. M. *et al.* Engineering robust and functional vascular networks in vivo with human adult and cord blood-derived progenitor cells. *Circ. Res.* **103,** 194–202 (2008).

353. Fuchs, S. *et al.* Contribution of outgrowth endothelial cells from human peripheral blood on in vivo vascularization of bone tissue engineered constructs based on starch polycaprolactone scaffolds. *Biomaterials* **30,** 526–534 (2009).

354. Tsigkou, O. *et al.* Engineered vascularized bone grafts. *Proc. Natl. Acad. Sci. U. S. A.* **107,** 3311–3316 (2010).

355. McFadden, T. M. *et al.* The delayed addition of human mesenchymal stem cells to pre-formed endothelial cell networks results in functional vascularization of a collagen-glycosaminoglycan scaffold in vivo. *Acta Biomater.* **9,** 9303–9316 (2013).

356. Friedenstein, A. J. Precursor cells of mechanocytes. *Int. Rev. Cytol.* **47,** 327–359 (1976).

357. Reynolds, B. A. & Weiss, S. Generation of neurons and astrocytes from isolated cells of the adult mammalian central nervous system. *Science* **255,** 1707–1710 (1992).

358. Osawa, M., Hanada, K., Hamada, H. & Nakauchi, H. Long-term lymphohematopoietic reconstitution by a single CD34-low/negative hematopoietic stem cell. *Science* **273,** 242–245 (1996).

359. Prockop, D. J. Marrow stromal cells as stem cells for nonhematopoietic tissues. *Science* **276,** 71–74 (1997).

360. Dezawa, M., Takahashi, I., Esaki, M., Takano, M. & Sawada, H. Sciatic nerve regeneration in rats induced by transplantation of in vitro differentiated bone-marrow stromal cells. *Eur. J. Neurosci.* **14,** 1771–1776 (2001).

361. Oyagi, S. *et al.* Therapeutic effect of transplanting HGF-treated bone marrow mesenchymal cells into CCl4-injured rats. *J. Hepatol.* **44,** 742–748 (2006).

362. Kuroda, Y. & Dezawa, M. Mesenchymal Stem Cells and Their Subpopulation, Pluripotent Muse Cells, in Basic Research and Regenerative Medicine. *Anat. Rec.* **297,** 98–110 (2014).

363. Vogel, W. *et al.* Heterogeneity among human bone marrow-derived mesenchymal stem cells and neural progenitor cells. *Haematologica* **88,** 126–133 (2003).

364. Phinney, D. G. Biochemical heterogeneity of mesenchymal stem cell populations: clues to their therapeutic efficacy. *Cell Cycle Georget. Tex* **6,** 2884–2889 (2007).

365. Jiang, Y. *et al.* Pluripotency of mesenchymal stem cells derived from adult marrow. *Nature* **418,** 41–49 (2002).

366. Ratajczak, M. Z., Kucia, M., Majka, M., Reca, R. & Ratajczak, J. Heterogeneous populations of bone marrow stem cells--are we spotting on the same cells from the different angles? *Folia Histochem. Cytobiol. Pol. Acad. Sci. Pol. Histochem. Cytochem. Soc.* **42,** 139–146 (2004).

367. D'Ippolito, G., Howard, G. A., Roos, B. A. & Schiller, P. C. Isolation and characterization of marrow-isolated adult multilineage inducible (MIAMI) cells. *Exp. Hematol.* **34,** 1608–1610 (2006).

368. Ratajczak, M. Z., Zuba-Surma, E. K., Wysoczynski, M., Ratajczak, J. & Kucia, M. Very small embryonic-like stem cells: characterization, developmental origin, and biological significance. *Exp. Hematol.* **36,** 742–751 (2008).

369. Majore, I., Moretti, P., Hass, R. & Kasper, C. Identification of subpopulations in mesenchymal stem cell-like cultures from human umbilical cord. *Cell Commun. Signal.* **7,** 6 (2009).

370. Wagner, W. & Ho, A. Mesenchymal Stem Cell Preparations—Comparing Apples and Oranges. *Stem Cell Rev. Rep.* **3,** 239–248 (2007).

371. Ho, A. D., Wagner, W. & Franke, W. Heterogeneity of mesenchymal stromal cell preparations. *Cytotherapy* **10,** 320–330 (2008).

372. Colter, D. C., Sekiya, I. & Prockop, D. J. Identification of a subpopulation of rapidly self-renewing and multipotential adult stem cells in colonies of human marrow stromal cells. *Proc. Natl. Acad. Sci.* **98,** 7841–7845 (2001).

373. Hung, S.-C. *et al.* Isolation and characterization of size-sieved stem cells from human bone marrow. *Stem Cells Dayt. Ohio* **20,** 249–258 (2002).

374. Verfaillie, C. M., Schwartz, R., Reyes, M. & Jiang, Y. Unexpected potential of adult stem cells. *Ann. N. Y. Acad. Sci.* **996,** 231–234 (2003).

375. Pochampally, R. R., Smith, J. R., Ylostalo, J. & Prockop, D. J. Serum deprivation of human marrow stromal cells (hMSCs) selects for a subpopulation of early progenitor cells with enhanced expression of OCT-4 and other embryonic genes. *Blood* **103,** 1647–1652 (2004).

376. Smith, J. R., Pochampally, R., Perry, A., Hsu, S.-C. & Prockop, D. J. Isolation of a highly clonogenic and multipotential subfraction of adult stem cells from bone marrow stroma. *Stem Cells Dayt. Ohio* **22,** 823–831 (2004).

377. Leyva-Leyva, M. *et al.* Characterization of mesenchymal stem cell subpopulations from human amniotic membrane with dissimilar osteoblastic potential. *Stem Cells Dev.* **22,** 1275–1287 (2013).

378. Kucia, M. *et al.* A population of very small embryonic-like (VSEL) CXCR4+SSEA-1+Oct-4+ stem cells identified in adult bone marrow. *Leukemia* **20,** 857–869 (2006).

379. Wojakowski, W. *et al.* Very small embryonic-like stem cells in cardiovascular repair. *Pharmacol. Ther.* **129,** 21–28 (2011).

380. Kuroda, Y. *et al.* Unique multipotent cells in adult human mesenchymal cell populations. *Proc. Natl. Acad. Sci.* **107,** 8639–8643 (2010).

381. D'Ippolito, G. *et al.* Marrow-isolated adult multilineage inducible (MIAMI) cells, a unique population of postnatal young and old human cells with extensive expansion and differentiation potential. *J. Cell Sci.* **117,** 2971–2981 (2004).

382. Yamawaki, H., Pan, S., Lee, R. T. & Berk, B. C. Fluid shear stress inhibits vascular inflammation by decreasing thioredoxin-interacting protein in endothelial cells. *J. Clin. Invest.* **115,** 733–738 (2005).

383. Neuhuber, B. *et al.* Reevaluation of in vitro differentiation protocols for bone marrow stromal cells: Disruption of actin cytoskeleton induces rapid morphological changes and mimics neuronal phenotype. *J. Neurosci. Res.* **77,** 192–204 (2004).

384. Murata, M. *et al.* Application of polyglycolic acid sheet (Neoveil®) and fibrin glue spray (Bolheal®) for open wounds in oral surgery. *J. Jpn. Stomatol. Soc.* **60,** 232–239 (2011).

385. Komura, M. *et al.* Study of mechanical properties of engineered cartilage in an in vivo culture for design of a biodegradable scaffold. *Int. J. Artif. Organs* **33,** 775–781 (2010).

386. Henstock, J. R., Rotherham, M., Rose, J. B. & El Haj, A. J. Cyclic hydrostatic pressure stimulates enhanced bone development in the foetal chick femur in vitro. *Bone* **53,** 468–477 (2013).

387. Schecroun, N. & Delloye, C. . Bone-like nodules formed by human bone marrow stromal cells: comparative study and characterization☆. *Bone* **32,** 252–260 (2003).

388. Shi, C., Wu, J., Yan, Q., Wang, R. & Miao, D. Bone marrow ablation demonstrates that estrogen plays an important role in osteogenesis and bone turnover via an antioxidative mechanism. *Bone* **79,** 94–104 (2015).

389. Wang, H. *et al.* Biglycan mediates suture expansion osteogenesis via potentiation of Wnt/β-catenin signaling. *J. Biomech.* **48,** 432–440 (2015).

390. Yang, C. *et al.* Streptozotocin Aggravated Osteopathology and Insulin Induced Osteogenesis Through Co-treatment with Fluoride. *Biol. Trace Elem. Res.* 1–9 (2015).

391. Gregory, C. A. An Alizarin red-based assay of mineralization by adherent cells in culture: comparison with cetylpyridinium chloride extraction. *Anal. Biochem.* **329,** 77 (2004).

392. Karp, J. M., Mahdavi, A., Ferreira, L. S., Khademhosseini, A. & Langer, R. in *Human Embryonic Stem Cells* (eds. Sullivan, S., Cowan, C. A. & Eggan, K.) 249–271 (John Wiley & Sons, Ltd, 2007).

393. Kinkel, A. D. *et al.* Oil red-O stains non-adipogenic cells: a precautionary note. *Cytotechnology* **46,** 49–56 (2004).

394. Mowry, R. W. The Special Value of Methods That Color Both Acidic and Vicinal Hydroxyl Groups in the Histochemical Study of Mucins. with Revised Directions for the Colloidal Iron Stain, the Use of Alcian Blue G8x and Their Combinations with the Periodic Acid-Schiff Reaction*. *Ann. N. Y. Acad. Sci.* **106,** 402–423 (1963).

395. Ramos-Vara, J. A. Technical aspects of immunohistochemistry. *Vet. Pathol.* **42,** 405–426 (2005).

396. Born, A.-K., Lischer, S. & Maniura-Weber, K. Watching osteogenesis: Life monitoring of osteogenic differentiation using an osteocalcin reporter. *J. Cell. Biochem.* **113,** 313–321 (2012).

397. Pusztaszeri, M. P., Seelentag, W. & Bosman, F. T. Immunohistochemical Expression of Endothelial Markers CD31, CD34, von Willebrand Factor, and Fli-1 in Normal Human Tissues. *J. Histochem. Cytochem.* **54,** 385–395 (2006).

398. German, A. E., Mammoto, T., Jiang, E., Ingber, D. E. & Mammoto, A. Paxillin controls endothelial cell migration and tumor angiogenesis by altering neuropilin 2 expression. *J. Cell Sci.* **127,** 1672–1683 (2014).

399. Warita, K. *et al.* Statin-induced mevalonate pathway inhibition attenuates the growth of mesenchymal-like cancer cells that lack functional E-cadherin mediated cell cohesion. *Sci. Rep.* **4,** (2014).

400. Wells, J. M., Pipa, J. & Shin, S. J. Lobular Neoplasia of the Breast Revisited With Emphasis on the Role of E-cadherin Immunohistochemistry: *Am. J. Surg. Pathol.* **38,** 434–435 (2014).

401. Rouwkema, J., de Boer, J. & Van Blitterswijk, C. A. Endothelial cells assemble into a 3-dimensional prevascular network in a bone tissue engineering construct. *Tissue Eng.* **12,** 2685–2693 (2006).

402. Arya, M. *et al.* Basic principles of real-time quantitative PCR. *Expert Rev. Mol. Diagn.* **5,** 209–219 (2005).

403. Hamid, H. E. *et al.* in *The 15th International Conference on Biomedical Engineering* (ed. Goh, J.) 239–242 (Springer International Publishing, 2014).

404. Rodrigues, A. I., Leonor, I. B., Reis, R. L., van Blitterswijk, C. & Habibovic, P. Stimulatory effects of inorganic ions on osteogenesis in vitro. *J. Tissue Eng. Regen. Med.* (2014).

405. Martín-Badosa, E. *et al.* Excised bone structures in mice: imaging at three-dimensional synchrotron radiation micro CT. *Radiology* **229,** 921–928 (2003).

406. Kallai, I. *et al.* Microcomputed tomography-based structural analysis of various bone tissue regeneration models. *Nat. Protoc.* **6,** 105–110 (2011).

407. Polak, S. J., Candido, S., Levengood, S. K. L. & Wagoner Johnson, A. J. Automated segmentation of micro-CT images of bone formation in calcium phosphate scaffolds. *Comput. Med. Imaging Graph.* **36,** 54–65 (2012).

408. Bobyn, J. D. *et al.* Local Alendronic Acid Elution Increases Net Periimplant Bone Formation: A Micro-CT Analysis. *Clin. Orthop. Relat. Res.* **472,** 687–694 (2013).

409. Taiani, J. T. *et al.* Embryonic stem cell therapy improves bone quality in a model of impaired fracture healing in the mouse; tracked temporally using in vivo micro-CT. *Bone* **64,** 263–272 (2014).

410. Tower, R. J., Campbell, G. M., Müller, M., Glüer, C. C. & Tiwari, S. Utilizing time-lapse micro-CT-correlated bisphosphonate binding kinetics and soft tissue-derived input functions to differentiate site-specific changes in bone metabolism in vivo. *Bone* **74,** 171–181 (2015).

411. Lienemann, P. S. *et al.* Longitudinal in vivo evaluation of bone regeneration by combined measurement of multi-pinhole SPECT and micro-CT for tissue engineering. *Sci. Rep.* **5,** (2015).

412. Miller, L. M. & Dumas, P. Chemical imaging of biological tissue with synchrotron infrared light. *Biochim. Biophys. Acta* **1758,** 846–857 (2006).

413. Paschalis, E. P., Mendelsohn, R. & Boskey, A. L. Infrared assessment of bone quality: a review. *Clin. Orthop.* **469,** 2170–2178 (2011).

414. Miller, L. M. *et al.* Accretion of Bone Quantity and Quality in the Developing Mouse Skeleton. *J. Bone Miner. Res.* **22,** 1037–1045 (2007).

415. ap Gwynn, I. A. & Gerber, I. Differentiation of rat osteoblast-like cells in monolayer and micromass cultures. (2002).

416. Ferrera, D. *et al.* Three-dimensional cultures of normal human osteoblasts: proliferation and differentiation potential in vitro and upon ectopic implantation in nude mice. *Bone* **30,** 718–725 (2002).

417. Wanka, G., Hoffmann, H. & Ulbricht, W. Phase Diagrams and Aggregation Behavior of Poly(oxyethylene)-Poly(oxypropylene)-Poly(oxyethylene) Triblock Copolymers in Aqueous Solutions. *Macromolecules* **27,** 4145–4159 (1994).

418. Bogner, A., Jouneau, P.-H., Thollet, G., Basset, D. & Gauthier, C. A history of scanning electron microscopy developments: Towards 'wet-STEM' imaging. *Micron* **38,** 390–401 (2007).

419. Lee, Y.-H. *et al.* Synthesis of Large-Area MoS2 Atomic Layers with Chemical Vapor Deposition. *Adv. Mater.* **24,** 2320–2325 (2012).

420. Cuisinier, M. *et al.* Sulfur Speciation in Li–S Batteries Determined by Operando X-ray Absorption Spectroscopy. *J. Phys. Chem. Lett.* **4,** 3227–3232 (2013).

421. Ragon, F. *et al.* In Situ Energy-Dispersive X-ray Diffraction for the Synthesis Optimization and Scale-up of the Porous Zirconium Terephthalate UiO-66. *Inorg. Chem.* **53,** 2491–2500 (2014).

422. Darzynkiewicz, Z. & Zhao, H. in *Cell Cycle Analysis by Glow Cytometry eLS* DOI: 10.1002/9780470015902.a0002571.p (John Wiley & Sons, Ltd, 2001).

423. Boonen, K. J. M., Koldewijn, E. L., Arents, N. L. A., Raaymakers, P. a. M. & Scharnhorst, V. Urine flow cytometry as a primary screening method to exclude urinary tract infections. *World J. Urol.* **31,** 547–551 (2012).

424. Mayle, A., Luo, M., Jeong, M. & Goodell, M. A. Flow cytometry analysis of murine hematopoietic stem cells. *Cytometry A* **83A,** 27–37 (2013).

425. Kelm, J. M., Timmins, N. E., Brown, C. J., Fussenegger, M. & Nielsen, L. K. Method for generation of homogeneous multicellular tumor spheroids applicable to a wide variety of cell types. *Biotechnol. Bioeng.* **83,** 173–180 (2003).

426. Hwang, N. S., Zhang, C., Hwang, Y. & Varghese, S. Mesenchymal stem cell differentiation and roles in regenerative medicine. *Wiley Interdiscip. Rev. Syst. Biol. Med.* **1,** 97–106 (2009).

427. Handschel, J. *et al.* Comparison of ectopic bone formation of embryonic stem cells and cord blood stem cells in vivo. *Tissue Eng. Part A* **16,** 2475–2483 (2010).

428. Boskey, A. & Camacho, N. P. FT-IR Imaging of Native and Tissue-Engineered Bone and Cartilage. *Biomaterials* **28,** 2465–2478 (2007).

429. Kennedy, D. F. Studies of peptides forming 310-and. alpha.-helixes and. beta.-bend ribbon structures in organic solution and in model biomembranes by Fourier transform infrared spectroscopy. *Biochemistry (Mosc.)* **30,** 6541 (1991).

430. Freij-Larsson, C., Nylander, T., Jannasch, P. & Wesslén, B. Adsorption behaviour of amphiphilic polymers at hydrophobic surfaces: effects on protein adsorption. *Biomaterials* **17,** 2199–2207 (1996).

431. Nejadnik, M. R., van der Mei, H. C., Norde, W. & Busscher, H. J. Bacterial adhesion and growth on a polymer brush-coating. *Biomaterials* **29,** 4117–4121 (2008).

432. Boehrs, J., Zaharias, R. S., Laffoon, J., Ko, Y. J. & Schneider, G. B. Three-Dimensional Culture Environments Enhance Osteoblast Differentiation. *J. Prosthodont.* **17,** 517–521 (2008).

433. Cancedda, R., Bianchi, G., Derubeis, A. & Quarto, R. Cell therapy for bone disease: a review of current status. *Stem Cells Dayt. Ohio* **21,** 610–619 (2003).

434. Lian, J. B. & Stein, G. S. Development of the osteoblast phenotype: molecular mechanisms mediating osteoblast growth and differentiation. *Iowa Orthop. J.* **15,** 118–140 (1995).

435. Owen, T. A. *et al.* Pleiotropic Effects of Vitamin D on Osteoblast Gene Expression Are Related to the Proliferative and Differentiated State of the Bone Cell Phenotype: Dependency upon Basal Levels of Gene Expression, Duration of Exposure, and Bone Matrix Competency in Normal Rat Osteoblast Cultures. *Endocrinology* **128,** 1496–1504 (1991).

436. Stein, G. S., Lian, J. B. & Owen, T. A. Relationship of cell growth to the regulation of tissue-specific gene expression during osteoblast differentiation. *FASEB J.* **4,** 3111–3123 (1990).

437. Quarles, L. D., Yohay, D. A., Lever, L. W., Caton, R. & Wenstrup, R. J. Distinct proliferative and differentiated stages of murine MC3T3-E1 cells in culture: an in vitro model of osteoblast development. *J. Bone Miner. Res. Off. J. Am. Soc. Bone Miner. Res.* **7,** 683–692 (1992).

438. Shalhoub, V. *et al.* Glucocorticoids promote development of the osteoblast phenotype by selectively modulating expression of cell growth and differentiation associated genes. *J. Cell. Biochem.* **50,** 425–440 (1992).

439. Zhu, J.-X., Sasano, Y., Takahashi, I., Mizoguchi, I. & Kagayama, M. Temporal and Spatial Gene Expression of Major Bone Extracellular Matrix Molecules During Embryonic Mandibular Osteogenesis in Rats. *Histochem. J.* **33,** 25–35 (2001).

440. Langenbach, F. *et al.* Scaffold-free microtissues: differences from monolayer cultures and their potential in bone tissue engineering. *Clin. Oral Investig.* **17,** 9–17 (2013).

441. Tzaphlidou, M. Bone Architecture: Collagen Structure and Calcium/Phosphorus Maps. *J. Biol. Phys.* **34,** 39–49 (2008).

442. Fountos, G., Kounadi, E., Tzaphlidou, M., Yasumura, S. & Glaros, D. The effects of inflammation-mediated osteoporosis (IMO) on the skeletal Ca/P ratio and on the structure of rabbit bone and skin collagen. *Appl. Radiat. Isot. Data Instrum. Methods Use Agric. Ind. Med.* **49,** 657–659 (1998).

443. Devanand Venkatasubbu, G., Ramasamy, S., Ramakrishnan, V. & Kumar, J. Nanocrystalline hydroxyapatite and zinc-doped hydroxyapatite as carrier material for controlled delivery of ciprofloxacin. *3 Biotech* **1,** 173–186 (2011).

444. Tzaphlidou, M. & Zaichick, V. Calcium, Phosphorus, calcium-phosphorus ratio in rib bone of healthy humans. *Biol. Trace Elem. Res.* **93,** 63–74 (2003).

445. Ergun, C. *et al.* Increased osteoblast adhesion on nanoparticulate calcium phosphates with higher Ca/P ratios. *J. Biomed. Mater. Res. A* **85,** 236–241 (2008).

446. Schneider, G. B., Boehrs, J. K., Hoopes, J. V. & Seabold, D. A. Use of 3-dimensional environments to engineer osseous-like tissue. *J. Dev. Biol. Tissue Eng.* **3,** 42–47 (2011).

447. Marí-Buyé, N., Luque, T., Navajas, D. & Semino, C. E. Development of a three-dimensional bone-like construct in a soft self-assembling peptide matrix. *Tissue Eng. Part A* **19,** 870–881 (2013).

448. Arufe, M. c., De la Fuente, A., Fuentes, I., de Toro, F. j. & Blanco, F. j. Chondrogenic potential of subpopulations of cells expressing mesenchymal stem cell markers derived from human synovial membranes. *J. Cell. Biochem.* **111,** 834–845 (2010).

449. Kim, I. S., Song, Y. M., Lee, B. & Hwang, S. J. Human mesenchymal stromal cells are mechanosensitive to vibration stimuli. *J. Dent. Res.* **91,** 1135–1140 (2012).

450. Radtke, C. L. *et al.* Osteogenic potential of sorted equine mesenchymal stem cell subpopulations. *Can. J. Vet. Res. Rev. Can. Rech. Vét.* **79,** 101–108 (2015).

451. Janicki, P. Prediction of in vivo bone forming potency of bone marrow-derived human mesenchymal stem cells. *Eur. Cell. Mater.* **21,** 488 (2011).

452. Feng, G. Mesenchymal Stem Cells and Senescence. *Cloning Transgenesis* **2,** (2012).

453. Stolzing, A., Jones, E., McGonagle, D. & Scutt, A. Age-related changes in human bone marrow-derived mesenchymal stem cells: Consequences for cell therapies. *Mech. Ageing Dev.* **129,** 163–173 (2008).

454. Leonardi, E., Devescovi, V., Perut, F., Ciapetti, G. & Giunti, A. Isolation, characterisation and osteogenic potential of human bone marrow stromal cells derived from the medullary cavity of the femur. *Chir. Organi Mov.* **92,** 97–103 (2008).

455. Yoo, J. J., Bang, J. H., Koo, K. H., Yoon, K. S. & Kim, H. J. Isolation Yield and Osteogenic Potential of Human Bone Marrow Stromal Cells are Maintained Irrespective of Age or Gender. *Key Eng. Mater.* **361–363,** 1149–1152 (2008).

456. Payne, K. A., Didiano, D. M. & Chu, C. R. Donor sex and age influence the chondrogenic potential of human femoral bone marrow stem cells. *Osteoarthritis Cartilage* **18,** 705–713 (2010).

457. Odorico, J. S., Kaufman, D. S. & Thomson, J. A. Multilineage differentiation from human embryonic stem cell lines. *Stem Cells Dayt. Ohio* **19,** 193–204 (2001).

458. Blancas, A. A., Chen, C.-S., Stolberg, S. & McCloskey, K. E. Adhesive forces in embryonic stem cell cultures. *Cell Adhes. Migr.* **5,** 472–479 (2011).

459. Gumbiner, B. M. Regulation of cadherin-mediated adhesion in morphogenesis. *Nat. Rev. Mol. Cell Biol.* **6,** 622–634 (2005).

460. Halbleib, J. M. & Nelson, W. J. Cadherins in development: cell adhesion, sorting, and tissue morphogenesis. *Genes Dev.* **20,** 3199–3214 (2006).

461. Lien, W.-H., Klezovitch, O. & Vasioukhin, V. Cadherin–catenin proteins in vertebrate development. *Curr. Opin. Cell Biol.* **18,** 499–506 (2006).

462. Eckfeldt, C. E., Mendenhall, E. M. & Verfaillie, C. M. The molecular repertoire of the ‘almighty’ stem cell. *Nat. Rev. Mol. Cell Biol.* **6,** 726–737 (2005).

463. Larue, L., Ohsugi, M., Hirchenhain, J. & Kemler, R. E-cadherin null mutant embryos fail to form a trophectoderm epithelium. *Proc. Natl. Acad. Sci.* **91,** 8263–8267 (1994).

464. Larue, L. *et al.* A role for cadherins in tissue formation. *Dev. Camb. Engl.* **122,** 3185–3194 (1996).

465. Vestweber, D. & Kemler, R. Rabbit antiserum against a purified surface glycoprotein decompacts mouse preimplantation embryos and reacts with specific adult tissues. *Exp. Cell Res.* **152,** 169–178 (1984).

466. Damjanov, I., Damjanov, A. & Damsky, C. H. Developmentally regulated expression of the cell-cell adhesion glycoprotein cell-CAM 120/80 in peri-implantation mouse embryos and extraembryonic membranes. *Dev. Biol.* **116,** 194–202 (1986).

467. Butz, S. & Larue, L. Expression of catenins during mouse embryonic development and in adult tissues. *Cell Adhes. Commun.* **3,** 337–352 (1995).

468. Herrmann, B. G. Expression pattern of the Brachyury gene in whole-mount TWis/TWis mutant embryos. *Dev. Camb. Engl.* **113,** 913–917 (1991).

469. Hoffmann, I. & Balling, R. Cloning and expression analysis of a novel mesodermally expressed cadherin. *Dev. Biol.* **169,** 337–346 (1995).

470. Hatta, K. & Takeichi, M. Expression of N-cadherin adhesion molecules associated with early morphogenetic events in chick development. *Nature* **320,** 447–449 (1986).

471. Miyatani, S. *et al.* Neural cadherin: role in selective cell-cell adhesion. *Science* **245,** 631–635 (1989).

472. Matsunami, H. & Takeichi, M. Fetal brain subdivisions defined by R- and E-cadherin expressions: evidence for the role of cadherin activity in region-specific, cell-cell adhesion. *Dev. Biol.* **172,** 466–478 (1995).

473. Okazaki, M. *et al.* Molecular cloning and characterization of OB-cadherin, a new member of cadherin family expressed in osteoblasts. *J. Biol. Chem.* **269,** 12092–12098 (1994).

474. Cheng, S. L. *et al.* Human osteoblasts express a repertoire of cadherins, which are critical for BMP-2-induced osteogenic differentiation. *J. Bone Miner. Res. Off. J. Am. Soc. Bone Miner. Res.* **13,** 633–644 (1998).

475. Kawaguchi, J., Kii, I., Sugiyama, Y., Takeshita, S. & Kudo, A. The transition of cadherin expression in osteoblast differentiation from mesenchymal cells: consistent expression of cadherin-11 in osteoblast lineage. *J. Bone Miner. Res. Off. J. Am. Soc. Bone Miner. Res.* **16,** 260–269 (2001).

476. Mbalaviele, G., Shin, C. S. & Civitelli, R. Perspective: Cell–Cell Adhesion and Signaling Through Cadherins: Connecting Bone Cells in Their Microenvironment. *J. Bone Miner. Res.* **21,** 1821–1827 (2006).

477. Gündüz, V., Kong, E., Bryan, C. D. & Hinds, P. W. Loss of the retinoblastoma tumor suppressor protein in murine calvaria facilitates immortalization of osteoblast-adipocyte bipotent progenitor cells characterized by low expression of N-cadherin. *Mol. Cell. Biol.* **32,** 2561–2569 (2012).

478. Lee, E. J. *et al.* Spherical Bullet Formation via E-cadherin Promotes Therapeutic Potency of Mesenchymal Stem Cells Derived From Human Umbilical Cord Blood for Myocardial Infarction. *Mol. Ther.* **20,** 1424–1433 (2012).

479. Carmeliet, P. & Jain, R. K. Angiogenesis in cancer and other diseases. *Nature* **407,** 249–257 (2000).

480. Haynesworth, S. E., Baber, M. A. & Caplan, A. I. Cell surface antigens on human marrow-derived mesenchymal cells are detected by monoclonal antibodies. *Bone* **13,** 69–80 (1992).

481. Le Blanc, K., Tammik, L., Sundberg, B., Haynesworth, S. E. & Ringdén, O. Mesenchymal stem cells inhibit and stimulate mixed lymphocyte cultures and mitogenic responses independently of the major histocompatibility complex. *Scand. J. Immunol.* **57,** 11–20 (2003).

482. Laschke, M. W. *et al.* Three-dimensional spheroids of adipose-derived mesenchymal stem cells are potent initiators of blood vessel formation in porous polyurethane scaffolds. *Acta Biomater.* **9,** 6876–6884 (2013).

483. Bhang, S. H., Lee, S., Shin, J.-Y., Lee, T.-J. & Kim, B.-S. Transplantation of cord blood mesenchymal stem cells as spheroids enhances vascularization. *Tissue Eng. Part A* **18,** 2138–2147 (2012).

484. Sikavitsas, V. I., van den Dolder, J., Bancroft, G. N., Jansen, J. A. & Mikos, A. G. Influence of the in vitro culture period on the in vivo performance of cell/titanium bone tissue-engineered constructs using a rat cranial critical size defect model. *J. Biomed. Mater. Res. A* **67,** 944–951 (2003).

485. Holtorf, H. L., Jansen, J. A. & Mikos, A. G. Modulation of cell differentiation in bone tissue engineering constructs cultured in a bioreactor. *Adv. Exp. Med. Biol.* **585,** 225–241 (2006).

486. Tzima, E. *et al.* A mechanosensory complex that mediates the endothelial cell response to fluid shear stress. *Nature* **437,** 426–431 (2005).

487. Saleh, F. A., Whyte, M. & Genever, P. G. Effects of endothelial cells on human mesenchymal stem cell activity in a three-dimensional in vitro model. *Eur. Cell. Mater.* **22,** 242–257; discussion 257 (2011).

488. Saleh, F. A., Whyte, M. & Genever, P. G. Effects of endothelial cells on human mesenchymal stem cell activity in a three-dimensional in vitro model. *Eur. Cell. Mater.* **22,** 242–257; discussion 257 (2011).

489. Stahl, A. *et al.* Bi-directional cell contact-dependent regulation of gene expression between endothelial cells and osteoblasts in a three-dimensional spheroidal coculture model. *Biochem. Biophys. Res. Commun.* **322,** 684–692 (2004).

490. Steinberg, M. S. ON THE MECHANISM OF TISSUE RECONSTRUCTION BY DISSOCIATED CELLS, III. FREE ENERGY RELATIONS AND THE REORGANIZATION OF FUSED, HETERONOMIC TISSUE FRAGMENTS*. *Proc. Natl. Acad. Sci. U. S. A.* **48,** 1769–1776 (1962).

491. Noria, S., Cowan, D. B., Gotlieb, A. I. & Langille, B. L. Transient and steady-state effects of shear stress on endothelial cell adherens junctions. *Circ. Res.* **85,** 504–514 (1999).

492. Kanatani, K. Effects of convection and diffusion of the vapour in evaporating liquid films. *J. Fluid Mech.* **732,** 128–149 (2013).

493. Scheid, B. *et al.* Onset of thermal ripples at the interface of an evaporating liquid under a flow of inert gas. *Exp. Fluids* **52,** 1107–1119 (2011).

494. Guillotin, B. *et al.* Human primary endothelial cells stimulate human osteoprogenitor cell differentiation. *Cell. Physiol. Biochem. Int. J. Exp. Cell. Physiol. Biochem. Pharmacol.* **14,** 325–332 (2004).

495. Villars, F. *et al.* Effect of HUVEC on human osteoprogenitor cell differentiation needs heterotypic gap junction communication. *Am. J. Physiol. Cell Physiol.* **282,** C775-785 (2002).

496. Bidarra, S. J. *et al.* Phenotypic and proliferative modulation of human mesenchymal stem cells via crosstalk with endothelial cells. *Stem Cell Res.* **7,** 186–197 (2011).